UNIVERSIDADE FEDERAL DO RIO GRANDE DO SUL
PROGRAMA DE PÓS-GRADUAÇÃO EM FÍSICA
Tese de Doutorado

# Integrability in the design and control of quantum devices *

Integrabilidade no projeto e no controle de dispositivos quânticos

**Karin Wittmann Wilsmann**

A Doctoral Thesis written under the supervision of Prof[a]. Dr[a]. Angela Foerster and presented at the Institute of Physics of Universidade Federal do Rio Grande do Sul in fulfillment of the requirements for the PhD in Physics degree.

Junho 2022

*Trabalho financiado pelo Conselho Nacional de Desenvolvimento Científico e Tecnológico (CNPq).

# Abstract

The precise control of quantum systems will play an important role in the realization of atomtronic devices. In this thesis, we show how to explore the concept of integrability to guide the design of ultracold atom devices with potential application in emerging quantum technologies. Starting from a family of integrable multi-well Hamiltonians, which describe interactions between dipolar bosons and tunneling of bosons between adjacent wells, we investigate and find physical applications for the three and the four well cases. Initially, we conduct a study of the quantum dynamics of the triple-well system to probe the conditions under which a switching behavior can occur. Through variation of the external field, we demonstrate how the system can be controlled between various "switched-on" and "switched-off" configurations. In addition, we investigate the generation of entangled states in this model for a large range of Fock initial states. In sequence, we study the four-well model, communicating the design of interferometric protocols through analytic formulae. These expose the system as an interferometric identifier and producer of NOON states (entangled state related to the Schrödinger cat state). Then, we design two protocols, one probabilistic and another deterministic, to transform initial Fock states into NOON states, enabling phase encoding with high fidelity. The physical feasibility of both devices is also discussed via ultracold dipolar atoms trapped in optical setups. Since these physical setups could, in principle, be utilized in other resources, we also make a preliminary discussion of the onset of quantum chaos in the triple-well model.

# Sumário

O controle preciso de sistemas quânticos desempenhará um papel importante na realização de dispositivos atomtrônicos. Nesta tese, mostramos como explorar o conceito de integrabilidade para orientar o projeto de dispositivos de átomos ultrafrios com potencial aplicação em tecnologias quânticas emergentes. Partindo de uma família de hamiltonianos multi-poços integráveis, que descrevem interações entre bósons dipolares e tunelamento de bósons entre poços adjacentes, escolhemos os casos de três e quatro poços para explorar possíveis aplicações físicas. Inicialmente, realizamos um estudo da dinâmica quântica do sistema de poço triplo para investigar as condições sob as quais um comportamento do tipo transistor pode ocorrer. Através da variação de um campo externo, demonstramos como o sistema pode ser controlado entre várias configurações de "ligado" e "desligado", simulando um *switching device*. Além disso, investigamos a capacidade do sistema em gerar estados emaranhados através de sua evolução temporal, para uma grande variedade de estados iniciais de Fock. Na sequência, estudamos o modelo de quatro poços, comunicando o projeto de protocolos interferométricos por meio de expressões analíticas. Estes expõem o sistema como um identificador interferométrico e produtor de estados NOON (estado emaranhado relacionado ao estado do gato de Schrödinger). Em seguida, projetamos dois protocolos, um probabilístico e outro determinístico, para transformar estados iniciais de Fock em estados NOON, indicando como codificar fases com alta fidelidade. A viabilidade física de ambos dispositivos é discutida através de átomos dipolares ultrafrios aprisionados em configurações ópticas. Como essas configurações físicas podem, em princípio, ser utilizadas para investigar outros fenômenos quânticos, também apresentamos uma discussão preliminar sobre o prefácio do caos quântico no modelo de poço triplo.

# Press Release

Quantum mechanics is a probabilistic theory that very accurately simulates the behavior of microscopic, atomic, and subatomic physical systems. It arises gradually, to account for experimental results not explained by Newtonian physics. One of the first important insights was the recognition that every quantum entity presents a dual wave-particle behavior, which reveals the probabilistic behavior of quantum systems. The wave-particle duality and the Uncertainty Principle are the soul of the Theory of Quantum Mechanics, and underlie quantum phenomena such as tunneling, superposition of states, and entanglement. These phenomena are still weird to us, but they have great potential to drive information technologies, mainly because quantum information can coexist, in an entangled way, in different locations, while they can also coexist in the same place, in a superposition of states, as in Schrödinger's thought experiment (1935), where a theoretical cat can be simultaneously in both "dead" and "alive" states.

Quantum phenomena, in general, are not easily observed. But there is a state of matter, predicted by Einstein in 1925, where these phenomena reveal themselves to the real world. One architecture for implementing this state is through ultracold atomic systems, where atoms are trapped and cooled to temperatures close to absolute zero. In this environment, the wave behavior of an atom is pronounced and the superposition of these waves forms a new state of matter known as a Bose-Einstein condensate (BEC). The BEC was obtained experimentally in 1995, stirring up the scientific milieu and boosting the area of ultracold atoms. Systems of ultracold atoms have been used as instruments of conceptual research and as an alternative to new quantum technologies, giving rise to the area of Atomotronics!

In this thesis, we present designs of quantum devices that can, in principle, be implemented through ultracold atom technologies. To describe these systems, we use integrable mathematical models. Integrability in mathematics refers to equations with special characteristics that allow a deep understanding of their properties. In our work, we find new applications of integrability to gain an understanding of how to prepare

physical quantum states and devices. First, we show how to accurately produce and control a switching device, analogous to a transistor, for ultracold atoms trapped in a three potential well optical system. We show that this system also has an intrinsic ability to generate entangled states. Stimulated by these findings, we study an integrable model of four potential wells, in the search for a certain class of entangled quantum states, known as NOON states, which are analogous to the *cat-states*. Using this structure, we design protocols to generate systems of both interferometry and NOON states, with accurate phase encoding, with potential applications in quantum metrology, sensing and information.

Our work exposes an important and inspiring role of integrability in the development of new technologies in quantum physics. We believe that the proposed models have great appeal in the implementation of ultracold atom technologies, possibly acting as building blocks in the emerging quantum technologies!

# Published Works

The thesis was structured from the articles listed below, that represent the research developed in my doctorate. The articles are distributed by chapter as follows:

1. Chapter 2:
   **Control of tunneling in atomtronic switching device**, Karin Wittmann Wilsmann, Leandro H. Ymai, Arlei P. Tonel, Jon Links, and Angela Foerster. *Comm. Phys.*, **1**, 91 (2018), doi:10.1038/s42005-018-0089-1.

   This work was recognized by the Nature Community, which invited us to contribute with different chronicles to the Nature Portfolio blog. The three texts were also published on Nature's twitter.

   * *Breaking eggs to make an omelette - how we cooked up an atomtronic switch*, 2018.
   * *A balancing act*, 2019. It was also released on Nature's twitter in honor of International Women's Day.
   * *Lunch will be served from NOON*, 2020.

2. Chapter 3:
   **Entangled states of dipolar bosons generated in a triple-well potential**, Arlei P. Tonel, Leandro H. Ymai, Karin Wittmann W., Angela Foerster, and Jon Links. *SciPost Phys. Core 2*, **2**, 3 (2020), doi:10.21468/SciPostPhysCore.2.1.003

3. Chapter 4:
   **Integrable atomtronic interferometry**, Daniel S. Grun, Leandro H. Ymai, Karin Wittmann W., Arlei P. Tonel, Angela Foerster, and Jon Links. *Phys. Rev. Lett.*, **129**, 020401 (2022), doi:10.1103/PhysRevLett.129.020401

4. Chapter 5:
   **Protocol designs for NOON states**, Daniel S. Grun, Karin Wittmann W., Leandro H. Ymai, Jon Links, and Angela Foerster. *Comm. Phys.*, **5**, 36 (2022), doi:10.1038/s42005-022-00812-7

Note: The first three authors contributed equally. The names are in alphabetical order!

5. Chapter 6:
   **Interacting bosons in a triple well: Preface of many-body quantum chaos**. Karin Wittmann W., Erick R. Castro, Angela Foerster, and Lea F. Santos. *Phys. Rev. E*, **105**, 034204 (2022), doi:10.1103/PhysRevE.105.034204

# Agradecimentos

Dedico meu profundo agradecimento à professora Angela Foerster, por me orientar ao longo desses anos com admirável serenidade, encorajamento e envolvimento!

Sou, também, eternamente grata às pessoas que me mostraram o caminho da ciência: meu primeiro mentor, Rogério Steffenon, que me incentivou e direcionou para a UFRGS; e Kepler de Souza Oliveira Filho e Paulo Machado Mors, outras duas pessoas admiráveis que me inspiraram, apoiaram e acolheram no início da trajetória, na UFRGS.

Estendo meus agradecimentos aos meus queridos colegas, por sua amizade e pelas frutíferas discussões. Em particular, agradeço a Leandro Hayato Ymai, por trazer sua clareza analítica, sua calma, e por me amparar nas diversas vezes em que precisei! Dedico um agradecimento especial ao Jon Links, que compartilhou, de forma resoluta, seu profundo conhecimento! Tive muita sorte em tê-lo no grupo. Também, agradeço imensamente a Lea Ferreira dos Santos, por me acolher em seu reduto, em New York, e me ensinar tanto sobre sua pesquisa!

Agradeço ao Programa de Pós-Graduação do Instituto de Física, da UFRGS, o apoio recebido, e ao CNPq o suporte financeiro.

Agradeço a meus pais e meus irmãos por sua compreensão e apoio!

Entrego meu infinito, imensurável, agradecimento para minha amada família, meu marido Fernando e meus filhos Thomas e Óliver, pelo seu amor, contínuo apoio e imensa paciência! Amo muito vocês!

# Contents

# Chapter 1

# Introduction

What are the possible shortcuts to more efficient technologies?

Recently, a promising path has been opened for the development of new quantum technologies, previously unimaginable. It accesses the deepest regimes of the quantum world, where uncertainties reign and strange quantum properties, such as tunneling, superposition of states and entanglement, emerge! In fact, tunneling is the quantum phenomenon behind several modern technological devices. It is the phenomenon behind the transistor, which is used to implement the binary digit 0 and 1 [1] (bit) - considered the most basic unit of information used in digital communication and modern computing, by controlling the flow of electrons in the circuit. Therefore, the transistor is considered the building block of modern electronics, and a precursor of the First Quantum Revolution and of the technological miniaturization. For this contribution, which has profoundly changed our lives, the creators John Bardeen and Walter Brattain and their adviser William Shockley, shared the Nobel Prize in Physics in 1956.

Technologies have evolved significantly after the production of the first transistor. Today we are experiencing a new technological revolution. In the words of Dowling and Milburn, "In the Second Quantum Revolution, we are now actively employing quantum mechanics to alter the quantum face of our physical world. (...) The objective of quantum technology is to deliver useful devices and processes that are based on quantum principles."[2] In quantum domain, the basic unit of information is the qubit (quantum bit), which is formed by a superposition of two coherent states, usually described by a linear combination of the basis vectors $|0\rangle$ and $|1\rangle$, which can be physically implemented by a two-state quantum device [3].

Quantum technologies have evolved mainly in the areas of electronics and photonics, but recently a new experiment has seduced the scientific community. It was in 1995, when Eric Cornell and Carl Wieman [4], and independently Wolfgang Ketterle, using atomic gas trapping and cooling techniques, achieved a Bose-Einstein condensate (BEC), as predicted by Albert Einstein from the statistics of Satyendra Nath Bose,

around 1925. The technique basically consists of using a laser to slow down a beam of atoms enough to be captured in a magneto-optical trap, where it is then cooled by evaporation. When the gas reaches the critical temperature, close to absolute zero, and the de Broglie wavelength reaches the order of spacing between the atoms, the Bose-Einstein condensate is formed [4]. For the realization of Bose-Einstein condensation in dilute gases of atoms, the three physicists shared the 2001 Nobel Prize in Physics [5]. Soon this cooling technology was implemented and improved in different experimental laboratories around the world.

This remarkable discovery boosted the field of ultracold atoms, from which several branches of investigation flourished. One of these areas specificall investigates configurations of BEC's trapped in optical lattices. These optical systems have, among others, the great advantage of being very adaptable[6]. An optical lattice is formed by the interference of counter-propagating laser beams, creating a spatially periodic pattern, up to three dimensions. By properly configuring the lasers (intensity, wavelength and relative angle between them), the shape of the potentials can be adjusted in order to control the interaction between the atoms and the probability of tunneling between sites, along with other features such as the choice of the atom itself. A 2D-optical lattice potential is illustrated in Figure 1.1.

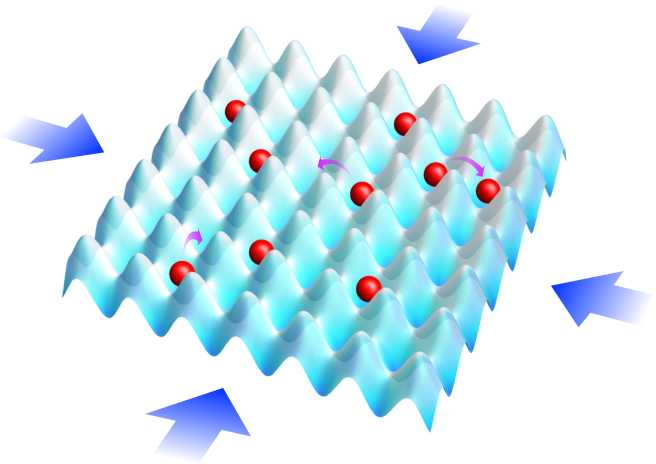

Figure 1.1: Scheme of a bosonic gas in a 2D-optical lattice. Cold atoms (represented by the red sphere) in a 2D optical lattice potential (represented as the blue surfaces) generated with two orthogonal sets of counter-propagating beams (indicated by the blue arrows). A vertical lattice (counter-propagating beam, not indicated here) provides confinement in the z-direction. The purple arrows represent the probability that an atom tunnels between neighboring sites (short-range tunneling). It is possible to generate a wide variety of potential configurations. Here we are presenting a basic 2D example.

The variety of geometries that can be created in optical lattice systems allow the physical realization of different Hamiltonians. One of the most popular models in this context is the Bose-Hubbard model (BHM) with short-range interactions and local

hopping terms [7, 8]. The particular case of the two-site (or two-well) Bose-Hubbard Hamiltonian has been very successful in modeling quantum tunneling [9, 10], displaying two principal dynamical scenarios. These are referred to as Josephson tunneling and self-trapping, and they have been experimentally observed [11]. In the case of tunneling, the system can also be controlled to produce either alternating or direct currents [12]. The success of the two-well BHM is also associated with its *integrability* [13–15]. However, the BHM with three or more wells is in general not integrable [16–23]. Integrability is achieved solely with two or with an infinite number of wells.

As the two-well BHM, a model idealized in the description of a physical system is one that provides accurate and reliable information about the evolution of the system and its physical properties. It is also desirable that it offers exact solutions that allow precise control, especially if it is designed to contribute to new quantum technologies. Physical systems that supposedly come closest to this idealization are those describing by *integrable* models. In this scenario, an integrable variant of the Bose-Hubbard model for multiple wells would be well received! A brief historical discussion on quantum integrability can be found in Appendix A, and a direct discussion of the subject can be seen in [14, 15].

A family of integrable multi-well tunneling models associated with exact solvability was proposed recently in [24, 25], which was achieved through the Yang-Baxter equation and associated algebraic Bethe Ansatz methods. Each model in this family is defined as a complete bipartite graph with $(n+m)$ modes that represent its number of degrees of freedom. Through a generalization of the algebraic Bethe ansatz technique, besides the (i) energy and (ii) total number of particles, all the (n + m)-2 additional independent conserved quantities required for integrability[1] were also derived, thus allowing for a complete solution of the models.

The general family of integrable multi-well Hamiltonians for $(n+m)$ wells in terms of a subset of canonical boson operators $a_i, a_i^\dagger$, $N_{a,i} = a_i^\dagger a_i$, $i = 1, ..., n$ and another subset $b_j, b_j^\dagger$, $N_{b,j} = b_j^\dagger b_j$, $j = 1, ..., m$, is given by

$$H_{n,m} = U(N_A - N_B)^2 + \sum_{i=1}^{n}\sum_{j=1}^{m} t_{i,j}(a_i b_j^\dagger + a_i^\dagger b_j), \tag{1.1}$$

where $N_A \equiv \sum_{i=1}^{n} a_i^\dagger a_i$ and $N_B \equiv \sum_{j=1}^{m} b_j^\dagger b_j$ represent the number of bosons in each subset of $n(m)$ wells, with $N = N_A + N_B$. It is worth noting that the exchange of indices of wells belonging to the same subset, leaves the Hamiltonian invariant. The coupling $U$ denotes the intra-well (short-range) and inter-well (long-range) interaction between

[1] One of the most common notions of integrability is that integrable systems have as many independent constants of motion as there are degrees of freedom. [14]

bosons, and $t_{ij}$ are the constant couplings for the tunneling amplitude. Physically, the Hamiltonians (1.1) describe quantum tunneling for bosonic systems in multiple (n + m) wells. Besides the apparent simplicity, these models show a rich and elegant mathematical structure. Note that integrability requires the presence of long-range couplings, which differentiates it from the usual Bose-Hubbard model. Notwithstanding, Bose-Hubbard models that include long-range interactions exist in the literature and are known as Extended Bose-Hubbard Models (EBHM), being also non-integrable in their general form. Here it is worth mentioning that EBHM have been realized in the lab by different groups using ultracold dipolar atoms, such as [26, 27].

An interesting feature of this integrable family is its bipartite structure, which can be divided into two subsets $A$ (with $n$ modes) and $B$ (with $m$ modes). In Figure 1.2 below, are shown geometric schemes for some of (n,m) cases of the general Hamiltonian (1.1). A broader description of the multi-well integrable Hamiltonian can be seen in Appendix B.

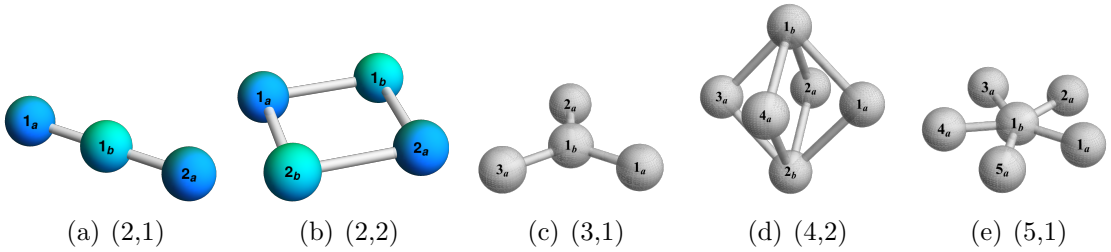

(a) (2,1) (b) (2,2) (c) (3,1) (d) (4,2) (e) (5,1)

Figure 1.2: Geometric schemes for some (n,m) modes cases of the multi-well integrable Hamiltonian (1.1). In panels (a) and (b) are shown the two models studied in this thesis, where the subsets $A$ and $B$ are highlighted in different colors.

Although this family of integrable Hamiltonians (1.1) has great potential for physical, and possibly technological, applications, its knowledge, until very recently, was essentially mathematical [28]. With the exception of the two-well $(1, 1)$ case, it was not known whether these models could describe any realistic physical system. However, as the two-well BHM had already shown itself to be a good model in the description of physical properties of ultracold matter, and ultracold dipolar atoms were already being theoretically and experimentally studied in this context, a deeper investigation of our new integrable models has become even more timely! From this perspective, in this thesis we investigate two of these new integrable models: the three-well $(2, 1)$ and four-well $(2, 2)$ cases of the general integrable Hamiltonian (1.1). Our purpose is to explore the possible advantages of integrability in the design of quantum devices for systems of ultracold dipolar atoms. As we will see, the systems describe dipole-dipole interactions (DDI) and tunneling between adjacent wells, for a population of ultracold dipole bosons loaded in an optical potential configuration. Atoms with large dipole

moments, such as chromium and dysprosium, were considered to implement the long-range interaction required for these integrable models. The three-well and the four-well models are presented separately below.

## 1.1 Integrable three wells model:

The three-well system opens up high possibilities for physical behavior [29–31], mainly as an ultracold version of a transistor [32], or a similar type of switching device. Therefore, we will study the triple-well model looking for a behavior similar to that of the electronic transistor, but in the domain of the emerging field of atomtronics (ultracold atoms tunneling between potential wells of optical systems)[33–36].

The (2,1) integrable Hamiltonian is given by

$$H_{(2,1)} = U(N_1 - N_2 + N_3)^2 + \frac{J_1}{\sqrt{2}}(a_1^\dagger a_2 + a_2^\dagger a_1) + \frac{J_3}{\sqrt{2}}(a_2^\dagger a_3 + a_3^\dagger a_2), \tag{1.2}$$

where $J_i$, $i = 1, 3$ are the coupling parameters for the tunneling between wells, $a_j^\dagger$, $a_j$ are the creation and annihilation operators for site $j$, $j = 1, 2, 3$ (the three bosonic degrees of freedom), respectively, while $N_j = a_j^\dagger a_j$ are the number operators. As the model has three degrees of freedom, three independent conserved quantities are required. In addition to the Hamiltonian and the total number of particles $N$, $N = N_1 + N_2 + N_3$, in this integrable case there is an extra conserved operator,

$$Q = J_1^2 N_3 + J_3^2 N_1 - J_1 J_3(a_1^\dagger a_3 + a_3^\dagger a_1),$$

satisfying the commutation relations

$$[H_{(2,1)}, N] = 0, \qquad [H_{(2,1)}, Q] = 0, \qquad [N, Q] = 0. \tag{1.3}$$

The conserved operator $Q$ will prove to be extremely relevant for the design and control of quantum systems, as it provides an effective Hamiltonian $H_{eff}$ which, in a resonant regime[2] that arises when $JN^{-1} \ll U \ll JN$ [10], produces analytic formulas for the tunneling frequency and amplitude, with remarkable accuracy when compared to numerical calculations.

*Relation between the integrable triple-well and the EBHM:* In order to discuss a possible physical realization of the system, we make contact with the work of Lahaye, Pfau and

[2]The resonant tunneling regime is characterised by near-perfect harmonic oscillations between the source (well 1) and the drain (well 3).

Santos, "Mesoscopic ensembles of polar bosons in triple-wells"[37], where they study the extended three-site Bose-Hubbard model. On this occasion, we found that our triple-well integrable model could be a particular case of the three-site EBHM for dipolar bosons, which is given by [26, 38],

$$\mathcal{H} = \frac{U_0}{2}\sum_{i=1}^{3} N_i(N_i-1) + \sum_{i=1}^{3}\sum_{j=1,j\neq i}^{3} \frac{U_{ij}}{2} N_i N_j + J_1(a_1^\dagger a_2 + a_1 a_2^\dagger) + J_3(a_2^\dagger a_3 + a_2 a_3^\dagger), \tag{1.4}$$

as long as the integrability condition[3] $U_{13} = U_0$ is satisfied. Here, $U_0$ is the coupling constant for on-site interactions, while the parameters $U_{ij} = U_{ji}$, $i \neq j$ characterize DDI between particles on different sites. The integrable parameter $U$ depends on $U_0$ through the condition $U = (\alpha - 1)U_0/4$, with the parameter $\alpha$ $(4 \leq \alpha \leq 8)$ (See details in the 3.7.1) depending only on the geometry of the trap [37]. A discussion about a possible physical realization of this system will be presented in the thesis. (See Appendix C for experimental feasibility details.)

**Breaking integrability to control**

To control the quantum dynamics of the system, an extra term $H_1 = \epsilon(N_3 - N_1)$ is added to the Hamiltonian (1.1), which breaks the integrability of the resulting Hamiltonian relative to the conserved quantity $Q$, resulting in a non-zero commutator $[H, Q] \neq 0$. This term can be understood as an external field applied to the wells labeled 1 and 3 (subset $A$).

A geometric scheme of the three well model and a representation of the external field acting on the triple wells is shown in Fig. 1.3, below.

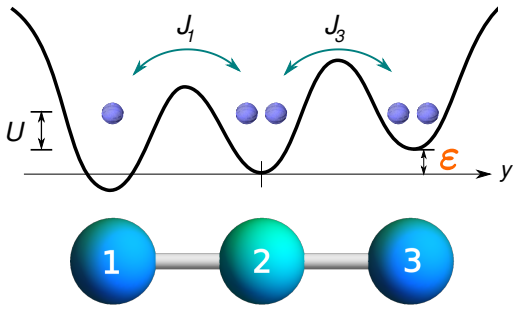


Figure 1.3: Geometric scheme (bottom) and potential representation (upper) of the triple-well Hamiltonian. The blue spheres represent wells $1, 3$ of the subset $A$ and the cyan sphere represents well 2 of the subset $B$. The bars indicate the tunneling $(J_i)$ between the neighboring wells and $\varepsilon$ the external field. The individual wells can be identified as source, port and drain.

[3]Condition that arises due to the bipartite structure of the integrable model.

Using this structure, we demonstrate how to design a theoretical and experimental configuration of a switching device with multi-level logical possibilities. As we will show, a surprising feature in this construction is that the ability to control the system in a predictable way arises through the breaking of integrability[4]. It is also established how to generate entangled states for different initial states. These subjects are the contents of Chapters 2 and 3.

## 1.2 Integrable four wells model:

The next challenge targetes quantum information technologies.

The long-range anisotropic nature of the dipole interaction plays a relevant role in the static and dynamic properties of ultracold atoms. In special, it offers insights into a rich variety of physical phenomena, among which interferometry[37] and macroscopic cat-states[42] stand out. These remarkable potentialities led us to investigate the four-well integrable model of the Hamiltonian (1.1), with the expectation of achieving high-sensitivity interferometric systems, in addition to identifying the relevance of integrability in the generation of NOON states (belonging to the class of Schrödinger cat states). The (2,2) integrable Hamiltonian describes dipolar bosons confined to a closed circuit of four sites, and is given by

$$H_{(2,2)} = U(N_1 - N_2 + N_3 - N_4)^2 + \frac{J}{2}\left[(a_1^\dagger + a_3^\dagger)(a_2 + a_4) + (a_1 + a_3)(a_2^\dagger + a_4^\dagger)\right], \quad (1.5)$$

where $J$ is the coupling parameter for isotropic tunneling between wells; $a_j^\dagger$, $a_j$ are the creation and annihilation operators for site $j$, $j = 1, 2, 3, 4$ (the four bosonic degrees of freedom) and $N_j = a_j^\dagger a_j$ are the number operators. This model has four degrees of freedom, so in addition to the energy and the total number of particles $N = N_1 + N_2 + N_3 + N_4$, two extra independent conserved operators $Q_1$ and $Q_2$ are expected, which are given by

$$Q_1 = \tfrac{1}{2}(N_1 + N_3 - a_1^\dagger a_3 - a_3^\dagger a_1),$$
$$Q_2 = \tfrac{1}{2}(N_2 + N_4 - a_2^\dagger a_4 - a_4^\dagger a_2),$$

satisfying the commutation relations

$$[H_{(2,2)}, N] = 0, \quad [H_{(2,2)}, Q_i] = 0, \quad [Q_1, Q_2] = 0, \quad [N, Q_i] = 0, \quad j = 1, 2. \quad (1.6)$$

[4]We notice that the breaking of integrability has also been discussed in other physical scenarios. Some examples can be seen in [39–41].

Analogous to what was observed in the integrable triple-well model [43, 44], in the resonant tunneling regime, an effective Hamiltonian $H_{\text{eff}}$ can be obtained from the conserved operators $Q_i$, through consideration of second-order tunneling processes.

*Relation between the integrable four-well and the EBHM:* The integrable four-well model (1.5) can be obtained from the four-site EBHM [26, 38],

$$\begin{aligned} H =& \frac{U_0}{2}\sum_{i=1}^{4} N_i(N_i-1) + \sum_{i=1}^{4}\sum_{j=1,j\neq i}^{4} \frac{U_{ij}}{2} N_i N_j \\ & - \frac{J}{2}\left[(a_1^\dagger + a_3^\dagger)(a_2 + a_4) + (a_1 + a_3)(a_2^\dagger + a_4^\dagger)\right], \end{aligned} \tag{1.7}$$

as long as it complies with the integrability condition $U_0 = U_{13} = U_{24}$ and $U_{12} = U_{23} = U_{34} = U_{14}$. The integrable parameter $U$ depends on $U_0, U_{ij}$ through the condition $U = (U_{12} - U_0)/4$, with $U_{ij} = U_{ji}$. As we will show later, this connection facilitates a discussion of experimental feasibility of the system.

**Breaking integrability to control**

As in the case of the triple well, the control of quantum dynamics is performed by breaking the integrability of the four-well Hamiltonian. Here, two breaking terms are needed, one for each subset of wells: $H_A = \epsilon_A(N_3 - N_1)$ and $H_B = \epsilon_B(N_4 - N_2)$, which breaks the integrability with respect to the conserved quantities $Q_1$ and $Q_2$, resulting in non-zero commutators $[H, Q_i] \neq 0$. These terms can be understood as external fields applied to wells $\{1, 3\}$ (subset $A$) and $\{2, 4\}$ (subset $B$), respectively. A schematic representation of the four wells model and an illustration of the external field acting on the wells are shown in Fig. 1.4

By properly employing this model we show how to introduce protocols to generate NOON states. The NOON state is one of the most fundamental quantum systems of the next generation of platforms in quantum computing, communication, measurement, and simulation. It is defined as an "all and nothing" superposition of two different modes [45, 46]. For $N$ particles, it has the form

$$|\text{NOON}\rangle = \frac{1}{\sqrt{2}}\left(|N, 0\rangle + e^{i\varphi}|0, N\rangle\right) \tag{1.8}$$

where the phase $\varphi$ is typically used to record information in applications. These include: in the fields of quantum metrology and sensing, performing precision phase-interferometry at the Heisenberg limit[47] and overcoming diffraction limits in quan-

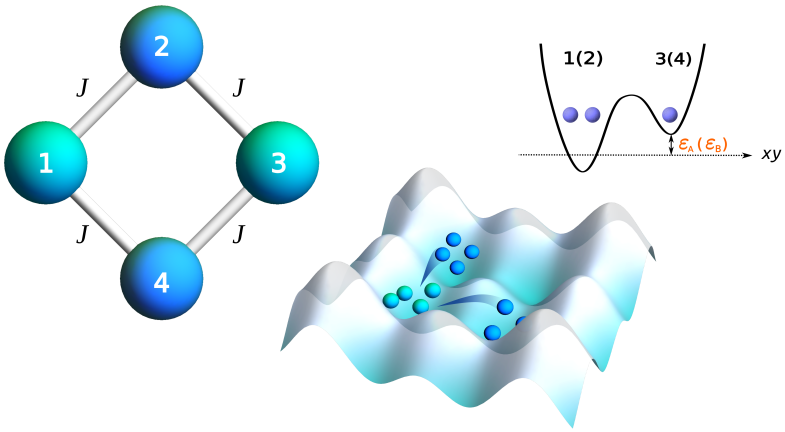


Figure 1.4: Geometric scheme (left) and potential representation (right) of the four-well Hamiltonian. Left: The spheres represent the four potential wells, while the bars refer to the tunneling ($J$) between neighboring wells. The different colors highlight the subset $A$ (wells 1 and 3) and $B$ (wells 2 and 4). Right: Sketch of the breaking of integrability through the external field $\varepsilon_A$ ($\varepsilon_B$) acting on the potential wells and, below, an illustrative detail of the four potential wells of an optical network is shown.

tum lithography[48]; in tests of fundamental physics, NOON states are used to study Bell-type inequalities violation[49]; they offer promising applications in Quantum Communication and Quantum Computing[50], and their utilization is expected to extend to areas such as chemistry and biology[51].

Here we propose two different atomtronic protocols to generate NOON states, exploring the four-well model. The integrability allows us to design a protocol with local measurement (deterministic) and another with post-selection measurement (probabilistic), while the external fields ($\varepsilon_A$, $\varepsilon_B$) can be used to control the system and encode phases into the NOON state. As we will show later, an added advantage of our protocols is that the evolution times are independent of total particle number, offering encouraging prospects for scalability.

In summary, the results obtained in this thesis for the triple and the four-well models demonstrate the potential and advantages of integrable systems in the design and control of quantum devices, providing new insights in the development of quantum technologies.

## Thesis Structuring

- In Chapter 2 we demonstrate how integrability, and the breaking of it, can be employed to investigate tunneling dynamics in a triple-well system. Using this knowledge, we show how to design a switching device. The experimental feasibility of this system is also discussed.

- In Chapter 3 we expand on the analysis conducted in Chapter 2. We first investigate the behavior of the system in relation to a variety of initial conditions and then turn our attention to analyzing the entanglement generation within the device under time-evolution.

- In Chapter 4 we discuss the main properties of the four-well integrable system, which describes the interaction of bosons confined to a closed circuit of four sites. We research an integrable atomtronic interferometry model with Heisenberg threshold sensitivity.

- The interferometric model obtained in Chapter 4 is proved to be a potential producer of NOON states. The production and control of NOON states is the subject of Chapter 5.

- In Chapter 6 we investigate the onset of chaos in the three-well model. We analyze under which conditions our integrable system can lead to chaos when its integrability is broken.

- Chapter 7 presents the conclusions and an outlook of the area.

# Chapter 2

# Control of tunneling in an atomtronic switching device

This chapter discusses how integrability, and the breaking of it, can be utilised to investigate the tunneling dynamics in a triple-well Hamiltonian with some control. We begin by identifying the resonant tunneling regime, where the particles can oscillate between well 1 (source) and well 3 (drain), by second-order processes. After that, we show that this resonant dynamics can be controlled through an applied external field, represented by adding a term that breaks the integrability of the Hamiltonian. Surprisingly, analytical formulae for the tunneling amplitude and frequency are obtained, even when the integrability is broken. As a major result, we show how this model can be implemented as an atomtronic switching device. In addition, we also discuss the experimental feasibility of the system. The main content of this chapter was published in Communications Physics[1]. This work was recognized by the Nature Research Communities, where we were invited to contribute in two blogs, [2] [3] [4] besides of being released on Nature's twitter.

## 2.1 Foreword

Here we investigate the control of tunneling in a triple-well system, for a population of ultracold dipolar bosons with large dipole moment, such as chromium and dysprosium,trapped in three aligned optical potentials. The main objective is to show how an integrable model can facilitate the creation of a switching device. The Hamiltonian has

[1] *Control of tunneling in an atomtronic switching*, K.W. Wilsmann, L.H. Ymai, A.P. Tonel, J. Links, and A. Foerster, Commun. Phys. **1**, 91 (2018), doi:10.1038/s42005-018-0089-1

[2] *Breaking eggs to make an omelette-how we cooked up an atomtronic switch*, Device Material Community - Nature, 2018.

[3] *A balancing act*, Nature Research Communities, 2019.

[4] *Lunch will be served from NOON*, Nature Communities, 2020.

the general structure [37]

$$\mathcal{H} = \frac{U_0}{2}\sum_{i=1}^{3} N_i(N_i-1) + \sum_{i=1}^{3}\sum_{j=1;j\neq i}^{3}\frac{U_{ij}}{2}N_iN_j - J_1(a_1^\dagger a_2 + a_1 a_2^\dagger) - J_3(a_2^\dagger a_3 + a_2 a_3^\dagger). \tag{2.1}$$

The canonical creation and annihilation operators, $a_i^\dagger$ and $a_i$, $i = 1, 2, 3$, represent the three bosonic degrees of freedom in the model, and $N_i = a_i^\dagger a_i$, $i = 1, 2, 3$ is the number operator for each well. The parameters $J_i$, $i = 1, 3$ are the couplings for the tunneling between wells, and $U_0$ is the coupling constant for on-site interactions which results from contact interactions and dipole-dipole interactions (DDI). Both of these can be either attractive or repulsive, which in principle allows for the manufacture of weak net on-site interaction. The parameters $U_{ij} = U_{ji}$, $i \neq j$ characterize DDI between particles on different sites. Although the DDI follows an inverse cubic law, it is also dependent on the angle between dipole orientation and the displacement between dipoles. In combination with the geometry of the trap potential (viz. oblate versus prolate), it is entirely feasible to adjust the system parameters across a wide range of values. Importantly, this includes the possibility for the inter-well couplings $U_{ij}$ to have greater magnitude than the on-site coupling $U_0$. The experimental feasibility of this system for dipolar bosons was detailed by Lahaye et al.[37], using a triple-well potential. The wells are aligned along the $y$-axis, separated by a distance $l$, with bosons polarized by a sufficiently large external field along the $z$-direction. It was shown that $U_{12} = U_{23} = \alpha U_{13}$, where the parameter $4 \leq \alpha \leq 8$ depends only on the ratio $l/\sigma_x$, where $\sigma_x$ is the width of the Gaussian cloud along the $x$-direction. (See Methods for further details.)

In the case when $U_{13} = U_0$, the Hamiltonian (2.1) is integrable [24]. In this limit there exists an additional conserved operator besides the Hamiltonian and the total particle number, such that the number of independent conserved operators is equal to the number of degrees of freedom. While for classical systems integrability is well-known to prohibit chaotic behavior, the consequences for quantum system are less understood [14, 15]. Notwithstanding, it is recognised that quantum integrability has far reaching impacts. One route to characterize the degree of chaoticity in a quantum system is through energy level spacing distributions [52]. Integrable systems tend to display Poissonian distributions [53], while non-integrable systems generally observe the Wigner surmise [54] following the Gaussian Orthogonal Ensemble, or similar [55, 56]. Another impact of quantum integrability is the absence of thermalisation, observed in a quantum version of Newton's cradle [13] and similar systems [57]. Here we will

demonstrate how integrability, and the breaking of it, can be utilised to investigate tunneling dynamics. This work contrasts the above mentioned studies in that it applies to a system with very low number of degrees of freedom.

## 2.2 Integrability

It has been established that an extension of the model (2.1) for the case of $N$-sites contains a family of integrable multi-well tunneling models [24] (See some information in Appendix B). In the three-wells case, when $U_{13} = U_0$, we can write it in the reduced form $H_0 = -\mathcal{H} + (\alpha + 1)U_0N^2/4 - U_0N/2$ yielding

$$\begin{aligned} H_0 = U(N_1 - N_2 + N_3)^2 \\ + J_1(a_1^\dagger a_2 + a_1 a_2^\dagger) + J_3(a_2^\dagger a_3 + a_2 a_3^\dagger), \end{aligned} \tag{2.2}$$

where $U = (\alpha - 1)U_0/4$ (See details in Suppl. Material 3.7.1). Note that (3.1) commutes with the total number operator $N = N_1 + N_2 + N_3$, and the interchange of the indices 1 and 3 leaves the Hamiltonian invariant. A schematic representation of this triple-well Hamiltonian is presented in Fig. 2.1 below.

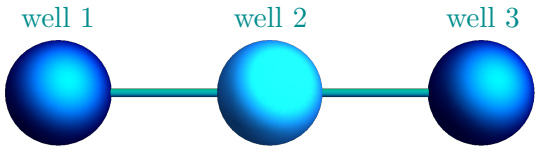


Figure 2.1: Geometric scheme of the integrable triple-well Hamiltonian. The spheres represent the wells 1,2 and 3, in sequence, and the bonds indicate the tunneling between the wells.

The Hamiltonian has, beyond the energy and the total number of particles $N$, another independent conserved quantity expressed through the operator [24]

$$Q = J_1^2 N_3 + J_3^2 N_1 - J_1 J_3(a_1^\dagger a_3 + a_3^\dagger a_1). \tag{2.3}$$

This conserved operator can alternatively be interpreted as a tunneling Hamiltonian for a two-well subsystem containing only wells 1 and 3. Because $Q$ admits the factorization $Q = \Omega^\dagger\Omega$, where $\Omega = J_1 a_3 - J_3 a_1$, the dynamical evolution governed by $Q$ is harmonic for any initial state. Later, it will be shown that $Q$ assumes a fundamental role in the analysis of resonant [58] quantum dynamics of the system (3.1). This arises due to an unexpected connection with virtual processes. Details are provided in Methods.

As the model has three degrees of freedom and three independent conserved quan-

tities satisfying

$$[H_0, N] = 0, \qquad [H_0, Q] = 0, \qquad [N, Q] = 0, \tag{2.4}$$

the model is integrable. Further details about the integrability, and associated exact solvability, have been established. This was achieved through the Yang-Baxter equation and associated Bethe Ansatz methods [24].

## 2.3 Breaking the integrability

In order to break the integrability we add to the Hamiltonian (3.1) the operator $H_1 = \epsilon(N_3 - N_1)$, which acts as an external field for the wells labeled 1 and 3. This is schematically shown in Fig. 2.2. It is important to observe that the above Hamiltonian still commutes with the operator $N$. However, the operator $Q$ is not conserved because the commutator $[H, Q] = 2\epsilon J_1 J_3 (a_1^\dagger a_3 - a_3^\dagger a_1)$ is non-zero when the parameters $\epsilon$, $J_1$ and $J_3$ are all non-zero.

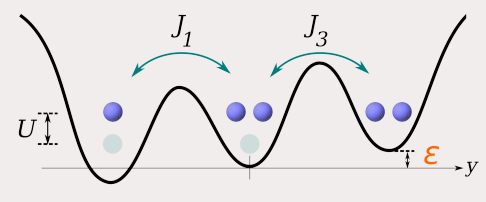


Figure 2.2: Schematic representation of the system. With reference to the Hamiltonian $H = H_0 + H_1$, the arrows $J_1$ and $J_3$ represent the tunneling couplings between the wells, $U$ characterizes inter-well and intra-well interaction between bosons, while $\epsilon$ is the coupling strength for an external field.

## 2.4 Structure of energy levels

The integrable three-well system (3.1) possesses many features in common with the two-well Bose-Hubbard model, which is also integrable because the total number operator is conserved and there are only two degrees of freedom. Set $J = \sqrt{J_1^2 + J_3^2}$. Following Leggett[10], it is useful to define the regimes:

*Rabi*: $U \ll JN^{-1}$.

*Josephson*: $JN^{-1} \ll U \ll JN$.

*Fock*: $JN \ll U$.

where in the two-well case the "Fock regime corresponds to a strongly quantum pendulum, while in the Rabi and Josephson regimes the behavior is (semi)classical"[10].

Adopting the same classification for the integrable three-well system given by (3.1), numerical computation of the energy spectrum shows that transition from the Rabi to the Josephson regime is accompanied by the emergence of energy bands. Illustrative results are depicted in Fig. 2.3. Hereafter units are chosen such that $\hbar = 1$, and for all figures isotropic tunneling $J_1/J = J_3/J = 1/\sqrt{2}$ is adopted for simplicity. The Hamiltonian acts on the Fock space spanned by the normalized vectors $|\mathcal{N}_1, \mathcal{N}_2, \mathcal{N}_3\rangle = \mathcal{C}^{-1}(a_1^\dagger)^{\mathcal{N}_1}(a_2^\dagger)^{\mathcal{N}_2}(a_3^\dagger)^{\mathcal{N}_3}|0\rangle$, where $\mathcal{C} = \sqrt{\mathcal{N}_1!\mathcal{N}_2!\mathcal{N}_3!}$ and $|0\rangle \equiv |0,0,0\rangle$ is the Fock vacuum. On each panel the line $E = UN^2$ is depicted. This quantity is the expectation value of the state $|N,0,0\rangle$. In the extreme Rabi regime with $U = 0$ the energy levels are uniformly distributed with spacing $\Delta E = J$. The line $E = UN^2$ emerges from the midpoint of the entire energy spectrum when $U = 0$, to lie on the lower edge of the uppermost energy band as $U$ is increased to bring the system into the Josephson regime. Note that the separation into distinct energy bands becomes very evident once the system is deep into the Josephson regime. These features significantly influence the dynamical evolution of the system from the initial state $|N,0,0\rangle$. In the Rabi regime, an accurate description of the initial state requires a linear combination over all eigenstates. However in the Josephson regime the state $|N,0,0\rangle$ can be accurately approximated as a linear combination of a subset of eigenstates, due to the band structure. This conclusion applies for all particles numbers, with the result represented in Fig. 2.3 depicting the cases $N = 30$ and $N = 60$. Provided $UN/J \gg 1$, the separation into bands is clearly identifiable. The consequences will be investigated at a deeper level in the next section, where we will fix $N = 60$. Moreover, it will be shown how the breaking of the integrability, through the application of an external field, allows for control of the dynamics in a predictable fashion.

## 2.5 Quantum dynamics

The time evolution of the expectation values for the number operators are computed using $\langle N_i\rangle = \langle\Psi(t)|N_i|\Psi(t)\rangle$, $i = 1,2,3$, where $|\Psi(t)\rangle = \exp(-iHt)|\phi\rangle$ and $|\phi\rangle$ represents an initial state. We adopt a protocol for which $|\phi\rangle = |N,0,0\rangle$, so the well labeled 1 is the source, the well labeled 2 is the gate, and the well labeled 3 is the drain.

We begin with the integrable model (3.1) and first consider variations in the interaction parameter $U$ to manipulate the tunneling across the wells. Fig. 2.4 presents results obtained for four choices of $U$. The dynamics typically display collapse and revival of oscillations in the Rabi regime, as in Fig. 2.4a. On increasing $U$, the period increases while the time-average of $\langle N_2\rangle$ decreases. Furthermore, the dynamics between wells 1 and 3 approach harmonic oscillations with $\langle N_1\rangle + \langle N_3\rangle \simeq N$. The transition between the Rabi and Josephson regimes can be seen, qualitatively, in the passage from Fig.

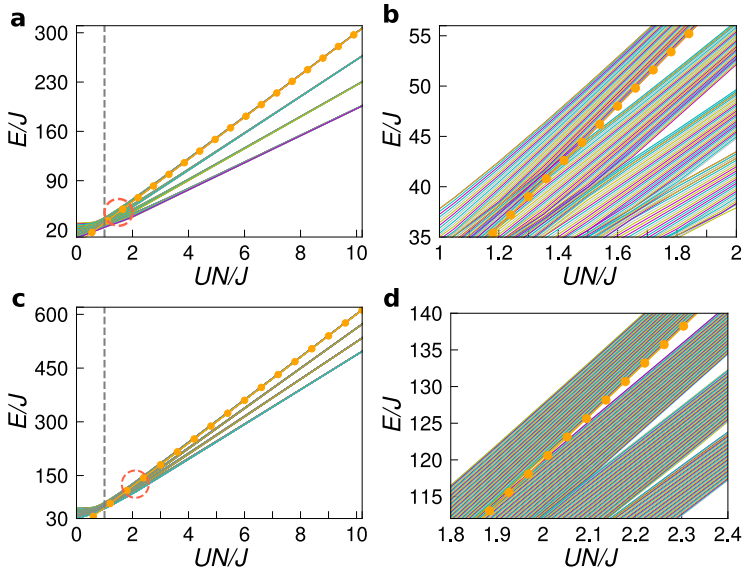


Figure 2.3: Energy level distributions. Results are shown for (3.1) in dimensionless units. Panels **a**, **b**: $N = 30$. Panels **c**, **d**: $N = 60$. The region marked with a circle on the panels **a**, **c** is enlarged in the panels **b**, **d**. The dashed vertical lines mark the threshold point, $UN/J = 1$, separating Rabi and Josephson regimes. The ball lines mark the expectation energy $E = UN^2$ of $|N, 0, 0, \rangle$. Only the four highest energy bands are plotted.

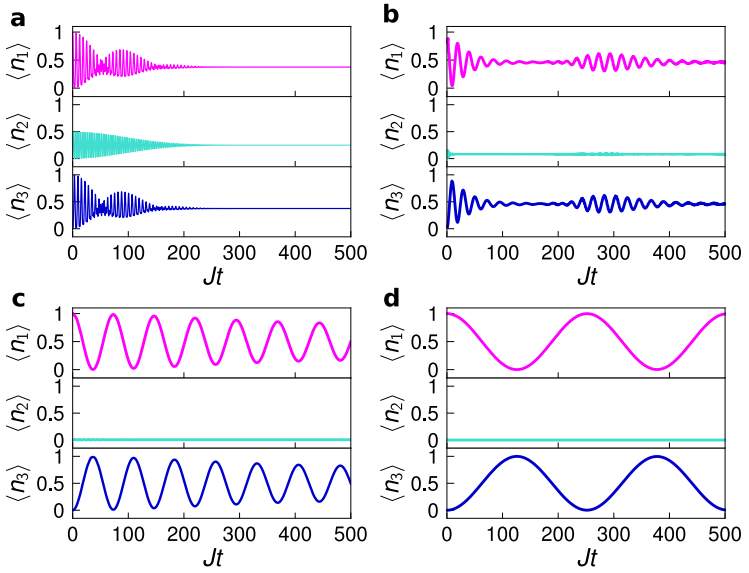


Figure 2.4: Time evolution of expectation values. Dimensionless units are used. In the integrable regime, the expectation values of the number operators are shown, with the initial state $|60, 0, 0\rangle$. The configuration used has $\epsilon/J = 0$. **a** $U/J = 0.001$; **b** $U/J = 0.015$; **c** $U/J = 0.05$; **d** $U/J = 0.17$. It is apparent that increasing $U$ leads to an increasing suppression of tunneling into the gate, while maintaining oscillations between the source and the drain. In the case **d** the expectation value of the number operator associated with the gate is negligible, so tunneling to the gate is considered to be switched-off. The oscillations between the source and the drain are close to being harmonic and coherent.

2.4b to Fig. 2.4c. This change in behaviour is in accord with the threshold point in Fig.2.3.

In this latter regime, Fig. 2.4c and 2.4d, these dynamical features can be understood by observing that the integrable Hamiltonian possesses a hidden two-well algebraic structure, with an effective well given by the combined source and drain. As is well known [9, 10, 59], the self-trapping regime is expected to occur in the two-well model in the Josephson regime. To be more precise, $\langle N_2\rangle/N < \tilde{\epsilon}$ when $UN > J/(2\sqrt{\tilde{\epsilon}-\tilde{\epsilon}^2})$ if well 2 is initially empty. Thus, for $UN \gg J$ we find $\langle N_2\rangle/N \simeq 0$, and almost all bosons are distributed between the source and the drain if only a small fraction of bosons are initially in the gate.

On the other hand, it has been pointed out [37] that for isotropic tunneling the source and the drain can form an effective non-interacting two-well system, by second-order processes [60–62] through the gate, such that $\langle N_2\rangle \simeq 0$. For general tunneling, we find the remarkable result that the effective Hamiltonian is simply given by $H_{\rm eff} = -\lambda Q$, where $Q$ is the conserved charge (2.3), and $\lambda^{-1} = 4U(N-1)$ (details are provided in Methods). This produces an effective tunneling coupling given by $J_{\rm eff} = \lambda J_1 J_3$, which decreases with increasing $N$, and therefore will only be observed in mesoscopic samples [37]. In view of the above observations, we formally identify the resonant tunneling regime of the system to be determined by $UN \gg J$, which contains the Josephson regime.

In Fig. 2.5 the time evolution of expectation values for number operators is displayed in a case of broken integrability. Increasing the value of $\epsilon$ suppresses the tunneling of particles into the drain, while increasing the time-average value of $\langle N_2\rangle$. For $\epsilon/J = 1.63$ this suppression of tunneling into the drain is strong enough that its number expectation value is close to negligible, i.e. tunneling into the drain has been switched-off.

## 2.6 Control of resonant tunneling

In Fig. 2.4d the dynamics is seen to be remarkably close to being harmonic over sufficiently short time scales, with the period monotonically increasing with interaction coupling $U$. This behavior supports the conclusion that the effective Hamiltonian for the resonant tunneling regime is simply related to the conserved charge $Q$. The frequency of oscillation in this regime is given by $\omega_{\rm J} = \lambda J^2$, with the amplitude also being $U$-dependent. When the initial state is $|N,0,0\rangle$, the oscillations between the source and drain are coherent, with tunneling to the gate switched-off. On the other hand, if the initial state is $|0,N,0\rangle$ the system will remain trapped in this initial state configuration, with tunneling from the gate switched-off.

Next, we maintain the system in the resonant tunneling regime $UN \gg J$ and study the non-integrable dynamics using the parameter $\epsilon$ to control the behavior of the source and drain subsystem. The approach here, following the study above, is to choose the

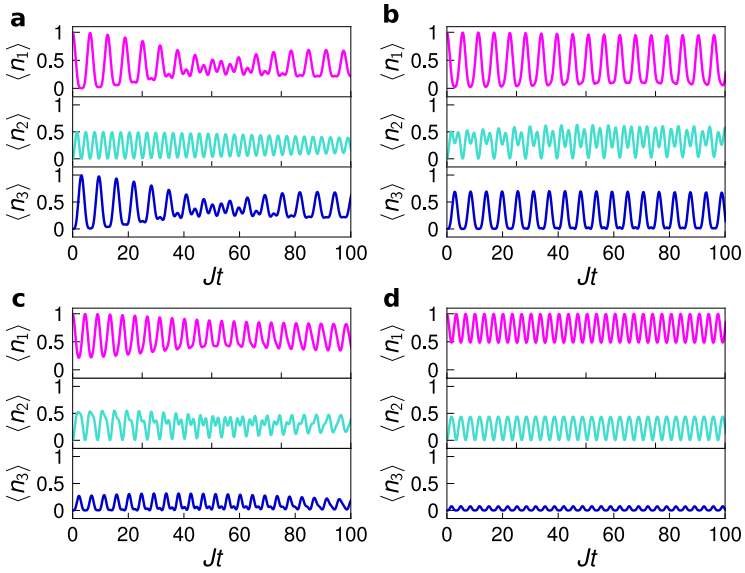


Figure 2.5: Time evolution of expectation values. Dimensionless units are used. The effects of breaking integrability for the expectation values of the number operators are shown, with the initial state $|60, 0, 0\rangle$. The configuration used has $U/J = 0.001$. **a** $\epsilon/J = 0$; **b** $\epsilon/J = 0.47$; **c** $\epsilon/J = 1.0$; **d** $\epsilon/J = 1.63$. It is apparent that increasing $\epsilon$ leads to greater suppression of tunneling into the drain. For **d** the expectation value of the number operator associated with the drain is negligible, so tunneling into the drain is considered to be switched-off.

initial state $|N, 0, 0\rangle$ and investigate the ability to control the frequency and amplitude of the populations oscillating between the source and the drain.

In Fig. 2.6a, 2.6b, 2.6c the interaction coupling is fixed as $U/J = 0.17$, and results are shown for the expectation values of the populations using three choices for $\epsilon$. It is seen that the presence of the external field does not significantly influence the gate, in the sense that it does not affect the negligible average population $\langle N_2 \rangle$. Fig. 2.6d shows how the amplitude decays while increasing the external field, as well as the dependence of the frequency. The three points highlighted in the curves correspond to the values of the amplitude and frequency of Figs. 2.6a (cyan circle), 2.6b (yellow triangle), and 2.6c (lime diamond).

In this non-integrable regime the effective Hamiltonian is given by

$$H_{\text{eff}} = -\lambda Q + \epsilon(N_3 - N_1). \tag{2.5}$$

For short time scales the dynamics exhibits Josephson-like oscillation [13] with frequency

$$\omega_{\text{J}} = \frac{2\lambda J_1 J_3}{\sqrt{\Delta n}}, \tag{2.6}$$

where $\Delta n = 1/(1+\gamma^2)$ is the amplitude and $\gamma = (\lambda(J_1^2 - J_3^2) - 2\epsilon)/2\lambda J_1 J_3$ (see Methods for details). Increasing the external field reduces the oscillation amplitude $\Delta n$ and the

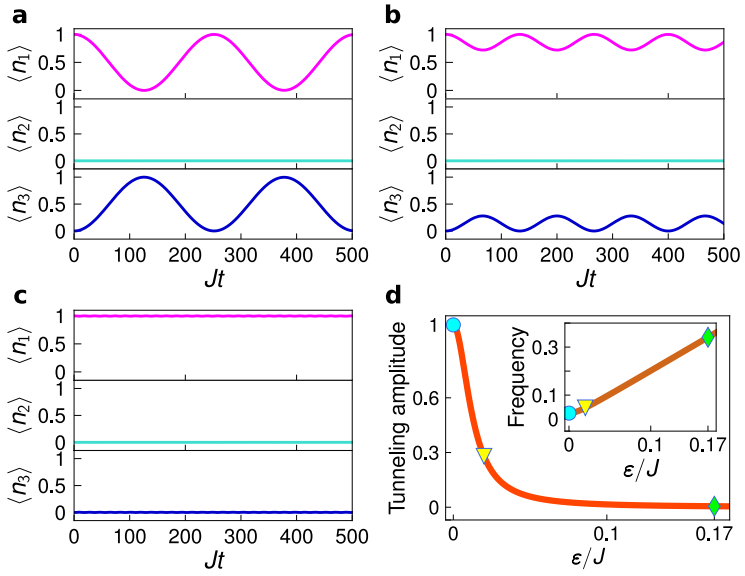


Figure 2.6: Amplitude and frequency of oscillations. The configuration used has $N = 60$, $U/J = 0.17$, and initial state $|60, 0, 0\rangle$. **a** Number operator expectation values for $\epsilon/J = 0$: switched-on configuration, with maximum tunneling amplitude between the source and the drain. **b** Expectation values for $\epsilon/J = 0.02$: approximately 30% of the maximal tunneling amplitude. **c** Expectation values for $\epsilon/J = 0.17$: switched-off configuration. **d** Tunneling amplitude as a function of the external field $\epsilon/J$. In the inset: tunneling frequency versus the external field $\epsilon/J$. The markers in the curves correspond to the values of the amplitude of Fig. 2.6**a** (cyan circle), 2.6**b** (yellow triangle), and 2.6**c** (lime diamond).

period between the source and the drain, until the amplitude of oscillation is completely suppressed i.e. all tunneling is switched-off, demonstrating various levels of control, especially in the range $0 < \epsilon < 0.2$. Through semiclassical analysis, one can obtain analytic expressions for the expectation values of the relative populations, $n_i \equiv N_i/N$ $(i = 1, 3)$, in the wells 1 and 3, given by $\langle n_1 \rangle = 1 - \langle n_3 \rangle$ and $\langle n_3 \rangle = \Delta n \sin^2(\omega_J t/2)$ (see details in Methods). In agreement with Chuang et al. [63], the maximum amplitude is obtained when the field is small.

Retirei a seção Discussion daqui

## 2.7 Methods

In this section we provide the details concerning algebraic structures behind the model, and complementary semiclassical approximations, which were used to derive analytic expressions characterizing quantum control in the resonant tunneling regime. These expressions were found to give close agreement with results obtained by exact numerical diagonalization (see Supplementary Material 2.9.2, Supplementary Figures 2 and 3 for more details). We also discuss the feasibility of physical realization of the system.

### 2.7.1 Two-mode structure and the resonant tunneling regime

The integrable three-well model can be structured through two modes, as follows. From Eq. 3.1 we define $J = \sqrt{J_1^2 + J_3^2}$ and the operators $N_{1,3} = N_1 + N_3$, $a_{1,3} = J^{-1}(J_1 a_1 + J_3 a_3)$ and $a_{1,3}^\dagger = J^{-1}(J_1 a_1^\dagger + J_3 a_3^\dagger)$ satisfying the Heisenberg algebra

$$[N_{1,3}, a_{1,3}] = -a_{1,3}, \qquad [N_{1,3}, a_{1,3}^\dagger] = a_{1,3}^\dagger, \qquad [a_{1,3}, a_{1,3}^\dagger] = 1.$$

Then

$$H_0 = U(N_{1,3} - N_2)^2 + J(a_{1,3}^\dagger a_2 + a_2^\dagger a_{1,3}),$$

such that the modes of wells 1 and 3 are now represented by the single mode "1, 3".

The two-well model exhibits a self-trapping regime, with onset in the vicinity of $\chi \equiv UN/J \simeq 1$ [9, 59]. This translates to a resonant tunneling regime for the triple-well model. Here we follow the approach of using semiclassical analysis [64], such that this regime may be clearly identified. Using the usual number-phase correspondence, that is, $a_2 = e^{i\theta_2}\sqrt{N_2}$, $a_{1,3} = e^{i\theta_{1,3}}\sqrt{N_{1,3}}$ and the conservation of boson number $N_{1,3} + N_2 = N$, we find

$$h = \frac{H_0}{N} = UN(1 - 2n_2)^2 + 2J\sqrt{(1 - n_2)n_2}\cos\phi,$$

where $n_2 = N_2/N$ and $\phi = \theta_{1,3} - \theta_2$. Consider the dynamics where the initial condition is $n_2 = 0$. At the initial time $t = 0$ the system has the energy $h = UN$. By energy conservation at all times, we obtain the expression

$$n_2 = \frac{1}{2} - \frac{\sqrt{\chi^2 - \cos^2\phi}}{2\chi}. \tag{2.7}$$

The conditions $\chi > 1$ and $|\cos\phi| = 1$ (maximum value) imply that $0 \leq n_2 \leq 0.5$. From Eq. 2.7, we conclude that when $\chi \gg |\cos\phi|$, $n_2 \to 0$, and the bosons are distributed between the wells labeled 1 and 3, producing the resonant tunneling regime.

### 2.7.2 Effective integrable Hamiltonian for resonant tunneling

In order to better understand the dynamics in the resonant tunneling regime, we first observe that the integrable Hamiltonian can be written, by using the conserved quantity $N$, as an effective Hamiltonian without on-site interaction (up to a global constant $UN^2$). Specifically $H_0 = H_I + V$, where the interaction term $H_I = -4UN_2(N_1 + N_3)$

has eigenstate and eigenvalues given by

$$H_I|\mathcal{N}_1,\mathcal{N}_2,\mathcal{N}_3\rangle = -4U\mathcal{N}_2(\mathcal{N}_1+\mathcal{N}_3)|\mathcal{N}_1,\mathcal{N}_2,\mathcal{N}_3\rangle,$$

and the tunneling term $V = (J_1 a_1^\dagger + J_3 a_3^\dagger)a_2 + \text{h.c.}$ is treated as a perturbation. For the isotropic case $J_1 = J_3 = J/\sqrt{2}$, [37], since $n_2 \simeq 0$ the interaction part is $H_I \simeq 0$ and the wells 1 and 3 form an effective non-interacting two-well system coupled through well 2 by a second-order process [37, 60–62] with the effective Hamiltonian $H_{\text{eff}} = J_{\text{eff}}(a_1^\dagger a_3 + a_3^\dagger a_1)$. Recall that the transition rate from initial state $|s\rangle$ to final state $|k\rangle$ is expressed

$$W^{(i)} = 2\pi|\langle k|V^{(i)}|s\rangle|^2\delta(E_k - E_s), \qquad i = 1, 2,$$

where $V^{(1)} = V$ for first-order transition (Fermi's golden rule), $\delta$ is the delta function and

$$V^{(2)} = \sum_m \frac{V|m\rangle\langle m|V}{E_s - E_m}$$

for second-order transitions. Equating second-order transition of $V$ with the first-order transition of $H_{\text{eff}}$ for the states $|N,0,0\rangle$ and $|N-1,0,1\rangle$, it is found that

$$J_{\text{eff}} = \frac{J^2}{8U(N-1)}.$$

Observing that $J_3^2 N_1 + J_1^2 N_3$ is constant for isotropic tunneling in the regime $\chi \gg 1$, then it does not affect the dynamics if we consider the linear combination $J_{\text{eff}}(a_1^\dagger a_3 + a_3^\dagger a_1) + \lambda'(J_3^2 N_1 + J_1^2 N_3)$. By numerical inspection we conclude that the effective Hamiltonian for general tunneling, which includes the anisotropic tunneling $J_1 \neq J_3$, is given by

$$H_{\text{eff}} = -\lambda Q,$$

where $Q = J_1^2 N_3 + J_3^2 N_1 - J_1 J_3(a_1 a_3^\dagger + a_1^\dagger a_3)$ is conserved and $\lambda^{-1} = 4U(N-1)$.

### 2.7.3 Effective non-integrable Hamiltonian and quantum control

For the non-integrable case, the effective Hamiltonian in the resonant tunneling regime $\chi \gg 1$ is given by $H_{\text{eff}} = -\lambda Q + \epsilon(N_3 - N_1)$. Returning to a semiclassical analysis it is

found that, up to an irrelevant constant,

$$h = \frac{H_{\text{eff}}}{N} = -\lambda J_1^2(1-n_1) - (\lambda J_3^2 + 2\epsilon)n_1 + 2\lambda J_1 J_3 \sqrt{n_1(1-n_1)}\cos\varphi,$$

where $n_1 = N_1/N$ and $\varphi = \theta_1 - \theta_3$. For initial condition $n_1 = 1$ and $n_3 = 0$ we have $h = -\lambda J_3^2$, a constant. Applying energy conservation and the condition $\cos\varphi = \pm 1$, we find that the amplitude of oscillation $\Delta n$ (Fig. 5d) is given by $\Delta n = 1/(1+\gamma^2)$, where $\gamma = [\lambda(J_1^2 - J_3^2) - 2\epsilon]/2\lambda J_1 J_3$. Hamilton's equation gives

$$\dot{N}_1 = -\frac{\partial H_{\text{eff}}}{\partial \theta_1} = 2\lambda J_1 J_3 \sqrt{N_1(N-N_1)}\sin\varphi,$$
$$\Rightarrow \qquad \dot{n}_1 = 2\lambda J_1 J_3 \sqrt{n_1(1-n_1)}\sin\varphi.$$

Using the *Ansatz* $n_1 = 1 - \Delta n \sin^2(\eta t)$, we can easily verify that the above results provide analytic expressions for the expectation values

$$\langle n_1 \rangle = 1 - \Delta n \sin^2(\omega_{\text{J}} t/2), \quad \langle n_3 \rangle = \Delta n \sin^2(\omega_{\text{J}} t/2),$$

where $\omega_{\text{J}}$ is the frequency given by Eq. 2.6. Results for similar types of investigation have been presented in the case of pair-tunneling between two wells[62].

### 2.7.4 Physical realization

Here we discuss the feasibility of physical realization of the triple-well Hamiltonian (3.1), through use of Bose-Einstein condensates (BECs) of dipolar atoms.

Three parallel, tightly focused Gaussian beams, with waist of 1 $\mu$m and wavelength $\lambda = 1.064$ nm, separated by a distance $l = 1.8\,\mu$m, form an optical triple-well potential aligned along the $y$-axis [37]. A transverse beam, with waist of 6 $\mu$m, provides $xz$-confinement. For such a setup, in the harmonic approximation the potential of each well $i = 1, 2, 3$ is symmetrically cylindrical and is given by

$$V_{trap}(x,y,z) = \sum_{i=1}^{3} \left( \frac{1}{2} m\omega_x^2 x^2 + \frac{1}{2} m\omega_r^2 ((y-y_i)^2 + z^2) \right),$$

where $y_i = l, 0, -l$. The trap frequencies $\omega_x$ and $\omega_r$ can be controlled by the intensity of the laser beams. This configuration facilitates the formation of three cigar-shaped wells. We consider a system of bosons with dipole-dipole interactions to provide long-range interactions, and weakly repulsive contact interactions to promote condensate stability [65]. The dipoles are oriented along the $z$-direction. See Fig. 2.7.

The transverse beam performs the function of the external field that controls the device. Its focus, when displaced along the $y$-axis by $\Delta y$, introduces the potential energy

$$V_{brak}(y) = \frac{1}{2} m\omega_y^2 \Delta y(2y + \Delta y).$$

This generates a potential difference, resulting in the external field strength $\epsilon = m\omega_y^2 \Delta y l$. The frequency of the transverse laser ($\omega_y$) is much lower than the frequency of the parallel lasers ($\omega_r$), so that displacement by $\Delta y$ introduces a "tilting" of wells 1 and 3. These are the relevant wells in the resonant tunneling regime. (More details can be seen in Appendix C).

For the case of a dipolar BEC of $^{52}$Cr [26], we numerically find that the integrability condition, with $\alpha \sim 5.8$, is achieved for $\omega_x \sim 2\pi \times 64$ Hz, $\omega_r \sim 2\pi \times 220$ Hz, where we assumed the Gaussian approximation for the ground state. The value of $U$ obtained in units of $J$ is $U/J \sim 7.5 \times 10^{-3}$, which means that the resonant tunneling regime can be achieved for $N \gg 130$ atoms. In principle, this condition can be satisfied experimentally [26]. As an example, for $N \sim 5000$ atoms, with $\omega_y \sim 2\pi \times 1.5$ Hz, translating the transverse laser by $\Delta y = 1.8\,\mu$m we obtain $\epsilon/h \sim 3.6 \times 10^{-2}$ Hz. It results in a tunneling amplitude $\Delta n \sim 0.25$, which means that 25% of the population of the source in the initial state $|N, 0, 0\rangle$ switch to the drain, and back, through harmonic tunneling. This example approaches the case of Fig. 2.6b.

Another strongly dipolar BEC which can be considered is $^{164}$Dy [66]. In this case, we calculate $\alpha \sim 5.9$ for $\omega_x \sim 2\pi \times 22.7$ Hz, $\omega_r \sim 2\pi \times 67.3$ Hz with $U/J \sim 2.2 \times 10^{-2}$. For $N \sim 500$ atoms, with $\omega_y \sim 2\pi \times 0.76$ Hz, this yields $\epsilon/h \sim 3.0 \times 10^{-2}$ Hz and $\Delta n \sim 0.23$.

In both cases above, the parameter choices are such that higher-order interaction terms, such as correlated hopping, are negligible [67].

An analysis of the effects of perturbations is provided in Supplementary Material 2.9.3: Fidelity dynamics, Supplementary Figures 4 and 5.

## 2.8 Discussion

We have analyzed a model for boson tunneling in a triple-well system. This was conducted in both integrable and non-integrable settings through variation of coupling parameters. The model draws an analogy with a transistor through identification of the wells as the source, gate, and drain.

In the integrable setting we identified the resonant tunneling regime between the source and drain, for which expectation values of particle numbers in the gate are neg-

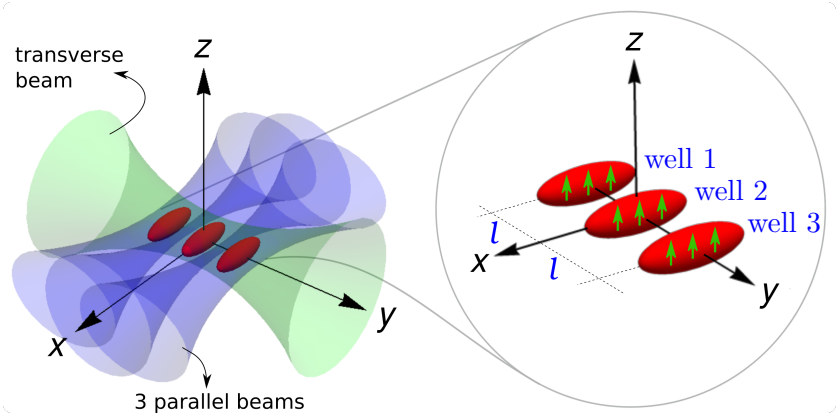


Figure 2.7: Schematic representation of the trap geometry. Three parallel lasers (blue) are crossed by a transverse beam (green). The cigar-shapes, in red, represent a dipolar Bose-Einstein condensate trapped in a triple-well potential, and the green internal arrows depict the orientation of the dipoles.

ligible. Moreover, it was found that a conserved operator of the integrable system acts as an effective Hamiltonian, which predicts coherent oscillations. This is in agreement with observations from numerical calculations. By breaking integrability through application of an external field to the source and the drain, we can, surprisingly, control with remarkable precision the amplitude and frequency of the tunneling dynamics between wells 1-3, without destroying the harmonic nature of the oscillations. Increasing the applied field allowed for tuning the system from the switched-on configuration through to switched-off, passing through different states.

Nonetheless, it is important to comment on the limitations of a three-mode Hamiltonian in the description of cold atom systems in a triple-well potential. Contributions from higher energy levels of the single-particle spectrum cannot be ignored under certain coupling regimes. For example, the presence of the external field will ultimately lead to level crossings as the field strength is increased. In the case of the analogous double-well system, estimates for when this may occur have been formulated [68]. We have undertaken checks to confirm that it is indeed possible to avoid these undesired scenarios, within an experimentally feasible scenario. (See Supplementary Material 2.9.1, Supplementary Figure 1 for further details). However it is also noteworthy that it is possible to include three-body, and higher, interaction terms as corrections [69] to compensate for when the three-mode approximation breaks down.

Our results open possibilities for multi-level logic applications and consequently new avenues in the design of atomtronic devices. In addition to what was discussed here, other important studies of the atomtronic switching device will be explored in the next chapter. Among them, we will extend the analysis of the quantum dynamics by choosing other initial states, also investigating the potential that each of these states presents to generate entangled states.

## 2.9 Supplementary Material

### 2.9.1 Energy levels for the non-integrable Hamiltonian

In Supplementary Figure 1, we show the behavior of the energy levels for the non-integrable Hamiltonian as we increase the external field $\epsilon$. This will allow us to determine the range of $\epsilon$ for which the switching device can operate.

In order to control the device without unwanted virtual processes, we need the parameter $\epsilon$ to be less than a threshold value $\epsilon_c$, defined by the point where the crossing between the energy level bands starts. For the case where $|4U(N-1)\epsilon| \gg |J_1 J_3|$, the crossing between the two upper bands occurs when

$$\begin{aligned} & \Delta E \simeq (E_0 - N\epsilon) - (E_1 + (N-1)\epsilon) = 0 \\ \Rightarrow \qquad & \epsilon_c \simeq 2U \end{aligned}$$

as can be seen in Supplementary Figure 1 by the brown dot-dashed lines. It is worth noting that the gap between adjacent energy levels of the same band, $2J_{\text{eff}} \simeq 2\epsilon$, increases with $\epsilon$. This increase causes a tendency toward self-trapping, as can be seen in the amplitude equation, $\Delta n = 1/(1+\gamma^2) \simeq 1/(1+(4U(N-1)\epsilon)^2/(J_1 J_3)^2)$, presented in Methods.

Considering switched-off states to be defined by the condition $\Delta n < 1/N$, the $\epsilon$ dependency for the switched-off configuration becomes

$$\frac{J_1 J_3}{4U\sqrt{(N-1)}} < \epsilon < 2U. \tag{2.8}$$

This means that the device's controlled tunneling occurs for $\epsilon < J_1 J_3/4U\sqrt{(N-1)}$,

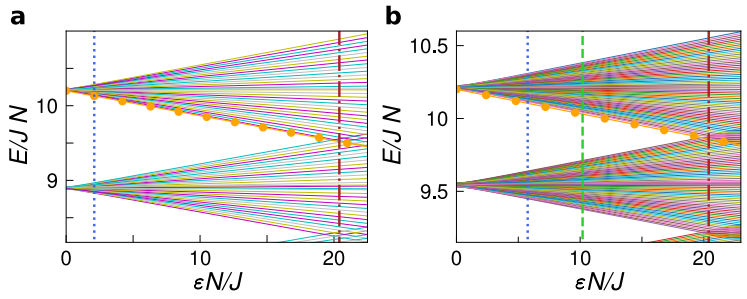


**Supplementary Figure 1.** Energy levels. $E/JN$ vs. external field $\epsilon N/J$. The orange ball lines mark the initial energy: $E = UN^2 - N\epsilon$. According to Eq. 2.8, the blue dot line marks the region of the parameter $\epsilon$ for which the switched-off configuration starts, while the brown dot-dashed lines mark the threshold parameter $\epsilon_c \simeq 2U$, above which unwanted virtual tunneling may occur. The green dashed line corresponds to the switched-off point shown in Supplementary Figure 2 with the diamond mark. The switching device operates between $0 \leq \epsilon < \epsilon_c$. **a**: $N = 30$ and $U = 0.34$, $UN/J \simeq 10$. **b**: $N = 60$ and $U = 0.17$, $UN/J \simeq 10$. Only the two highest energy bands are plotted.

while the off-state range occurs between $J_1 J_3/4U\sqrt{(N-1)} < \epsilon < 2U$. For the case of Supplementary Figure 1b, the off-state range is given by $0.1 \leq \epsilon < 0.34$, in accordance with Fig. 2.6 of the main article.

### 2.9.2 Comparison between analytic expressions and numerical diagonalization

Supplementary Figure 2 presents the period dependence on the external field obtained from the analytic expression for the frequency, Eq.(2.6) in the main article. It compares three points obtained from numerical analysis, giving support that the analytic expressions are in accordance with quantum dynamics. In Supplementary Figure 3, it is shown how the temporal evolution of amplitude oscillation depends on the external field for the resonant tunneling case.

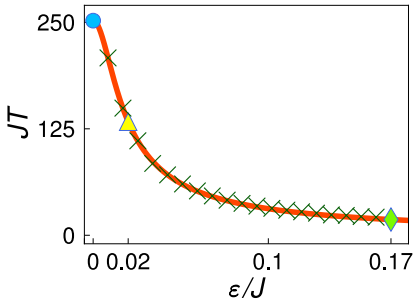


**Supplementary Figure 2.** Period of oscillation. $JT$ vs. the external field $\epsilon/J$. The orange line shows the period function obtained from the analytic expression through Eq.(2.6) in the main text, compared with numerical points marked in "x". The other markers correspond to the values of the period of Figs. 5a (blue circle), 5b (yellow triangle) and 5c (lime diamond) in the main article, also obtained from numerical analysis. The configuration used here has $N = 60, U/J = 0.17$, and initial state $|60, 0, 0\rangle$.

### 2.9.3 Fidelity dynamics

In using properties of integrability to draw conclusions about this model, it is important to understand the effects of perturbations away from the integrable point. It has been found that breaking the integrability, through an external field, still allowed for predictions of the amplitude and frequency in the resonant tunneling case. Here an extended analysis is presented to highlight the effects of another integrability-breaking perturbation.

We use fidelity, which is computed through $F(t) = |\langle\psi_0|\psi(t)\rangle|^2$ where $|\psi_0\rangle = |N, 0, 0\rangle$, and time-evolution is governed by the Hamiltonian

$$H = H_0 + \xi N_1 N_3 + \epsilon(N_3 - N_1) \tag{2.9}$$

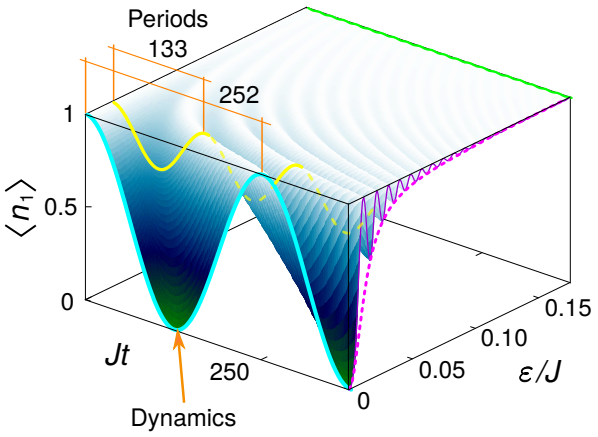


**Supplementary Figure 3.** Source dynamics. $\langle n_1 \rangle$ vs. the external field $\epsilon/J$. The graph shows the harmonic dynamic evolution of the fractional occupation in well 1 (source) as a function of time and external field parameter $\epsilon$. The dynamics of $\epsilon/J = 0$ (cyan line), $\epsilon/J = 0.02$ (yellow line) and $\epsilon/J = 0.17$ (lime line) are highlighted and the dashed pink line is marking the amplitude function $\Delta n$. The configuration used here has $N = 60$, $U/J = 0.17$, and initial state $|60, 0, 0\rangle$, as in Fig. 2.6 of the main text. Recall that the dynamics of well 3 (drain) has the same configuration, however it is out of phase by $\pi$, while $\langle n_2 \rangle = 0$.

where $\xi$ is the perturbation parameter. This quantity allows for an investigation of the probability to revisit the initial state configuration after some period of time evolution, complementing the earlier dynamics studies.

Supplementary Figure 4 presents fidelity dynamics in the integrable case for different values of the interacting parameters $U$. Clearly, the probability to find the initial state becomes relevant in the Josephson and Fock regimes, cf. Fig. 2.3 in the main article. In the resonant regime, the initial state can be recovered to a high degree of accuracy. As $\langle N_2 \rangle \simeq 0$ in this regime, almost the entire boson population periodically tunnels back and forth. The probability of the initial state $|N, 0, 0\rangle$ to be transferred to the drain as $|0, 0, N\rangle$, is close to 1.

Supplementary Figure 5 illustrates the impacts of perturbation, through $\xi \neq 0$, for the cases analogous to those of Fig. 2.6 a, 2.6 b in the main article. It is verified that increasing the value of the perturbation leads to a decrease in the fidelity until there are no oscillations. This limit occurs when the perturbation is less than the order of $J_{\text{eff}}$. Interestingly, when the external field $\epsilon$ is included (dotted lines of the graphs), it improves the fidelity compared $\epsilon = 0$ (solid lines of the graphs). Thus the external field term renders the harmonic dynamics of the system in the resonant tunneling regime to be more resistant to perturbation.

In summary, the integrability breaking coupling $\epsilon$ does not destroy the harmonic nature of oscillations in the resonant tunneling regime. It does influence the period and amplitude, resulting in localization in wells 1 and 3. But this occurs in a fashion which is predictable, through the results of the classical analysis. In contrast, the coupling $\xi$ does

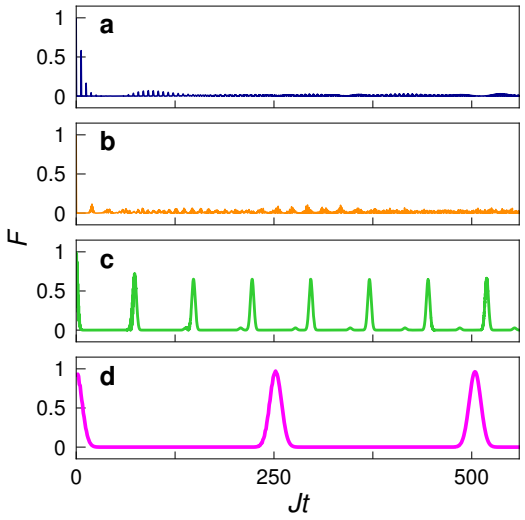


**Supplementary Figure 4.** Fidelity. $F$ vs. time $Jt$ for the Hamiltonian Eq. 2.9, with $\xi/J = 0$ and $\epsilon/J = 0$, and four different parameter values of $U/J$ as in Fig. 2.3 in the main article. **a** $U/J = 0.001$, **b** $U/J = 0.015$, **c** $U/J = 0.05$, and **d** $U/J = 0.17$. The configuration has initial state $|60, 0, 0\rangle$. Observe the transition from the Rabi regime to Josephson from panel **b** to panel **c**.

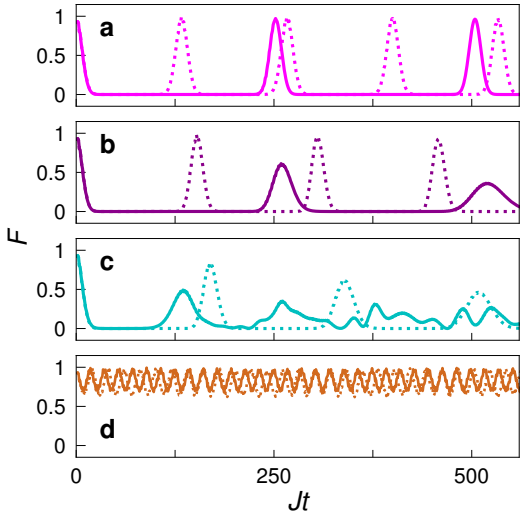


**Supplementary Figure 5.** Fidelity. $F$ vs. time $Jt$ for the Hamiltonian Eq. 2.9, with $\epsilon/h = 0$ (continuous line), $\epsilon/J = 0.02$ (dotted line) and $\xi/J$ varying between panels. **a** $\xi/J = 0$, **b** $\xi/J = 0.0003$, **c** $\xi/J = 0.001$, **d** $\xi/J = 0.01 \simeq J_{\text{eff}}/J$. The configuration has initial state $|60, 0, 0\rangle$ and $U/J = 0.17$. The parameters $\epsilon$ are chosen according to the values used in Fig. 2.6 a and 2.6 b in the main article.

destroy the harmonic nature and produces more pronounced localization, however the effects are mitigated through increasing $\epsilon$. When the coupling $\xi$ is seen as a perturbation in the sense that $\xi \ll \epsilon$, the device dynamics are robust against this perturbation.

# Chapter 3

# Entangled states of dipolar bosons generated in a triple-well potential

This chapter investigates the generation of entangled states in the resonant dynamic regime of the integrable triple-well Hamiltonian presented in the previous Chapter 2. In addition to the initial state proposed there, we extend the analysis of the entanglement dynamics to other initial states. We also identify the instant in time evolution at which entanglement is maximum, with precise approximations given by analytical formulas, providing a physical discussion of this state. The main content of this chapter was published in SciPost Physics[1].

## 3.1 Foreword

Entanglement is a fundamental quantum resource, one which underpins many proposals for the implementation of quantum technology. Ultracold quantum gases have been viewed, for some time, as one of the most promising avenues for the physical production and manipulation of entangled states [70]. Experimental efforts towards achieving macroscopic entanglement continue to drive significant research activity, e.g. [71–76].

Our main objective here is to expand on the analysis conducted in Chapter 2 [43] in two complementary directions. The first of these is to investigate and understand the behaviour of the device with respect to a variety of initial conditions. In the previous Chapter 2, the dynamical evolution was only considered for an initial state with all particles in well 1, $|N,0,0\rangle$. Here, we extend the investigations to the case of initial states with bosons distributed over the wells. It is found that the harmonic character of oscillations is still present for appropriately chosen interaction strengths,

[1] *Entangled states of dipolar bosons generated in a triple-well potential*, Arlei P. Tonel, Leandro H. Ymai, Karin Wittmann W., Angela Foerster, Jon Links, SciPost Phys. Core 2 **2**, 3 (2020), doi:10.21468/SciPostPhysCore.2.1.003

and the dynamics can be succinctly described. Encouraged by that result, we then turn attention to an analysis of the entanglement generated within the device under time-evolution. That is, our aim is to input non-entangled states and analyse the capacity of the device to produce entangled states of an ultracold quantum gas. Due to the integrability of the system, many results can be obtained through analytic formulae.

The chapter is organised as follows. The integrable Hamiltonian is presented in Sect. 2, and an analysis is given for the energy spectrum. In Sect. 3.3 we conduct computations for the quantum population dynamics, and identify the resonant tunneling regime. We then introduce an effective Hamiltonian, which leads to analytic expressions for the frequency and amplitude of coherent oscillations between the outer wells. We also undertake numerical calculations for the quantum fluctuations. Sect. 3.4 deals with entanglement dynamics for different initial states, and in Sect. 3.5 we obtain an analytic expression for the time-evolution of states in the resonant regime. Sect. 3.6 contains final remarks.

## 3.2 Integrable Hamiltonian

An integrable model for a dipolar bosons loaded in an aligned triple-well potential was recently studied in [43]. In particular, the breaking of integrability was used to control the tunneling between the two external wells, thus implementing an atomtronic switching device. In this work, we investigate this model in more detail. The integrable triple-well Hamiltonian is given by

$$H = U\left(N_1 - N_2 + N_3\right)^2 + J_1\left(a_1^\dagger a_2 + a_2^\dagger a_1\right) + J_3\left(a_2^\dagger a_3 + a_3^\dagger a_2\right). \tag{3.1}$$

It describes interactions between dipolar bosons in a triple well potential (with strength $U$), and tunneling between neighbouring wells (with strength $J_1$ and $J_3$). See Suppl. Material 3.7.1. The derivation of the Hamiltonian from first principles, and experimental feasibility, is discussed in Supp. Material 3.7.2 (In Appendix C, a slightly more detailed version is shown.) Hereafter, we set $J_1 = J_3 = J/\sqrt{2}$, and work in units such that $\hbar = 1$.

The Hamiltonian commutes with the total number operator $N = N_1 + N_2 + N_3$. For each fixed value of $N$, the Hamiltonian acts on a Hilbert space with dimension $d = (N+1)(N+2)/2$. Beyond the total number of bosons, the operator

$$Q = \frac{J^2}{2}\left(N_1 + N_3 - a_1^\dagger a_3 - a_1 a_3^\dagger\right) \tag{3.2}$$

is also conserved. We remark that $Q$ does not commute with the Hamiltonian if periodic

boundary conditions are imposed.

First, we illustrate the structure of the energy levels. We fix the parameters $J = 1$ and $N = 20$ and only consider $U > 0$. In Fig. 3.1, we plot the ordered energies for four choices of the interaction parameter $U$. For $U = 0$, there are $2N + 1$ distinct energy levels and a high level of degeneracy, with a uniform gap $\Delta E = J$ between adjacent levels. For $U \neq 0$ the energies mix and it is clearly seen that the energy spectrum undergoes qualitative changes as $U$ is varied. In particular, we observe the emergence of new energy bands, for sufficiently large values of $U$, with the gap between bands occurring at a larger energy scale.

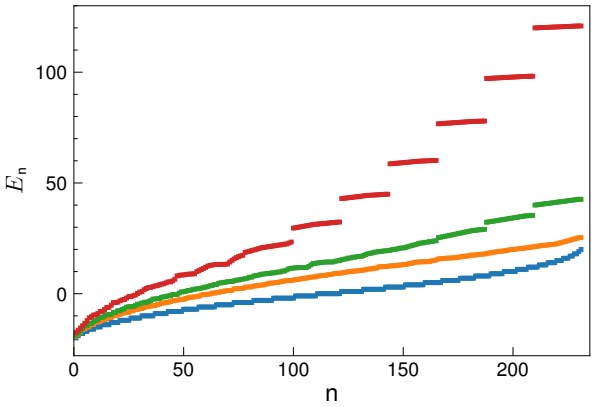


Figure 3.1: Ordered energy levels. Arranging the energy levels according to $E_n \leq E_m$ for n<m, the figure shows $E_n$ versus the level n. From top to bottom: $U = 0.3$ (red), $U = 0.1$ (green), $U = 0.05$ (orange) and $U = 0$ (blue), for $N = 20$.

A complementary presentation is provided in Fig. 3.2, where the energy level dependence is plotted against the dimensionless parameter $UN/J$.

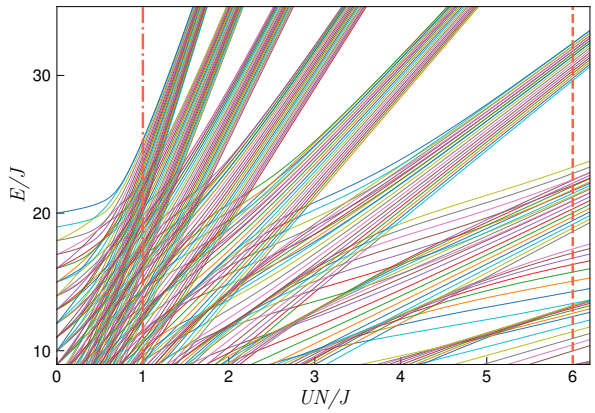


Figure 3.2: Energy level distribution. The dimensionless energies $E/J$ are plotted against dimensionless coupling parameter $UN/J$. At $UN/J = 0$ the energies are equidistant and degenerate. As $UN/J$ increases, the energies mix until reaching a nearly uniform distribution around $UN/J \simeq 1$ (the dot-dashed vertical line). Increasing $UN/J$ further leads to the re-emergence of energy bands.

At the intermediate interaction regime, $UN/J \sim 1$, a band structure begins to

emerge (see the vertical line in Fig. 3.2). By increasing the dimensionless coupling parameter, the number of bands increases with non-uniform spacing between them. In the strong interaction regime $UN/J \gg N^2$, all energy levels tend to degenerate into bands. In the extreme limit $UN/J \to \infty$, the number of bands is $(N+2)/2$ if $N$ is even and $(N+1)/2$ if $N$ is odd.

## 3.3 Quantum population dynamics

The time evolution of any state is governed by

$$|\Psi(t)\rangle = \sum_{n=1}^{d} a_n \exp(-iE_n t)|\phi_n\rangle, \tag{3.3}$$

where $a_n = \langle\phi_n|\Psi_0\rangle$ for initial state $|\Psi_0\rangle$, and $\{|\phi_n\rangle\}$ is a set of normalised eigenvectors associated with the energy eigenvalues $\{E_n\}$. We will analyse the dynamical evolution for the following class of initial Fock states

$$|N-l-z,l,k\rangle = \frac{(a_1^\dagger)^{N-l-k}}{\sqrt{(N-l-k)!}}\frac{(a_2^\dagger)^l}{\sqrt{l!}}\frac{(a_3^\dagger)^k}{\sqrt{k!}}|0,0,0\rangle, \tag{3.4}$$

where $l = 0, 1, 2, \ldots, N$ and $0 \leq k \leq N-l$. These Fock states are the most general non-entangled, number-conserving, pure states. The expectation value of the population in each well is computed through

$$\langle N_i(t)\rangle = \langle\Psi(t)|N_i|\Psi(t)\rangle, \quad i = 1, 2, 3. \tag{3.5}$$

In [43], the dynamics of the population expectation values was studied for the initial state $|N,0,0\rangle$. There a resonant tunneling regime was identified for $UN/J >> 1$, where near-coherent oscillations occurred between wells 1 and 3. By coherent, we mean oscillations in the expectation values which have the same waveform, the same frequency, and constant phase difference. This regime coincides with the emergence of energy bands as depicted in Fig. 2. Below we extend this analysis to the class of initial states (3.4). First, we find that each of the energy bands can be associated with labels $l$ and $N-l$. In particular, all states in each band have, approximately, the expectation value $\langle N_2\rangle \approx l$ or $\langle N_2\rangle \approx N-l$. Moreover, it is anticipated that there will still be oscillations between wells 1 and 3 for initial states (3.4). An example is given in Fig. 3.3.

Fig. 3.3 shows two distinctive characteristics. The first is confirmation that $\langle N_2\rangle$ is

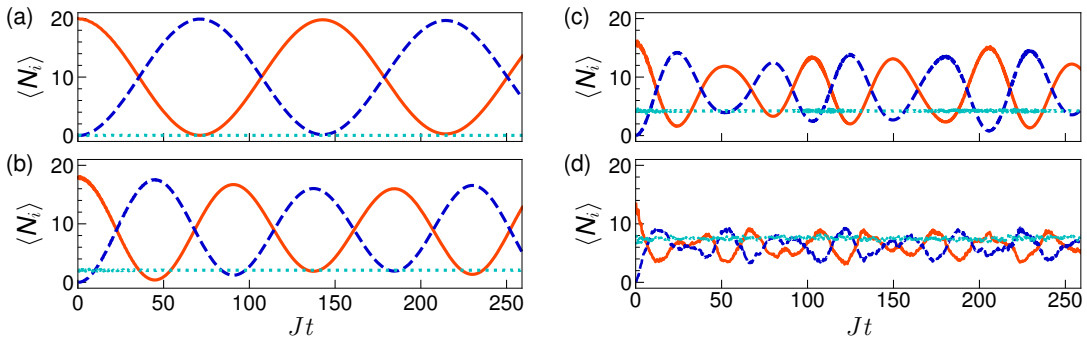


Figure 3.3: Expectation value dynamics. Dimensionless units are used. The panels show results for $\langle N_i \rangle$, $i = 1, 2, 3$, with $UN/J = 6$ and the choice of initial states: (a) $|20, 0, 0\rangle$; (b) $|18, 2, 0\rangle$; (c) $|16, 4, 0\rangle$ and (d) $|14, 6, 0\rangle$. $\langle N_1 \rangle$ is represented by the solid red line, $\langle N_2 \rangle$ by the dotted cyan line, and $\langle N_3 \rangle$ by the dashed blue line.

approximately constant for all choices of the initial states shown. The second, however, is that as the parameter $l$ in (3.4) is increased, there is a loss of coherence in the oscillations between wells 1 and 3. The reason for that loss of coherence can be appreciated from Fig. 3.4.

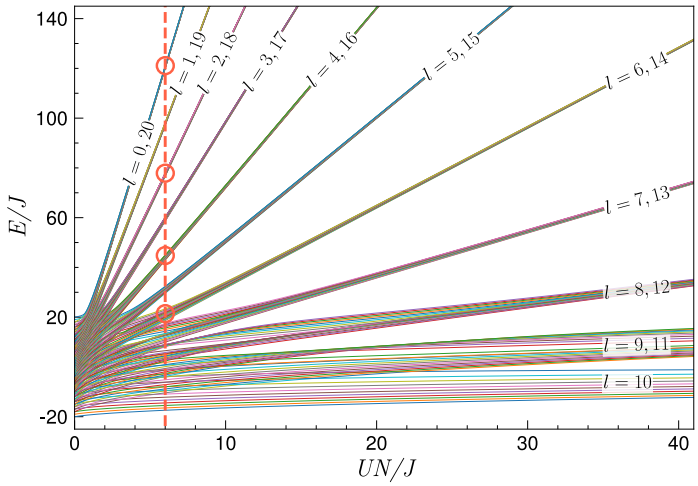


Figure 3.4: Energy level distribution. Dimensionless units are used. This figure is similar to Fig. 2, but displayed at a different scale. The labels shown on each band give the (approximate) possible values of $\langle N_2 \rangle$ for states within the band. The vertical line indicates $UN/J = 6$. The circles point out the four energy bands associated with the four initial states for the dynamics shown in Fig. 3.3.

To understand the above behaviour we define the sets $V_l = \{|N - k - l, l, k\rangle : k = 0, ..., N - l\}$. Then $V_l \cup V_{N-l}$ provides a basis for each band in the $UN/J \to \infty$ limit. When $UN/J$ is sufficiently large, but finite, these sets still provide accurate approximations for the bases. But as $l$ increases for $l \leq N/2$, or alternatively $l$ decreases for $l \geq N/2$, the threshold value of $UN/J$ which ensures well-separated bands increases. For $l = 0$ the band in Fig. 3.4 is clearly identifiable, whereas that for $l = 6$ is not. As we can see in Fig. 3.3, the dynamics for the initial state $|20, 0, 0\rangle$ leads to coherent oscillations, whereas the dynamics for $|14, 6, 0\rangle$ is not coherent.

The identification of approximate bases for the energy bands leads to a significant simplification in the computation of the dynamics, in the case when $UN/J$ is sufficiently large that the bands are well separated. This is what we term the *resonant tunneling* regime. In this case the analysis is simplified through use of an effective Hamiltonian defined through the conserved operator $Q$. Using the technique of first-order and second-order transition processes [60, 62], we find that for an initial state of the form (3.4) the effective Hamiltonian is

$$H_{\text{eff}} = -\lambda_l Q, \tag{3.6}$$

where $Q$ is given by (3.2) and

$$\lambda_l = \frac{1}{4U}\left(\frac{l+1}{N-2l-1} - \frac{l}{N-2l+1}\right). \tag{3.7}$$

Using semiclassical analysis (see details in [43]), we obtain analytic expressions for the time evolution of the expectation value of populations in wells 1 and 3. Specifically

$$\langle N_1 \rangle = \frac{1}{2}\left(N - l + (N - l - 2k)\cos(\omega_l t)\right) \tag{3.8}$$

$$\langle N_3 \rangle = \frac{1}{2}\left(N - l - (N - l - 2k)\cos(\omega_l t)\right), \tag{3.9}$$

where $\omega_l = \lambda_l J^2$ is the frequency.

The formulae indicate that the initial population in well 3, i.e. $k$, does not affect the frequency of oscillation. However, it does impact on the amplitude. For $k = l = 0$ we recover the results discussed in [43] and maximum amplitude oscillations are attained. It is easily seen from (3.8,3.9) that equality of the expectation values $\langle N_1 \rangle$ and $\langle N_3 \rangle$ occurs when $t = (2n+1)T/4$, $n \in \mathbb{N}$, where $T = 2\pi/\omega_l$ is the period of oscillation. We confirm from numerical computations that this is also the case when the Hamiltonian (3.1) is used, rather than the effective Hamiltonian (3.6). See Fig. 3.5, where $N = 60$ is used to allow comparison with the results of [43]. For **(a)** – **(c)** the parameter $U = 0.17$ was chosen to lie in the resonant regime, as explained above (see Fig. 3.3). The value of $U = 0.7$ for the panels **(d)** – **(f)** was chosen such that the oscillations have, approximately, half the frequency of those in **(a)** – **(c)**.

A method to approximately identify the beginning of the resonant regime in terms of the parameter $U$ as a function of the band $l$ (See Fig. 3.4), can be found in Appendix E of the thesis.

In order to gain insights into the quantum fluctuations of the coherent oscillations in the resonant regime, we now consider the variance of the expectation values. The

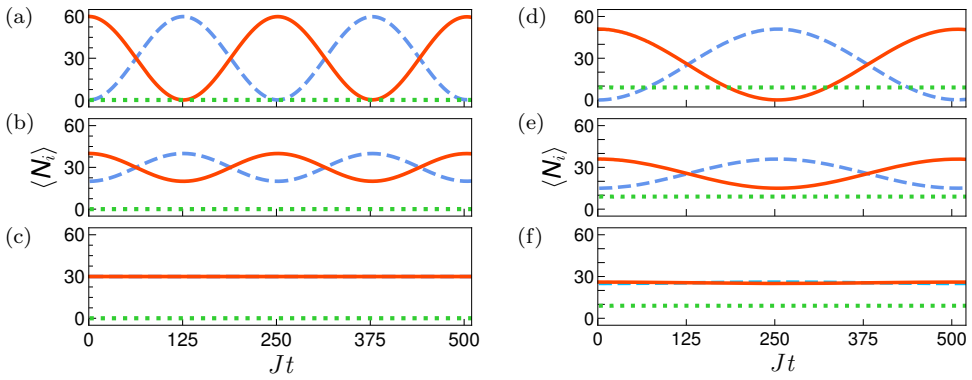


Figure 3.5: Expectation value dynamics. Dimensionless units are used. We set $J = 1$ and $N = 60$. The left panels are for $U = 0.17$ and the initial states : $|60, 0, 0\rangle$ [43], $|40, 0, 20\rangle$ and $|30, 0, 30\rangle$. The right panels are for $U = 0.7$ and the initial states: $|51, 9, 0\rangle$, $|36, 9, 15\rangle$ and $|26, 9, 25\rangle$. The solid red line is for $\langle N_1 \rangle$, the dotted green line is for $\langle N_2 \rangle$ and the dashed blue line is for $\langle N_3 \rangle$.

variance $\sigma_j^2$ of the expectation value $\langle N_j \rangle$ is defined by

$$\sigma_j^2(t) = \langle N_j^2(t) \rangle - \langle N_j(t) \rangle^2. \tag{3.10}$$

Obviously, a semi-classical calculation leads to the result that the fluctuations are zero. Consequently, we compute values of the variance obtained through numerical diagonalisation of the Hamiltonian (3.1). Fig. 3.6 shows the normalised variance of $\langle N_1 \rangle$, $\sigma_1^2/(N-l)^2$, for the same initial states as in Fig. 3.5. For each $N$ (assumed even), the maximum amplitude for the variance occurs when wells 1 and 3 of the initial state are equally populated, while the minimum amplitude is obtained when one of the wells 1 or 3 is empty for the initial state. Observe that the period of the variance is $T/2$, where $T$ is the period of the expectation value oscillations in wells 1 and 3. The maximum amplitude occurs at the times $(2n+1)T/4$, $n \in \mathbb{N}$. These times will be seen to be significant in the subsequent discussion on entanglement.

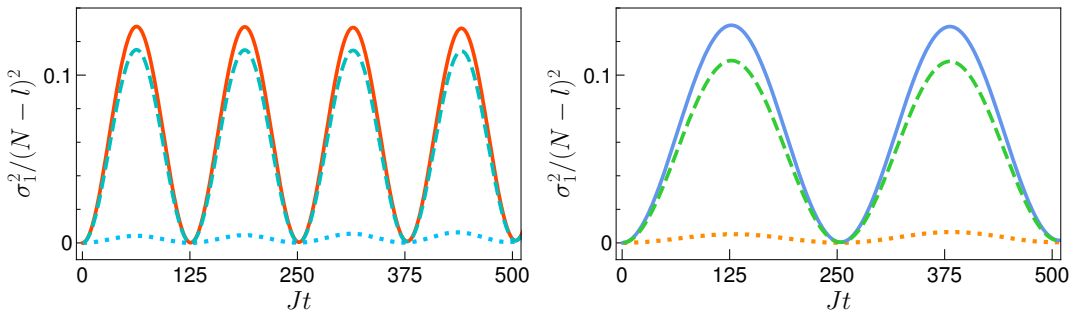


Figure 3.6: Time evolution of quantum fluctuations. Dimensionless units are used, and the fluctuations are normalised by $(N-l)^2$. We set $J = 1$ and $N = 60$. The left panel is for $U = 0.17$, $l = 0$ and initial states: $|60, 0, 0\rangle$ (dot blue line), $|40, 0, 20\rangle$ (dashed cyan line) and $|30, 0, 30\rangle$ (solid red line). The right panel is for $U = 0.7$, $l = 9$ and initial states: $|51, 9, 0\rangle$ (dotted orange line), $|36, 9, 15\rangle$ (dashed green line) and $|26, 9, 25\rangle$ (solid blue line).

## 3.4 Entanglement dynamics

For the following discussion we define the density matrix as

$$\rho(t) = |\Psi(t)\rangle\langle\Psi(t)|$$

and the reduced density matrices

$$\rho_1(t) = \mathrm{tr}_2\,\mathrm{tr}_3\,\rho(t), \qquad \rho_2(t) = \mathrm{tr}_1\,\mathrm{tr}_3\,\rho(t), \qquad \rho_3(t) = \mathrm{tr}_1\,\mathrm{tr}_2\,\rho(t)$$

where $\mathrm{tr}_j$ denotes the partial trace over the space of states for well $j$. The von Neumann entropy, defined as [77]

$$S_j(\rho(t)) = -\mathrm{tr}\,(\rho_j(t)\log\rho_j(t)) \tag{3.11}$$

provides a measure of the bipartite entanglement between the subsystem of well $j$ and the other two wells[2]. We also define the effective von Neumann entropy, which is calculated through the effective Hamiltonian (3.6). That is, for state evolution governed by

$$|\tilde{\Psi}(t)\rangle = \exp(-itH_{\mathrm{eff}})|\Psi_0\rangle$$

we define

$$\tilde{\rho}(t) = |\tilde{\Psi}(t)\rangle\langle\tilde{\Psi}(t)|$$

and the reduced density matrices

$$\tilde{\rho}_1(t) = \mathrm{tr}_2\,\mathrm{tr}_3\,\tilde{\rho}(t), \qquad \tilde{\rho}_2(t) = \mathrm{tr}_1\,\mathrm{tr}_3\,\tilde{\rho}(t), \qquad \tilde{\rho}_3(t) = \mathrm{tr}_1\,\mathrm{tr}_2\,\tilde{\rho}(t)$$

where $\mathrm{tr}_j$ denotes the partial trace over the space of states for well $j$. Then the effective von Neumann entropy is simply

$$S_j(\tilde{\rho}(t)) = -\mathrm{tr}\,(\tilde{\rho}_j(t)\log\tilde{\rho}_j(t)). \tag{3.12}$$

Fig. 3.7 shows evolution of the entanglement between well 1 and the rest of the system, calculated from Eq. (3.11) for the Hamiltonian (3.1), and Eq. (3.12) for the effective Hamiltonian (3.6). The initial state is $|20,0,0\rangle$, and four values are shown for the parameter $UN/J$ from weak interaction (Fig. 3.7 (a)) into the resonant tunneling regime (Fig.3.7 (d)). In the latter case there is excellent agreement between $S_1(\rho(t))$ and $S_1(\tilde{\rho}(t))$. It is seen that the entanglement is a decreasing function of $UN/J$, indicating a tendency towards localisation. Note that the maximum entanglement that can be generated is $S^{\max} = \log d$ (dashed blue line), where $d = (N+1)(N+2)/2$. However,

[2]There is freedom to choose the base for the logarithm. Throughout, we use base 2.

for the effective Hamiltonian the maximum entanglement that can be generated is $\tilde{S}^{\max} = \log(N - l + 1))$ (dot-dashed blue line).

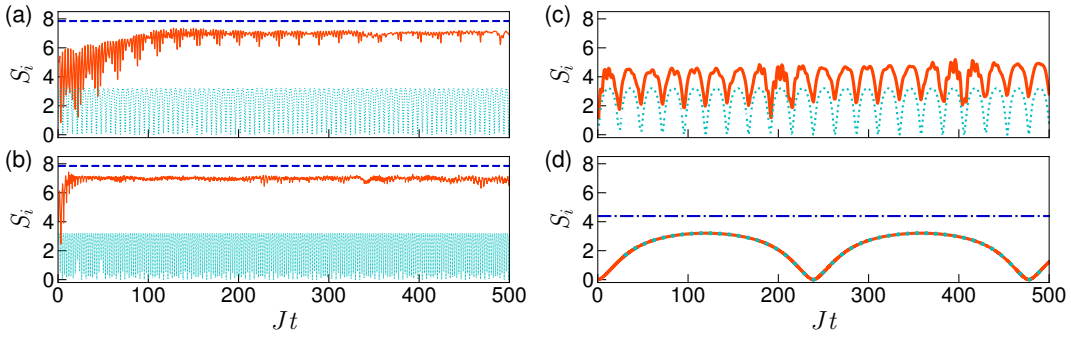


Figure 3.7: Entanglement dynamics. Dimensionless units are used. For all cases, $N = 20$ and $J = 1$, and the initial state is $|20, 0, 0\rangle$. (a): $UN/J = 0.02$, (b): $UN/J = 0.2$, (c): $UN/J = 2$, and (d): $UN/J = 20$. The orange lines depict $S_1(\rho(t))$ and the dotted cyan lines depict $S_1(\tilde{\rho}(t))$. The dashed blue lines (panels (a) and (b)) depict the maximum entanglement, while the dot-dashed line (panel (d)) represents the maximum entanglement that can be generated by the effective Hamiltonian (3.6).

In Fig. 3.8 the entanglement dynamics governed by the effective Hamiltonian is shown for six initial states in the resonant regime, the same as in Figs. 3.5 and 3.6. The maximum entanglement occurs in the vicinity of $t = (2n + 1)T/4$. (These curves exhibit some irregular behaviours. It is difficult to precisely identify the times at which the maxima occur.) The times $t = (2n+1)T/4$ are also those for which the expectation values $\langle N_1 \rangle$ and $\langle N_3 \rangle$ are equal (Fig. 3.5), and their quantum fluctuations are maximal (Fig. 3.6).

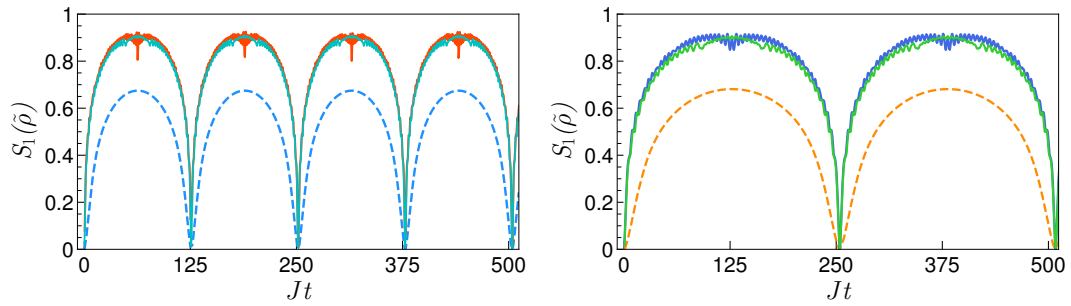


Figure 3.8: Entanglement dynamics under the effective Hamiltonian. Dimensionless units are used. We set $J = 1$ and $N = 60$. The left panel is for $U = 0.17$, $l = 0$ and initial states : $|60, 0, 0\rangle$ (dashed blue line), $|40, 0, 20\rangle$ (cyan line) and $|30, 0, 30\rangle$ (thicker red line). The right panel is for $U = 0.7$, $l = 9$ and initial states: $|51, 9, 0\rangle$ (dashed orange line), $|36, 9, 15\rangle$ (green line) and $|26, 9, 25\rangle$ (thicker blue line).

## 3.5 Coherent state description

In this section we provide an explicit formula for states evolving under the effective Hamiltonian (3.6). These states belong to the class of $su(2)$ coherent states [78], and

an expression for them can be compactly presented. Recall the Jordan-Schwinger representation of $su(2)$

$$\mathcal{J}_x = \frac{1}{2}(a_1^\dagger a_3 + a_1 a_3^\dagger), \qquad \mathcal{J}_y = -\frac{i}{2}(a_1^\dagger a_3 - a_1 a_3^\dagger), \qquad \mathcal{J}_z = \frac{1}{2}(N_1 - N_3)$$

satisfying the commutation relations $[\mathcal{J}_a, \mathcal{J}_b] = i\epsilon_{abc}\mathcal{J}_c$. The time evolution operator $\tilde{U}(t) = \exp(-itH_{\text{eff}}) = \exp(i\omega_l t(N_1 + N_3)/2)\exp(-i\omega_l\, t\mathcal{J}_x)$ has the action (neglecting, without loss of generality, the overall phase $\exp(i\omega_l t(N_1 + N_3)/2)$)

$$\begin{aligned}
&\tilde{U}(t)a_1^\dagger\tilde{U}^\dagger(t) \propto \left(\cos(\omega_l t/2)a_1^\dagger - i\sin(\omega_l t/2)a_3^\dagger\right),\\
&\tilde{U}(t)a_2^\dagger\tilde{U}^\dagger(t) \propto a_2^\dagger,\\
&\tilde{U}(t)a_3^\dagger\tilde{U}^\dagger(t) \propto \left(-i\sin(\omega_l t/2)a_1^\dagger + \cos(\omega_l t/2)a_3^\dagger\right).
\end{aligned}$$

For initial state $|N-l-k,l,k\rangle$, the above expressions lead to the following form for the time-dependent state

$$\begin{aligned}
|\tilde{\Psi}(t)\rangle &= \tilde{U}(t)|N-l-k,l,k\rangle\\
&\propto \sqrt{(N-l-k)!}\sqrt{k!}\sum_{j=0}^{k}\sum_{p=0}^{N-l-k}\frac{(-i)^{(j-p-k)}\sqrt{(j+p)!}}{p!(N-l-k-p)!}\frac{\sqrt{(N-l-p-j)!}}{j!(k-j)!}\\
&\quad\times(\sin(\omega_l t/2))^{(k+p-j)}(\cos(\omega_l t/2))^{(N+j-l-k-p)}|N-l-p-j,l,j+p\rangle
\end{aligned} \tag{3.13}$$

that can be rearranged to provide the wavefunction in a closed form (including the overall phase $\exp(i\omega_l t(N_1+N_3)/2) = \exp(i\omega_l t(N-l)/2)$)

$$|\tilde{\Psi}(t)\rangle = \exp(it\omega_l(N-l)/2)\sum_{n=0}^{N-l}b_n(k,l,t)|N-l-n,l,n\rangle, \tag{3.14}$$

where $b_n(k,l,t)$ is given explicitly in Suppl. Material 3.7.3. Note that $\sum_{n=0}^{N-l}|b_n(k,l,t)|^2 = 1$ for all $t$.

While the formulae (3.13), (3.14) are not exact for the Hamiltonian (3.1), they provide an excellent approximation in the resonant tunneling regime. This is confirmed by calculations for the *fidelity*, $F$, defined by [3]

$$F = |\langle\Psi(t)|\tilde{\Psi}(t)\rangle|.$$

Illustrative examples are depicted in Fig. 3.9 below, where the parameter values are the

same cases as those for Figs. 3.5, 3.6 and 3.8. The high values for the fidelity confirm the validity of the coherent state approximation. Note that the right panels in Fig. 3.9, where $l = 9$, are shown for a higher value of $U$ compared to $l = 0$ shown in the left panels. As mentioned earlier, this higher value of $U$ is required in order to reach the resonant tunneling regime with well separated energy bands.

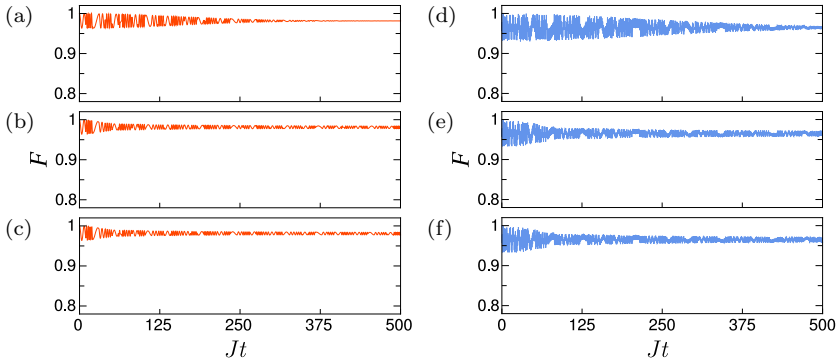


Figure 3.9: Fidelity as a function of time. Left panels: $U = 0.17$ and $l = 0$, for $N = 60$ and initial states **(a)**: $|60, 0, 0\rangle$, **(b)**: $|40, 0, 20\rangle$ and **(c)**: $|30, 0, 30\rangle$. Right panels: $U = 0.7$ and $l = 9$, for $N = 60$ and initial states **(d)**: $|51, 9, 0\rangle$, **(e)**: $|36, 9, 15\rangle$ and **(f)**: $|26, 9, 25\rangle$.

In principle, the coherent state expression (3.13) can be used to compute several important physical properties in the resonant tunneling regime for initial states (3.4). In Figure 3.10 below, the Fock state probabilities at $t = T/4$ are depicted. Each probability $|c_n|^2$ is associated with the basis vector $|60 - l - n, l, n\rangle$. These quantities are obtained through the dynamics of the Hamiltonian (3.1). The values closely match those given by the equivalent coherent state approximation through (3.14). The most probable states are: **(a)**: $|30, 0, 30\rangle$, **(b)**: $|58, 0, 2\rangle$ and $|2, 0, 58\rangle$, **(c)**: $|60, 0, 0\rangle$ and $|0, 0, 60\rangle$, **(d)**: $|26, 9, 25\rangle$ and $|25, 9, 26\rangle$, **(e)**: $|48, 9, 3\rangle$ and $|3, 9, 48\rangle$ and **(f)**: $|51, 9, 0\rangle$ and $|0, 9, 51\rangle$.

From these results one can identify that panels **(c)** and **(f)** show the states with the most uniform probability distribution. This helps to understand why the variance, and the entanglement entropy, increases with increasing number of particles $k$ in well 3 of the initial state. The decomposition of the state in terms of Fock states comprises an increasing number of components with increasing $k$. This correlates with the cases for $k = N/2$ ($N$ even), or $k = (N \pm 1)/2$ ($N$ odd) having the highest variance, as shown in Fig. 3.6, and the most entanglement, as shown in Fig. 3.8.

## 3.6 Discussion

In this work we analysed the capacity for entanglement generation in the integrable triple well model. Our study was mostly undertaken in the resonant tunneling regime.

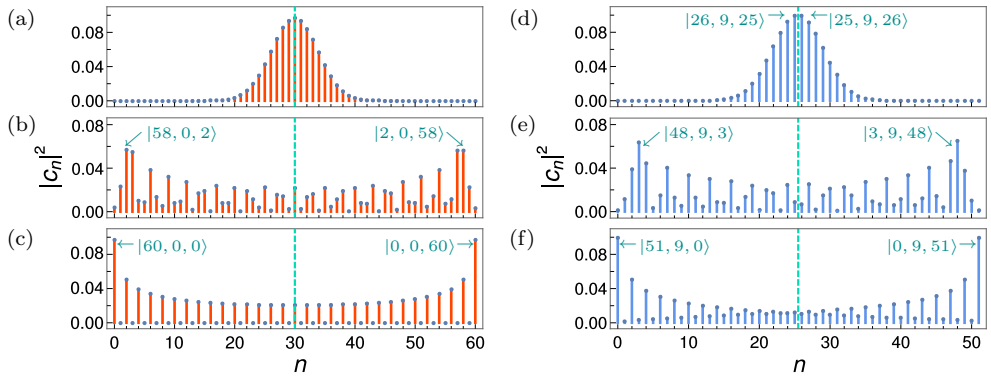


Figure 3.10: Fock state probabilities. Results shown for $t = T/4$ and $N = 60$. The index $n$ labels the Fock state $|N - l - n, l, n\rangle$, and $|c_n|^2$ denotes the probability associated to it. Left panels: $U = 0.17$ and $l = 0$ for initial states **(a)**: $|60, 0, 0\rangle$, **(b)**: $|40, 0, 20\rangle$ and **(c)**: $|30, 0, 30\rangle$. Right panels: $U = 0.7$ and $l = 9$ for initial states **(d)**: $|51, 9, 0\rangle$, **(e)**: $|36, 9, 15\rangle$ and **(f)**: $|26, 9, 25\rangle$. The vertical dashed lines mark the midpoints of the probability distributions. In the right column, where $l = 9$, the results display a slight asymmetry with respect to reflections about the midpoints.

We considered a class of unentangled initial states and studied the quantum evolution. We conducted calculations of population expectation values, quantum fluctuations, and entanglement. We found that the maximum entanglement occurred when the expectation values for populations in wells 1 and 3 are equal, where also their variances are maximal. We identified the time interval required to achieve the maximum entanglement. Analytic formulae for the evolution of the states were also obtained.

The next natural step is to study a more complex system of the integrable family of multi-well Hamiltonians presented in the Introduction. In this sense, we will subsequently investigate the integrable closed four-well model, which consists of 2+2 modes. Through an analysis of the quantum dynamics of this four-well system in the resonant tunneling regime, we will observe interesting interference arising between these two modes. This effect, which is not present in the triple well case, opens new possibilities for physical applications, as we will see in the next chapter.

## 3.7 Supplementary Material

### 3.7.1 Integrable Hamiltonian

The extended triple-well Hamiltonian has the general structure [37]

$$\mathcal{H} = \frac{U_0}{2}\sum_{i=1}^{3} N_i(N_i-1) + \sum_{i=1}^{3}\sum_{j=1;j\neq i}^{3}\frac{U_{ij}}{2}N_iN_j - J_1(a_1^\dagger a_2 + a_1 a_2^\dagger) - J_3(a_2^\dagger a_3 + a_2 a_3^\dagger). \tag{3.15}$$

Observing that $N^2 = (N_1^2 + N_2^2 + N_3^2) + 2N_1N_2 + 2N_1N_3 + 2N_2N_3$ leads to

$$\begin{aligned}\mathcal{H} = \frac{U_0}{2}(N^2 - N) + (U_{12}-U_0)N_1N_2 + (U_{13}-U_0)N_1N_3 + (U_{23}-U_0)N_2N_3 \\ - J_1(a_1^\dagger a_2 + a_1 a_2^\dagger) - J_3(a_2^\dagger a_3 + a_2 a_3^\dagger).\end{aligned} \tag{3.16}$$

Considering the particular case where $U_{13} = U_0$, and the symmetry configuration where $U_{12} = U_{23} = \alpha U_0$, the resulting Hamiltonian is integrable [24, 43] and can be written as

$$\mathcal{H}_0 = \frac{U_0}{2}(N^2 - N) + (\alpha-1)U_0N_2(N_1+N_3) - J_1(a_1^\dagger a_2 + a_1 a_2^\dagger) - J_3(a_2^\dagger a_3 + a_2 a_3^\dagger)$$

where $\alpha$ is a constant parameter that depends only on the ratio $l/\sigma_x$, while $\sigma_x$ is the width of the Gaussian cloud along the $x$-direction. Now, setting $U = (\alpha-1)U_0/4$, we demonstrate that the integrable Hamiltonian (3.1) is related to $\mathcal{H}$ through

$$\begin{aligned}H &= -\mathcal{H}_0 + (\alpha+1)U_0N^2/4 - U_0N/2 \\ &= U(N_1 - N_2 + N_3)^2 + J_1(a_1^\dagger a_2 + a_2^\dagger a_1) + J_3(a_2^\dagger a_3 + a_3^\dagger a_2).\end{aligned}$$

### 3.7.2 Experiment feasibility

In order to discuss how to physically implement our proposal in a laboratory setting, and to provide numerical values of parameters for experimental setups in the cases of Chromium and Dysprosium, which produce the desired dipole-dipole coupling parameters, we follow the main lines of the discussion presented in [26, 37]. For the general Hamiltonian that takes into account both contact and dipole-dipole interactions, we have

$$H = \int d^3\vec{r}\,\Psi^\dagger(\vec{r})\,(H_0)\,\Psi(\vec{r}) + \frac{1}{2}\int d^3\vec{r}d^3\vec{r'}\Psi^\dagger(\vec{r})\Psi^\dagger(\vec{r'})V(\vec{r}-\vec{r'})\Psi(\vec{r'})\Psi(\vec{r}), \tag{3.17}$$

where

$$H_0 = -\frac{\hbar^2}{2m}\nabla^2 + V_{trap}(\vec{r})$$

for suitable trapping potential $V_{trap}$. The interaction potential is given by

$$V(\vec{r} - \vec{r'}) = V_{sr}(\vec{r} - \vec{r'}) + V_{dd}(\vec{r} - \vec{r'}),$$

where the short-range ($V_{sr}$) and the dipole-dipole interaction ($V_{dd}$) potentials have the form

$$V_{sr}(\vec{r} - \vec{r'}) = g\delta(\vec{r} - \vec{r'}),$$
$$V_{dd}(\vec{r} - \vec{r'}) = \frac{C_{dd}}{4\pi}\frac{(1 - 3\cos^2\theta)}{|\vec{r} - \vec{r'}|^3}$$

where $g = 4\pi\hbar^2 a/m$, $a$ is the $s$-wave scattering length, $C_{dd} = \mu_0\mu^2$, $\mu$ is the magnetic dipole moment, $\mu_0$ is the permeability of the vacuum and $\theta$ is the angle between the magnetic dipole moment (which is fixed in the $z$-direction) and the vector $(\vec{r} - \vec{r'})$. The scattering length $a(B) = a_{bg}\,(1 - \Delta B/(B - B_0))$ can be controlled by a magnetic field $B$, in the vicinity of a Feshbach resonance.

Consider the approximation

$$\Psi(\vec{r}) = \sum_{i=1}^{3} \phi_i(\vec{r})a_i,$$

where $\phi_i(\vec{r}) = w_0(\vec{r} - \vec{r_i})$ is the localized Wannier function in the center of well $i$ for a single particle. The localized Wannier function is the ground state of $H_0$ within a harmonic approximation.

Using the above approximations, the Hamiltonian (3.17) reduces to

$$\begin{aligned} H =& \frac{U_0}{2}\sum_{i=1}^{3} N_i(N_i - 1) + U_{12}N_1N_2 + U_{23}N_2N_3 + U_{13}N_1N_3 \\ & - J_1(a_1^\dagger a_2 + a_2^\dagger a_1) - J_3(a_2^\dagger a_3 + a_3^\dagger a_2), \end{aligned}$$

where

$$J_k = -\int d^3\vec{r}\phi_k^*(\vec{r})H_0\phi_2(\vec{r}),$$
$$U_{sr} = g\int d^3\vec{r}|\phi_1(\vec{r})|^4,$$
$$U_{dd} = \int d^3\vec{r}d^3\vec{r'}|\phi_1(\vec{r})|^2|\phi_1(\vec{r'})|^2V_{dd}(\vec{r}-\vec{r'}),$$
$$U_{ij} = \int d^3\vec{r}d^3\vec{r'}|\phi_i(\vec{r})|^2|\phi_j(\vec{r'})|^2V_{dd}(\vec{r}-\vec{r'}),$$

and $U_0 = U_{sr} + U_{dd}$. By symmetry $U_{12} = U_{23}$, and the Hamiltonian becomes

$$\begin{aligned} H =& \frac{U_0}{2}\sum_{i=1}^{3} N_i(N_i-1) + U_{12}N_2(N_1+N_3) + U_{13}N_1N_3 \\ & - J_1(a_1^\dagger a_2 + a_2^\dagger a_1) - J_3(a_2^\dagger a_3 + a_3^\dagger a_2). \end{aligned}$$

Using the conservation of $N$, we devolve into the same equation as Eq. (3.16).

A schematic representation of the experimental configuration is shown in Fig. 3.11. Three cigar-shaped Bose-Einstein condensates are trapped in a triple-well potential generated by three Gaussian beams, separated by a distance $l = 1.8\,\mu$m (one beam for each potential) along the $y$-axis. They are crossed by a transverse beam which provides $xz$-confinement. The (approximate) harmonic potential of each well $i = 1, 2, 3$ is symmetrically cylindrical and is locally given by

$$V_{trap}(x, y, z) = \frac{1}{2}m\omega_x^2x^2 + \frac{1}{2}m\omega_r^2((y-y_i)^2 + z^2),$$

where $y_i = l, 0, -l$, $\omega_x$ is the frequency along the $x$-axis, and $\omega_r$ is the radial frequency in the $yz$-plane.

Table 3.1 lists experimental values, and resulting coupling parameters, for two different dipolar atoms, Chromium, $^{52}$Cr, and Dysprosium, $^{164}$Dy [43]. Some of the coupling parameters are indicated in Fig. 3.12.

### 3.7.3 Coherent state approximation in closed form

Consider $\exp(-itH_{\text{eff}}) = VU$, where

$$V = \exp\left(\frac{i\omega_l t}{2}(N_1+N_3)\right), \qquad \omega_l = \lambda_l J^2,$$
$$U = \exp(-i\omega_l t\mathcal{J}_x), \qquad \mathcal{J}_x = \frac{1}{2}(a_1^\dagger a_3 + a_3^\dagger a_1).$$

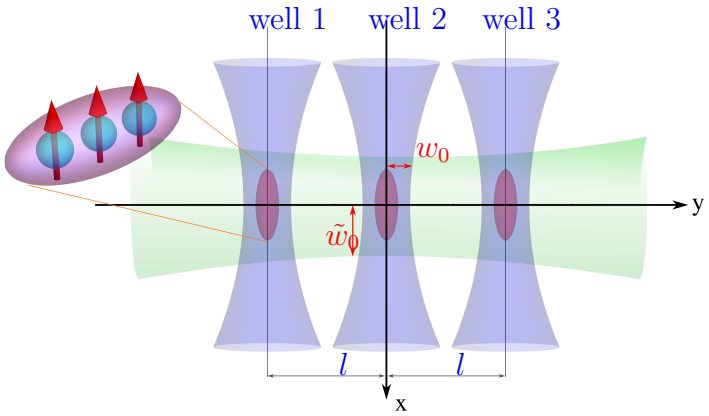


Figure 3.11: Schematic representation of the trap geometry. The three cigar-shapes (purple) represent the dipolar Bose-Einstein condensates, trapped in a triple-well potential formed by three parallel beams (blue), with waist $w_0$. The three beams are crossed by a transverse beam (green) with waist $\tilde{w}_0$. The wells are separated by a distance $l = 1.8\,\mu$m. The dipolar atoms are aligned to the $z$-axis by a magnetic field (red arrows).

| | Parameters | $^{52}$Cr | $^{164}$Dy |
|---|---|---|---|
| distance between wells | $l$ | 1.8 $\mu$m | 1.8 $\mu$m |
| parallel laser wavelength | $\lambda$ | 1.064 $\mu$m | 1.064 $\mu$m |
| parallel laser waist | $w_0$ | 1 $\mu$m | 1 $\mu$m |
| transverse laser wavelength | $\lambda$ | 1.064 $\mu$m | 1.064 $\mu$m |
| transverse laser waist | $\tilde{w}_0$ | 6 $\mu$m | 5 $\mu$m |
| $y-z$ radial trap frequency | $\omega_r/(2\pi)$ | 220 Hz | 67 Hz |
| $x$ trap frequency | $\omega_x/(2\pi)$ | 64 Hz | 23 Hz |
| $s$-wave scattering length | $a/a_B$ | 0.1 | 1 |
| dipolar scattering length | $a_{dd}/a_B$ | 16 | 131 |
| trap geometry parameter | $\alpha = U_{12}/U_0$ | 5.81 | 5.89 |
| one-site interaction | $U_0/(2\pi\hbar)$ | 0.019 Hz | 0.046 Hz |

Table 3.1: Experimental values and resulting parameters for $^{52}$Cr and $^{164}$Dy.

Using the identity

$$\sum_{j=0}^{k}\sum_{p=0}^{N-l-k} f(p+j,p-j,p,j) = \sum_{n=0}^{N-l}\sum_{j\in S_n(k,l)} f(n,n-2j,n-j,j),$$

where

$$I_k = \{0,1,2,\cdots,k\},$$
$$S_n(k,l) = \{j \in I_k : j = n-p, \text{ where } p \in I_{N-l-k}\},$$

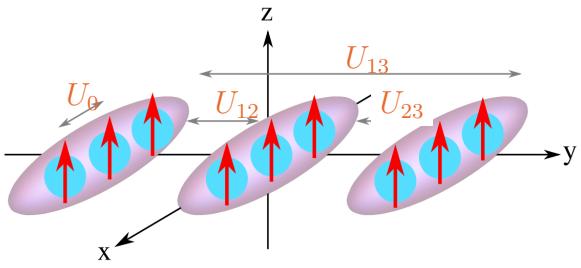


Figure 3.12: Schematic representation of the device. The cigar-shapes (purple), represent dipolar Bose-Einstein condensates, whose Gaussian distribution occurs predominantly in the $x$-direction. Dipole-dipole interactions are characterized by $U_{12} = U_{23} = \alpha U_0$, and $U_{13} = U_0$ is the integrability condition. Recall that $U = (\alpha - 1)U_0/4$ is the parameter that appears in the Hamiltonian (3.1).

we find

$$U|N-l-k,l,k\rangle = \sum_{n=0}^{N-l} b_n(k,l,t)|N-l-n,l,n\rangle,$$

with

$$b_n(k,l,t) = \sqrt{\frac{C_k^{N-l}}{C_n^{N-l}}} \sum_{j\in S_n(k,l)} (-i)^{k+n-2j} c_l^{N-l-k-n+2j} s_l^{k+n-2j} C_{n-j}^{N-l-k} C_j^k,$$

In the above expressions, the following shorthand notation is adopted for the binomial coefficients and trigonometric functions:

$$\begin{aligned} C_k^n = \binom{n}{k} &= \frac{n!}{k!(n-k)!}, \\ c_l &= \cos\left(\omega_l t/2\right), \\ s_l &= \sin\left(\omega_l t/2\right). \end{aligned}$$

Note that, for all $t$,

$$\sum_{n=0}^{N-l} |b_n(k,l,t)|^2 = 1.$$

Thus, we have the normalised states

$$|\tilde{\Psi}(t)\rangle = \exp(it\omega_l(N-l)/2) \sum_{n=0}^{N-l} b_n(k,l,t)|N-l-n,l,n\rangle.$$

Using the above formula, we find

$$\langle\tilde{\Psi}(t)|N_1|\tilde{\Psi}(t)\rangle = \sum_{n=0}^{N-l}(N-l-n)|b_n(k,l,t)|^2 = \frac{1}{2}(N-l+(N-l-2k)\cos(\omega_l t)),$$
$$\langle\tilde{\Psi}(t)|N_2|\tilde{\Psi}(t)\rangle = \sum_{n=0}^{N-l} l|b_n(k,l,t)|^2 = l,$$
$$\langle\tilde{\Psi}(t)|N_3|\tilde{\Psi}(t)\rangle = \sum_{n=0}^{N-l} n|b_n(k,l,t)|^2 = \frac{1}{2}(N-l-(N-l-2k)\cos(\omega_l t)),$$

which agree with the semiclassical result presented in the main text.

# Chapter 4

# Integrable atomtronic interferometry

In this chapter, we proceed to investigate the integrable four-well model looking for applications in interferometry. As in the previous triple well case, we consider the system in the resonant tunneling regime. Analytic formulae for the quantum dynamics of certain observables are derived using the conserved operators of the system. We present the temporal evolution of the population imbalance, showing an excellent agreement between numerical and analytical behavior, evidencing the phenomenon of interferometry. By designing interferometric protocols, we expose the functionality of the system as a high-sensitivity interferometer and also as a producer of NOON states. Finally, we show that the system is capable of interferometry with sensitivity at the Heisenberg limit, highlighting a connection with quantum information. The main content of this Chapter was published in Physical Review Letter[1].

## 4.1 Foreword

Recent developments in the manipulation of wave-like properties in matter are driving a raft of atom-interferometric applications, in the vicinity of the Heisenberg limit, within the field of quantum metrology [79, 80]. It has long been recognized that the ability to effectively and efficiently harness quantum interference is equivalent to implementing certain tasks in quantum computation [45]. Nowadays, ultracold quantum gases are proving to be successful in enabling quantum simulations, for phenomena such as quantum magnetism and topological states of matter, beyond the capabilities of classical supercomputers [81]. Through a confluence of these types of investigations, there are several efforts to push research towards designs for atomtronic devices [36, 82, 83],

[1] *Integrable atomtronic interferometry*, D.S. Grun, Karin Wittmann W., L.H. Ymai, J. Links, and A. Foerster, *Phys. Rev. Lett.*, **129**, 020401 (2022), doi:10.1103/PhysRevLett.129.020401

based on circuits with atomic currents [84–87]. These devices promise high levels of control in the manipulation of many-body systems, leading to advanced sensitivity in metrology [88] and other quantum technologies [33, 43, 89–91].

Around a decade ago [37] a class of models was identified for physical realization of an interferometer, using dipolar atoms. The Hamiltonian governing the time evolution of the system is the extended Bose-Hubbard model on four sites, with closed boundary conditions and long-ranged interactions. Here, we will study the integrable four-well Hamiltonian that governs the temporal evolution of ultracold dipolar bosons with large dipole moment, such as dysprosium, trapped in a circuit of four optical potentials. We will show that it can be seen as a particular case of the four-site extended Bose-Hubbard model. In this integrable case, there are four conserved operators, equal to the number of degrees of freedom.

The conserved operators of the integrable system are used to guide the design of measurement protocols for interferometric tasks (see Fig. 4.1). Our results are applicable in a particular regime, designated as *resonant tunneling*, whereby the energy levels separate into distinct bands. Through an effective Hamiltonian approach, the entire energy spectrum and structure of eigenstates becomes explicit for resonant tunneling. Moreover, the system's behavior is clear in quantum information theoretic terms. The interferometer is equivalent to a system of two *hybrid qudits* [92], and the time-evolution of states is equivalent to the operation of a *controlled-phase* gate [93, 94]. We describe proof of principle examples of high-fidelity measurement protocols to identify and produce certain NOON states [45, 80, 95–97], We also provide a physical-feasibility analysis of the system with first-principles calculations of the Hamiltonian parameters within an explicit Bose-atom setup (see Supplemental Material 4.7.1).

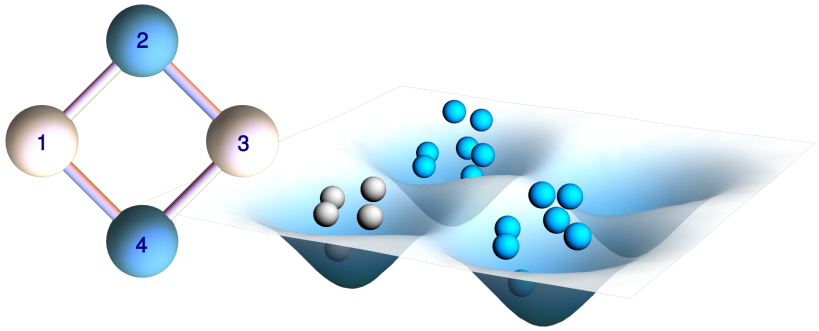


Figure 4.1: Schematic representation of the interferometric circuit with tunneling between nearest neighbors. An initial state is prepared with $M$ particles in site 1, and $P$ particles in a (generally entangled) state across sites 2 and 4. After Hamiltonian time-evolution, measurement of particle number at site 3 is used to deduce information about the initial, or post-measurement, state across sites 2 and 4.

## 4.2 The model

An extended Bose-Hubbard Hamiltonian on a square plaquette has the form [26, 38]

$$\begin{aligned} H = & \frac{U_0}{2}\sum_{i=1}^{4} N_i(N_i-1) + \sum_{i=1}^{4}\sum_{j=1,j\neq i}^{4} \frac{U_{ij}}{2} N_i N_j \\ & - \frac{J}{2}[(a_1^\dagger + a_3^\dagger)(a_2+a_4) + (a_2^\dagger + a_4^\dagger)(a_1+a_3)]. \end{aligned} \tag{4.1}$$

where $\{a_j,\, a_j^\dagger : j = 1,2,3,4\}$ are canonical boson annihilation and creation operators, $U_0$ characterizes the short-range interactions between bosons at the same site, $U_{ij} = U_{ji}$ accounts for long-range (e.g. dipole-dipole) interactions between sites, and $J$ represents the tunneling strength between neighboring sites. The Hamiltonian commutes with the total particle number $N = N_1 + N_2 + N_3 + N_4$ where $N_j = a_j^\dagger a_j$. Moreover, the Hamiltonian is integrable when $U_{13} = U_{24} = U_0$ and $U_{12} = U_{14} = U_{23} = U_{34}$. It acquires two additional conserved operators

$$\begin{aligned} Q_1 &= \frac{1}{2}(N_1 + N_3 - a_1^\dagger a_3 - a_3^\dagger a_1), \\ Q_2 &= \frac{1}{2}(N_2 + N_4 - a_2^\dagger a_4 - a_4^\dagger a_2), \end{aligned}$$

such that $[Q_1, Q_2] = [Q_j, H] = [Q_j, N] = 0$, $j = 1, 2$. Integrability results from derivation of the model through the Quantum Inverse Scattering Method. It is intimately related to exact solvability, due to the algebraic Bethe Ansatz [98]. Hereafter we only consider the integrable case.

## 4.3 Resonant tunneling regime

It is straightforward to check that there are large energy degeneracies when $J = 0$. From numerical diagonalization of (4.1), with $N$ particles and sufficiently small value of $J$, it is seen that the low-energy levels coalesce into well-defined bands [99], similar to that observed in an analogous integrable three-site model [43, 44]. In this regime, an effective Hamiltonian $H_{\text{eff}}$ is obtained through consideration of second-order tunneling processes. For an initial Fock state $|M-l, P-k, l, k\rangle$, with total boson number $N = M + P$, the effective Hamiltonian is a simple function of the conserved operators

$$H_{\text{eff}} = (N+1)\Omega(Q_1 + Q_2) - 2\Omega Q_1 Q_2, \tag{4.2}$$

where $\Omega = J^2/(4U((M-P)^2-1))$ with $U = (U_{12}-U_0)/4$. This result is valid for $J \ll U(M-P)$, which characterizes the resonant tunneling regime. For time evolution under $H_{\text{eff}}$, both $N_1+N_3 = M$ and $N_2+N_4 = P$ are constant. The respective $(M+1)$-dimensional subspace associated with sites 1 and 3 and $(P+1)$-dimensional subspace associated with sites 2 and 4 serve as two, coupled, hybrid qudits [92], and provide the state space for the relevant energy band. This yields a robust approximation for the dynamics under (4.1), which we benchmark below. For later use we will designate the qudit associated with sites 1 and 3 as *qudit A*, and that associated with sites 2 and 4 as *qudit B*.

It is found through Bogoliubov transformations that the spectrum of $H_{\text{eff}}$ is $E_{\text{eff}} = (N+1)\Omega(q_1+q_2) - 2\Omega q_1 q_2$ with $q_1 = 0, ..., M$ and $q_2 = 0, ..., P$. Thus the time evolution under $H_{\text{eff}}$ is recognized as a controlled-phase gate [93, 94]. From here, several analytic results are accessible. For initial Fock state $|M, P, 0, 0\rangle$, the expectation value of the fractional imbalance $\mathcal{I}(t)$ between sites 1 and 3 is (in units where $\hbar = 1$)

$$\mathcal{I}(t) \equiv \langle N_1 - N_3\rangle/M = \cos((M+1)\Omega t)[\cos(\Omega t)]^P. \tag{4.3}$$

When $P = 0$, there are harmonic oscillations in the imbalance. For non-zero $P$, the oscillations are no longer harmonic due to interference. For comparison, results from numerical diagonalization of (4.1) are shown in the upper panels of Fig. 4.2

Other initial states can be studied, such as

$$|\Phi(\phi)\rangle = \frac{1}{\sqrt{2}}|M, P, 0, 0\rangle + \frac{\exp(i\phi)}{\sqrt{2}}|M, 0, 0, P\rangle, \tag{4.4}$$

which is a product of a number state for site 1, vacuum for site 3 (qudit A), and a phase-dependent NOON state [45, 80] across sites 2 and 4 (qudit B). We find the following result for the fractional imbalance between sites 1 and 3:

$$\begin{aligned}\langle N_1 - N_3\rangle/M = &\cos((M+1)\Omega t)\,[\cos(\Omega t)]^P \\ &+ \cos(\phi)\cos((M+1)\Omega t + \pi P/2)[\sin(\Omega t)]^P.\end{aligned} \tag{4.5}$$

This formula provides excellent agreement with numerical calculations using (4.1). Examples are provided, for choices $\phi = 0$ and $\phi = \pi$, in the lower panels of Fig. 4.2 using experimentally feasible parameters evaluated in Supplemental Material 4.7.1.

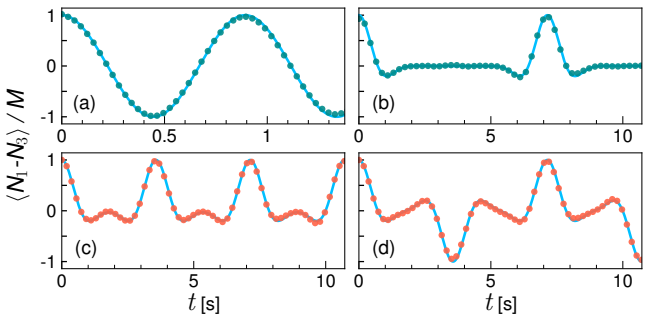


Figure 4.2: Time evolution of expected fractional imbalance $\langle N_1 - N_3 \rangle / M$ (dot points) for the Hamiltonian (4.1) as a function of time $t$ in units of seconds, with $U/J \simeq 1.2$, $U/\hbar \simeq 2\pi \times 19.5$ Hz, $J/\hbar \simeq 2\pi \times 16.2$ Hz, and different initial states : **(a)** $|4,0,0,0\rangle$. **(b)** $|4,11,0,0\rangle$. **(c-d)** $(|4,11,0,0\rangle + \exp(i\phi)\,|4,0,0,11\rangle)/\sqrt{2}$ with $\phi = 0$ **(c)** and $\phi = \pi$ **(d)**. The top panels display agreement with the formula (4.3) (solid lines), while the bottom panels are in agreement with (4.5) (solid lines).

## 4.4 NOON state identification and production

The above results are sufficient to demonstrate the efficacy of the system to perform certain interferometric tasks. First consider a black box processor $\mathbb{P}$ that outputs one of two possible NOON states, either symmetric or antisymmetric. The output state, with particle number $P$, is loaded into qudit B. With $M$ particles in site 1 and zero in site 3 of qudit A, this composite initial state is given by (5.1) with either $\phi = 0$ (symmetric) or $\phi = \pi$ (anti-symmetric). Choose $M$ such that $N = M + P$ is odd, let the system evolve for time $t_m = \pi/(2\Omega)$, and then measure the particle number at site 3. According to (4.5), there are only two possible measurement outcomes. One is to obtain the outcome zero, which occurs with probability 1 when $\phi = \pi$. The other is to obtain the outcome $M$, which occurs with probability 1 when $\phi = 0$ (cf. the lower panels of Fig. 4.2, where the time of measurement is $t_m \simeq 3.57$s). Moreover, this measurement is non-destructive and the NOON state in qudit B is preserved [2].

This analytic result is an excellent approximation for the behavior governed by (4.1). From numerical results using the parameters of Fig. 4.2, we find that the success probability when $\phi = 0$ is 0.98334, and it is 0.99383 when $\phi = \pi$. This delivers a proof of principle example to show that the model (4.1) has capacity to perform interferometry with high accuracy.

Remarkably, the earlier analysis on NOON state identification can now be inverted to show that the interferometer itself provides a high-fidelity simulation of the black

[2]Within the superlattice configuration described in Supplemental Material 4.7.1, non-destructive measurement can be physically realized through Faraday imaging [100, 101] or site-selective measurement [102, 103] combined with off-resonant fluorescence imaging [104].

box processor $\mathbb{P}$. For $|\Psi_0\rangle = |M, P, 0, 0\rangle$ with $N = M + P$ odd, it can be shown that

$$|\Psi(t_m)\rangle = \frac{(-1)^{(N+1)/2}}{2}|M, P, 0, 0\rangle + \frac{1}{2}|M, 0, 0, P\rangle + \frac{1}{2}|0, P, M, 0\rangle + \frac{(-1)^{(N-1)/2}}{2}|0, 0, M, P\rangle . \tag{4.6}$$

In accordance with the previous discussion, measurement at site 3 produces one of only two possible outcomes. A measurement outcome of $M$ causes wavefunction collapse such that the state of qudit B is the symmetric (antisymmetric) NOON state if $(N+1)/2$ is odd (even). Conversely, a measurement outcome of zero causes wavefunction collapse with an antisymmetric (symmetric) NOON state in qudit B if $(N+1)/2$ is odd (even).

As before, it is useful to compare this result obtained from (5.3) against the analogous predictions of (4.1). Numerically, using the parameters of Fig. 4.2, we find that the outcome fidelity of this processor simulation for (4.1) is 0.97831 for outcome zero, and 0.99298 for outcome $M$, with respective probabilities of 0.49611 and 0.47639, close to the theoretically predicted values of 1/2 in each case. See Supplemental Material 4.7.2 for further details, including probabilities and fidelities for intermediate outcomes.

*Entanglement and correlations.*– The ability to produce NOON states as described above is clearly dependent on the ability to create entanglement. More important is the ability to create "useful" entanglement since, as emphasized in the review article [80]: "Not all entangled states are useful for quantum metrology". See also [105]. Below we demonstrate how this notion applies in the present context by analyzing the entanglement produced and the correlations present in the system.

It is convenient for our study to use the entanglement measure of *linear entropy* $\mathcal{E}(\rho)$, defined in terms of a density matrix $\rho(t) = |\Psi(t)\rangle\langle\Psi(t)|$ as [106, 107] $\mathcal{E}(\rho) = 1 - \mathrm{tr}(\rho^2)$. The linear entropy is bounded between 0 and $1 - 1/d$, where $d$ is the dimension of the space on which the density matrix acts. For initial state $|\Psi_0\rangle = |M, P, 0, 0\rangle$ the entanglement between qudits A and B at time $t_m$ is quantified through $\mathcal{E}(\rho_{1,3}(t_m)) = 1/2$, where $\rho_{1,3}(t_m) \equiv \mathrm{tr}_{2,4}\ \rho(t_m)$ is the reduced density matrix (see Supplemental Material 4.7.2 for details). This result is independent of $P$. It asserts that immediately prior to making measurement at site 3, at time $t = t_m$, the entanglement between qudits A and B is *independent* of whether $N = M + P$ is even or odd.

Further, let $\rho_3(t_m) = \mathrm{tr}_1(\rho_{1,3}(t_m))$, which can be compactly expressed as

$$\rho_3(t_m) = \sum_{q=0}^{M} \mathcal{P}(q)\,|q\rangle\,\langle q|\,,$$

where $\mathcal{P}(q)$ refers to the probability of measuring $q$ particles at site "3". The linear entropy of $\rho_3$ quantifies the entanglement between the subsystems, sites 1 and 3, within

qudit A. Now we encounter a significant difference between the even and odd cases. When $N$ is odd, $\mathcal{E}(\rho_3(t_m)) = 1/2$. For even $N$, $\mathcal{E}(\rho_3(t_m)) = 1 - \frac{1}{2^{2M}}\binom{2M}{M} \sim 1 - \frac{1}{\sqrt{M\pi}}$, where the second step invokes Stirling's approximation. By symmetry, the same conclusion can be drawn for qudit B (with $M$ replaced by $P$). The curious observation to make here is that in the odd case, which enables a protocol for NOON state production, the pre-measurement entanglement *within* the qudits is substantially *less* than that for the even case. This is despite the pre-measurement entanglement *between* the qudits being independent of number parity. While number-parity effects are ubiquitous in fermionic systems [108–112], they are less frequently encountered in bosonic models. The situation reported here displays some features in common with the work of [113].

A similar feature is observed in the correlations of the system. In order to quantify the effects of odd/even $N$, we first define the following NOON correlation function between sites "1" and "3",

$$C_{1,3} = \frac{4}{M^2}\left(\langle N_1\rangle\langle N_3\rangle - \langle N_1 N_3\rangle\right), \tag{4.7}$$

where $C_{1,3} = 1$ if there exists a NOON state at qudit A. Again for initial state $|\Psi_0\rangle = |M, P, 0, 0\rangle$, using (4.3) and the result $\langle (N_1 - N_3)^2\rangle/M^2 = 1 + \alpha_M\left(\mathcal{I}(2t) - 1\right)$, $\alpha_M \equiv (M-1)/(2M)$, yields

$$C_{1,3}(t) = 1 - \mathcal{I}^2(t) + \alpha_M\left(\mathcal{I}(2t) - 1\right)$$

and $C_{2,4}(t) = C_{1,3}(t)\Big|_{M\leftrightarrow P}$ by symmetry. At $t = t_m$, we obtain $C_{1,3}(t_m) = M^{-1}$, $C_{2,4}(t_m) = P^{-1}$ for $N$ even, and $C_{1,3}(t_m) = C_{2,4}(t_m) = 1$ for $N$ odd where the last result asserts the simultaneous existence of NOON states in each of the qudits only for the odd case. The presence of a NOON state at $t = t_m$ is signalled by attaining the maximum of the NOON correlation function $C_{1,3}$ and a simultaneous dip in the normalized linear entropy $\tilde{\mathcal{E}}(\rho_3(t)) = (M+1)\mathcal{E}(\rho_3(t))/M$, as shown in Fig. 4.3. Further details on correlations between the qudits, and in particular the role of Eq. (4.5), are discussed in Supplemental Material C.

## 4.5 Heisenberg-limited interferometry.

Finally, we establish that the system is capable of interferometry with sensitivity at the Heisenberg limit, through the archetypal example of parameter estimation through the

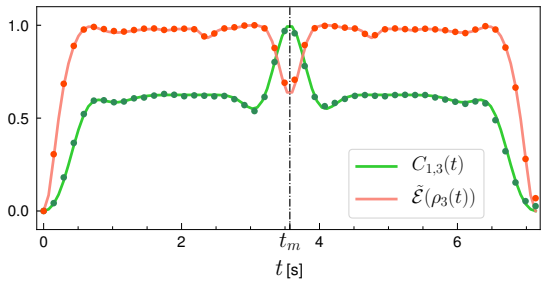


Figure 4.3: Normalized linear entropy and NOON correlation function. The red (green) line depicts $\tilde{\mathcal{E}}(\rho_3(t))$ ($C_{1,3}(t)$) calculated with the effective Hamiltonian $H_{\text{eff}}$ of (5.3), while the dots illustrate the numerical values obtained with the Hamiltonian (4.1). The initial state is $|\Psi_0\rangle = |4, 11, 0, 0\rangle$, and the Hamiltonian parameters are $U/\hbar = 2\pi \times 19.5$ Hz and $J/\hbar = 2\pi \times 16.2$ Hz.

phase of a NOON state [45, 80]. Consider initial state (5.1) with $N = M + P$ odd, and $\phi = 0$. A new phase $\varphi$ is encoded into the bosons at site 4 through a transformation, $a_4^\dagger \mapsto \exp(i\varphi)a_4^\dagger$ (cf. [37, 99]). This still corresponds to (5.1), but now with $\phi = P\varphi$, a phenomenon known as *phase super-resolution* [96, 97]. Again for time interval $t = t_m$, the imbalance between sites 1 and 3 is obtained from (4.5) as

$$\langle N_1 - N_3 \rangle = (-1)^{(N+1)/2} M \cos(P\varphi) \tag{4.8}$$

providing the interference fringe with maximal contrast. Fig. 4.4 shows the dependence of the fractional imbalance $\langle N_1 - N_3 \rangle / M$ on parameters $\varphi$ and the time $t$.

Next, it can be confirmed that $\langle (N_1 - N_3)^2 \rangle = M^2$, so

$$\begin{aligned} \Delta\langle N_1 - N_3 \rangle &= \sqrt{\langle (N_1 - N_3)^2 \rangle - \langle N_1 - N_3 \rangle^2} \\ &= M |\sin(P\varphi)|, \end{aligned}$$

where $\Delta$ denotes the standard deviation. Using the standard estimation theory approach [45, 80], it is found that the system achieves Heisenberg-limited phase sensitivity since

$$\Delta\varphi = \frac{\Delta\langle N_1 - N_3 \rangle}{|\mathrm{d}\langle N_1 - N_3 \rangle / \mathrm{d}\varphi|} = \frac{1}{P}.$$

This is an improvement on the classical shot-noise case where $\Delta\varphi \sim 1/\sqrt{P}$ [45, 80]. In Supplemental Material 4.7.4, we present a discussion on the robustness of the system with respect to perturbation about the integrable case.

## 4.6 Discussion

We have provided an example of integrable atomtronic interferometry, through an extended Bose-Hubbard model, with four sites arranged in a closed square. The integrable

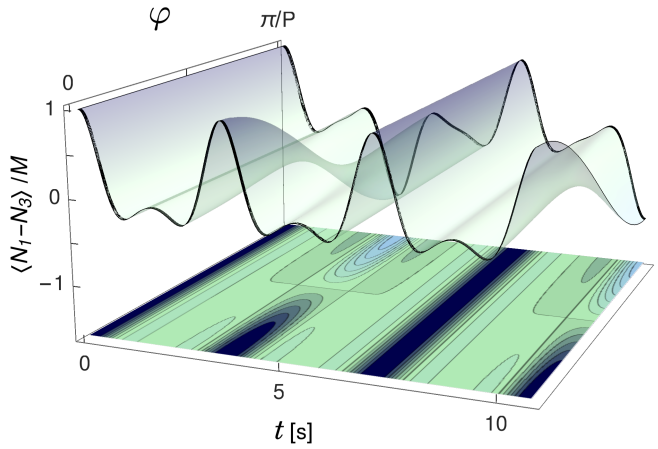


Figure 4.4: Dependence of $\langle N_1 - N_3 \rangle / M$ as a function of time $t$ (in units of seconds) and phase $\varphi$, for initial state (5.1) with $M = 4$, $P = 11$, $\phi = P\varphi$, and $U/J \simeq 1.2$. Upper surface: The colors range from light to dark blue, indicating lower and higher values for the imbalance fraction. The green color represents the region where $\langle N_1 \rangle \approx \langle N_3 \rangle$. Lower plane: The effect on the system's dynamics is highlighted, specifically for the limiting cases $\varphi = 0$ and $\varphi = \pi/P$, where it is seen that there is a minimum-maximum inversion at $\varphi = \pi/(2P)$.

properties of the model furnished the necessary tools to understand the dynamics of the system in the resonant tunneling regime. It allowed for the analytic calculation of dynamical expectation values and correlation functions heralding NOON state formation. This, in turn, informed the relevant time interval required to implement certain measurement protocols. The probabilities for measurement outcomes were computed via the density matrix. We demonstrated proof of principle examples that the integrable system functions as an identifier of NOON states produced by a black box processor, and as a simulator of such a processor.

Our study highlights the quantum information connections of the model by detailing its function as a hybrid qudit system subjected to a controlled-phase gate operation. Besides providing feasibility for the physical set up and identifying means to experimentally probe the correlations between the qudits, the proposed scheme also allows for the further investigations of measurement-based protocols for novel quantum technologies.

In the next chapter, we will expand on this study by designing two protocols, one probabilistic and another deterministic, to generate, control and encode a phase into the NOON state.

## 4.7 Supplementary Material

### 4.7.1 Physical setup and parameter evaluations for the integrable system

We describe a physical setup for the system based on superlattices, which allows for the creation of many copies of disconnected four-well square plaquettes [114]. This configuration can be obtained by the overlapping of two 2D optical lattices - generated separately by laser beams with wavelengths $\lambda = 532$ nm and $2\lambda$, added to a vertical 1D lattice generated by a laser with wavelength $2\lambda$ to provide pancake-shaped trapping [3]. A scheme of the superlattice is shown in Supplemental Figure 4.5.

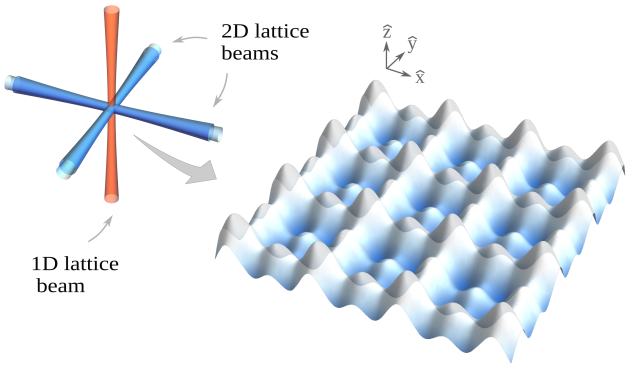


Figure 4.5: Schematic representation of the superlattice beams. Left, the two-dimensional lattice with two sets of counterpropagating beams crossing each other at 90° is represented in cyan. The one-dimensional vertical lattice with a counterpropagating beam along the **z**-axis, whose purpose is to create a pancake-shaped potential is represented in orange. Right, a schematic of the 2D superlattice with four-well square plaquettes.

The total potential is given by:

$$\begin{aligned} V_{trap}(x,y,z) = &-V_0 \sin^2(kx) - V_0 \sin^2(ky) \\ &+ V_1 \sin^2(kx/2) + V_1 \sin^2(ky/2) + \frac{1}{2} m\omega_z^2 z^2, \end{aligned} \tag{4.9}$$

where $\omega_z = \sqrt{k^2 V_2/(2m)}$ is the **z**-direction trapping frequency, $k \equiv 2\pi/\lambda$ and $m$ is the mass of the atomic species and the depths $V_i$, $(i = 0, 1, 2)$ of optical lattices control the geometry of potential trap and, consequently, the energy parameters of Hamiltonian. We set $V_1/V_0 = V_2/9V_0 = 1$, which allows for a pancake-shaped potential trap with aspect ratio $\kappa^2 \equiv \omega_z/\omega_r = 1.5$. Here we focus on only one plaquette with four sites around the origin (0,0). By performing a harmonic approximation of (4.9), we obtain

[3] A setup for cigar-shaped trapping is discussed in [99]

the potential for the $i$-th site of the chosen plaquette:

$$V^{(i)}_{\text{trap}}(x,y,z) = \frac{1}{2}m\omega_r^2\left[(x-x_i)^2+(y-y_i)^2\right] + \frac{1}{2}m\omega_z^2 z^2,$$

where $\omega_r = \sqrt{2V_0k^2/m}$ is the radial trapping frequency and $\mathbf{r}_i = (x_i, y_i) = (\zeta_{i-1}d/2,\, \zeta_i d/2)$, $\zeta_i \equiv (-1)^{\lfloor i/2 \rfloor}$, is the center of site $i = 1, 2, 3, 4$. The distance between the nearest wells is given by $d = l/\delta$, where $l = \pi/k = \lambda/2$ is the usual lattice spacing constant, and $\delta = [1 - V_1/(2\pi V_0)]^{-1}$ is a constant that arises in this approximation.

We assume that the atoms are tightly confined in the trap, such that the wavefunction for each site - $\phi_i(\mathbf{r})$ - can be defined as the ground-state of $V_{\text{trap}}(\mathbf{r})$ in the harmonic approximation. In the usual second quantization formalism, the bosonic field operator is written as $\Psi(\mathbf{r}) = \sum_{i=1}^{4}\phi_i(\mathbf{r})a_i$. Due to the tight confinement, the second-nearest-neighbors tunneling term vanishes, and we can recover the Hamiltonian (4.1), where the parameters are defined as $U_0 = g\int d\mathbf{r}\,|\phi_1(\mathbf{r})|^4 + U_{11}$, $U_{ij} = \frac{C_{dd}}{4\pi}\int d\mathbf{r}\int d\mathbf{r'}|\phi_i(\mathbf{r})|^2|\phi_j(\mathbf{r'})|^2\frac{1-3\cos^2\theta_P}{|\mathbf{r}-\mathbf{r'}|^3}$ and $J = 2\int d\mathbf{r}\,\phi_1(\mathbf{r})\left[\frac{\hbar^2\nabla^2}{2m} - V_{trap}(\mathbf{r})\right]\phi_2(\mathbf{r})$.

The respectively on-site and inter-site energies $U_0$ and $U_{ij}$ are consequences from the interaction potential :

$$V(\mathbf{r}-\mathbf{r'}) = \underbrace{g\,\delta(\mathbf{r}-\mathbf{r'})}_{V_{SR}} + \underbrace{\frac{C_{dd}}{4\pi}\frac{1-3\cos^2\theta_P}{|\mathbf{r}-\mathbf{r'}|^3}}_{V_{DDI}}.$$

The first term ($V_{SR}$) characterizes the short-range interaction with coupling constant $g = 4\pi\hbar^2 a/m$, where $a$ is the s-wave scattering length, which can be positive or negative - yielding, respectively, a repulsive and attractive contact interaction -, and whose values can be tuned through a magnetic field via Feshbach Resonance. In the dipole-dipole interaction (DDI) potential ($V_{DDI}$), $C_{dd} = \mu_0\mu^2$, where $\mu_0 = 4\pi\times10^{-7}N/A^2$ is the vacuum magnetic permeability, $\mu$ is the atom's magnetic dipole moment and $\theta_P$ is the angle between the dipole orientation and the direction of $\mathbf{r}-\mathbf{r'}$. The insertion of $\phi_i(\mathbf{r})$ as the ground-state of $V_{\text{trap}}(\mathbf{r})$ in the above equations results in $U_0 = \kappa\left(\frac{\eta}{\pi}\right)^{3/2}\left(g - \frac{C_{dd}}{3}f(\kappa)\right)$

$U_{ij} = \dfrac{C_{\text{dd}}}{4\pi}\displaystyle\int_0^\infty \mathrm{d}r\, r\exp\left(-\frac{r^2}{4\eta}\right)J_0(rd_{ij})Z(r)$,

with $Z(r) = \dfrac{4}{3}\sqrt{\dfrac{\kappa^2\eta}{\pi}} - r\exp\left(\dfrac{r^2}{4\kappa^2\eta}\right)\operatorname{erfc}\left(\dfrac{r}{2\sqrt{\kappa^2\eta}}\right)$ and $J_0$ is the Bessel function of first kind. We define $\eta \equiv m\omega_r/(2\hbar)$, and $d_{ij}$ stands for the distance between the two sites. Here we also notice that, in the limit $d_{ij}\to 0$, $U_{ij} \to -\dfrac{\kappa C_{dd}}{3}\left(\dfrac{\eta}{\pi}\right)^{3/2}f(\kappa)$, where $f(\kappa)$ is a function that relates the trap aspect ratio $\kappa^2$ with the DDI [26]. A schematic representation of the interactions $U_0$ and $U_{ij}$ is depicted in Supplemental Figure 4.6.

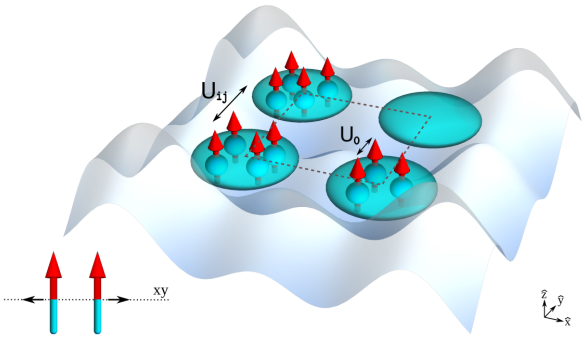


Figure 4.6: Schematic representation of the on-site ($U_0$) and inter-site ($U_{ij}$) interactions of ultracold Bose gases trapped in a four-site square plaquette. The oblate shapes in cyan represent the trap and the arrows depict the polarization of the dipoles aligned in the $z$-direction. The resulting parallel alignment of the dipoles causes a repulsive dipole-dipole interaction both within the same well and between neighboring wells, as depicted in the sketch on the lower left.

As stated in the article, the Hamiltonian acquires two additional independent, conserved operators when the integrability condition, $U_0 - U_{13} = 0$, is fulfilled. This condition can be solved numerically in the following way: by choosing a value for the s-wave scattering length ($a$), the value of the parameter $\omega_r$ is varied up to the point where $U_0$ is equal to $U_{13}$. This means that it is the condition of integrability that states the value for the trapping frequencies, thereby ensuring it's fulfillment.

For the Hamiltonian parameters in this work, we considered $^{164}$Dy, for which the magnetic dipole moment is $\mu = 9.93$ (in units of Bohr magneton $\mu_B$), with $a = -21.4$ (in units of Bohr radius $a_0$) and $V_1/V_0 = V_2/9V_0 = 1$. Here, the DDI provides significant long-range interactions and the trap geometry favors the repulsive on-site DDI which dominates the short-range attractive contact interaction, such that $U_0 > 0$. From the integrability condition, we obtain $\omega_r \approx 2\pi \times 51.46$ kHz, resulting in $U_0/\hbar \approx 2\pi \times 41.38$ Hz, $U_{12}/\hbar \approx 2\pi \times 119.25$ Hz and $J/\hbar \approx 2\pi \times 16.18$ Hz, as used throughout the analysis.

### 4.7.2 Probabilities, fidelities and trade-off between fidelity and protocol time

Here we provide benchmarks establishing the effectiveness of Hamiltonian (4.1) in the simulation of the black box processor $\mathcal{P}$, through numerical calculation of probabilities and outcome fidelities. A general $N$-particle state is expressed as $|\Theta\rangle = \sum_{j,k,l=0}^{N} c_{j,k,l}|j,k,l,N-j-k-l\rangle$ such that $c_{j,k,l} = 0$ if $j+k+l > N$, and $\sum_{j,k,l=0}^{N} |c_{j,k,l}|^2 = 1$. When a measurement is made at site 3, the probability $\mathcal{P}(r)$ to obtain the measurement

outcome $r$ is

$$\mathcal{P}(r) = \sum_{j,k=0}^{N} |c_{j,k,r}|^2 \tag{4.10}$$

satisfying $\sum_{r=0}^{N} \mathcal{P}(r) = 1$. After the measurement, the wavefunction collapses to

$$|\Theta(r)\rangle = \frac{1}{\sqrt{\mathcal{P}(r)}} \sum_{j,k=0}^{N} c_{j,k,r} |j, k, r, N-j-k-r\rangle$$

such that $\langle\Theta(r)|\Theta(r)\rangle = 1$. Set

$$|\Phi(r,\phi)\rangle = \frac{1}{\sqrt{2}} |M-r, P, r, 0\rangle + \frac{\exp(i\phi)}{\sqrt{2}} |M-r, 0, r, P\rangle$$

and define the outcome fidelity $\mathcal{F}(r,\phi)$ to be

$$\mathcal{F}(r,\phi) = |\langle\Phi(r,\phi)|\Theta(r)\rangle|. \tag{4.11}$$

We take $|\Theta\rangle = \exp(-it_m H)\,|4, 11, 0, 0\rangle$ and use (4.1) with $U/\hbar \simeq 2\pi \times 19.5$ Hz, $J/\hbar \simeq 2\pi \times 16.2$ Hz to numerically calculate the measurement probabilities and outcome fidelities through (4.10,4.11). Results are given in Table I.

| Measurement $r$ | Probability $\mathcal{P}(r)$ | Phase $\phi$ | Fidelity $\mathcal{F}(r,\phi)$ |
|---|---|---|---|
| 4 | 0.47639 | $\pi$ | 0.99298 |
| 3 | 0.00729 | $\pi$ | 0.12352 |
| 2 | 0.00368 | $\pi$ | 0.02552 |
| 2 | 0.00368 | 0 | 0.01375 |
| 1 | 0.00625 | 0 | 0.13710 |
| 0 | 0.49611 | 0 | 0.97831 |

Table 4.1: Measurement probabilities and fidelities after evolution under (4.1) until time $t_m$. The initial state is $|4, 11, 0, 0\rangle$, and $U/\hbar \simeq 2\pi \times 19.5$ Hz, $J/\hbar \simeq 2\pi \times 16.2$ Hz as used in Figs. 4.2, 4.4 of the main text. The calculations show that the highest fidelity outcomes, close to 1, occur with the highest probabilities, close to 1/2. This is in agreement with the results predicted by the effective Hamiltonian (5.3).

To analyze the trade-off between protocol time and fidelity, we evaluate the fidelity (4.11) for different values of $t_m$ (determined by different values of $U$) for both $\phi = 0$ and $\pi$. We find that the system reaches proximity to the resonant regime for parameters $U$ and $J$ such that $t_m > 1.75$s. Note that lifetimes of atoms in optical lattices may be as large as 300s [115]. As seen in Supplemental Figure 4.7, the parameters $U/\hbar \simeq 2\pi \times 19.5$ Hz and $t_m \simeq 3.57$s (used in the main text and marked by the dashed vertical line) are within the stable resonance region.

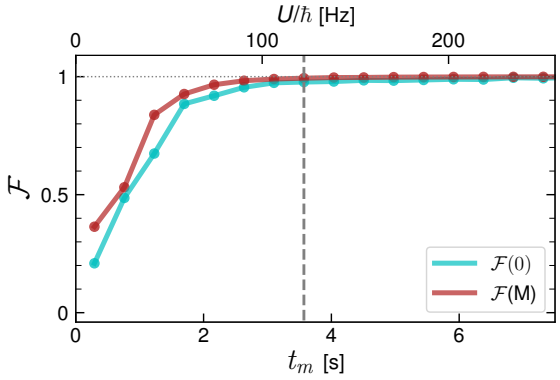


Figure 4.7: Trade-off between fidelity and protocol time. The fidelities of the NOON states (obtained after the measurement procedure) for initial state $|4,11,0,0\rangle$ with $J/\hbar \simeq 2\pi \times 16.2$ Hz and varying $U/\hbar$ from $\sim 2\pi \times 2$ Hz to $\sim 2\pi \times 40$ Hz (top axis), such that $t_m$ varies accordingly between $\sim 0.3$ s and $\sim 7.3$ s. Cyan line: $\phi = 0$. Brown line: $\phi = \pi$. The vertical dashed line shows $t_m \simeq 3.57$s corresponding to $U/\hbar \simeq 2\pi \times 19.5$ Hz as used in the main text.

One of the counter-intuitive features of this theoretical framework is the acute dependence on whether the total particle number $N = M + P$ is even or odd. To provide an understanding of this phenomenon, we take the initial state $|M,P,0,0\rangle$ and consider the time evolution of the *reduced density matrix* $\rho_{1,3}(t)$ for qudit A, $\rho_{1,3}(t) = \mathrm{tr}_{2,4}\left(|\Psi(t)\rangle\langle\Psi(t)|\right)$, where $\mathrm{tr}_{2,4}$ is the partial trace taken over the state space for qudit B, and $|\Psi(t)\rangle = \exp(-itH_{\text{eff}})\,|M,P,0,0\rangle$. We then obtain

$$\begin{aligned}
\rho_{1,3}\left(t_m\right) &= \frac{1}{2}|\Psi_+\rangle\langle\Psi_+| + \frac{1}{2}|\Psi_-\rangle\langle\Psi_-|, \\
|\Psi_\pm\rangle &= \frac{1}{\sqrt{2^M}}\sum_{r=0}^{M}\sqrt{\binom{M}{r}}\exp\left(-i\frac{(N\pm 1)r\pi}{2}\right)|\chi(r)\rangle\,, \\
|\chi(r)\rangle &= \frac{1}{\sqrt{2^M(M-r)!r!}}(a_1^\dagger + a_3^\dagger)^{M-r}(a_1^\dagger - a_3^\dagger)^r\,|0\rangle\,.
\end{aligned}$$

The above results then allow for a calculation of the probability $\mathcal{P}(r)$ that, measurement of the number of particles at site 3, when $t = t_m$, yields the outcome $r$, resulting

$$\mathcal{P}(r) = \frac{1}{2}b_{M,r}(\sin^2((N-1)\pi/4)) + \frac{1}{2}b_{M,r}(\sin^2((N+1)\pi/4))$$

where $b_{M,r}(x) = \binom{M}{r}x^r(1-x)^{M-r}$, $r = 1,...,M$, are the *Bernstein polynomials*. When $N$ is even, $\mathcal{P}(r) = \frac{1}{2^M}\binom{M}{r}$. When $N$ is odd, $\mathcal{P}(r) = (\delta_{r,0} + \delta_{r,M})/2$. The binomial distribution of the even case has maximal support, in stark contrast to the double-delta function distribution of the odd case.

### 4.7.3 Correlations between qudits

The interdependence between the measurement of particle number in qudit A and the symmetry of NOON state produced in qudit B, as discussed below Eq. (4.6), can be characterized in terms of the *swapped fractional imbalance correlation* (SFIC). This is defined as $C_{AB}^{X} \equiv \langle I_A V_B \rangle - \langle I_A \rangle \langle V_B \rangle$ for a given initial state $|X\rangle$, where $I_A = (N_1 - N_3)/M$ is the fractional imbalance operator of the qudit A and $V_B$ is the *swap operator* [116] acting on qudit B as $V_B|a,b,c,d\rangle = |a,d,c,b\rangle$. Since $V_B^2 = Id$, the swap operator has eigenvalues $\pm 1$ that allow to distinguish between a symmetric $(+1)$ or antisymmetric $(-1)$ NOON state in qudit B. The value of the SFIC is bounded, $|C_{AB}^{X}| \leq 1$. After the initial state $|\Psi_0\rangle = |M,P,0,0\rangle$ evolves for time $t = t_m$, the SFIC achieves the boundary values $C_{AB}^{\Psi_0} = +1$ or $C_{AB}^{\Psi_0} = -1$. Throughout the evolution from the initial state $|\Psi_0\rangle$ the expectation value of the swap operator is $\langle V_B \rangle = 0$. This result allows Eq. (4.5) to be formulated as

$$\begin{aligned} \mathcal{I}_{\Phi(\phi)}(t) &\equiv \langle \Phi(\phi)| e^{iHt} I_A e^{-iHt} |\Phi(\phi)\rangle \\ &= \mathcal{I}(t) + C_{AB}^{\Psi_0} \cos\phi, \end{aligned} \tag{4.12}$$

and the SFIC for initial NOON state $|\Phi(\phi)\rangle$ as a phase-controlled quantity given by $C_{AB}^{\Phi} = C_{AB}^{\Psi_0} \sin^2\phi$. These formulae reveal two important aspects: $(i)$ since $|C_{AB}^{\Psi_0}| = 1$ at $t = t_m$, the interference fringe emerges with maximal contrast when $|C_{AB}^{\Phi}|$ achieves its maximum, see Eq. (4.8); $(ii)$ Eq. (4.12) provides $C_{AB}^{\Psi_0} = \mathcal{I}_{\Phi(0)}(t) - \mathcal{I}(t)$, meaning the SFIC $C_{AB}^{\Psi_0}$ can be determined in terms of fractional imbalances for the initial states $|M,P,0,0\rangle$ and the NOON state $|\Phi(0)\rangle$. The SFIC $C_{BA}^{\Psi_0}$ can be defined in an analogous way. These correlations simultaneously attain the maximum value $|C_{BA}^{\Psi_0}| = |C_{AB}^{\Psi_0}| = 1$ at $t = t_m$.

### 4.7.4 Robustness of the interferometer

An important consideration is the robustness of an integrable system against noise [117]. Here, we discuss the interferometric performance under perturbations away from integrability, allowing for $U_0 - U_{13} \neq 0$. Specifically,

$$H_\epsilon = H + \epsilon\nu(N_1 N_3 + N_2 N_4).$$

where the parameter $\epsilon$ has the magnitude of $U_0 - U_{13} \neq 0$ and $\nu \in [-1,1]$ is a random fluctuation number that models experimental noise, such as that resulting from laser intensity variations or magnetic field fluctuations [118].

To quantify the robustness, we examine the time evolution of the fidelity between

the initial state

$$|\Psi\rangle = \frac{1}{\sqrt{2}}(|4, 11, 0, 0\rangle + |4, 0, 0, 11\rangle),$$

evolving under $H$, and the same state evolving under $H_\epsilon$. The state evolving under $H$ is expressed as $|\Psi(t, 0)\rangle = \exp(-itH)|\Psi\rangle$ while the state evolving under $H_\epsilon$ is iteratively defined as $|\Psi(t + \delta t, \epsilon)\rangle = \exp(-i\delta t H_\epsilon)|\Psi(t, \epsilon)\rangle$ where the fluctuation $\nu$ is applied in each time step $\delta t = t_m/\mathcal{N} \sim 4$ ms. Then for each value of $\epsilon$, 100 numerical data points are considered to compute the average fidelity $F_\epsilon(t) = \overline{|\langle\Psi(t, 0)|\Psi(t, \epsilon)\rangle|}$. The results are presented in Supplemental Figure 4.8.

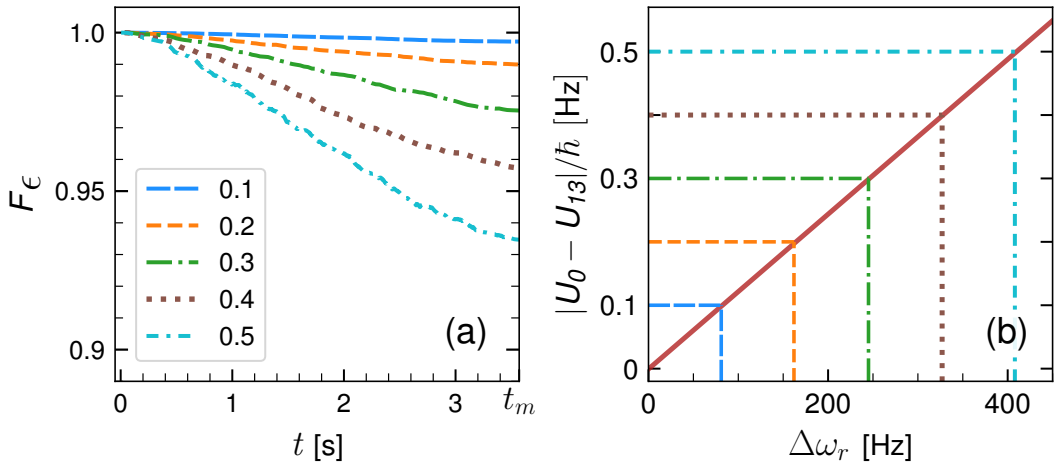


Figure 4.8: Robustness analysis. **(a)** time evolution of the fidelity $F_\epsilon$ until $t = t_m \simeq 3.57$s (endpoint of the axis), for different values of the parameter $\epsilon = 0.1, 0.2, 0.3, 0.4, 0.5$ (in units of $\hbar\,\mathrm{s}^{-1}$, according to the legend) with $\mathcal{N} = 900$, $\phi = 0$, $U/\hbar \simeq 2\pi \times 19.5$ Hz and $J/\hbar \simeq 2\pi \times 16.2$ Hz. **(b)** $|U_0 - U_{13}|$ vs $\Delta\omega_r = |\omega_r' - \omega_r|$ where $\omega_r = 2\pi \times 51.4619$ kHz at $U_0 = U_{13}$. The dashed lines mark the cases where $|U_0 - U_{13}| = 0.1, 0.2, 0.3, 0.4, 0.5$ (in units of $\hbar\,\mathrm{s}^{-1}$).

# Chapter 5

# Protocol designs for NOON states

Here we show how to generate NOON states using the integrable four-well model discussed in the previous chapter. This is achieved by designing protocols to transform initial Fock states to NOON states through use of time evolution, application of an external field, and local projective measurements. By variation of the external field strength, we demonstrate how the system can be controlled to encode a phase into the NOON state. The main content of this chapter was published in Communications Physics [1].

## 5.1 Foreword

Quantum systems are widely considered to be the most promising foundation for the next generation of platforms in computing, communication, measurement and simulation. This is primarily due to the properties of state superposition and entanglement. To realize the potential for progress, it is necessary to establish protocols that are capable of generating important quantum states.

The NOON state is a relevant quantum state, belonging to the class of Schrödinger cat states. More specifically, it is defined as an "all and nothing" superposition of two different modes [45, 46]. For $N$ particles, it has the form

$$|\mathrm{NOON}\rangle = \frac{1}{\sqrt{2}}\left(|N,0\rangle + e^{i\varphi}|0,N\rangle\right) \tag{5.1}$$

where the phase $\varphi$ is typically used to record information.

The creation of Bose-atom NOON states would enable new tests, using massive states, of the foundations for quantum mechanics. A step in this direction was taken with the demonstration of the matter-wave equivalent of the HOM effect [119, 120].

[1] *Protocol designs for NOON states*, D.S. Grun, L.H. Ymai, Karin Wittmann Wilsmann, A.P. Tonel, A. Foerster, J. Links, Comm. Phys., **5**, 36 (2022), doi:10.1038/s42005-022-00812-7

Prospects for creating Bose-atom NOON states using a double-well potential were first floated some time ago [121]. This early work considered an attractive system, which is prone to instability. In principle a more robust repulsive system can be prepared to evolve to a high-fidelity approximation of a NOON state. However, the drawback there is that the process is associated with an extremely large time scale. Recently, new studies of the double-well system have been undertaken to reduce the time scale. One example proposes to adiabatically vary the system parameters through an excited-state phase transition during the process [122]. Another study employs periodic driving to lower the NOON-state evolution time [123]. Nonetheless, the time to generate a NOON state in these examples still, increasingly, scales with the total number of particles. Here we present an alternative to circumvent these issues.

Our approach adopts a closed-circuit of four sites, with a Fock-state input of $M$ particles in site 1, $P$ particles in site 2, and no particles in sites 3 and 4, denoted as $|\Psi_0\rangle = |M, P, 0, 0\rangle$. The initial step is to create an uber-NOON state, with the general form

$$|\text{u-NOON}\rangle = \frac{1}{2}\big(|M, P, 0, 0\rangle + e^{i\varphi_1}|M, 0, 0, P\rangle + e^{i\varphi_2}|0, P, M, 0\rangle + e^{i\varphi_3}|0, 0, M, P\rangle\big)$$

for a set of phases $\{\varphi_1, \varphi_2, \varphi_3\}$. This state may be viewed as an embedding of NOON states (5.1) within two-site subsystems. We then describe two protocols to extract a NOON state from an uber-NOON state, one through dynamical evolution followed by local projective measurement and post-selection, the other from dynamical evolution alone. The protocols are schematically presented in Fig. 5.1.

The approach taken has the following properties: (i) The system has long-ranged interactions, described by the Extended Bose-Hubbard Model (EBHM)[124]. There exists a choice of the coupling parameters for which this model is integrable[98]. As in other physically realized integrable systems [13, 102, 125–130], this property facilitates several analytic calculations for physical quantities. Here, integrability exposes the protocols available for NOON state generation. The execution time is found to be dependent on the difference between the two initially populated sites within the four-site system. It is independent of total particle number, opening a means for scalability. (ii) The system can be controlled by breaking the integrability over small time scales. Encoding of the phase into a NOON state only requires breaking of integrability over an interval that is several orders of magnitude smaller than the entire execution time. This causes minimal loss in fidelity. (iii) With currently available technology, the system may be realized and controlled using dipolar atoms (e.g. dysprosium or erbium) with repulsive interactions, trapped in optical lattices[131, 132]. In this setup, the evolution

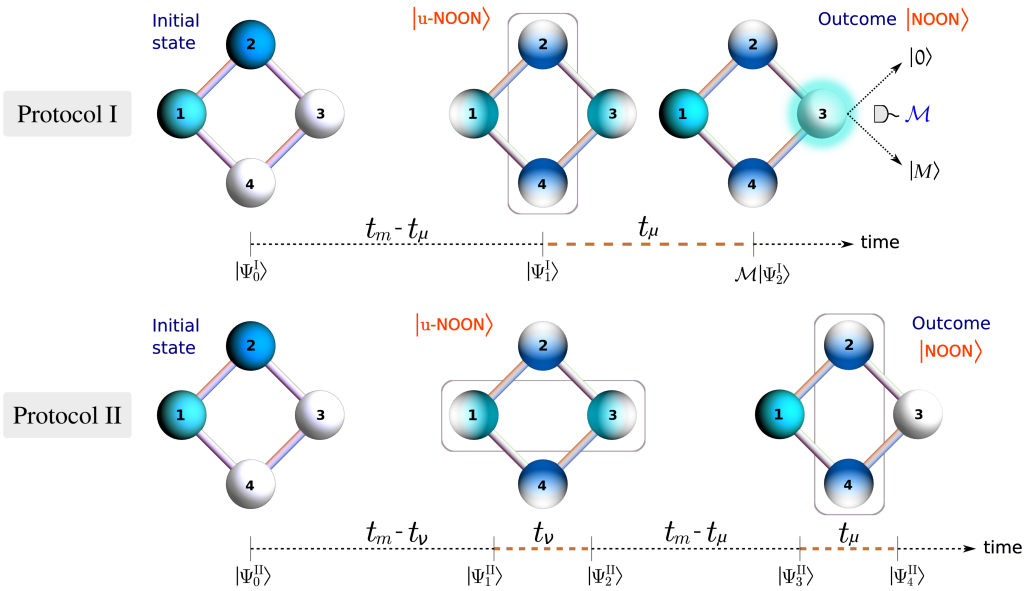


Figure 5.1: NOON state generation scheme. The four spheres on the left represent the initial state, with white indicating an empty site. Cyan and blue correspond to $M$ and $P$ particles respectively. In time-evolved states, gradient colors are used to indicate that the state of a site is entangled with the rest of the system - superposition states for each step are shown in the framed legend. The bars connecting the spheres denote tunneling between nearest-neighbor sites, while the rectangles represent applied external fields to sites 1-3 ($\nu$) and 2-4 ($\mu$). In Protocol I, the system initially evolves for time $t_{\rm m} - t_\mu$, towards the u-NOON state. Then, a field is applied across sites 2-4 for time $t_\mu$ (dashed brown time line), to encode a phase. Finally, the light cyan halo portrays a projective measurement process at site 3, denoted by $\mathcal{M}$. The outcomes $|0\rangle$ and $|M\rangle$ signify which of two possible NOON states results across sites 2-4. Similarly in Protocol II, the system first evolves for time $t_{\rm m} - t_\nu$, then a field is applied to sites 1-3 for time $t_\nu$ to implement the phase $\pi/2$. Next, the system evolves for time $t_{\rm m} - t_\mu$, after which a field is applied to sites 2-4 to encode a phase during time $t_\mu$. This results in a NOON state across sites 2-4, without performing a measurement procedure.

times that we compute for NOON-state generation are of the order of seconds.

For the four-site configuration, the EBHM Hamiltonian is

$$\begin{aligned} H =& \frac{U_0}{2}\sum_{i=1}^{4} N_i(N_i-1) + \sum_{i=1}^{4}\sum_{j=1,j\neq i}^{4}\frac{U_{ij}}{2}N_iN_j \\ &- \frac{J}{2}\left[(a_1^\dagger + a_3^\dagger)(a_2+a_4) + (a_1+a_3)(a_2^\dagger + a_4^\dagger)\right], \end{aligned} \tag{5.2}$$

where $a_j^\dagger$, $a_j$ are the creation and annihilation operators for site $j$, and $N_j = a_j^\dagger a_j$ are the number operators. The total number operator $N = N_1 + N_2 + N_3 + N_4$ is conserved. Above, $U_0$ characterizes the interaction between bosons at the same site, $U_{ij} = U_{ji}$ is related to the long-range (e.g. dipole-dipole) interaction between bosons at sites $i$ and $j$, and $J$ accounts for the tunneling strength between different sites.

Below, we describe two protocols that enable the generation of NOON states, with fidelities greater than 0.9. A physical setup to implement them is also discussed.

*Results.-* Insights into the physical behaviour of Eq. (5.2) become accessible at integrable coupling. Setting $U_{13} = U_{24} = U_0$, the system acquires two additional conserved quantities, $Q_1$ and $Q_2$, such that $2Q_1 = N_1 + N_3 - a_1^\dagger a_3 - a_1 a_3^\dagger$ and $2Q_2 = N_2 + N_4 - a_2^\dagger a_4 - a_2 a_4^\dagger$. Together with the total number of particles $N$ and the Hamiltonian $H$, the system possesses four independent, conserved quantities. This is equal to the number of degrees of freedom, satisfying the criterion for integrability. Suppose that, initially, there are $M$ atoms in site 1 and $P$ atoms in site 2. We identify the resonant tunneling regime as being achieved when $U|M - P| \gg J$ (see Methods for details), where $U = (U_{12} - U_0)/4$. This regime is characterized by sets of bands in the energy spectrum (see Supplementary Material 5.7.1). In this region, an effective Hamiltonian $H_{\text{eff}}$ enables the derivation of analytic expressions for several physical quantities.

In the settings discussed above, the system described by Eq. (5.2) provides the framework to generate uber-NOON states when $N = M + P$ is odd [133]. To encode phases, however, it is necessary to break the integrability in a controllable fashion. Here, we introduce two idealized protocols to produce NOON states with general phases by breaking the system's integrability with externally applied fields. We call the subsystem containing sites $1, 3$ as $A$, and the one containing sites $2, 4$ as $B$. We denote three time intervals: $t_{\text{m}}$, $t_\mu$ and $t_\nu$. The first, corresponding to integrable time evolution, is associated with evolution to a particular uber-NOON state. The others, associated with smaller scale non-integrable evolution, produce phase encoding. Both protocols are built around a general time-evolution operator

$$\mathcal{U}(t, \mu, \nu) = \exp\left(-\frac{it}{\hbar}[H + \mu(N_2 - N_4) + \nu(N_1 - N_3)]\right),$$

where the applied field strengths $\mu$, $\nu$ implement the breaking of integrability. It is convenient to introduce the phase variable $\theta = 2\mu t_\mu/\hbar$, and to fix $t_\nu = \hbar\pi/(4M\nu)$, with $\hbar$ the reduced Planck constant.

## 5.2 Protocol I

In this protocol we employ breaking of integrability through an applied field to subsystem $B$ and a measurement process. The protocol consists of three sequential steps, schematically depicted in Fig. 5.1:

(i) $|\Psi_1^{\text{I}}\rangle = \mathcal{U}(t_{\text{m}} - t_\mu, 0, 0)\,|\Psi_0\rangle$;

(ii) $|\Psi_2^{\text{I}}\rangle = \mathcal{U}(t_\mu, \mu, 0)\,|\Psi_1^{\text{I}}\rangle$;

(iii) $|\Psi_3^{\text{I}}\rangle = \mathcal{M}\,|\Psi_2^{\text{I}}\rangle$,

where $t_{\rm m} = \hbar\pi/(2\Omega)$ (see Methods) and $\mathcal{M}$ represents a projective measurement of the number of bosons at site 3 (which could be implemented, in principle, through site-selective imaging [114, 134, 135] or Faraday rotation detection[100, 101, 136]). A measurement outcome of 0 or $M$ heralds a high-fidelity NOON state in subsystem $B$. For other measurement outcomes, the output is discarded and the process repeated (post-selection).

**Idealized limit**

There is an idealized limit for which the above protocol has perfect success probability and output fidelity. Taking $t_\mu \to 0$, $\mu \to \infty$ such that $\theta$ remains finite, and using the effective Hamiltonian, provides explicit expressions for the uber-NOON states that result at steps (i) and (ii)

$$\begin{aligned}
|\Psi_1^{\rm I}\rangle &= \frac{1}{2}\Big(\beta\,|M,P,0,0\rangle + |M,0,0,P\rangle \\
&\qquad + |0,P,M,0\rangle - \beta\,|0,0,M,P\rangle\Big) \\
|\Psi_2^{\rm I}\rangle &= \frac{1}{2}\Big(\beta\,|M,P,0,0\rangle + e^{iP\theta}\,|M,0,0,P\rangle \\
&\qquad + |0,P,M,0\rangle - \beta e^{iP\theta}\,|0,0,M,P\rangle\Big)
\end{aligned}$$

Note that due to the conservation of $N_1 + N_3$ and $N_2 + N_4$ under the effective Hamiltonian, Fock states such as $|M,0,P,0\rangle$ and $|0,M,0,P\rangle$ do not appear in the above expression. Next, the two possible states at step (iii) depend on the measurement outcome $r$ at site 3:

$$|\Psi_3^{\rm I}\rangle = \begin{cases} \frac{1}{\sqrt{2}}\left(\beta\,|M,P,0,0\rangle + e^{iP\theta}\,|M,0,0,P\rangle\right), & r=0, \\ \frac{1}{\sqrt{2}}\left(|0,P,M,0\rangle - \beta e^{iP\theta}\,|0,0,M,P\rangle\right), & r=M, \end{cases}$$

with $\beta = (-1)^{(N+1)/2}$. These states are recognized as products of a NOON state for subsystem $B$ with Fock basis states for subsystem $A$.

In the non-ideal case with non-zero $t_\mu$ and finite $\mu$, there is a small probability that the measurement outcome $r$ is neither 0 or $M$. Numerical benchmarks for the measurement probabilities and NOON state output fidelities are provided in a later section. Next, we describe a second protocol.

## 5.3 Protocol II

Now we specify an alternative protocol that does not involve measurements, so post-selection is not required. Employing the same initial state $|\Psi_0\rangle$, the following sequence of steps are implemented to arrive at a NOON state in subsystem $B$ (illustrated in Fig. 5.1):

(i) $|\Psi_1^{\rm II}\rangle = \mathcal{U}(t_{\rm m} - t_\nu, 0, 0)\,|\Psi_0\rangle$;

(ii) $|\Psi_2^{\rm II}\rangle = \mathcal{U}(t_\nu, 0, \nu)\,|\Psi_1^{\rm II}\rangle$;

(iii) $|\Psi_3^{\rm II}\rangle = \mathcal{U}(t_{\rm m} - t_\mu, 0, 0)\,|\Psi_2^{\rm II}\rangle$;

(iv) $|\Psi_4^{\rm II}\rangle = \mathcal{U}(t_\mu, \mu, 0)\,|\Psi_3^{\rm II}\rangle$.

### Idealized limit

Similar to Protocol I, in the limit $\mu, \nu \to \infty$, $t_\mu, t_\nu \to 0$, and implementing $\mathcal{U}(t, \mu, \nu)$ with the effective Hamiltonian produces

$$
\begin{aligned}
|\Psi_1^{\rm II}\rangle &= \frac{1}{2}\Big(\beta\,|M,P,0,0\rangle + |M,0,0,P\rangle \\
&\qquad + |0,P,M,0\rangle - \beta\,|0,0,M,P\rangle\Big); \\
|\Psi_2^{\rm II}\rangle &= \frac{1}{2}\Big(\beta\,|M,P,0,0\rangle + |M,0,0,P\rangle \\
&\qquad + i\,|0,P,M,0\rangle - i\beta\,|0,0,M,P\rangle\Big); \\
|\Psi_3^{\rm II}\rangle &= \frac{1}{\sqrt{2}}\Big(\,|M,P,0,0\rangle + \beta e^{-i\pi/2}\,|M,0,0,P\rangle\Big); \\
|\Psi_4^{\rm II}\rangle &= \frac{1}{\sqrt{2}}\Big(\,|M,P,0,0\rangle + \Upsilon\,|M,0,0,P\rangle\Big)
\end{aligned}
$$

where $\Upsilon = \beta\exp(i(P\theta - \pi/2))$.

## 5.4 Protocol fidelities

The analytic results provided above are obtained by employing the effective Hamiltonian in an extreme limit, with divergent applied fields acting for infinitesimally small times. Below we give numerical simulations of the protocols to show that, for physically realistic settings where the fields are applied for finite times, high-fidelity outcomes for NOON state production persist.

Throughout this section, we use $|\Psi\rangle$ to denote an analytic state, obtained in an idealized limit. We adopt $|\Phi\rangle$ to denote a numerically calculated state, obtained by

time evolution with the EBHM Hamiltonian (5.2). Two sets of parameters are chosen to illustrate the results (expressed in Hz):

Set 1: $\{U/\hbar = 104.85,\ J/\hbar = 71.62,\ \mu/\hbar = 30.02\}$;
Set 2: $\{U/\hbar = 105.60,\ J/\hbar = 104.95,\ \mu/\hbar = 27.42\}$.

For all numerical simulation results presented below, the initial state is chosen as $|\Psi_0\rangle = |4, 11, 0, 0\rangle$, i.e. $M = 4$ and $P = 11$.

The fidelities of Protocols I and II are defined as [3] $F_{\rm I} = |\langle\Psi_3^{\rm I}|\Phi_3^{\rm I}\rangle|$ and $F_{\rm II} = |\langle\Psi_4^{\rm II}|\Phi_4^{\rm II}\rangle|$, respectively. This is computed for $P\theta$ ranging from 0 to $\pi$, achieved by varying $t_\mu$. In the case of Protocol II, we use $\nu = \mu$ for both sets of parameters. The systems considered here can, in principle, be implemented using existing hardware – see Physical proposal.

Illustrative results are presented in Table 5.1, where it is seen that $F_{\rm II}$ is lower than $F_{\rm I}$. This can be attributed to two primary causes. The first is that, while Protocol I takes $\tau_I \sim t_{\rm m}$ to produce the final state, Protocol II requires double the evolution time $\tau_{II} \sim 2t_{\rm m}$. The longer evolution time contributes to a loss in fidelity. The second reason is that, the measurement occurring in the final step of Protocol I has the effect of renormalizing the quantum state after collapse, which increases the fidelity of the resulting NOON state when a measurement of $r = 0$ or $r = M$ is obtained. However, there is a finite probability that the measurement outcome is neither $r = 0$ nor $r = M$ (see Supplementary Material 5.7.2).

In summary, both protocols display high fidelity results greater than 0.9. For Protocol I the outcomes are probabilistic (See Supplementary Material 5.7.2 for data). By contrast, the slightly lower fidelity results of Protocol II are deterministic. These results also reflect the trade-off between fidelity and total evolution time. The higher fidelity results associated to parameter Set 1, compared to Set 2, are produced through longer evolution time.

| | $F_{\rm I}$ | | $F_{\rm II}$ | $P\theta = \pi/2$ | | |
|---|---|---|---|---|---|---|
| | $r = 0$ | $r = M$ | | $t_\mu$ | $t_\nu$ | $t_m$ |
| Set 1 | 0.986 | 0.997 | 0.974 | 0.0024 s | 0.0065 s | 6.1639 s |
| Set 2 | 0.964 | 0.991 | 0.920 | 0.0026 s | 0.0072 s | 2.8913 s |

Table 5.1: Fidelities for Protocols I and II. Numerical calculations of the fidelities $F_{\rm I}$ and $F_{\rm II}$ and related times $t_m$, $t_\mu$ and $t_\nu$ concerning to the parameters of Set 1 and Set 2 for $M = 4$ and $P = 11$. As the values remain almost constant for $P\theta \in [0, \pi]$, varying less than 1%, we displayed here only the values corresponding to the phase $P\theta = \pi/2$, for fixed $t_\nu$ and $t_\mu$. Set 1: $U/\hbar = 104.846$ Hz, $J/\hbar = 71.62$ Hz, $\mu/\hbar = 30.02$ Hz and $t_{\rm m} \sim 6.16$s. Set 2: $U/\hbar = 105.60$ Hz, $J/\hbar = 104.95$ Hz, $\mu/\hbar = 27.42$ Hz and $t_{\rm m} \sim 2.89$s. The required times $t_{\rm m}$, $2t_{\rm m}$ to produce the NOON states are comparable with typical lifetimes of optical lattice traps, which can be as large as a few minutes[115]

### 5.4.1 Readout statistics

A means to test the reliability of the system, through a statistical analysis of local measurement outcomes, is directly built into the design. This results from the system's capacity to function as an interferometer[133]. For both protocols, once the output state has been attained we can continue to let the system evolve under $\mathcal{U}(t_{\rm m},0,0)$. This yields the readout states, denoted as $|\Psi^{\rm I}_{\rm RO}\rangle$, $|\Psi^{\rm II}_{\rm RO}\rangle$ respectively for protocols I and II. In the idealized limits these are

$$|\Psi^{\rm I}_{\rm RO}\rangle = \begin{cases} \dfrac{c(\theta)}{\sqrt{2}}(|M,P,0,0\rangle + \beta\,|M,0,0,P\rangle) \\ \quad + \dfrac{is(\theta)}{\sqrt{2}}(\beta\,|0,P,M,0\rangle - |0,0,M,P\rangle),\ r=0, \\ \\ \dfrac{c(\theta)}{\sqrt{2}}(|M,P,0,0\rangle - \beta\,|M,0,0,P\rangle) \\ \quad - \dfrac{is(\theta)}{\sqrt{2}}(\beta\,|0,P,M,0\rangle - |0,0,M,P\rangle),\ r=M, \end{cases}$$

$$\begin{aligned} |\Psi^{\rm II}_{\rm RO}\rangle = &\frac{1}{\sqrt{2}}s\left(\theta-\frac{\pi}{2P}\right)(|M,P,0,0\rangle + \beta\,|M,0,0,P\rangle) \\ &-\frac{i}{\sqrt{2}}c\left(\theta-\frac{\pi}{2P}\right)(\beta\,|0,P,M,0\rangle - |0,0,M,P\rangle)\,, \end{aligned}$$

where $c(\theta)\equiv\cos(P\theta/2)$ and $s(\theta)\equiv\sin(P\theta/2)$. For $|\Psi^{I}_{\rm RO}\rangle$, the measurement probabilities at site 3 are $\mathcal{P}(0)=\cos^2(P\theta/2)$ and $\mathcal{P}(M)=\sin^2(P\theta/2)$. Combined with the probability of measuring $r=0,M$ in step (iii), we obtain four possibilities for the total probabilities as $\mathcal{P}_{\rm I}(0,0)=\mathcal{P}_{\rm I}(M,0)=0.5\cos^2(P\theta/2)$ and $\mathcal{P}_{\rm I}(0,M)=\mathcal{P}_{\rm I}(M,M)=0.5\sin^2(P\theta/2)$. Meanwhile, for $|\Psi^{II}_{\rm RO}\rangle$, the measurement probabilities at site 3 are $\mathcal{P}_{\rm II}(0)=\sin^2(P\theta/2-\pi/4)$ and $\mathcal{P}_{\rm II}(M)=\cos^2(P\theta/2-\pi/4)$. As a numerical check, we consider the same sets of parameters from previous section. Then, we numerically calculate the above probabilities using the Hamiltonian (5.2), comparing the predicted analytic results with the numerical ones, as shown in Fig. 5.2. See Supplementary Material 5.7.2 for numerical probabilities of Protocol I, and related fidelity data. For results with Set 2, see Supplementary Material 5.7.3.

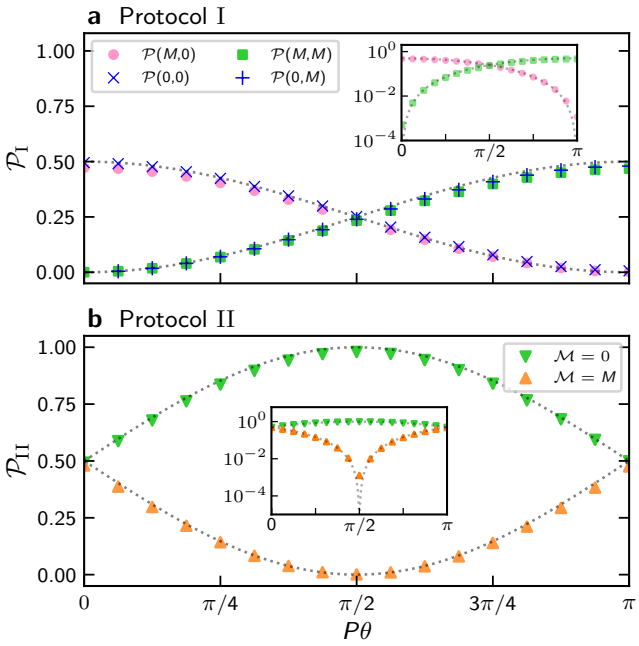


Figure 5.2: Readout probabilities for Protocols I and II. Comparison between analytic and numerically-calculated probabilities for parameters of Set 1 for different values of $P\theta$. **a** Results for Protocol I. The pink dot and the blue "x" (green square and the blue "+") depict the probabilities of measuring $r = 0$ ($r = M$) during the readout, having measured $r = M$ or $r = 0$ in step (iii) respectively. **b** Results for Protocol II. The probabilities of measuring $N_3 = 0$ ($N_3 = M$) in the readout are shown as green (orange) triangles. The dotted line depicts the analytic predictions of the probabilities with respect to $P\theta$. The insets show the accordance between predicted and calculated probabilities in semilogarithmic scale.

## 5.5 Methods

### 5.5.1 Resonant tunneling regime

The Hamiltonian (5.2) has large energy degeneracies when $J = 0$. Through numerical diagonalization of the intergable Hamiltonian for sufficiently small values of $J$, it is seen that the levels coalesce into well-defined bands, similar to that observed in an analogous integrable three-site model[43, 44]. By examination of second-order tunneling processes in this regime (see Supplementary Material 5.7.1), an effective Hamiltonian $H_{\mathrm{eff}}$ is obtained.

For an initial Fock state $|M-l, P-k, l, k\rangle$, with total boson number $N = M + P$, the effective Hamiltonian is a simple function of the conserved operators with the form

$$H_{\mathrm{eff}} = (N+1)\Omega(Q_1 + Q_2) - 2\Omega Q_1 Q_2, \tag{5.3}$$

where $\Omega = J^2/(4U((M-P)^2-1))$ and $U = (U_{12} - U_0)/4$. This result is valid for $J \ll U|M-P|$, and it is this inequality that we use to define the resonant tunneling regime.

A very significant feature is that, for time evolution under $H_{\text{eff}}$, both $N_1 + N_3 = M$ and $N_2 + N_4 = P$ are constant. The respective $(M+1)$-dimensional subspace associated with sites 1 and 3 and $(P+1)$-dimensional subspace associated with sites 2 and 4 provide the state space for the relevant energy band (see Supplementary Material 5.7.1). Restricting to these subspaces and using the effective Hamiltonian (5.3) yields a robust approximation for (5.2).

### 5.5.2 Physical proposal

We propose a physical construction, consisting of ultracold dysprosium $^{164}$Dy atoms trapped in an optical superlattice [114], to test the theoretical results. The trapping is accomplished by superimposing two 2D square optical lattices, one with "short" periodicity $\lambda/2$ and another with "long" periodicity $\lambda_l/2 = \lambda$, where the wavelength $\lambda = 2\pi/k = 532$ nm. The potential of the superlattice is given by

$$\begin{aligned} V(\mathbf{r}) = &- V_{\text{s}} \sin^2(kx) - V_{\text{s}} \sin^2(ky) \\ &+ V_{\text{l}} \sin^2(kx/2) + V_{\text{l}} \sin^2(ky/2) + \frac{1}{2} m\omega_z^2 z^2, \end{aligned}$$

where $V_{\text{s}}$ and $V_{\text{l}}$ are the depths of the short and long lattices, respectively. The trap frequency $\omega_z = \sqrt{V_z k^2/(2m)}$ of the harmonic confinement in $z$ direction is controlled by the depth $V_z$ of vertical counter-propagating laser beams with wavelength $\lambda_l = 1064$ nm, and $m$ is the atom's mass. We are interested in only one plaquette with four wells around the origin of the $xy$-plane, for which the potential of the $i$-th well $(i = 1, 2, 3, 4)$ in the harmonic approximation is given by

$$V^{(i)}(\mathbf{r}) = \frac{1}{2} m\omega_{\text{r}}^2 [(x - x_i)^2 + (y - y_i)^2] + \frac{1}{2} m\omega_z^2 z^2,$$

where the radial trap frequency $\omega_{\text{r}} = \sqrt{2V_{\text{s}} k^2/m}$ is determined by the depth of the short lattice. The $i$-th well is centered at one of the $(x_i, y_i) = (\zeta_{i-1} d/2, \zeta_i d/2)$, $\zeta_i \equiv (-1)^{\lfloor i/2 \rfloor}$, positions in the $xy$-plane. The distance between nearest wells is $d = \lambda/(2\delta)$, where the parameter $\delta = [1 - V_{\text{l}}/(2\pi V_{\text{s}})]^{-1}$ is constant, which results from the harmonic approximation and causes the sites to slightly approach each other. In our studies we consider $V_{\text{l}} = V_{\text{s}}$.

To establish equivalency between $V(\mathbf{r})$ and the Hamiltonian of Eq. (5.2), we employ the standard second-quantization procedure. From this, we calculate the on-site interaction parameter $U_0$ as:

$$
\begin{aligned}
U_0 &= U_{\text{contact}} + U_{\text{dip}} \\
&= \kappa \left(\frac{\eta}{\pi}\right)^{3/2} \left(g - \frac{C_{\text{dd}}}{3} f(\kappa)\right),
\end{aligned} \tag{5.4}
$$

where the value of $\kappa^2 \equiv \omega_z/\omega_{\text{r}} = 0.53$ (0.56) establishes the cigar-shaped harmonic potential, $\eta \equiv m\omega_{\text{r}}/(2\hbar)$, $g \equiv 4\pi\hbar^2 a/m$, with $a$ being the s-wave scattering length (tunable via Feshbach Resonance), $C_{\text{dd}} \equiv \mu_0\mu_1^2$ is the coupling constant, where $\mu_0$ is the vacuum magnetic permeability, $\mu_1$ is the atomic magnetic moment, and $f(\kappa)$ is a function that describes how the dipolar interaction behaves for different geometries (encoded in $\kappa$)[26]. Taking site 1 as the "starting point', the parameter $U_{1\text{j}}$, which accounts for the dipole-dipole interaction between atoms at sites 1 and $j$, is expressed as:

$$
\begin{aligned}
U_{1j} =& \frac{C_{\text{dd}}}{4\pi} \int_0^\infty \mathrm{d}r\, r \exp\left(-\frac{r^2}{4\eta}\right) J_0(r d_{1j}) Z(r), \\
Z(r) =& \left(\frac{4}{3}\sqrt{\frac{\kappa^2\eta}{\pi}} - r \exp\left(\frac{r^2}{4\kappa^2\eta}\right) \operatorname{erfc}\left(\frac{r}{2\sqrt{\kappa^2\eta}}\right)\right),
\end{aligned} \tag{5.5}
$$

where $J_0$ is the Bessel function of first kind, $d_{1j} = \lambda/(2\delta)$, if $j = 2, 4$, and $d_{1j} = \lambda/(\sqrt{2}\delta)$ , if $j = 3$. Here, the on-site dipolar interaction is given by $U_{\text{dip}} = \lim_{d_{ij}\to 0} U_{1j} \propto f(\kappa)$.

In this environment, the preparation of arbitrary initial Fock states, as in our protocols, may be accomplished [103, 134] by changing one of the superimposed optical lattices' phase with respect to the other, creating imbalances in the trapping potentials in a controllable way, such that the desired initial state becomes favourable within a Mott Insulator regime (see Supplementary Material 5.7.4).

### Integrability condition

The physical setup above is able to simulate the EBHM. The ability to generate NOON states, however, relies on the particular case for which the EBHM is integrable; as explained previously, this can be accomplished by making $U_0 = U_{13}$, which we call the "integrability condition". The approach is to first choose a value for the s-wave scattering length by changing the magnetic field. Then, from the condition just stated, one has to adjust $\omega_{\text{r}}$ by varying the laser beams intensities[8] such that, at some point, $U_0$ becomes the same as $U_{13}$. From this point every Hamiltonian parameter is evaluated only after the integrability condition is satisfied, which sets the intensity of the trapping scheme.

By considering $a = 32.5$ (30) $a_0$, the system becomes integrable at $\omega_{\text{r}} \approx 2\pi \times 54.110$

$(2\pi \times 51.759)$ kHz, as is depicted in Fig. 5.3. This frequency implies a 2D-lattice depth of $V_s \approx 39.953 E_R$ $(36.558 E_R)$, where $E_R/\hbar = 2\hbar(k\pi)^2/(m\lambda^2) = 26.894$ kHz is the recoil energy, characterizing a deep lattice. This configuration infers a stable system. [124, 137]. Then, by using this trapping frequency to calculate the Hamiltonian parameters, one finds $U/\hbar \approx 104.846$ $(105.600)$ Hz and $J/\hbar \approx 71.624$ $(104.953)$ Hz.

It is also important to highlight that the tunneling parameter $J_{13}/\hbar \sim 3.2 \times 10^{-4}$ Hz $(J_{13}/\hbar \sim 7.7 \times 10^{-4}$ Hz) between diagonal sites 1-3, which is nullified by the condition $U_0 = U_{13}$ in (5.2), is less than $1/t_m \sim 0.16$ Hz $(1/t_m \sim 0.35$ Hz), relative to Set 1 (Set 2), ensuring the integrability requirement, considering $J_{13} = J_{24}$, since $U_0 = U_{13} = U_{24}$.

From this, one infers that the tunneling between different horizontal layers of the optical lattice is even smaller, since the distance between these layers is bigger than the distance between diagonal sites by a factor of $\sqrt{2}$.

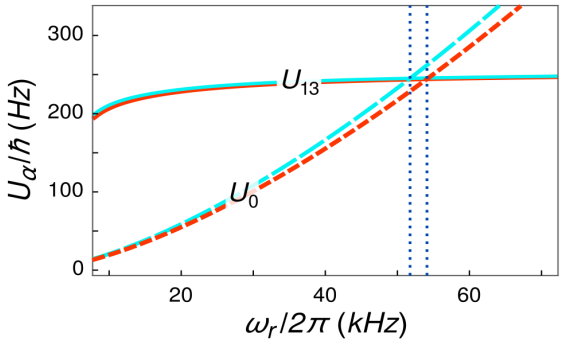


Figure 5.3: Fulfillment of integrability condition. The s-wave scattering length value is set, followed by a variation of the radial trapping frequency $\omega_r$ up to the point at which $U_0 = U_{13}$, corresponding to the frequency required for the system to be integrable. The red dashed (solid) and cyan long dashed (solid) depict $U_0$ $(U_{13})$ for $a = 32.5\ a_0$ and $a = 30\ a_0$, respectively, for different values of $\omega_r$. By setting $a = 32.5\ a_0$ $(30\ a_0)$, we find $\omega_r \approx 2\pi \times 54.110$ kHz $(51.759$ kHz ) as the frequency for integrability, which results in $U_0/\hbar = U_{13}/\hbar \approx 244.405$ Hz $(245.141$ Hz). The points where $U_0 = U_{13}$ and the corresponding frequencies $\omega_r$ are highlighted by the dotted lines. The system is robust for small deviations from the integrable point (see Supplementary Material 5.7.5 for more details).

### Breaking of integrability

To produce a controllable breaking of integrability, it is sufficient to consider an additional 2D square long-lattice with the potential

$$V_{\text{break}} = V_b \sin^2(kx/2 + \varphi) + V_b \sin^2(ky/2 + \epsilon\varphi),$$

where the depth $V_b = 10^{-3} V_s$ and phase $\varphi$ control the potential offset $\Delta = 2V_b \sin(2\varphi) \sin[\pi/(2\delta)]$ of sites 1-3 $(\epsilon = +1)$ and 2-4 $(\epsilon = -1)$. When this additional long-lattice is switched on, the depth of the fixed long-lattice is ramped down to $V_l \to V_l - V_b$ to keep the parameter $\delta$ constant and it implements the terms $\mu = 0.5\,\Delta \exp(-k^2/(8\eta_r))\,\delta_{\epsilon,+1}$ and $\nu = 0.5\,\Delta \exp(-k^2/(8\eta_r))\,\delta_{\epsilon,-1}$. For $\varphi = 15$ mrad

and the previously obtained radial trapping frequency, the parameters $\mu/\hbar$ and $\nu/\hbar$ can (non-simultaneously) assume the value of 30.016 (27.415) Hz. Therefore, considering $M = 4$ and $P = 11$, one should vary $t_\mu$ from 0 to $\sim 4.8$ (5.2) ms to encode $P\theta$ from 0 to $\pi$. Notice that for the case presented on Table 5.1, where $P\theta = \pi/2$, $t_\mu \sim 2.4$ (2.6) ms. Also, from the condition $2\nu t_\nu/\hbar = \pi/(2M)$, corresponding to $P\theta = \pi/2$, $t_\nu \sim 6.5$ (7.2) ms. Fig. 5.4 illustrates the complete trapping scheme.

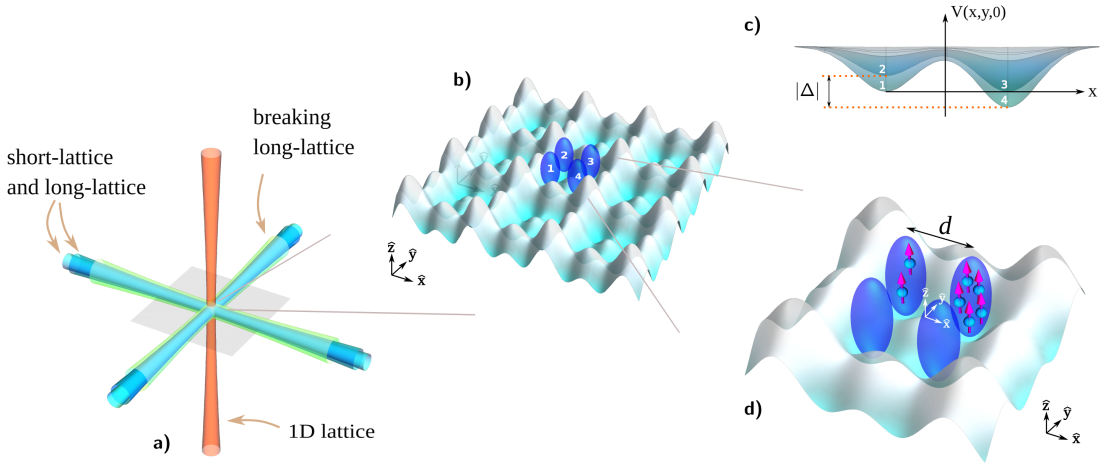


Figure 5.4: **a** Trapping scheme of the four-site model. The 2D square optical lattice is generated with two sets of counter-propagating laser beams crossing at 90° with the other. The superlattice of four-site model is achieved overlapping the 2D short-lattice (cyan) and long-lattice (blue). The vertical lattice (orange) provides confinement in $z$ direction. An additional 2D square long-lattice (green) is used to implement the integrability break control. **b** Zoom into the region of the superlattice which contains the four-site plaquette. **c** Breaking-of-integrability scheme. The system's integrability can be broken by changing the phase difference between the superlattice and the additional 2D square long-lattice, effectively causing a potential imbalance $|\Delta|$ between wells 1 and 3 or wells 2 and 4, as in the detail. **d** The light grey background represents the trapping potential in the vicinities of the four-well system. The cigar-shaped of isosurfaces of the ground-state density, at a distance of $d$ between nearest neighbors, are depicted in blue with direction of dipole aligned in $z$-direction represented by purple arrows.

## 5.6 Discussion

We have addressed the challenging problem of designing protocols to facilitate NOON state creation, based on the formation of an uber-NOON state. The insights gained from integrability allowed us to develop two protocols. Protocol I employs a local measurement procedure to produce NOON states with slightly higher fidelities, over a shorter time, than Protocol II. However Protocol I is probabilistic, requiring post-selection on the measurement outcome. This is in contrast to the deterministic approach of Protocol II. For both protocols, phase-encoding is performed by breaking the system's integrability, in a controllable fashion, at specific moments during the time evolution. And in both protocols the output states were shown to have high-fidelity in numerical

simulations. We also identified a readout scheme, by converting encoded phases into a population imbalance, that allows verification of NOON state production through measurement statistics. Due to its natural ability to works as an interferometer and to produce NOON states with high fidelity, we can consider the integrable four well model as a second building block in the family of integrable multi-well models, with the triple well being considered as the first one. This configurates our basic "toolbox" that will, hopefully open new avenues in integrability-enhanced atomtronic quantum technologies.

So far, besides demonstrating the feasibility of the switching device and the NOON state generation, the physical setups we provided can also be employed in the study of thermalization processes and other many-body features of the EBHM. An approach towards thermalization will be presented in the next chapter, for the simplest case of the triple well model.

## 5.7 Supplementary Material

### 5.7.1 Energy bands and effective Hamiltonian

Here we give an overview of the origin for the effective Hamiltonian. Recall that the integrability condition is $U_{13} = U_{24} = U_0$ and $U_{12} = U_{23} = U_{34} = U_{14}$. When $J = 0$, the Fock state $|M - l, P - k, l, k\rangle$ is eigenstate of the Hamiltonian Eq. (2) of the main text, with energy

$$E = C - U(M - P)^2 \tag{5.6}$$

where $C = (U_0 + U_{12})N^2/4 - U_0/2$. The result is independent of $l$ and $k$, indicating degeneracies. For small values of $J$, the degeneracies are broken and lead to energy levels in well-defined bands, each with $2(M + 1)(P + 1)$ energy levels, except for $N$ even, where the band with the highest energy, $M = P$, will have $(M+1)(P+1)$ levels. The level energy structure of the case we are analyzing, with $N = 15$, is shown in Figure 1. In it, we highlight in cyan the band with $M = 4$ and $P = 11$ (and vice versa), while the vertical lines marks the two sets of parameters pointed in the main text (repeated here, expressed in Hz):

Set 1: $\{U/\hbar = 104.85,\ J/\hbar = 71.62,\ \mu/\hbar = 30.02\}$;
Set 2: $\{U/\hbar = 105.60,\ J/\hbar = 104.95,\ \mu/\hbar = 27.42\}$.

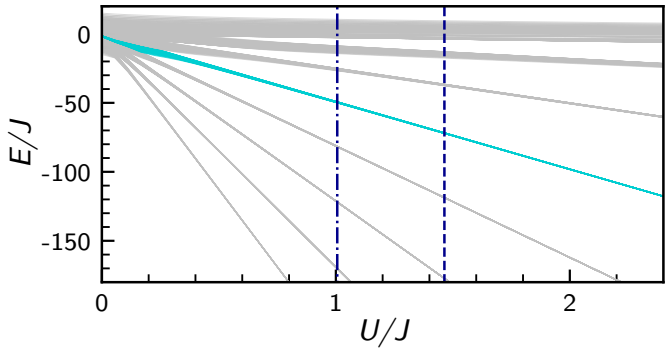


Figure 5.5: Energy band formation. Dimensionless energy eigenvalues $E/J$ as a function of dimensionless coupling $U/J$, where $U = (U_{12} - U_0)/4$ and considering $C = 0$ in (5.6). The dashed vertical line marks $U/J \sim 1.5$ (concerning parameter Set 1) and the dot-dashed line marks $(U/J \sim 1)$ (concerning parameter Set 2), while cyan depicts the band containing the expectation energy of the initial state $|\Psi_0\rangle = |4, 11, 0, 0\rangle$. The formation of the bands is due to the quadratic dependence of $(M - P)$ in the energy (5.6).

An effective Hamiltonian for each band is obtained by consideration of second-order

processes. Associated to labels $M$ and $P$, such that $N = M + P$, we obtain

$$
\begin{aligned}
H_{\text{eff}} = & \frac{J^2}{16U(M-P+1)}\left(a_1 a_3^\dagger + a_3 a_1^\dagger\right)\left(a_2^\dagger a_2 + a_4^\dagger a_4\right) \\
& + \frac{J^2}{16U(M-P+1)}\left(a_1 a_1^\dagger + a_3 a_3^\dagger\right)\left(a_2^\dagger a_4 + a_4^\dagger a_2\right) \\
& - \frac{J^2}{16U(M-P-1)}\left(a_2 a_2^\dagger + a_4 a_4^\dagger\right)\left(a_1^\dagger a_3 + a_3^\dagger a_1\right) \\
& - \frac{J^2}{16U(M-P-1)}\left(a_2 a_4^\dagger + a_4 a_2^\dagger\right)\left(a_1^\dagger a_1 + a_3^\dagger a_3\right) \\
& + \frac{J^2}{16U}\left(\frac{1}{M-P+1} - \frac{1}{M-P-1}\right) \\
& \times \left(a_1^\dagger a_2 a_3 a_4^\dagger + a_1^\dagger a_2^\dagger a_3 a_4 + a_1 a_2^\dagger a_3^\dagger a_4 + a_1 a_2 a_3^\dagger a_4^\dagger\right).
\end{aligned}
$$

For a given initial Fock state, the resonant regime is achieved when the expectation energy lies in a region characterized by an energy band. There, the values of the integrability-breaking parameters $\mu$, $\nu$ may be as large as the band-separation allows, which is depicted in Figure 5.6.

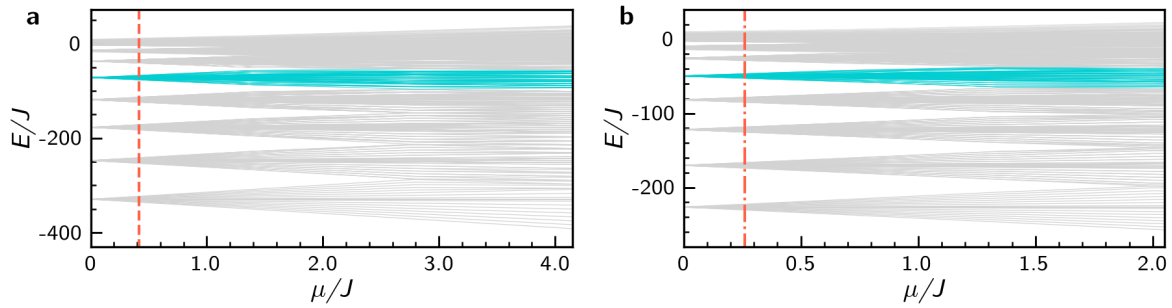


Figure 5.6: Energy bands for broken integrability. Four-site model energy distribution for the two sets of parameters $U$ and $J$, as in the main text. **a** Set 1: $U/J \sim 1.5$ and **b** Set 2: $U/J \sim 1$. The vertical lines indicate the respective integrability-breaking parameters $\mu/\hbar = 30.016$ Hz (**a**) and $\mu/\hbar = 27.415$ Hz (**b**). The cyan lines represent the energy band associated to the initial state $|\Psi_0\rangle = |4, 11, 0, 0\rangle$.

### 5.7.2 Probabilities and fidelities

Supplementary Table 1 shows the measurement probabilities of Protocol I, as well as the fidelity of the resulting state with the respective NOON state, for $M = 4$, $P = 11$ and the two aforementioned sets of parameters. The resulting NOON state from Protocol I can be either symmetric ($r = 0$) or antisymmetric ($r = M$). For intermediate values for the outcome of measuring $N_3$, we calculate the fidelity of the resulting state with the symmetric NOON state ($r = 0, 1$) or the antisymmetric state ($r = 2, 3, 4$), respectively.

**Protocol I:**

**Set 1**

| | Phase ($P\theta$) | | | | | | | | | | | |
|---|---|---|---|---|---|---|---|---|---|---|---|---|
| Measurement | 0 | | $\pi/6$ | | $\pi/4$ | | $\pi/3$ | | $\pi/2$ | | $\pi$ | |
| $r$ | $\mathcal{P}(r)$ | $F_{\mathrm{I}}$ | $\mathcal{P}(r)$ | $F_{\mathrm{I}}$ | $\mathcal{P}(r)$ | $F_{\mathrm{I}}$ | $\mathcal{P}(r)$ | $F_{\mathrm{I}}$ | $\mathcal{P}(r)$ | $F_{\mathrm{I}}$ | $\mathcal{P}(r)$ | $F_{\mathrm{I}}$ |
| 0 | 0.4982 | 0.9850 | 0.4969 | 0.9742 | 0.4968 | 0.9774 | 0.4974 | 0.9846 | 0.4984 | 0.9859 | 0.4984 | 0.9867 |
| 1 | 0.0046 | 0.0953 | 0.0060 | 0.0976 | 0.0061 | 0.1136 | 0.0055 | 0.1057 | 0.0045 | 0.0575 | 0.0044 | 0.0823 |
| 2 | 0.0027 | 0.0117 | 0.0026 | 0.0087 | 0.0026 | 0.0262 | 0.0027 | 0.0303 | 0.0027 | 0.0307 | 0.0027 | 0.0356 |
| 3 | 0.0067 | 0.0955 | 0.0056 | 0.0793 | 0.0046 | 0.0892 | 0.0056 | 0.0929 | 0.0067 | 0.0823 | 0.0048 | 0.0901 |
| 4 | 0.4816 | 0.9966 | 0.4831 | 0.9969 | 0.4837 | 0.9969 | 0.4823 | 0.9969 | 0.4815 | 0.9969 | 0.4832 | 0.9972 |

**Set 2**

| | Phase ($P\theta$) | | | | | | | | | | | |
|---|---|---|---|---|---|---|---|---|---|---|---|---|
| Measurement | 0 | | $\pi/6$ | | $\pi/4$ | | $\pi/3$ | | $\pi/2$ | | $\pi$ | |
| $r$ | $\mathcal{P}(r)$ | $F_{\mathrm{I}}$ | $\mathcal{P}(r)$ | $F_{\mathrm{I}}$ | $\mathcal{P}(r)$ | $F_{\mathrm{I}}$ | $\mathcal{P}(r)$ | $F_{\mathrm{I}}$ | $\mathcal{P}(r)$ | $F_{\mathrm{I}}$ | $\mathcal{P}(r)$ | $F_{\mathrm{I}}$ |
| 0 | 0.4911 | 0.9568 | 0.4912 | 0.9711 | 0.4893 | 0.9613 | 0.4886 | 0.9533 | 0.4918 | 0.9639 | 0.4924 | 0.9661 |
| 1 | 0.0107 | 0.1518 | 0.0108 | 0.1491 | 0.0125 | 0.1641 | 0.0131 | 0.1703 | 0.0101 | 0.0915 | 0.0095 | 0.1182 |
| 2 | 0.0053 | 0.0450 | 0.0052 | 0.0436 | 0.0052 | 0.0145 | 0.0053 | 0.0487 | 0.0051 | 0.0436 | 0.0052 | 0.0526 |
| 3 | 0.0104 | 0.1527 | 0.0145 | 0.1382 | 0.0109 | 0.1560 | 0.0096 | 0.1624 | 0.0148 | 0.1077 | 0.0095 | 0.1168 |
| 4 | 0.4660 | 0.9879 | 0.4604 | 0.9881 | 0.4646 | 0.9874 | 0.4671 | 0.9885 | 0.4616 | 0.9912 | 0.4667 | 0.9925 |

Table 5.2: Measurement probabilities and NOON state fidelities. Probability of measuring $r$ particles at site 3 of Protocol I, and fidelity of the resulting state with the symmetric NOON state ($r = 0, 1$) or the antisymmetric NOON state ($r = 2, 3, 4$). In this calculation, we employed the parameters Set 1 and Set 2 and considered $M = 4$ and $P = 11$.

### 5.7.3 Readout statistics

For less ideal choices of parameters, it is possible to perform a fitting on the readout probabilities amplitudes, such that

$$\text{Protocol I} \begin{cases} \mathcal{P}(0,0) = \mathcal{P}(M,0) = \dfrac{c_{00}}{2}\cos^2\left(\dfrac{P\theta}{2}\right) \\ \mathcal{P}(0,M) = \mathcal{P}(M,M) = \dfrac{c_{MM}}{2}\sin^2\left(\dfrac{P\theta}{2}\right) \end{cases}$$

$$\text{Protocol II} \begin{cases} \mathcal{P}(0) = c_0 \sin^2\left(\dfrac{P\theta}{2} - \dfrac{\pi}{4}\right) \\ \mathcal{P}(M) = c_M \cos^2\left(\dfrac{P\theta}{2} - \dfrac{\pi}{4}\right) \end{cases}$$

where $c_{00}$, $c_{MM}$, $c_0$ and $c_M$ are constants that are obtained by fitting the numerically-evaluated data with the analytic models. By choosing the parameters of Set 2, we

obtain the following constants from a least-squares fitting: $c_{00} = 0.938$, $c_{MM} = 0.893$, $c_0 = 0.954$ and $c_M = 0.909$. The results are shown in Figure 5.7.

### 5.7.4 Initial state preparation

Based on previous works [103, 134] on optical superlattices, here we point out how to generate the proposed initial state by manipulating the potential depths and relative phase $\varphi$ of the 2D short and long lattices. In this environment, the preparation of arbitrary initial Fock states can be carried out by loading the 2D long-lattice with relative phase $\varphi = \pi/4$ along $x$-direction in the MI (Mott Insulator) regime [26, 38] and controlling the atomic density by adjusting an additional transverse trap. A resonant laser pulse removes atoms from the first and second wells neighboring the one of interest [134]. After adiabatically ramping up the 2D short-lattice the remaining atoms occupy a double well plaquette. The imbalanced population between the wells can be determined by applying a biased potential, which is tuned by the depth and relative phase along the $y$-direction of an additional shallow 2D long-lattice. By switching off the shallow 2D long-lattice, a four-site plaquette emerges by tuning the relative phase to $\varphi = 0$ while the all depths of the superlattice are adjusted to fulfill the integrability condition, then the time evolution of protocols can commence.

### 5.7.5 Robustness

Here we analyze the system's robustness in response to perturbation. Consider that, relative to the integrability condition, the system parameters are subject to error estimated as $|U_0 - U_{13}|/\hbar \approx \alpha\, \Delta\omega_r$, where $\alpha \simeq 6.586 \times 10^{-3}$ for Set 1, $\alpha \simeq 6.919 \times 10^{-3}$ for Set 2. The parameter $\Delta\omega_r = |\omega_r' - \omega_r|$ denotes the maximal amplitude of fluctuation of the trap frequency $\omega_r'$ around the frequency $\omega_r$ at the integrability condition. To quantify the robustness, we generate the state $|\Psi(\Delta\omega_r)\rangle$ by iteratively evolving the initial state $|\Psi_0\rangle$ under the perturbed Hamiltonian

$$H' = H + \alpha\, s\, \Delta\omega_r (N_1 N_3 + N_2 N_4), \tag{5.7}$$

where $s \in [-1, 1]$, for each time-step $\delta t \approx 4\,\mathrm{ms}$ over the protocol time. The variable $s$ obeys a truncated Gaussian distribution, with standard deviation $\sigma = 1/4$ . For each $\Delta\omega_r$, 100 time evolutions were simulated to compute the average fidelity $F_{I(II)} = \overline{|\langle \Psi_{3(4)}^{I(II)} | \Psi(\Delta\omega_r)\rangle|}$ with phase $\theta = 0$. Numerical results are presented in Figure 5.8. The average fidelities for both Set 1 and Set 2 are above 0.9, with $|\Delta\omega_r/\omega_r|$ up to $\sim 0.01$.

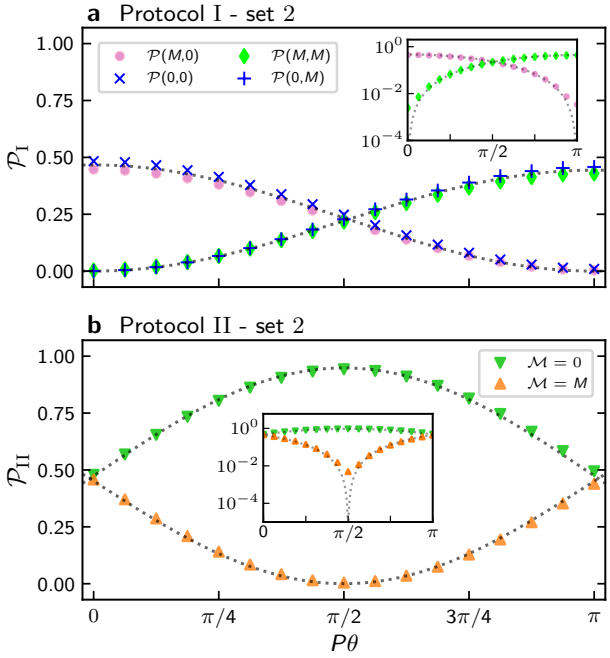


Figure 5.7: Readout probabilities. Comparison between analytic and numerically-calculated probabilities relating to the parameters of Set 2 with $\mu/\hbar = \nu/\hbar = 27.415$ Hz, for different values of $P\theta$. **a** Probability distributions for measuring $N_3 = 0$ ($N_3 = M$) after time evolution subsequent to Protocol I. **b** Probability distributions of measuring $N_3 = 0$ ($N_3 = M$) after time evolution subsequent to Protocol II. In both cases, the dotted lines refer to the analytic probabilities adjusted to the numerical points according to the Eqs. (5.7). The coefficients used were $c_{00} = 0.934$, $c_{MM} = 0.888$, $c_0 = 0.901$ and $c_M = 0.948$. The insets show the accordance between predicted and calculated probabilities in semilogarithmic scale.

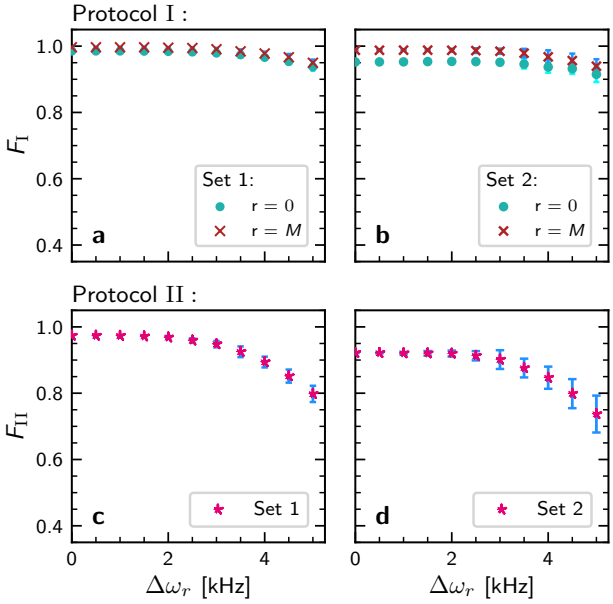


Figure 5.8: Robustness. Average NOON states fidelities with respect to perturbation parameter $\Delta\omega_r$, for Protocols I (panels **a** and **b**) and II (panels **c** and **d**). Panels **a** and **c**: Set 1. Panels **b** and **d**: Set 2. For each $\Delta\omega_r$, the fidelity is numerically computed at the NOON-state evolution time under the Hamiltonian (5.7), for each respective protocol. The average fidelity is calculated as the mean of 100 temporal evolutions, and the error bars represent the standard deviation. These are subject to fluctuations around $\omega_r$, drawn from a truncated Gaussian, every 4 ms. Both Set 1 and Set 2 exhibit average fidelities above 0.9 for $|\Delta\omega_r/\omega_r|$ up to $\sim 0.01$.

# Chapter 6

# Interacting bosons in a triple well: Preface of many-body quantum chaos

In this chapter, we systematically investigate the onset of quantum chaos in the triple-well model when moving away from integrability as its potential gets tilted. We show that even in its deepest chaotic regime, the system presents features reminiscent of integrability. Our studies are based on level spacing distribution and spectral form factor, structure of the eigenstates, and diagonal and off-diagonal elements of observables in relationship to the eigenstate thermalization hypothesis. The main content of this chapter was published in Physical Review E[1].

## 6.1 Foreword

The interest in many-body quantum chaos has grown significantly in recent years due to its close connection with thermalization [138–140], scrambling of quantum information [141], and the fact that many-body quantum systems can now be studied experimentally in a controllable way with a variety of experimental set-ups, from cold atoms and ion traps to superconducting devices and nuclear magnetic resonance. In studies of many-body quantum chaos, the focus is usually on interacting lattice systems with many sites and many particles, where the Hilbert space grows exponentially with the system size. Here, instead, we investigate the onset of quantum chaos in a system that has only three wells, but where the number $N$ of particles is large. The Hilbert space grows quadratically with $N$, and as $N$ increases, the system is brought closer to the

[1] *Interacting bosons in a triple well: Preface of many-body quantum chaos*, D.S. Grun, L.H. Ymai, Karin Wittmann Wilsmann, A.P. Tonel, A. Foerster, J. Links, Phys. Rev. E, **105**, 034204 (2022), doi:10.1103/PhysRevE.105.034204

classical limit.

By tilting the potential through an external field, the bosonic triple-well model discussed in Chapters 2,3 becomes chaotic. However, while previously the model was investigated in the strong interaction regime (resonant tunneling regime), here it will be studied in the weak interaction regime, which, as will be shown, is the potentially chaotic region - see Fig. 6.2 below. We provide a systematic study of this transition based not only on spectral correlations, but also on the structure of the eigenstates and its consequences to the eigenstate expectation values and the distributions of the off-diagonal elements of the number operator of each well, in close connection with the notion of the eigenstate thermalization hypothesis (ETH).

Contrary to systems where the number of wells and particles are increased, the number of degrees of freedom in the triple-well model is fixed. Increasing its number of bosons does not enhance its chaotic features. The range of values of the integrability breaking parameter that leads to chaos is not extended for larger $N$'s and the eigenstates do not reach higher degrees of ergodicity. Even for energies close to the middle of the spectrum, for which a semiclassical analysis gives positive Lyapunov exponents [142], the distributions of the components of the eigenstates and of the off-diagonal elements of the number operators are not Gaussian, which contrasts with what happens for multi-well systems.

## 6.2 Model

The quantum system that we study consists of $N$ bosons in an aligned triple-well potential described by the Hamiltonian[2] [43],

$$\begin{aligned}\hat{H} =& \frac{U}{N}\left(\hat{N}_1^2+\hat{N}_2^2+\hat{N}_3^2\right)+\epsilon\left(\hat{N}_3-\hat{N}_1\right)\\ &+\frac{2U}{N}\left(-\hat{N}_1\hat{N}_2-\hat{N}_2\hat{N}_3+\hat{N}_1\hat{N}_3\right)\\ &+\frac{J}{\sqrt{2}}\left(\hat{a}_1^\dagger\hat{a}_2+\hat{a}_2^\dagger\hat{a}_1\right)+\frac{J}{\sqrt{2}}\left(\hat{a}_2^\dagger\hat{a}_3+\hat{a}_3^\dagger\hat{a}_2\right),\end{aligned} \tag{6.1}$$

where $\hat{N}_i=\hat{a}_i^\dagger\hat{a}_i$ is the number operator of the well $i$, $\hat{a}_i$ ($\hat{a}_i^\dagger$) is the annihilation (creation) operator, $U$ is the onsite interaction strength and also the strength of the interactions between wells, $J$ is the tunneling amplitude between wells, and $\epsilon$ is the amplitude of the tilt between the wells. We consider repulsive interaction, $U\geq 0$.

Hamiltonian (6.1) conserves the total number of bosons, $N=N_1+N_2+N_3$, and when $\epsilon=0$, it commutes with the parity operator. The matrix has dimension $D=$

[2]This Hamiltonian is the same discussed in Chapters 2 and 3, with a slight change of notation to preserve the form used in the reference [143]

$(N+2)!/(2!N!)$. Our studies of the structure of the eigenstates are done in the Fock basis, $|n\rangle = |N_1, N_2, N_3\rangle$. We denote the eigenstates and eigenvalues of $\hat{H}$ by $|\alpha\rangle$ and $E_\alpha$.

A schematic representation of our model is shown in Fig. 6.1. When $\epsilon = 0$ [Fig. 6.1 (a)], the model is integrable and solvable with the algebraic Bethe ansatz [24]. At this point, in addition to energy and the total number of particles, our three-degree-of-freedom model has a third independent conserved quantity, $Q = J^2N_3/2 + J^2N_1/2 - J^2(a_1^\dagger a_3 + a_3^\dagger a_1)/2$ [24, 43]. The system becomes nonintegrable [Fig. 6.1 (b)] when the tilt is included. As discussed in Sec. 6.3.1, the model shows signatures of quantum chaos when the tilt amplitude is of the order of the hopping and interaction strengths, $\epsilon \sim J, U$.

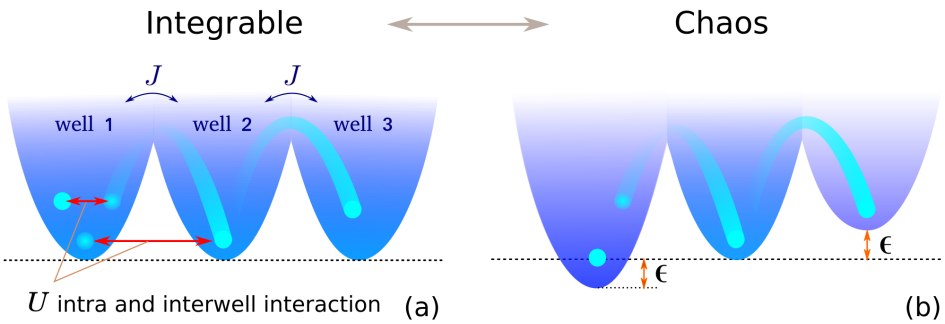


Figure 6.1: Schematic representation of the three-well system described by Eq. (6.1) for both the integrable (a) and the non-integrable (b) regime. The red arrows indicate the intrawell and interwell interaction strength $U$, the black arrows indicate the tunneling amplitude $J$ between adjacent wells, and $\epsilon$ represents the tilt of the potentials of wells 1 and 3 with respect to well 2.

In the absence of the potential tilt and of the interaction between wells, our model coincides with the bare Bose-Hubbard model with 3 sites. Signatures of quantum chaos were studied in this model, for example, in [18, 23]. This case and also the extended triple-well Bose-Hubbard model with dipolar interaction [37] exhibit properties similar to those of our system in the chaotic domain. Comparisons between the three models are presented in the Suppl. Material 6.7.1.

### 6.2.1 Parameters and density of states

In our numerical analysis, we fix $J = 1$, $U/J = 0.7$, and vary $\epsilon$ for different numbers of particles. The choice of $U$ is justified with Fig. 6.2 (a), where we show the eigenvalues as a function of the interaction strength for $\epsilon = 0$. When $U = 0$, there is only hopping and the model is trivially solved. This is usually referred to as Rabi regime [43] in analogy with the double-well model [10, 144, 145]. As the interaction strength increases and becomes larger than the hopping amplitude, $U/J > 1$, energy bands are formed. The extreme scenario of $U \gg J$ is the Fock regime, where the eigenstates approach the Fock states, and the model is again trivially solved. The region where we can expect chaos

to develop is therefore for $0 < U/J < 1$, which explains the choice $U/J = 0.7$ indicated with the red dotted vertical line in Fig. 6.2 (a).

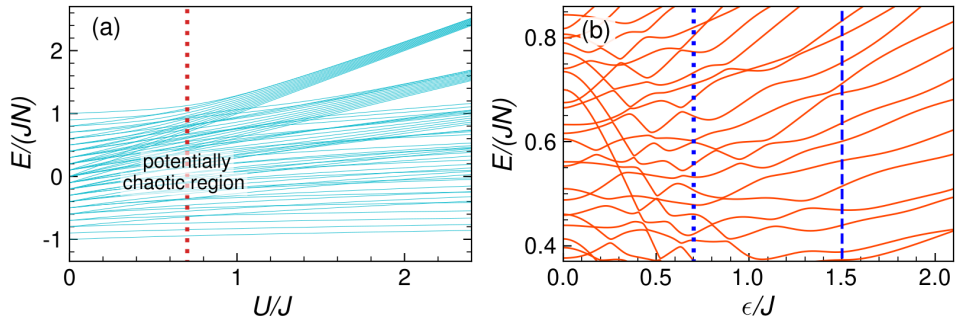


Figure 6.2: Normalized eigenvalues as a function of the interaction strength, $U/J$, for $\epsilon = 0$ (a) and as a function of the tilt amplitude, $\epsilon/J$, for $U/J = 0.7$ (b). The vertical line in Fig. 6.2 (a) marks the value $U/J = 0.7$, which is used in panel (b) and in all of our subsequent studies. In Fig. 6.2 (b), the vertical lines marks the values $\epsilon/J = 0.7$ (dotted line) and $\epsilon/J = 1.5$ (dashed line) used in our studies of the chaotic regime. In all panels N=10.

In chaotic systems, the eigenvalues are correlated and avoid each other [146, 147], while in integrable models (apart from the picket-fence scenario [53, 148, 149]), the energy levels can cross. This difference is clearly seen in Fig. 6.2 (b), where we fix $U/J = 0.7$ and vary $\epsilon/J$. Level crossing happens when $0 \leq \epsilon/J < 1$, but is avoided for $\epsilon/J \gtrsim 1$, where the "spaghetti structure", typical of repulsive energy levels, becomes visible.

In Fig. 6.3, we compare the density of states (DOS),

$$\nu(E) = \sum_{\alpha=1}^{D} \delta(E - E_\alpha), \tag{6.2}$$

of the model (6.1) for three values of the tilt, $\epsilon/J = 0$, 0.7, and 1.5. In realistic interacting many-body quantum systems with many degrees of freedom, such as spin models with many excitations [150] or Bose-Hubbard models with many particles and many sites [17, 151], the DOS is typically Gaussian [152, 153], which can be explained using the central limit theorem. This contrasts with our model [Figs. 6.3 (a)-(c)], which has few degrees of freedom.

Systems with few-degrees of freedom, such as the Dicke model [154], spin-1/2 models with less than 4 excitations [155], and multi-well Kronig-Penney-like systems with few particles [156], often present shapes other than Gaussian. We see in the Suppl. Material 6.7.1 that the bare triple-well Bose-Hubbard model and the extended triple-well Bose-Hubbard model show distributions that, similarly to our model in Fig. 6.3 (c), are not yet Gaussian, but get close to it. The DOS for the extended Bose-Hubbard model and for our model are comparable, since both have long-range couplings.

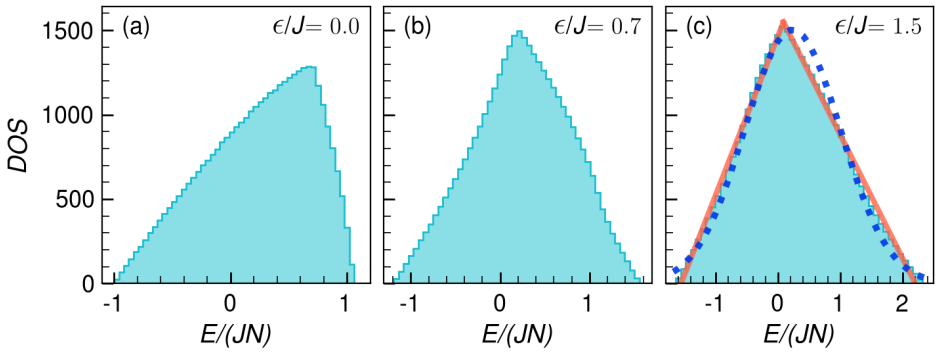


Figure 6.3: Density of states for $N = 270$, $U/J = 0.7$, and $\epsilon/J = 0$ (a), 0.7 (b) and 1.5 (c). The solid line in (c) is a linear fitting for the left and right sides of the distribution, while the dotted line is a Gaussian distribution fitting.

## 6.3 Spectral correlations

To quantify the degree of correlations between the eigenvalues, we study the level spacing distribution and the spectral form factor. We show that for $U/J \sim 0.7$, as $\epsilon$ in Eq. (6.1) increases from zero, our triple-well model leaves the integrable point ($\epsilon = 0$) and moves towards the chaotic domain.

### 6.3.1 Level spacing distribution

The transition to quantum chaos can be verified with the distribution $P(s)$ of the spacings $s$ between nearest unfolded energy levels. For chaotic systems with real and symmetric Hamiltonian matrices, as in Eq. (6.1), $P(s)$ follows the Wigner surmise [147, 157], $P_{\rm W}(s) = (\pi s/2)\exp(-\pi s^2/4)$, as obtained also for the eigenvalues of full random matrices from a Gaussian orthogonal ensemble (GOE). This distribution indicates that the eigenvalues are correlated and repel each other, that is, $P(s = 0) = 0$. In integrable models, the level spacing distribution is Poissonian, $P_{\rm P}(s) = e^{-s}$, since the energy levels are uncorrelated [3].

The analysis of the level spacing distribution requires unfolding the eigenvalues and separating them by symmetry sectors. The unfolding procedure corresponds to rescaling the eigenvalues, so that the local density of states of the rescaled energies is 1. The separation by subspaces is necessary, because eigenvalues from different symmetry sectors have no reason to be correlated.

In Figs. 6.4 (a)-(c), we illustrate $P(s)$ for $\epsilon/J = 0$, 0.7, and 1.5, respectively. The Poissonian distribution is obtained for the integrable point $\epsilon = 0$ in Fig. 6.4 (a), and the Wigner shape is seen for $\epsilon/J = 1.5$ in Fig. 6.4 (c), as we had anticipated from the

[3] As mentioned above, this excludes integrable models with picket-fence kind of spectra [53, 148, 149] and also integrable models with an excessive number of degeneracies [158].

"spaghetti structure" in Fig. 6.2 (b). An intermediate picture emerges for $\epsilon/J = 0.7$ in Fig. 6.4 (b).

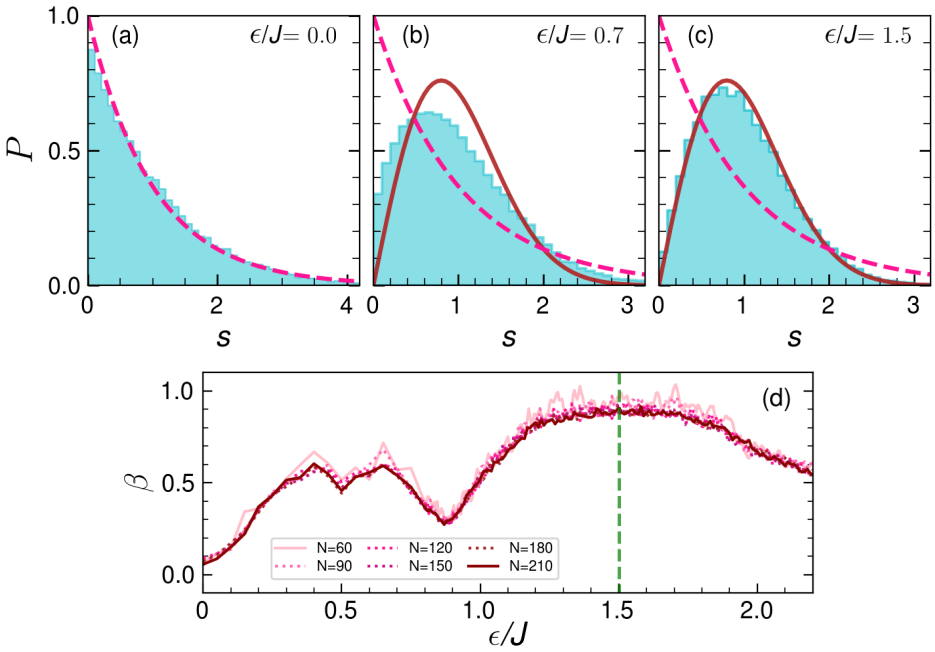


Figure 6.4: Level spacing distribution for $N = 270$ and $\epsilon/J = 0$ (a), $\epsilon/J = 0.7$ (b), and $\epsilon/J = 1.5$ (c); and chaos indicator $\beta$ as a function of the tilt amplitude for various $N$'s (d). In (a)-(c): The dashed (solid) line represents the Poissonian (Wigner) distribution. In (d): The green vertical line at $\epsilon/J = 1.5$ marks where $\beta$ gets the closest to 1, indicating the Wigner distribution.

The proximity of the level spacing distribution to the Poissonian or the Wigner distribution can be quantified with the chaos indicator $\beta$, which is obtained by fitting $P(s)$ with the Brody distribution [153] (see also [159]),

$$P_\beta(s) = (\beta+1)bs^\beta \exp(-bs^{\beta+1}), \quad b = \left[\Gamma\left(\frac{\beta+2}{\beta+1}\right)\right]^{\beta+1} \tag{6.3}$$

For chaotic systems, $\beta \sim 1$ and for a Poissonian distribution, $\beta \sim 0$.

In Fig. 6.4 (d), we show $\beta$ as a function of $\epsilon/J$ for $N = 60, 90, \ldots, 210$. As evident from the figure, a high degree of chaos happens for $\epsilon/J \in [1.3, 1.7]$. Notice that this range of values does not grow as $N$ increases, which contrasts with interacting many-body quantum systems with many sites [160–162], where studies of chaos indicators for different system sizes suggest that in the thermodynamic limit, an infinitesimal integrability breaking term may be enough to bring those systems to the chaotic domain. In addition and also contrary to the results for systems with many sites [161, 162], larger values of $N$ do not take $\beta$ closer to 1. The only effect that an increased value of $N$ appears to have for the triple-well model is to reduce the fluctuations in the values of $\beta$ for nearby $\epsilon$'s, which concurs with improved statistics.

### 6.3.2 Spectral form factor

The level spacing distribution detects only short-range correlations. To get a better idea of the degree of spectral correlations, one may resort to other indicators of quantum chaos, such as the spectral form factor,

$$S_{FF}(t) = \left\langle \left| \sum_{\alpha=1}^{D} f(E_\alpha) e^{-iE_\alpha t} \right|^2 \right\rangle , \tag{6.4}$$

which captures both short- and long-range correlations. The spectral form factor is used to study level statistics in the time domain. When the eigenvalues are correlated as in random matrices, $S_{FF}(t)$ develops the so-called correlation hole [163–168], which we further discuss below Eq. (11). The spectral form factor is advantageous over the direct analysis of the eigenvalues, because it does not require unfolding the spectrum or separating the eigenvalues by symmetry sectors [162, 169], although averages, indicated by $\langle . \rangle$ in Eq. (6.4), are needed, since this quantity is non-self-averaging [170, 171].

A filter function $f(E_\alpha)$, as used in Eq. (6.4), is often added to the spectral form factor [172]. When $f(E_\alpha)$ coincides with the components of an initial state projected in the energy eigenbasis, the spectral form factor becomes the survival probability [171]. In our analysis, we choose [173]

$$f(E_\alpha) = \frac{r_\alpha g(E_\alpha)}{\sum_\beta r_\beta g(E_\beta)}, \tag{6.5}$$

where $r_\alpha$ are random numbers from a uniform distribution in the interval $[0, 1]$, the function $g(E) = \rho(E)/\nu(E)$, and $\rho(E)$ is a chosen energy profile, which, in our case, is a rectangular function,

$$\rho(E) \;=\; \begin{cases} \dfrac{1}{2\sigma} & \text{for } E \in [E_c - \sigma, E_c + \sigma] \\ \\ 0 & \text{otherwise,} \end{cases} \tag{6.6}$$

of width $\sigma$, centered at the energy $E_c$, and with bounds at $E_{min} = E_c - \sigma$ and $E_{max} = E_c + \sigma$. The division of $\rho(E)$ by $\nu(E)$ is done using the linear fits for the DOS in Fig. 6.3 (c). This procedure compensates for variations in the density of states and ensures the rectangular shape of the filter function [173]. As it will become clear in Sec. 6.4, the region where the eigenstates are mostly chaotic happens for $E/(JN) \in [-0.2, 1]$. For this reason, we choose $E_c/(JN) = 0.5$ and $\sigma/(JN) = 0.35$.

In Fig. 6.5, we consider a large Hilbert space and show $S_{FF}(t)$ in the chaotic region of strong level repulsion averaged over various realizations of the random numbers $r_\alpha$

and taking into account also a moving time average starting at $t \sim 5/J$, where the fluctuations are large. The numerical results are presented together with the analytical expression obtained following Refs. [173–175],

$$S_{FF}^{analyt}(t) = \frac{1 - \langle\overline{S_{FF}}\rangle}{\eta - 1}\left[\eta\frac{\sin^2(\sigma t)}{(\sigma t)^2} - b_2\left(\frac{t}{2\pi\nu_c}\right)\right] + \langle\overline{S_{FF}}\rangle, \tag{6.7}$$

where

$$\eta = \frac{\langle r_\alpha^2\rangle}{\langle r_\alpha\rangle^2\langle\overline{S_{FF}}\rangle} = \frac{4}{3\langle\overline{S_{FF}}\rangle}$$

is the effective dimension associated with the chosen filter function, and

$$\nu_c = \frac{\eta}{2\sigma} \tag{6.8}$$

is the density of states at $E = E_c$, or equivalently, the inverse mean level spacing probed by the chosen energy profile [173].

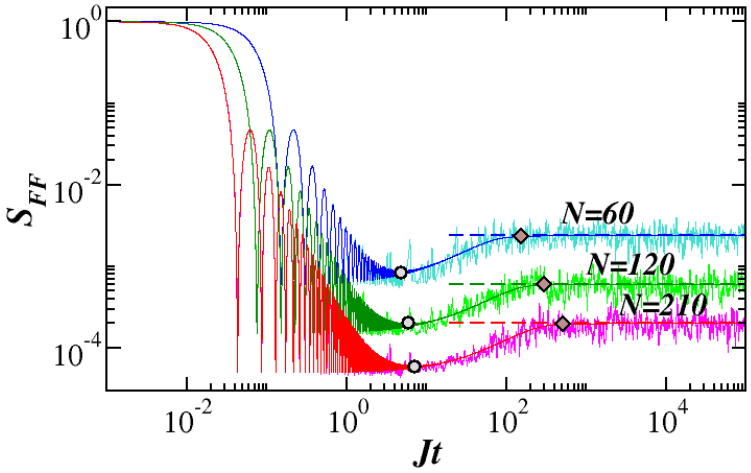


Figure 6.5: Spectral form factor for three values of $N$. The lines with fluctuations, which have lighter colors, represent numerical results; the thin smooth lines give the analytical expression in Eq. (6.7); and the dashed horizontal lines indicate the saturation point $\langle\overline{S_{FF}}\rangle$ in Eq. (6.11). The symbols mark the time to reach the minimum of the correlation (circle) and the saturation time (diamond). For the numerical results: Averages over 500 random realizations and also running averages.

The first term in the square brackets of Eq. (6.7) describes the behavior of $S_{FF}(t)$ at short times. It is obtained by writing Eq. (6.4) as an integral,

$$S_{FF}(t) = \left\langle \left| \int_{E_{min}}^{E_{max}} \rho_0(E) e^{-iEt} dE \right|^2 \right\rangle, \tag{6.9}$$

and substituting the energy distribution,

$$\rho_0(E) = \sum_{\alpha=1}^{D} f(E_\alpha)\delta(E - E_\alpha), \tag{6.10}$$

with the smoothed energy profile $\rho(E)$ from Eq. (6.6), which can be done for large Hilbert spaces. The Fourier transform in Eq. (6.9) gives $\dfrac{\sin^2(\sigma t)}{(\sigma t)^2}$. This function leads to a power-law decay with exponent 2 due to the bounds of the filter function [176–178].

The effects of the spectral correlations get manifested at larger times, when the discreteness of the spectrum is resolved and the correlations are then detected. This results in the dip in Fig. 6.5 below the horizontal dashed line that represents the infinite-time average

$$\langle \overline{S_{FF}} \rangle = \sum_{\alpha} |f(E_\alpha)|^2. \tag{6.11}$$

This dip is known as correlation hole [163–168] and it does not exist in models that present a Poissonian level spacing distribution. In the case of GOE full random matrices, the dip is described by the two-level form factor [157],

$$b_2(\bar{t}) = \begin{cases} 1 - 2\bar{t} + \bar{t}\ln(2\bar{t}+1) & \bar{t} \leq 1 \\ \bar{t}\ln\left(\dfrac{2\bar{t}+1}{2\bar{t}-1}\right) - 1 & \bar{t} > 1 \end{cases}. \tag{6.12}$$

This function describes very well our numerical results and confirms the chaoticity of our triple-well model.

By comparing the results for different numbers of bosons in Fig. 6.5, it is clear that the time to reach the minimum of the correlation hole and the time to reach saturation increase with $N$. Analytical expressions for these times are given in the Suppl. Material 6.7.2. They are much shorter than those obtained for interacting many-body quantum systems with many sites [175].

## 6.4 Eigenstates

In chaotic quantum systems, the eigenvalues are correlated and the eigenstates are uncorrelated. In this section, we analyze the transition to quantum chaos through the changes in the structure of the eigenstates. As $\epsilon$ increases from zero and the system moves from the integrable to the chaotic domain, we expect the eigenstates away from the edges of the spectrum to become closer to the eigenstates of GOE full random matrices [138, 139]. The GOE eigenstates are random vectors with components that are real and which correspond to independent Gaussian random numbers satisfying the

normalization condition. In realistic many-body quantum systems, a fraction of the components of the chaotic eigenstates can be nearly zero, but the nonzero components follow a Gaussian distribution [150].

To detect the onset of chaotic eigenstates, one can employ measures of delocalization [159, 179] and fractality [151], and analyze the distributions of the components of the eigenstates. These methods are, of course, attached to a basis choice. We use here the Fock basis, $|n\rangle$, which are the eigenstates of the number operators studied in Sec. V. This basis is in close connection with cold-atom experiments, where dynamics are initiated by preparing the system in Fock states. Nevertheless, in the Suppl. Material 6.7.4 and Suppl. Material 6.7.5, we also provide the analysis of the eigenstates using as basis the eigenstates of the $\hat{H}(\epsilon = 0)$ part of the total Hamiltonian in Eq. (6.1). Our main conclusion that the components of the eigenstates of the triple-well model do not follow a Gaussian distribution holds for either choice of basis.

Even the most delocalized eigenstates of our triple-well model are not fully chaotic. A similar conclusion can be drawn for the triple-well Bose-Hubbard model in Ref. [23]. The anomalous scaling of the eigenstate-to-eigenstate fluctuations of expectation values of local observables with the Hilbert space found in that work might be attributed to eigenstates that are not fully chaotic.

### 6.4.1 Delocalization Measures

In Figs. 6.6 (a)-(c), we show the Shannon entropy, $S_h^\alpha$, of each eigenstate $|\alpha\rangle$ written in the Fock basis $|n\rangle$,

$$S_h^\alpha \equiv -\sum_{n=1}^{D} |C_n^\alpha|^2 \ln |C_n^\alpha|^2, \tag{6.13}$$

as a function of energy. In the equation above, $C_n^\alpha = \langle n|\alpha\rangle$. This entropy measures the degree of delocalization of the eigenstates in the chosen basis. If the eigenstate coincides with a basis vector, there is a single $|C_n^\alpha|^2 = 1$ and the state is completely localized. In this case, $S_h^\alpha = 0$. If the eigenstate is homogeneously spread in the Hilbert space, being therefore completely delocalized, then all $|C_n^\alpha|^2 = 1/D$ and the entropy reaches its maximum value $S_h^\alpha = \ln(D)$. An equivalent measure of delocalization is the participation ratio,

$$P_R^\alpha \equiv \sum_{n=1}^{D} \frac{1}{|C_n^\alpha|^4}, \tag{6.14}$$

whose figures are provided in the Suppl. Material 6.7.3. The participation ratio was also considered in the analysis of the triple-well Bose-Hubbard model in Ref. [23].

For GOE full random matrices, the components $C_n^\alpha$ of the eigenstates are independent real random variables from a Gaussian distribution with weights $|C_n^\alpha|^2$ that

fluctuate around $1/D$, so $S_h^{\rm GOE} \sim \ln(0.48D)$. In Figs. 6.6 (a)-(c), we show $S_h^\alpha$ divided by $S_h^{\rm GOE}$.

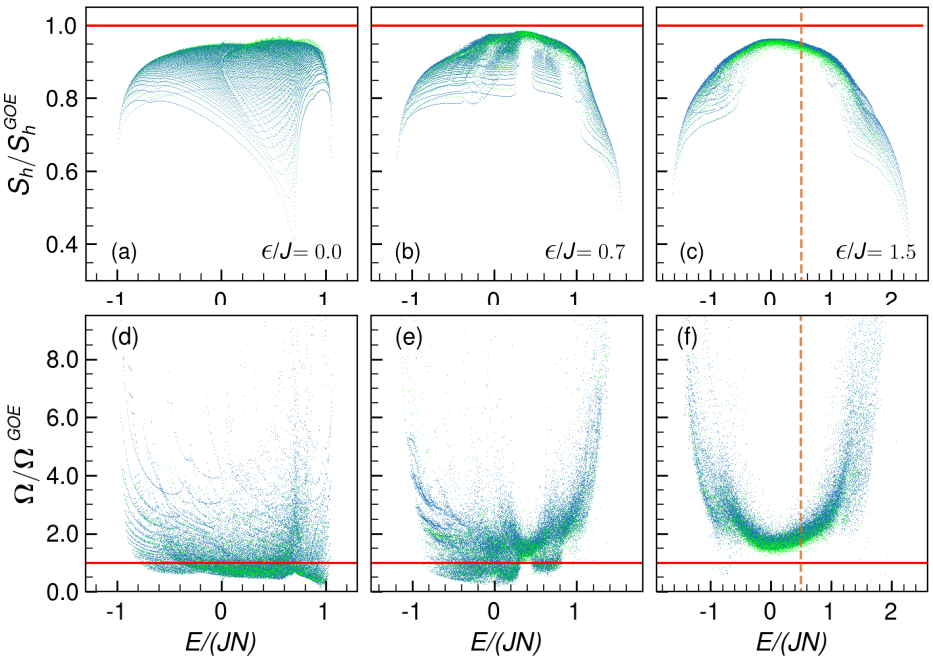


Figure 6.6: Shannon entropy $S_h$ and overlaps of neighboring eigenstates $\Omega$ as a function of energy for $N = 90$ (light lime dots) and $N = 270$ (dark blue dots). In (a) and (d): $\epsilon/J = 0$, in (b) and (e): $\epsilon/J = 0.7$, and in (c) and (f): $\epsilon/J = 1.5$. The solid horizontal lines mark the results for GOE full random matrices. The dashed vertical lines in (c) and (f) mark approximately the center of the chaotic region.

In the integrable regime [Fig. 6.6 (a)], we see a pattern of lines that must be associated with periodic orbits, likely to be found in the phase space of the classical limit of our model. This subject will be discussed in detail in a future publication [4]. As $\epsilon/J$ increases, regions of chaos begin to emerge [Fig. 6.6 (b)], where the fluctuations decrease significantly and $S_h^\alpha$ reaches values closer to $S_h^{\rm GOE}$, as in the vicinity of $E/(JN) \sim 0.3$ and $E/(JN) \sim 0.9$. For $\epsilon/J = 1.5$ [Fig. 6.6 (c)], an evident chaotic region emerges for $E/(JN)$ in the interval given approximately by [-0.2,1]. This energy range explains our choice for $E_c/(JN) = 0.5$ in the analysis of the spectral form factor in Eq. (6.6). We have also verified that the semiclassical analysis of the model in this region of energy leads to positive Lyapunov exponents[5].

Notice, however, that the regular pattern of lines seen in Fig. 6.6 (a) persists in the edges of the spectrum for Fig. 6.6 (b) and even for Fig. 6.6 (c). Our system is clearly separated into regions of chaos and non-chaos, independently of the number of bosons. This is confirmed by comparing the results for $N = 90$ (light color) and $N = 270$ (dark color) in Fig. 6.6 (c).

[4]Forthcoming publication.
[5]Forthcoming publication.

In Figs. 6.6 (d)-(f), we show the quantity $\Omega_{\alpha,\alpha'}$ first proposed in Ref. [150] to measure how similar two neighboring eigenstates $|\alpha\rangle$ and $|\alpha'\rangle$ are,

$$\Omega_{\alpha,\alpha'} \equiv \sum_{n=1}^{D} |C_n^{\alpha}|^2 |C_n^{\alpha'}|^2. \tag{6.15}$$

In full random matrices, where the components $|C_n^{\alpha}|^2$ and $|C_n^{\alpha'}|^2$ are uncorrelated Gaussian random numbers, $\Omega^{\rm GOE} \sim 1/D$. Correlations result in values of $\Omega_{\alpha,\alpha'} > 1/D$. Large values of $\Omega_{\alpha,\alpha'}$ and large fluctuations are found throughout the spectrum of the integrable model [Fig. 6.6 (d)], while in the chaotic domain [Fig. 6.6 (f)] they are restricted to the edges of the spectrum, $E/(JN) < -0.2$ and $E/(JN) > 1$, where chaos does not develop. Notice, however, that even in the chaotic region, $\Omega > \Omega^{\rm GOE}$, which indicates that some level of correlation among the components persists.

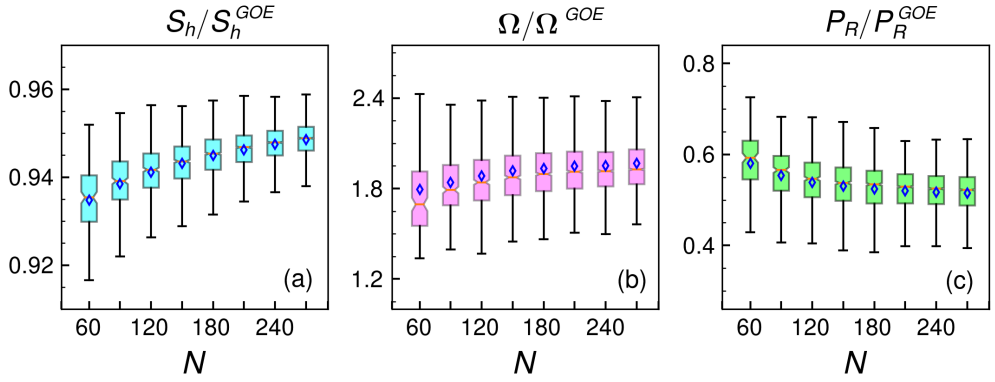


Figure 6.7: Box-and-whisker plots for the Shannon entropy (a), overlaps of neighboring eigenstates (b), and participation ratio (c) for various $N$'s. The data range comprises eigenstates with energies $E/(JN) \in [0.4, 0.6]$ from those presented in Fig. 6.6 (c), where $U/J = 0.7$ and $\epsilon/J = 1.5$. The median for each $N$ is marked with the orange line inside each box and the average with the diamond symbol.

To get some insight on how the level of correlations depend on $N$, in Figs. 6.7 (a)-(c), we select the eigenstates in the chaotic region with energies $E/(JN) \in [0.4, 0.6]$ and study how the averages over these states for $\langle S_h\rangle/S_h^{GOE}$, $\langle\Omega\rangle/\Omega^{GOE}$, and $\langle P_R\rangle/P_R^{GOE}$ change from $N = 60$ to $N = 270$. The analysis is done with box-and-whisker plots [180], which displays the data distribution through its quartiles. The horizontal line drawn in the middle of the boxes indicates the median and the whiskers (the lines extending from the boxes) indicate variability outside the upper and the lower quartiles. The averages are marked with symbols.

The medians in Fig. 6.7 change as $N$ grows. The fact that the values for all three quantities are below those for random matrices is understandable, since we are dealing with the eigenstates of realistic systems with two-body couplings, so some level of correlation always exists. It calls attention, however, that the normalized averages for the entropy grows with $N$ [Fig. 6.7 (a)], while the averages for $\Omega$ [Fig. 6.7 (b)] and

$P_R$ [Fig. 6.7 (c)] move further away from the random matrix results. The overlaps of neighboring states and the participation ratio are more sensitive to fluctuations in the tails of their distributions than the Shannon entropy, due to the logarithm present in the latter [181].

We note that the growth of $\langle\Omega\rangle/\Omega^{\mathrm{GOE}}$ and the decay of $\langle P_R\rangle/P_R^{\mathrm{GOE}}$ with $N$ in Fig. 6.7 are not artifacts of the Fock basis. They hold also for the basis corresponding to the eigenstates of $\hat{H}(\epsilon = 0)$ [not shown].

From Fig. 6.7 (c), it is not possible to conclude whether $\langle P_R\rangle/P_R^{\mathrm{GOE}}$ tends to a constant for larger $N$'s or keeps decreasing. The latter would imply absence of fully developed chaos, in contrast with what is observed for chaotic multi-well systems, and would suggest multifractality. Motivated by this discussion, the next subsection investigates whether the eigenstates with energies in the most chaotic region, those with $E/(JN) \sim 0.5$, might indeed be multifractal.

### 6.4.2 Multifractality

For a state that is extended, but not fully delocalized, $\langle P_R\rangle$ is not proportional to $P_R^{\mathrm{GOE}}$. This can be indicated by writing $\langle P_R\rangle \propto D^{-D_2}$, where $D_2$ is known as the generalized dimension. If $D_2 = 1$, the state is fully delocalized and $\langle P_R\rangle \propto P_R^{\mathrm{GOE}}$. When $D_2 = 0$, the state is localized in the chosen basis. Contrary to these two cases, for $0 < D_2 < 1$, the state is fractal, meaning that it is extended, but not ergodic.

The analysis of multifractality requires one further step. To verify whether a state is multifractal, we study how the generalized dimension $D_q$, obtained from the generalized inverse participation ratio, $I_{PR}^q = \sum_n |C_n^\alpha|^{2q}$, depends on $q$ [182, 183]. The generalized dimension is extracted from the scaling analysis of

$$\langle I_{PR}^q\rangle \propto D^{-(q-1)D_q}. \tag{6.16}$$

Multifractality implies that $0 < D_q < 1$ and that $D_q$ exhibits a nonlinear behavior with $q$.

We extract the generalized dimension $D_q$ for the eigenstates with energy $E/(JN) \sim 0.5$ by analyzing how $\langle I_{PR}^q\rangle$ scales with the Hilbert space dimension $D$. The slope of the curve for $\ln\langle I_{PR}^q\rangle$ as a function of $\ln D$ gives $D_q$, as illustrated in Fig. 6.8 (a) for $q = 0.5$ and Fig. 6.8 (b) for $q = 1.5$, where we vary the dimension of the Hilbert space from $D = 1\,891$ (for $N = 60$) to $D = 36\,856$ (for $N = 270$).

Our results for $D_q$ as a function of $q$ are shown in Fig. 6.8 (c). The values of $D_q$ are larger than 0.9, but always smaller than 1, and they are nonlinear in $q$, suggesting multifractality.

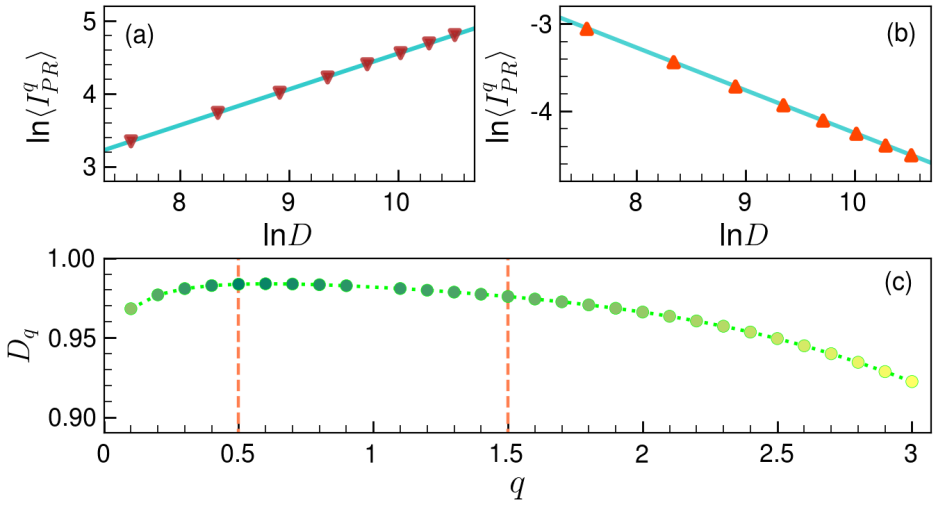


Figure 6.8: Scaling analysis of the generalized inverse participation ratio averaged over 300 eigenstates with $E/(JN) \sim 0.5$ for $q = 0.5$ in (a) and $q = 1.5$ in (b), and generalized dimension $D_q$ as a function of $q$ in (c); $\epsilon/J = 1.5$. In (a) and (b), the solid line is a linear fitting and the symbols are the numerical results obtained by varying the dimension of the Hilbert space from $D = 1\,891$ ($N = 60$) to $D = 36\,856$ ($N = 270$).

### 6.4.3 Distribution of Components

The discussion above prompts a more detailed analysis of the components of the eigenstates. We select a representative eigenstate $|\alpha\rangle = \sum_n C_n^\alpha |n\rangle$ with energy $E/(JN) \sim 0.5$. The distribution of its components in Fig. 6.9 (a) shows a high peak at $C_n^\alpha \sim 0$. This excessive number of zero amplitudes comes mostly from the Fock states that have energy $e_n = \langle n|H|n\rangle$ outside the chaotic region, that is $e_n/J < -0.2$ or $e_n/J > 1$. By removing the components associated with these states, the peak is erased, as seen in Fig. 6.9 (b). The remaining Fock states constitute 59% of the Hilbert space, but they are the main constituents of the selected eigenstate, leading to $\sum_{\substack{n \\ -0.2 \le e_n/J \le 1}} |C_n^\alpha|^2 = 0.90$.

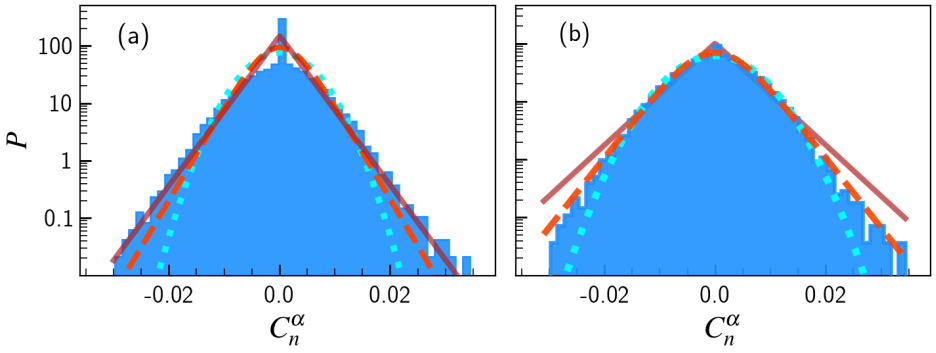


Figure 6.9: Distribution of the components $C_n^\alpha$ of an eigenstate with energy $E/(JN) \sim 0.5$; $\epsilon/J = 1.5$, $N = 270$. In (a), all components are considered, while in (b), only those for which $-0.2 \le e_n/J \le 1$. Solid line: Laplace distribution; dashed line: Logistic distribution; dotted line: Gaussian distribution.

The best distribution in Fig. 6.9 (a) is Laplace. After removing the peak, in

Fig. 6.9 (b), the best distribution becomes Logistic, which is more similar to a Gaussian, but exhibits longer tails. A Gaussian distribution is what one would expect for a fully chaotic state. This is the distribution obtained for the components of the eigenstates of full random matrices and also for chaotic systems with many wells and particles. Thus, the analysis in Fig. 6.9 shows that the eigenstates of our triple-well model do not reach fully chaotic structures. A similar conclusion is reached when the zero-detuning basis is employed, as shown in the Suppl. Material 6.7.5.

The lack of ergodicity of the eigenstates is valid also for the triple-well Bose-Hubbard models presented in the Suppl. Material 6.7.1. The distributions of the components of their most delocalized eigenstates are also Logistic.

## 6.5 Eigenstate thermalization hypothesis

Chaotic eigenstates explain and ensure the validity of the eigenstate thermalization hypothesis (ETH) [160, 184]. The ETH says that when the eigenstate expectation values of a few-body observable $\mathcal{O}$, that is $\mathcal{O}_{\alpha\alpha} = \langle\alpha|\hat{\mathcal{O}}|\alpha\rangle$, are smooth functions of the eigenenergies, these values approach the result from the microcanonical ensemble, $\mathcal{O}_{mic}$, as the system size increases [140]. The hypothesis is also attached to the conditions of absence of degeneracies and $\mathcal{O}_{\alpha\beta} \ll \mathcal{O}_{\alpha\alpha}$, where $\mathcal{O}_{\alpha\beta} = \langle\beta|\hat{\mathcal{O}}|\alpha\rangle$ are the off-diagonal elements of the observable. These are the prerequisites for thermalization, where the infinite-time average of the observable coincides with its thermodynamic average.

In the case of interacting many-body quantum systems, the onset of chaotic eigenstates also leads to the Gaussian distribution of the off-diagonal elements of few-body observables [185], [6]. In this section, we investigate the consequences that the lack of gaussianity of the eigenstates of our model has on the diagonal and off-diagonal elements of the number operator of each well. This observable, which is diagonal in the Fock basis, is chosen for its experimental accessibility.

### 6.5.1 Diagonal Elements

We start the analysis by investigating the diagonal elements of $\hat{N}_i$ in Fig. 6.10. As the integrability breaking term increases from $\epsilon/J = 0$ in Fig. 6.10 (a) to $\epsilon/J = 1.5$ in Fig. 6.10 (c), the fluctuations decrease significantly, reflecting the similar behavior of the eigenstates illustrated in Fig. 6.6. For the integrable model in Fig. 6.10 (a), there is a clear regular structure, and $(N_1)_{\alpha\alpha} = (N_3)_{\alpha\alpha}$ due to the Hamiltonian parity symmetry. In Fig. 6.10 (b), smaller fluctuations appear for $E/(JN) \sim 0.3$ and $E/(JN) \sim 0.9$, as

[6] In interacting many-body quantum systems, deviations from Gaussian distributions occur for many-body observables [186]. If the Hamiltonian is quadratic, deviations happen also for few-body observables [187].

it happens also for the entropy in Fig. 6.6 (b). In Fig. 6.10 (c), smaller fluctuations are seen throughout the spectrum, consistent with the notion of ETH. Notice, however, that outside the chaotic region, for $E/(JN) < -0.2$ and $E/(JN) > 1$, one still sees regular structures that resemble the pattern of lines seen for the eigenstates in Fig. 6.6 (c).

Close to $E/(JN) \sim 0.5$ in Fig. 6.10 (c), the population inversion, where $(N_2)_{\alpha\alpha}$ (red) and $(N_3)_{\alpha\alpha}$ (green) become larger than $(N_1)_{\alpha\alpha}$ (blue), is consistent with the tilt, which causes states with occupation on site 2 and, especially, on site 3 to have larger energies than states with population on site 1. For very high energies, it is therefore natural that $(N_1)_{\alpha\alpha} \simeq (N_2)_{\alpha\alpha} \to 0$. In contrast, for low energies, the distribution of particles is relatively symmetric around $(N_2)_{\alpha\alpha}$, with $N_1 > N_2 > N_3$ and $(N_3)_{\alpha\alpha} \to 0$, as expected.

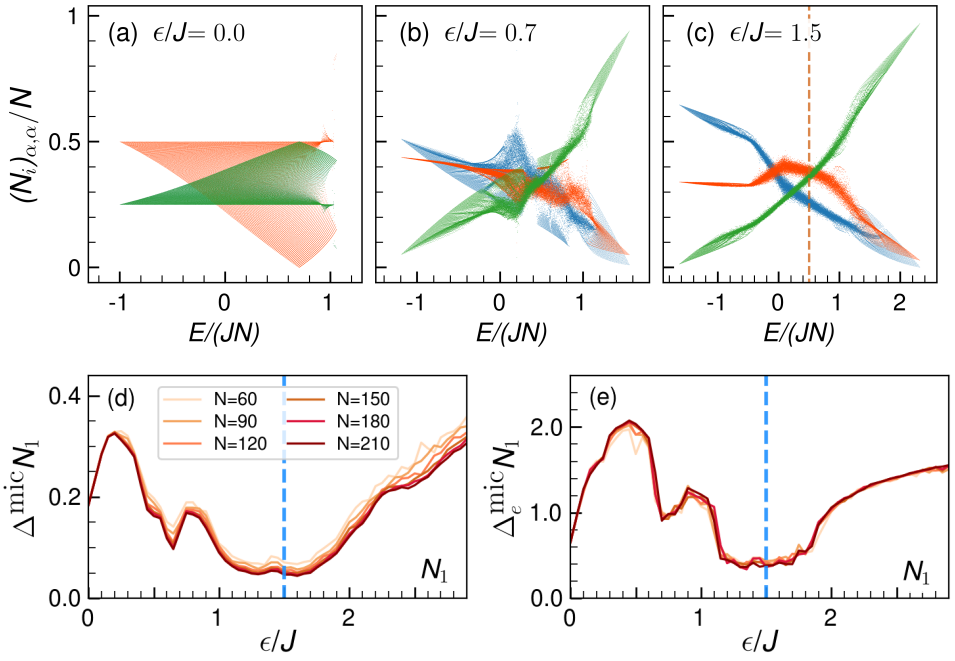


Figure 6.10: Eigenstate expectation values for $(N_1)_{\alpha,\alpha}$ (blue), $(N_2)_{\alpha,\alpha}$ (red), and $(N_3)_{\alpha,\alpha}$ (green) as a function of energy, for $\epsilon/J = 0.0$ (a), $\epsilon/J = 0.7$ (b), and $\epsilon/J = 1.5$ (c); $N = 270$. Average relative deviation of the eigenstate expectation values of $\hat{N}_1$ with respect to the microcanonical average (d) and the normalized extremal fluctuations of the eigenstate expectation values of $\hat{N}_1$ (e) both as a function of the integrability breaking term $\epsilon$. In (d) and (e), the eigenstates lie in the energy range $[E/(JN) - \Delta E/(JN), E/(JN) + \Delta E/(JN)]$ with $E/(JN) = 0.5$ and $\Delta E/(JN) = 0.1$.

To study the fluctuations of an observable around the microcanonical expectation value, we consider the deviation of its eigenstate expectation value,

$$\Delta^{mic}\mathcal{O} = \frac{\sum_\alpha |\mathcal{O}_{\alpha\alpha} - \mathcal{O}_{mic}|}{\sum_\alpha \mathcal{O}_{\alpha\alpha}}, \tag{6.17}$$

with respect to the microcanonical result,

$$\mathcal{O}_{mic} = \frac{1}{\mathcal{N}}_{E,\Delta E} \sum_{\substack{\alpha, \\ |E-E_\alpha|<\Delta E}} \mathcal{O}_{\alpha\alpha}, \tag{6.18}$$

where $\mathcal{N}_{E,\Delta E}$ is the number of energy eigenstates with energy in the window $\Delta E$. We also study the normalized extremal fluctuation [184],

$$\Delta_e^{mic}\mathcal{O} = |\frac{\max \mathcal{O} - \min \mathcal{O}}{\mathcal{O}_{mic}}|, \tag{6.19}$$

where $\max \mathcal{O}$ and $\min \mathcal{O}$ are the maximum and minimum values of $\mathcal{O}_{\alpha\alpha}$. In Fig. 6.10 (d) [Fig. 6.10 (e)], we present the results for $\Delta^{mic}N_1$ [$\Delta_e^{mic}N_1$] for eigenstates with $E/(JN) = 0.5$ in the window of width $\Delta E/(JN) = 0.1$. The results for $(N_2)_{\alpha\alpha}$ and $(N_3)_{\alpha\alpha}$ are similar (not shown).

Figures 6.10 (d)-(e) are analogous to Fig. 6.4. They show that the smallest fluctuations of the eigenstate expectation values happen in the vicinity of $\epsilon/J \sim 1.5$, where the chaos indicator $\beta$ is also the largest . The fluctuations increase as the system approaches both integrable limits, as $\epsilon/J \to 0$ (Bethe ansatz) and as $\epsilon/J \to \infty$ (self-trapping).

At a fixed value of $\epsilon/J$, one sees that $\Delta^{mic}N_1$ in Fig. 6.10 (d) decreases slightly as the total number of particles increases. A discussion of how $\Delta^{mic}\mathcal{O}$ scales with the dimension $D$ of the Hilbert for the triple-well Bose-Hubbard model is provided in Ref. [23], where it is found that the scaling does not follow expectations consistent with fully chaotic eigenstates. Similarly to our analysis of Fig. 6.4, the results in Fig. 6.10 (d) suggest that the reduction of the fluctuations for larger $N$'s is caused by better statistics, not necessarily improved levels of chaos. Contrary to multi-well systems, our model is limited to three degrees of freedom.

Our results for the extremal fluctuations in Fig. 6.10 (e) add to the above discussion. We see that $\Delta_e^{mic}N_1$ does not decrease as $N$ increases. This contrasts with the case of interacting many-body quantum systems with many sites, where the extremal fluctuations do decrease as the number of particles and wells increase. The extremal fluctuation is a more rigorous test of the validity of the ETH [184], and by extension of the degree of quantum chaos.

### 6.5.2 Off-diagonal elements

The strongest signatures of quantum chaos for our triple-well model happen for $\epsilon/J \sim 1.5$, but the results for level statistics [Fig. 6.4], structure of the eigenstates [Fig. 6.9], and extremal fluctuations [Fig. 6.10 (e)] indicate that even at this point, full chaos is not achieved. Here, we investigate how this saturated level of chaos, in particular the

non-Gaussian distribution of the eigenstates components in Fig. 6.9, gets reflected into the distribution of the off-diagonal elements of the number operators.

The off-diagonal elements of $\hat{N}_i$ is given by

$$\begin{aligned}\langle\alpha|\hat{N}_i|\beta\rangle &= \sum_{n=1}^{D} C_n^\alpha C_n^\beta \langle n|\hat{N}_i|n\rangle \\ &= \sum_{\substack{n=1 \\ \langle n|\hat{N}_i|n\rangle=1}}^{N} C_n^\alpha C_n^\beta + 2\sum_{\substack{n=1 \\ \langle n|\hat{N}_i|n\rangle=2}}^{N-1} C_n^\alpha C_n^\beta + \ldots + N\sum_{\substack{n=1 \\ \langle n|\hat{N}_i|n\rangle=N}}^{1} C_n^\alpha C_n^\beta.\end{aligned} \tag{6.20}$$

In the case of fully chaotic eigenstates, where $C_n^\alpha$'s are independent Gaussian random numbers, the distribution of $(N_i)_{\alpha\beta}$ should also be Gaussian. This is evident from the equation above. The product of independent random variables is again an independent random variable, and according to the central limit theorem, the sum of random variables from any distribution follows a Gaussian distribution.

In Fig. 6.11, we show the distribution of the number operator of well 1 (for equivalent results for wells 2 and 3, see the Suppl. Material 6.7.6.) As the integrability term $\epsilon/J$ increases from zero [Fig. 6.11 (a)] to 1.5 [Figs. 6.11 (c)], the peak at $(N_1)_{\alpha\beta}/N \sim 0$ decreases and the distribution gets more similar to a Gaussian, although this shape is never achieved, independently of the number of particles.

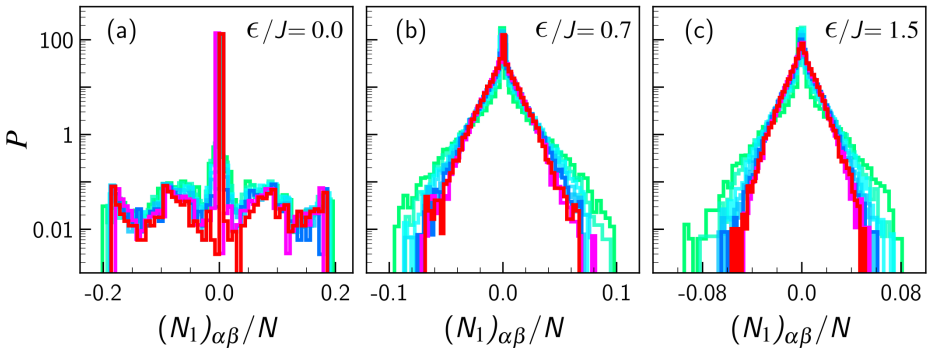


Figure 6.11: Distributions of the off-diagonal elements of the number operator of well 1, $\langle\alpha|\hat{N}_1|\beta\rangle$, for 300 eigenstates with energy $E/(JN) \sim 0.5$. The value of the integrability breaking parameter is indicated in the panels. The distributions are shown for different numbers of particles, $N = 60$ (green) to $N = 270$ (red) in increments of 30.

In Fig. 6.12 (a), we select only the curve for $N = 270$ from Fig. 6.11 (c) and show that its best fit is a Laplace distribution. Some explanations are now in order. The Laplace distribution (more precisely, a modified Bessel function of the second kind) describes the off-diagonal elements of single-particle eigenstates in chaotic quadratic Hamiltonians [187]. In this case, $N = 1$ and the only term that survives in Eq. (6.20) is the last one. This term is a single product of two Gaussian random variables, whose

distribution is indeed Laplace. Our scenario is completely different from this one, since in Eq. (6.20), we have large sums of the products $C_n^\alpha C_n^\beta$.

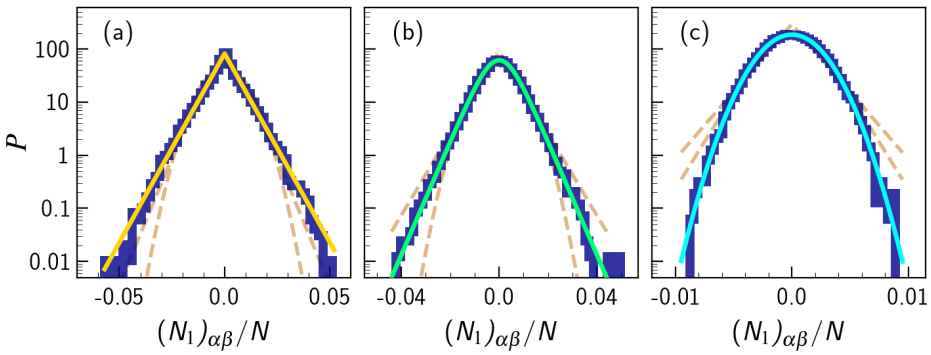


Figure 6.12: Distributions of the off-diagonal elements of the number operator of well 1, $\langle\alpha|\hat{N}_1|\beta\rangle$, for 300 eigenstates with $E/(JN) \sim 0.5$, $N = 270$, $\epsilon/J = 1.5$. The solid line indicates the best fit: (a) Laplace, (b) Logistic, and (c) Gaussian distribution. In (a), just as in Fig. 6.11 (c), all the components $C_n^\alpha$ of the eigenstates are considered. In (b), only those components for which $0.25 \leq e_n/J \leq 0.7$ are taken into account. In (c), the components are those from Gaussian random vectors.

Similar to our analysis in Fig. 6.9, a closer study of Fig. 6.12 (a) reveals that the peak at $(N_1)_{\alpha\beta}/N \sim 0$ is caused by the Fock states with energies outside the chaotic region. By removing the contributions from the states with $e_n/J < 0.25$ and $e_n/J > 0.75$, the distribution of $(N_1)_{\alpha\beta}$ becomes Logistic, as seen in Fig. 6.12 (b), which is closer but not yet Gaussian. If, however, we calculate Eq. (6.20) using eigenstates from GOE random matrices, then we finally reach the Gaussian shape, as expected from the central limit theorem and as illustrated in Fig. 6.12 (c).

The study of the off-diagonal elements corroborates our claims that the triple-well model in Eq. (6.1) do not have fully chaotic eigenstates. The same holds for the triple-well Bose-Hubbard models presented in the Suppl. Material 6.7.1, where the distributions of the off-diagonal elements of the number operators are not Gaussian either.

## 6.6 Discussion

We investigated the spectrum, eigenstates, and occupation numbers of an integrable bosonic triple-well model that becomes chaotic with the addition of a external potential. The analysis of the structure of the eigenstates shows that for values of the tilt where chaos emerges, there are still regions of energy where the system remains non-chaotic. Furthermore, even within the energy interval of chaos, the eigenstates are not fully chaotic (ergodic), that is, their components do not follow Gaussian distributions and the generalized dimensions are smaller than 1, which suggest reminiscences of correlations.

Diagonal and off-diagonal ETH, which are other good indicators of the level of chaoticity of a many-body quantum system, were also not entirely fulfilled by our

model.

Studies of the eigenstates and off-diagonal elements of observables can reveal details about quantum systems that are not always easily accessible from a direct study of their eigenvalues. In our specific case, the analysis of the eigenstates and observables shows that three wells constitute the preface for many-body quantum chaos.

A natural extension of this work is to examine how our results change by increasing the number of wells, specially the four-well model presented in Chapters 4 and 5, the role played by the geometry of the system, and the addition of nonlinear terms [64] or external drives [188, 189].

## 6.7 Supplementary Material

### 6.7.1 Bose-Hubbard Models

Bose-Hubbard models describe interacting spinless bosons on a discrete lattice [7] and are experimentally implemented with ultracold atoms in optical lattices [8]. In the case of three wells, the bare Bose-Hubbard model is represented by the Hamiltonian

$$\begin{aligned}\hat{H} =& \frac{U_0}{N}\left(\hat{N}_1\left(\hat{N}_1-1\right)+\hat{N}_2\left(\hat{N}_2-1\right)+\hat{N}_3\left(\hat{N}_3-1\right)\right)\\ &+\frac{J}{\sqrt{2}}\left(\hat{a}_1^\dagger\hat{a}_2+\hat{a}_2^\dagger\hat{a}_1\right)+\frac{J}{\sqrt{2}}\left(\hat{a}_2^\dagger\hat{a}_3+\hat{a}_3^\dagger\hat{a}_2\right),\end{aligned} \tag{6.21}$$

where $U_0$ is the onsite interaction, $J$ is the hopping (tunneling) parameter, and $N = N_1 + N_2 + N_3$ is the total number of particles.

This system presents signatures of quantum chaos when the number $L$ of wells coincides with the number particles, $L = N \geq 5$ [17]. However, as shown in [23], the model is also chaotic for only 3 sites and $N \gg 3$. Notice that the Hamiltonian has parity symmetry, so to study level statistics, one should either break this symmetry, as done in [23], or separate the eigenvalues by symmetry sector. An alternative is to resort to the correlation hole, which detects level repulsion even in the presence of symmetries [162, 169].

The extended version of the Bose-Hubbard model,

$$\begin{aligned}\hat{H} =& \frac{U_0}{N}\left(\hat{N}_1\left(\hat{N}_1-1\right)+\hat{N}_2\left(\hat{N}_2-1\right)+\hat{N}_3\left(\hat{N}_3-1\right)\right)\\ &+\frac{U_1}{N}\left(\hat{N}_1\hat{N}_2+\hat{N}_2\hat{N}_3+\frac{1}{\alpha}(\hat{N}_1\hat{N}_3)\right)\\ &+\frac{J}{\sqrt{2}}\left(\hat{a}_1^\dagger\hat{a}_2+\hat{a}_2^\dagger\hat{a}_1\right)+\frac{J}{\sqrt{2}}\left(\hat{a}_2^\dagger\hat{a}_3+\hat{a}_3^\dagger\hat{a}_2\right),\end{aligned} \tag{6.22}$$

includes also interactions between the wells, which emerge in dipolar gases. As discussed in [37], the parameter $\alpha$ depends on the geometry of the trap and can vary between $4 \leq \alpha \leq 8$. The extended Bose-Hubbard model also has parity symmetry through exchange of wells 1 and 3. Depending on the choices of parameters and with some rearrangement of the signs, Eq. (6.22) coincides with the Hamiltonian of our model in Eq. (6.1) in the integrable limit.

In Fig. 6.13, we show the DOS for the two Bose-Hubbard models above for parameters that lead to approximate Wigner-Dyson distributions. For $N = 180$ and the positive parity sector, we get Brody factors $\beta \approx 0.8$. Figure 6.13 can be compared with the DOS for the chaotic triple-well model with the external tilt in Fig. 6.3 (c). None of the distributions, that in Fig. 6.3 (c) or the ones in Fig. 6.13, have a Gaussian shape.

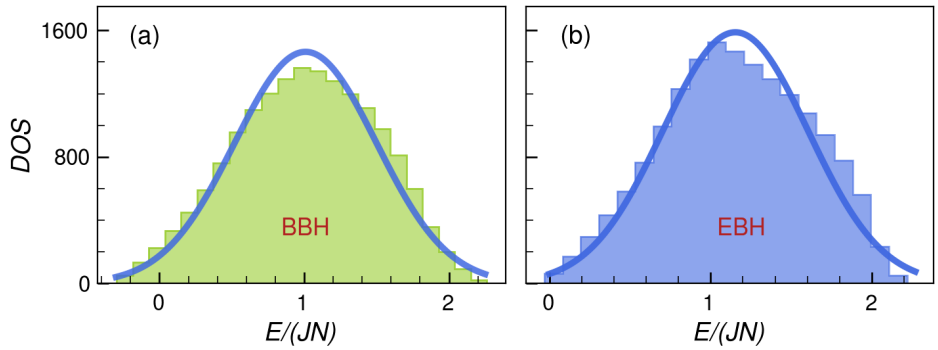


Figure 6.13: Density of states for (a) the bare Bose-Hubbard model from Eq. (6.21) and (b) the extended Bose-Hubbard model from Eq. (6.22). All eigenvalues from both symmetry sectors are considered; $N = 180$. The parameters used lead to Wigner-Dyson distributions: (a) $U_0/J = 2.03$, (b) $U_0/J = 1.85$, $U_1/J = 1.2$ and $\alpha = 2\sqrt{2}$. The solid lines are Gaussian fits.

In Fig. 6.14, we show results for the Shannon entropy, components of the eigenstates, and off-diagonal elements of $\hat{N}_1$ for both Bose-Hubbard models in the chaotic domain. The plot for the Shannon entropy in Fig. 6.14 (a), and Fig. 6.14 (d) can be compared with Fig. 6.6. Similarly to our model, the Bose-Hubbard models present a region of energy away from the edges of the spectrum where the entropy is larger and has smaller fluctuations. As we move closer to borders of the spectrum, a pattern of regular lines similar to those in Fig. 6.6 appear.

We studied the distributions of the components of various eigenstates in the chaotic region of the spectrum, with energy $E/(JN) \sim 1$ [$E/(JN) \sim 1.4$] for the bare Bose-Hubbard model [extended Bose-Hubbard model]. In most cases, the best fit is a Logistic distribution, as illustrated in Fig. 6.14 (b) [Fig. 6.14 (e)]. For the Bose-Hubbard models, we do not find an excessive number of $C_n^\alpha \sim 0$ as in Fig. 6.9 (a), but the tails are still longer than in Gaussian distributions.

The lack of gaussianity of the eigenstates result in the non-Gaussian distributions of the off-diagonal elements of the number operators. This is illustrated in Fig. 6.14 (c) and Fig. 6.14 (f) for $\hat{N}_1$. Contrary to Fig. 6.12, none of the usual distributions, Laplace, Logistic, Gaussian, or Lorentzian, capture well the histogram for $(N_1)_{\alpha\beta}$.

### 6.7.2 Additional results for our triple-well model

We leave to this Suppl. Materail some further details about our triple-well model. This includes the dependence of the timescales of the spectral form factor on $N$, a plot for the participation ratio, and the distributions of off-diagonal elements for the number operators of the three wells.

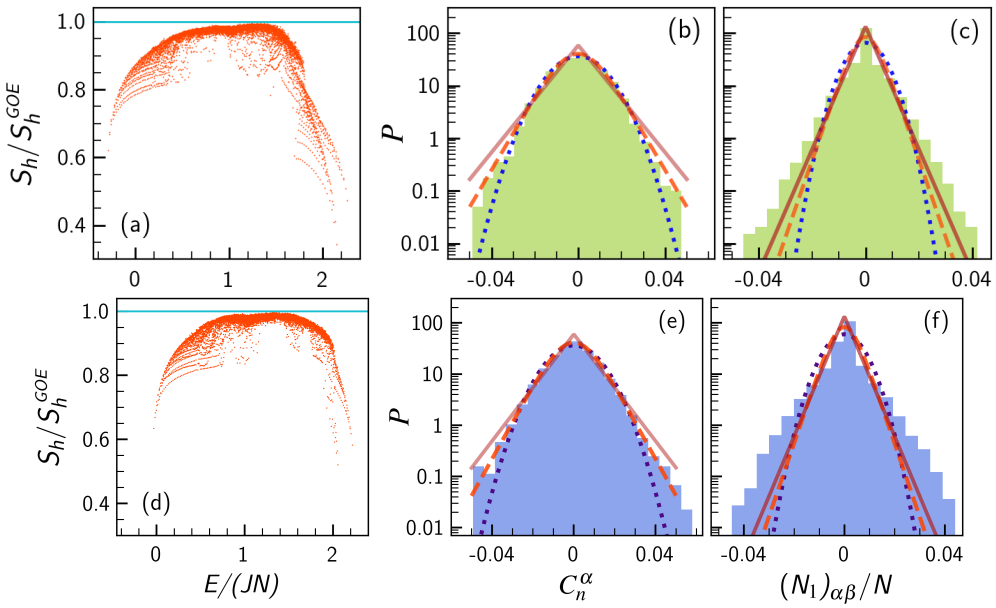


Figure 6.14: Shannon entropy (a,d), distribution of the components of an eigenstate in the chaotic region (b,e), and distribution of the off-diagonal elements of the number operator of well 1 (c,f) for the bare Bose-Hubbard model (a)-(c) and the extended Bose-Hubbard model (d)-(f) in the positive parity sector; $N = 180$. The parameters are the same as in Fig. 6.13. In (a,d): Solid line indicates the result for random matrix theory. In (b,c,e,f): Solid line represents the Laplace; dashed line, the Logistic; and dotted line, the Gaussian distribution. The best fit in (b) and (e) is the Logistic distribution. In (b), $E/(JN) = 1.16$ and in (e), $E/(JN) = 1.33$.

### Timescales for the spectral form factor

The time $t_{\min}$ to reach the minimum of the correlation hole and the time for the saturation of the spectral form factor (Heisenberg time) can be derived using the analytical expression in Eq. (6.7).

### Time for the minimum of the correlation hole

To determine the time $t_{\min}$, we consider the envelope of the initial oscillatory decay, $\sin^2(\sigma t) \to 1$, (the choice $\sin^2(\sigma t) \to 1/2$ would also be suitable) and use the expression of the function $b_2(t/(2\pi\nu_c))$ for short times, $t \leq 2\pi\nu_c$. The latter is justified, because the minimum of $S_{FF}(t)$ is the point where the function $[\eta \sin^2(\sigma t)]/(\sigma t)^2$, that causes the decay of the spectral form factor, meets the $b_2(t/(2\pi\nu_c))$ function, which is responsible for bringing $S_{FF}(t)$ up to saturation. The time is then obtained from

$$\frac{dS_{FF}^{analyt}}{dt} = 0 \tag{6.23}$$

$$\frac{4\eta}{\sigma^2 t_{\min}^3} = \frac{1}{\pi\nu_c} + \frac{1}{\pi\nu_c(1+\frac{t_{\min}}{\pi\nu_c})} - \frac{\ln\left(1+\frac{t_{\min}}{\pi\nu_c}\right)}{\pi\nu_c},$$

which can be solved numerically to determine $t_{\min}$. By expanding the equation above, using $t_{\min} \ll \pi\nu_c$, we get that

$$t_{\min} = \left(\frac{2\pi\nu_c\eta}{\sigma^2}\right)^{1/3} = \left(\frac{16\pi}{9\langle\overline{S_{FF}}\rangle^2\sigma^3}\right)^{1/3}. \tag{6.24}$$

Since $\langle\overline{S_{FF}}\rangle$ scales with the inverse of the dimension of the Hilbert space, that is $\langle\overline{S_{FF}}\rangle \propto N^{-2}$, and $\sigma \propto N$, we have that $t_{\min}$ grows with the number of particles as

$$t_{\min} \propto N^{1/3}. \tag{6.25}$$

This is confirmed numerically for all $N$'s considered here, as indicated by the values of $t_{\min}$ marked with circles in Fig. 6.5.

### Saturation time

The saturation time, $t_{\rm S}$, corresponds to the time when $S_{FF}(t)$ reaches its infinite-time average $\langle\overline{S_{FF}}\rangle$. At these very long times, only the $b_2$ function is relevant, and since it shows a power-law behavior, $b_2\left(\frac{t}{2\pi\nu_c}\right) \to \frac{\pi^2\nu_c^2}{3t^2}$, the complete saturation is not well determined [175]. We define $t_{\rm S}$ as the moment when $S_{FF}(t_{\rm S}) = (1-\delta)\langle\overline{S_{FF}}\rangle$, where $\delta$ is a small value that guarantees that $S_{FF}(t)$ is already within the fluctuations around the infinite-time average. This gives

$$\frac{t_{\rm S}}{2\pi\nu_c}\ln\left(\frac{t_{\rm S}/\pi\nu_c+1}{t_{\rm S}/\pi\nu_c-1}\right) = \delta\frac{(\eta-1)\langle\overline{S_{FF}}\rangle}{1-\langle\overline{S_{FF}}\rangle} + 1 \tag{6.26}$$

and using that $t_{\rm S} \gg \pi\nu_c$, we arrive at

$$t_{\rm S} = \frac{\pi\nu_c}{2\sqrt{\delta}} \propto N, \tag{6.27}$$

which shows that the saturation time grows linearly with $N$, as confirmed in Fig. 6.5, where $t_{\rm S}$ is marked with diamonds.

It is instructive to compare $t_{\min}$ and $t_{\rm S}$ for our model with the same timescales for the Dicke model [173], which has two degrees of freedom, and for the one-dimensional disordered spin-1/2 model with many excitations [175], which has many degrees of freedom and a Hilbert space that grows exponentially with the number of sites. While for our model and the Dicke model, $t_{\min}$ scales with the number of particles as $N^{1/3}$ and $N^{1/2}$, respectively, and $t_{\rm S} \propto N$, for the interacting many-body spin system, $t_{\min}$ grows with the size of the Hilbert space as $D^{2/3}$ and $t_{\rm R} \propto D$. Based on these timescales, it might be possible to detect the correlation hole experimentally with the triple-well

model, but more unlikely to get this done with many-body systems with many sites and short-range couplings.

### 6.7.3 Participation ratio in the Fock basis

We show in Fig. 6.15 the participation ratio obtained for eigenstates written in the Fock basis and divided by the result for GOE random matrices, $P_R^{\rm GOE} \sim D/3$. In comparison to the results for the Shannon entropy presented in Fig. 6.6, we see that the fluctuations are larger for the participation ratio.

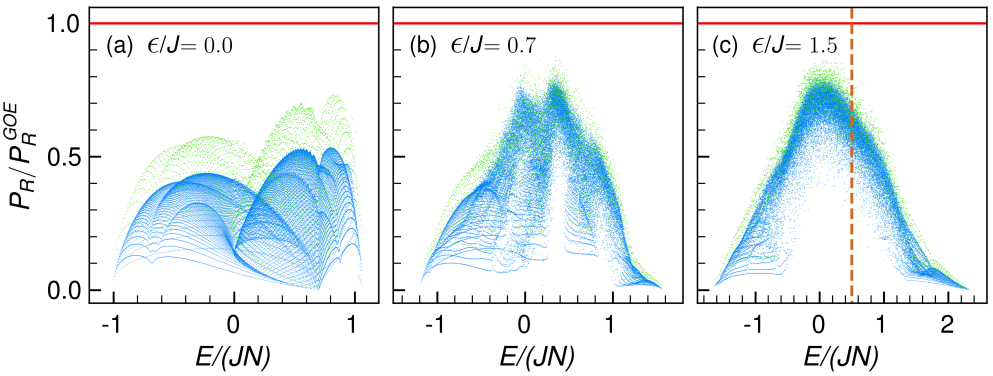


Figure 6.15: Participation ratio as a function of energy for $N = 90$ (light green dots) and $N = 270$ (blue dots). The solid horizontal lines mark the results for GOE random matrices. The dashed vertical line in (c) marks approximately the center of the chaotic region.

The fluctuations decrease as the system moves from the integrable limit of Fig. 6.15 (a) to the chaotic domain of Fig. 6.15 (c), but even for $\epsilon = 1.5$, we still find regions closer to the edges of the spectrum with patterns of lines similar to those found in the regular regime. In addition, the participation ratio is throughout smaller than $P_R^{\rm GOE}$ and this does not improve as $N$ increases [cf. $N = 270$ (dark dots) with $N = 90$ (light dots)].

### 6.7.4 Shannon entropy in the zero-detuning basis

When computing delocalization measures, the results depend on the basis used. The basis choice is done according to the question under investigation. Our studies of ETH focus on the occupations of each well, which are observables measured in cold atoms. It is therefore natural to perform the analysis of the eigenstates in a basis, where $\hat{N}_i$ is diagonal, that is, in the Fock basis $|n\rangle$, as done in Sec. IV. In studies of the transition to chaos, however, the most appropriate basis corresponds to the eigenstates of the integrable part of the model considered. In our case, this basis coincides with the eigenstates $|\phi\rangle$ of the Hamiltonian in Eq. (6.1) with zero detuning ($\epsilon = 0$).

The purpose of Fig. 6.16 is to compare the Shannon entropy calculated in the Fock basis $|n\rangle$ in Fig. 6.6 (b) and Fig. 6.6 (c) [light points in Fig. 6.16 (a) and Fig. 6.16 (b)]

with the Shannon entropy computed in the zero-detuning basis $|\phi\rangle$ [dark points in Fig. 6.16 (a) and Fig. 6.16 (b)]. The data show that using this zero-detuning basis does not qualitatively change the results for $\epsilon/J = 0.7$ and $\epsilon/J = 1.5$. For $\epsilon/J = 0.7$ in Fig. 6.16 (a), patches of high degrees of delocalization appear for both bases for $E/(JN) \sim 0.3$ and $E/(JN) \sim 0.9$; and for $\epsilon/J = 1.5$ in Fig. 6.16 (b), the chaotic region is evident for both bases for $E/(JN) \in [-0.2, 1]$.

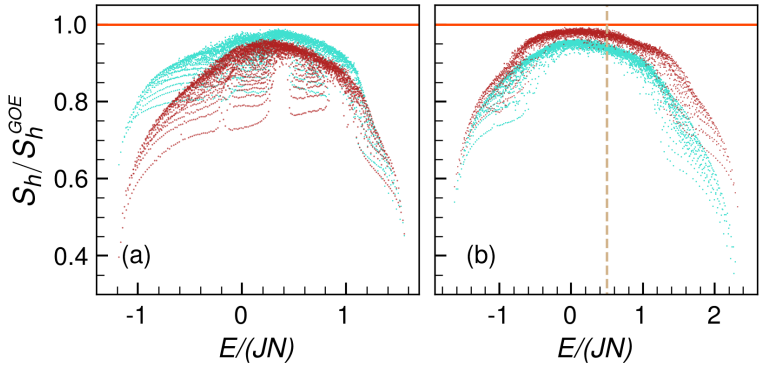


Figure 6.16: Shannon entropy $S_h$ in the Fock basis (light dots, as in Fig. 6.6) and in the zero-detuning basis (dark dots) as a function of energy for $N = 90$, $U/J = 0.7$, and $\epsilon/J = 0.7$ (a) [$\epsilon/J = 1.5$ (b)]. The solid horizontal lines mark the results for GOE full random matrices. The dashed vertical line in (b) marks approximately the center of the chaotic region.

If we compare the value of $S_h/S_h^{\rm GOE}$ as a function of $\epsilon/J$, from $\epsilon = 0$ to $\epsilon/J = 1.5$, it grows dramatically for the zero-detuning basis, since in this case, $S_h^{|\phi\rangle}(\epsilon = 0) = 0$. One also notices that $S_h^{(|\phi\rangle)}(\epsilon = 1.5)/S_h^{\rm GOE}$ reaches values closer to 1 for the zero-detunig basis than $S_h^{(|n\rangle)}(\epsilon = 1.5)/S_h^{\rm GOE}$ for the Fock basis. But the overall structure of the eigenstates for $\epsilon/J$ in the chaotic region does not change much from one basis to the other, as suggested by Fig. 6.16 and by the results below in Fig. 6.17.

### 6.7.5 Distribution of the components of the eigenstates in the zero-detuning basis

The distributions of all the components of an eigenstate written in the zero-detuning basis and having energy close to the middle of the chaotic region is given in Fig. 6.17 (a). In contrast with the case of the Fock basis presented in Fig. 6.9 (a), here we did not find an excessive number of zero valued components. Yet, in Fig. 6.17 (b), we follow the same procedure used in Fig. 6.9 (b) and kept only the components associated with states that have energy in $[-0.2, 1]$. With that, the small central peak in Fig. 6.17 (a) is erased.

Similarly to what is observed in Fig. 6.9 (b), the best fit in Fig. 6.17 (b) [and even in Fig. 6.17 (a)] is again Logistic instead of Gaussian. This indicates that the eigenstates

of our triple-well model written in the zero-detuning basis, just as in the Fock basis, are not ergodic.

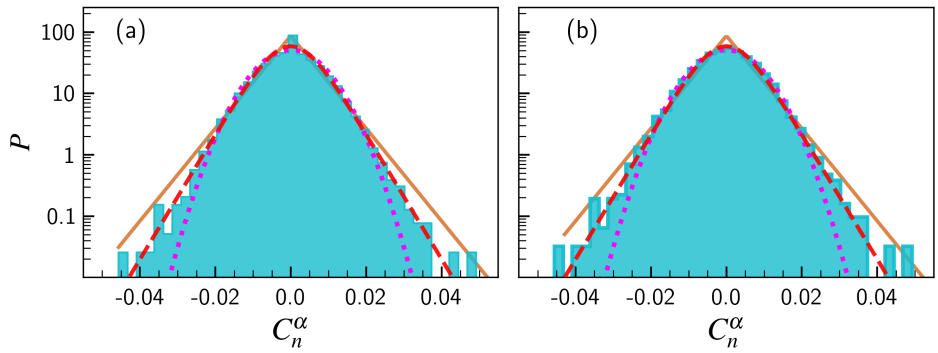


Figure 6.17: Distributions of the components $C_n^\alpha$ of an eigenstate with energy $E/(JN) \sim 0.5$; $N = 180$, $U/J = 0.7$ and $\epsilon/J = 1.5$. In (a), all components are considered, while in (b), only those for states with energy in $[-0.2, 1]$ are kept. Solid line: Laplace distribution; dashed line: Logistic distribution; dotted line: Gaussian distribution.

### 6.7.6 Distributions of off-diagonal elements

In the main text, we show the distribution of the off-diagonal elements of the number operators of well 1 in Fig. 6.12 (a). Here, we repeat this figure in Fig. 6.18 (a), but show also the distributions of the off-diagonal elements of the number operators of well 2 (b) and 3 (c) in comparison with Laplace, Logistic, and Gaussian distributions. The best fit for the three observables is the Laplace distribution.

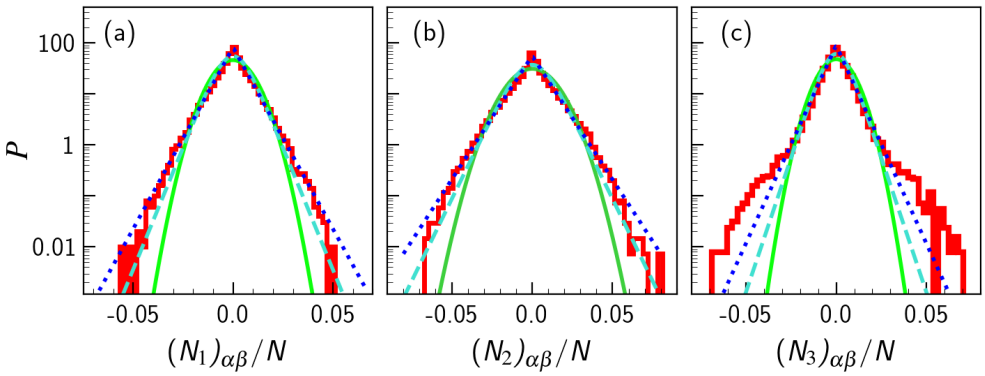


Figure 6.18: Distributions of the off-diagonal elements of (a) $\hat{N}_1$, (b) $\hat{N}_2$, and (c) $\hat{N}_3$ for 300 eigenstates with energy $E/(JN) \sim 0.5$; $N = 270$, $U/J = 0.7$ and $\epsilon/J = 1.5$. The fitting curves correspond to Laplace (dashed line), Logistic (dashed line) and Gaussian (solid line) distributions.

# Chapter 7

# Conclusions and Outlook

We have studied models of dipolar bosons confined to 3 and 4 wells. The analysis considered both integrable and non-integrable regimes within the models. Through variation of the external field, we demonstrated how the triple-well system can be controlled between various "switched-on" and "switched-off" configurations. A discussion about the generation of entanglement in this system was also presented. Then we investigated the four-well model, revealing how the system can become a natural high-sensitivity interferometer; in addition, we presented protocols to produce and encode phases into a NOON state. The physical feasibility was also discussed for both systems through configurations of ultracold dipole atoms arranged in optical potentials. Finally, we return to the three-well model to investigate many-body quantum chaos. We show that the three-well system does not have a fully chaotic structure. A more specific summary of what was investigated in this thesis is presented below, by chapter.

In Chapter 2 we studied the triple well model. In it's integrable setting, we first identified the resonant tunneling regime between the source and drain, for which expectation values of particle numbers in the gate are negligible. Moreover, it was found that a conserved operator of the integrable system acts as an effective Hamiltonian, which predicts coherent oscillations. This is in agreement with observations from numerical calculations. We then broke integrability through application of an external field to the source and the drain. It was shown in Fig. 2.5 that the applied field, in the resonant regime, did not destroy the harmonic nature of the oscillations, but did influence the amplitude and frequency. Increasing the applied field allowed for tuning the system from the switched-on configuration through to switched-off (Fig. 2.6). Results from semiclassical analyses produced formulae for the amplitude and frequency, which proved to be remarkably accurate when compared to numerical calculations. This demonstrates the possibility to reliably control the harmonic dynamical behavior of the model in certain regimes, turning this device into a very promising atomtronic *building*

*block* for future applications in quantum technologies. A surprising feature of this result is that the ability to control the system in a predictable manner arises through the breaking of integrability.

In Chapter 3 we analysed the capacity for entanglement generation in the three-well atomtronic device obtained in the resonant tunneling regime, where the particle exchange between wells 1 and 3 is very well described as coherent oscillation. We considered a larger class of non-entangled initial states that still belong to the resonant regime, and studied the quantum evolution. We conducted calculations of population expectation values, quantum fluctuations, and entanglement. We found that the maximum entanglement occurred when the expectation values for populations in wells 1 and 3 are equal, where also their variances are maximal. For this study, a more general effective Hamiltonian was constructed, also expressed in terms of the conserved operator for the integrable system, which allowed us to obtain analytic formulae for the evolution of the states, that may be useful for future studies of both flow and entanglement control.

In Chapter 4 we have provided an example of integrable atomtronic interferometry, through an integrable model with four sites arranged in a closed square. The integrable properties of the model furnished the necessary tools to understand the dynamics of the system in the resonant tunneling regime. It allowed for the analytic calculation of dynamical expectation values and correlation functions heralding NOON state formation. This, in turn, informed the relevant time interval required to implement certain measurement protocols. The probabilities for measurement outcomes were computed via the density matrix. We demonstrated proof of principle examples that the integrable four-well system functions as an identifier of NOON states produced by a black box processor, and as a simulator of such a processor.

In Chapter 5 we have addressed the challenging problem of designing protocols to facilitate NOON state creation. Our approach employed dipolar atoms confined to four sites of an optical superlattice. The insights gained from integrability allowed us to develop two protocols, that are based on the formation of an uber-NOON state en route to the final state. Protocol I employs a local measurement procedure to produce NOON states over a shorter time than Protocol II. However Protocol I is probabilistic, requiring post-selection on the measurement outcome. This is in contrast to the deterministic approach of Protocol II. For both protocols, phase-encoding is performed by breaking the system's integrability. And in both protocols, the output states were shown to have high-fidelity in numerical simulations. We also identified a readout scheme that allows verification of NOON state production through measurement statistics. The

approaches we have described have two significant advantages. One is that the evolution time does not scale with the total number of particles. The other advantage is that all measurements are made in the local Fock-state basis. We conducted an analysis of the feasibility of a physical proposal, providing realistic values for the Hamiltonian parameters. We also analyze the robustness of the system in response to perturbations.

In Chapter 6 we investigated the spectrum, eigenstates, and occupation numbers of the integrable bosonic triple-well model that becomes chaotic with the addition of a tilting potential, which breaks the integrability of the Hamiltonian. The analysis of the structure of the eigenstates shows that for values of the breaking parameter where chaos emerges, there are still regions of energy where the system remains non-chaotic. Furthermore, even within the energy interval of chaos, the eigenstates are not fully chaotic (ergodic), and indicate reminiscences of correlations. We also analyze the system through diagonal and off-diagonal ETH and neither of the two criteria are entirely fulfilled by our model. In our specific case, the analysis of eigenstates and observables shows that three wells (1D) constitute the preface to many-body quantum chaos.

While the results obtained for the three-well model open possibilities for multi-level logic applications, with entanglement control through an external field, the protocols designed for the four-well model highlight the quantum information connections of the model by detailing its function as a hybrid qudit system subjected to a controlled-phase gate operation. This description complements other qudit studies in photonic [190–192] and NMR [193] settings, which are attracting attention due to the promise of increasing quantum computational capacity. It is anticipated that our results, in an atomtronic framework, may be transferable to these and other contexts. By establishing a link between integrability and quantum technologies, this work promotes advances in the field of neutral-atom quantum information processing. Both the switching device and the NOON interferometric device may be considered building blocks for ultracold atomic technologies.

*Current research topics:* The three-well model is very rich, still exhibiting properties worth being explored. Among them, two directions are being investigated. One of these is related to grasping the mechanisms for controlling the entanglement generation through the application of external fields. The other is the understanding of the chaotic behavior from the perspective of quantum dynamics and of a quantum-classical correspondence. Regarding the four-well model, we are investigating a different integrable geometric configuration, the open 3+1 system (See Fig. 1.2(c) and Fig. B.2(a)). It has

the potential to generate identical parallel outputs, create chiral currents, design directional switches [194], and simulate some molecules [195, 196], among other possibilities that deserve to be examined.

*Future research topics:* In future research, we will undertake studies involving the effects of external drivings in the dynamics of both systems, which is feasible using Floquet theory, e.g. see [197]. It is also possible to carry out investigations in search of other quantum states that may be useful for metrological applications, such as coherent states and Dicke states, among others. Another natural extension of the thesis is to examine how chaos indicators vary with an increasing number of wells, with the system geometry, the addition of non-linear terms [64], or external drives [188, 189]. Besides, the multi-well model offers several other configurations worth being investigated, especially focusing on the possibility of generating other quantum devices. A challenging question in this scenario is to prospect the formation of quantum circuits.

# Appendix A

# Quantum Integrability: a brief discussion

We bring here some discussions about quantum integrability that may complement the subject of this thesis. The approach certainly does not contemplate the full scope of the issue.

The notion of integrability in physics originated in the former studies of classical mechanics. One of the most powerful classical concepts is Liouville's (Liouville–Arnold)[198] theorem about integrable systems[199]. In 1853, Liouville proved that if, "in a system with $n$ degrees of freedom (i.e., with a 2n-dimensional phase space), $n$ first independent integrals in involution (i.e., Poisson commutation, $\{H, F\} = 0$ ) are known, then the system is quadrature integrable[1]." In this case, the solutions of the equations of motion (using action angle variables), "exhibit periodic tori motion in phase space, and ergodicity is absent, in contrast to non-integrable models that explore phase space densely over time." [14, 200]

Transferring classical definitions to quantum Hamiltonian systems is an intriguing question that has long been investigated [14]. The problem arises mainly due to the number of degrees of freedom which, for quantum systems, is generally a finite (discrete) Hilbert space dimension; whereas classically the degrees of freedom are continuous variables. One of the first to realize the difficulty of connecting classical-quantum processes was Einstein, around 1917 when studying a generalization of the Bohr, Sommerfeld, and Epstein quantization rule, which was valid only for separable coordinate systems. Einstein showed how to quantize non-separable systems, provided they have as many independent constants of motion (first integrals of motion) as there were degrees of freedom. These systems came to be called *integrable*. In his study of integrable models,

[1]Integration by quadrature means solving an integral analytically (i.e., symbolically in terms of known functions). From https://mathworld.wolfram.com/Quadrature.html

Einstein observed that in the case of non-integrable systems, the transition from classical to quantum methods is not trivial as in the integrable case. This observation made him one of the pioneers of quantum chaos. The quantum-classical incompatibility of chaotic systems is a subject still under investigation, as is quantum chaos itself, and has its own field of research [201].

The quantization problem was facilitated with the emergence of Schrödinger's equation, which treats the quantization as an eigenvalue problem, through a Hamiltonian operator. Schrödinger presented exact solutions, especially for systems of one particle in the presence of a potential, such as the non-relativistic hydrogen atom. However, when the number of particles is very large, the system needs to be manipulated by statistical mechanics, where an average of the properties of an ensemble of initially identical systems is calculated. In this case, integrable systems present a conserved density in the temporal evolution (flow) of this ensemble (Liouville's Theorem [202]).

In 1931, Hans Bethe presented a new method for finding exact eigenvalues and eigenvectors for physical many-body systems. The method, known as Bethe ansatz in its coordinated form, was formulated by Bethe to solve the one-dimensional (1D) Heisenberg spin chain model [203] and was soon successfully extended to other models such as the Lieb-Liniger model[204, 205] (the 1D Bose gas with contact interactions), the 1D Fermi gas with contact interactions, the massive Thirring model, the Hubbard model, the Kondo model, and the Anderson impurity model, among many others, generating a new area in mathematical physics. Although Bethe's method is efficient in finding the exact spectrum of many-body (1+1) dimensional quantum models, the complicated structures of the eigenfunctions mainly made it difficult to calculate the correlation functions.

Subsequently, in 1979, Faddeev, Sklyanin, and Takhtadzhyan formulated the quantum method[206, 207] of the inverse scattering problem[2], which led to a generalized Bethe ansatz. In the Quantum Inverse Scattering Method (QISM), an algebraic version of the Bethe ansatz is developed, and a methodology for obtaining the solution of the models through the Yang–Baxter equation is proposed and discussed in detail[3]. This elegant and systematic method allows, in some cases, for the computation of correlation functions. The QISM has led the scientific community to a new understanding of quantum integrable systems. [4]. The method has been significantly improved, and

[2]The inverse scattering transform is a (semi-classical) method for solving some non-linear partial differential equations, which were first introduced by Clifford S. Gardner, John M. Greene, and Martin D. Kruskal et al. (1967, 1974) for the Korteweg–de Vries equation, and then extended to the nonlinear Schrödinger equation, the Sine-Gordon equation, and the Toda lattice equation. Wikipedia

[3]Notice that besides the coordinate and the algebraic Bethe Ansatz (BA), other variants of the BA, such as the analytical BA [208, 209] and the off-diagonal BA [210] also exist.

[4]It is worth mentioning that a precise definition of quantum integrability remains still an issue of discussion[14]

it has been extended to models from different areas of physics, which permeate statistical mechanics [211], quantum field theory [212, 213], condensed matter [214–216], atomic, molecular, and optical physics [217–220], AdS/CFT correspondence (anti-de Sitter spaces/conformal field theories)[221], in addition to ultracold atoms[127] and other systems where perturbative methods often fail. It is an incredibly potent method to deal with quantum integrable systems and it is basically the method that we employ (with some generalizations) in this thesis.

# Appendix B

# Integrable multi-well Hamiltonians

A general family of integrable multi-well Hamiltonians containing $n+m$ modes (wells) was introduced in [24] and is given by

$$H_{n,m} = U(N_A - N_B)^2 + \mu(N_A - N_B) + \Sigma_{i=1}^{n}\Sigma_{i=1}^{m} t_{i,j}(a_i b_j^\dagger + a_i^\dagger b_j), \tag{B.1}$$

where $N_A \equiv \sum_{i=1}^{n} N_{a,i}$ and $N_B \equiv \sum_{j=1}^{m} N_{b,j}$ represent the number of bosons in the wells of the subsets $A$ and $B$, $a_i, b_j$ are the canonical boson operators, $U$ is the intra-well and inter-well interaction between bosons, $\mu$ is the chemical potential and $t_{ij}$ are the constant couplings for the tunneling amplitude.

For each choice of $n, m$ we have an integrable tunneling model. To exemplify, we write below explicit Hamiltonians for some simple cases: 2 wells $(1,1)$, 3 wells $(2,1)$, and 4 wells $(2,2)$ and $(3,1)$, respectively

$$H_{1,1} = U(N_{a,1} - N_{b,1})^2 + \mu(N_{a,1} - N_{b,1}) + t_{1,1}(a_1 b_1^\dagger + a_1^\dagger b_1), \tag{B.2}$$

$$\begin{aligned} H_{2,1} = \; & U(N_{a,1} + N_{a,2} - N_{b,1})^2 + \mu(N_{a,1} + N_{a,2} - N_{b,1}) \\ & + t_{1,1}(a_1 b_1^\dagger + a_1^\dagger b_1) + t_{2,1}(a_2 b_1^\dagger + a_2^\dagger b_1), \end{aligned} \tag{B.3}$$

$$\begin{aligned} H_{2,2} = \; & U(N_{a,1} + N_{a,2} - N_{b,1} - N_{b,2})^2 + \mu(N_{a,1} + N_{a,2} - N_{b,1} - N_{b,2}) \\ & + t_{1,1}(a_1 b_1^\dagger + a_1^\dagger b_1) + t_{1,2}(a_1 b_2^\dagger + a_1^\dagger b_2) \\ & + t_{2,1}(a_2 b_1^\dagger + a_2^\dagger b_1) + t_{2,2}(a_2 b_2^\dagger + a_2^\dagger b_2) \end{aligned} \tag{B.4}$$

$$\begin{aligned} H_{3,1} = \; & U(N_{a,1} + N_{a,2} + N_{a,3} - N_{b,1})^2 + \mu(N_{a,1} + N_{a,2} + N_{a,3} - N_{b,1}) \\ & + t_{1,1}(a_1 b_1^\dagger + a_1^\dagger b_1) + t_{2,1}(a_2 b_1^\dagger + a_2^\dagger b_1) + t_{3,1}(a_3 b_1^\dagger + a_3^\dagger b_1) \end{aligned} \tag{B.5}$$

An interesting property of this family of integrable multi-well Hamiltonians is its bipartite structure. Here, we are considering a complete bipartite system which is characterized by a set of $(n+m)$ modes (wells), that can be divided into two subsets, such that each well in subset $A$ connects to all wells in subset $B$ and wells in the same subset do not connect to each other. These connections can be understood as the tunneling possibilities. Fig. B.1 shows a complete bipartite scheme for the case of $n = 4, m = 5$, as an example.

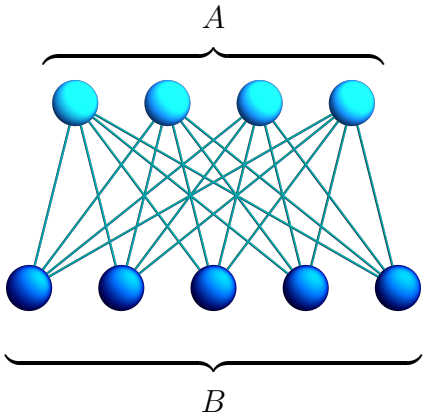


Figure B.1: A bipartite scheme for $(4+5)$ modes. The light blue circles represent the subset $A$ with $n = 4$ modes and the dark blue circles, the subset $B$ with $m = 5$ modes. The lines represent the connections (possibility of tunneling, in our case).

The long-range interaction (connection between subspaces) is guaranteed by dipole-dipole interaction (DDI). However, the DDI will also be perceived between atoms belonging to wells of the same subset, in addition to the interaction within the well. The integrability condition ($U_{13} = U_0$, for the 3-well case, and $U_{13} = U_{24} = U_0$ for the 4-well case) is responsible to neutralize this unwanted interaction, while allowing that $U_{12} = U_{14} = U_{23} = U_{34}$. These restrictions are closely associated with physical parameters, which have to be respected when designing the experimental models.

In Fig B.2, below, are shown the bipartite schemes for the open 4-well model and for two 5-well configurations, that will be investigated in the next stage of the research.

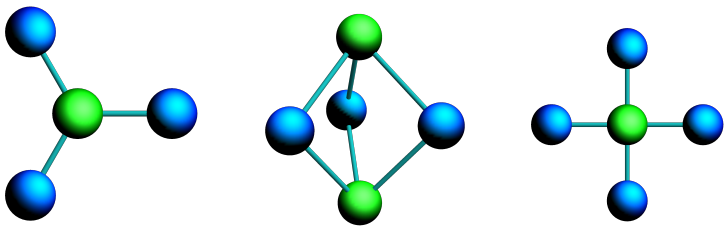

(a) (3,1) (b) (3,2) (c) (4,1)

Figure B.2: Schemes for some (n,m) bipartite geometries with 4 and 5 modes (wells). The blue spheres represent the subset $A$ and the green, the subset $B$. The lines represent the allowed tunnelings.

# Appendix C

# Experimental feasibility details for the triple-well model

Here we show how to implement the switching device model in a system of ultracold atoms trapped in optical potentials. The physical system of ultracold atoms is considered a standard realization for Bose-Hubbard models. The usual method for deriving the experimental Hamiltonian, consists of first writing a suitable second quantized Hamiltonian which describes a gas configuration of ultracold atoms at optical potential, and then approximating the wavefunction by $\Psi(\vec{r}) = \sum_{i=1}^{3} \phi_i(\vec{r})a_i$, where $\phi_i$ is a Wannier function located at the center of well $i$ for a single particle. For this, it is assumed that the energies involved are weak enough for the atom to be kept in the first band. The physical parameters are then obtained by following the procedure developed in [26, 37].

Special thanks to Leandro Ymai for this experimental discussion!

## The model

In order to discuss how to experimentally implement the triple-well switching device in a real lab and to provide numerical values of parameters for experimental setups in the cases of Chromium and Dysprosium we follow the main lines of the discussion presented in [26, 37]. The general Hamiltonian that takes into account all interactions (contact and dipole-dipole ones), the trap potential and the external field (for the breaking) is given by:

$$\begin{aligned} H =& \int d^3\vec{r}\,\Psi^\dagger(\vec{r})\left(H_0 + V_{break}(\vec{r})\right)\Psi(\vec{r}) + \frac{1}{2}\int d^3\vec{r}d^3\vec{r'}\Psi^\dagger(\vec{r})\Psi^\dagger(\vec{r'})V(\vec{r}-\vec{r'})\Psi(\vec{r'})\Psi(\vec{r}), \\ =& H_1 + H_2 + H_3, \end{aligned}$$

where

$$
\begin{aligned}
H_1 &= \int d^3\vec{r}\,\Psi^\dagger(\vec{r})H_0\Psi(\vec{r}) \\
H_2 &= \int d^3\vec{r}\,\Psi^\dagger(\vec{r})V_{break}(\vec{r})\Psi(\vec{r}), \\
H_3 &= \frac{1}{2}\int d^3\vec{r}d^3\vec{r'}\Psi^\dagger(\vec{r})\Psi^\dagger(\vec{r'})V(\vec{r}-\vec{r'})\Psi(\vec{r'})\Psi(\vec{r}),
\end{aligned}
$$

and,

$$
H_0 = -\frac{\hbar^2}{2m}\nabla^2 + V_{trap}(\vec{r}).
$$

The interaction potential is given by

$$
V(\vec{r}-\vec{r'}) = V_{sr}(\vec{r}-\vec{r'}) + V_{dd}(\vec{r}-\vec{r'}),
$$

where the short-range ($V_{rs}$) and the dipole-dipole interaction potential ($V_{dd}$) are:

$$
\begin{aligned}
V_{sr}(\vec{r}-\vec{r'}) &= g\delta(\vec{r}-\vec{r'}), \\
V_{dd}(\vec{r}-\vec{r'}) &= \frac{C_{dd}}{4\pi}\frac{(1-3\cos^2\theta)}{|\vec{r}-\vec{r'}|^3}.
\end{aligned}
$$

where $g = 4\pi\hbar^2 a/m$, $a$ is the $s$-wave scattering length, $C_{dd} = \mu_0\mu^2$, $\mu$ is the magnetic dipole moment, $\mu_0$ is the permeability of vacuum and $\theta$ is the angle between the magnetic dipole moment (which is fixed in $z$ direction) and the vector $(\vec{r}-\vec{r'})$. Figure C.1 illustrates some schemes of dipolar interactions of two polarized dipoles, relative to their positions.

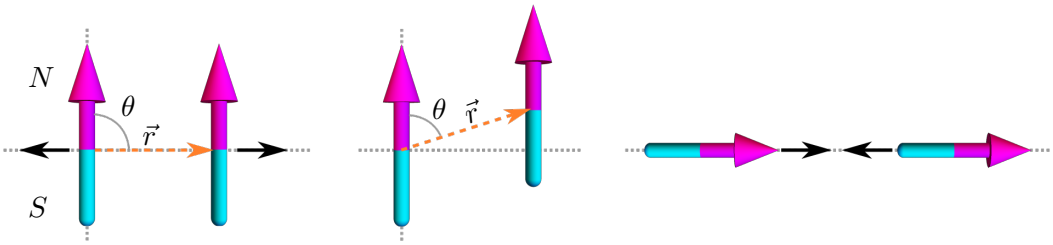


Figure C.1: Diagram for dipole-dipole interaction. The angle $\theta$ is formed by the dipole moment vector and the position vector $(\vec{r}-\vec{r'})$ (dashed orange arrow). The interaction varies from repulsive (panel 1, $\theta = \pi/2$) to attractive (panel 3, $\theta = 0$ head-to-tail). It depends on the alignment of the magnetic poles: equal poles repel and opposite poles attract each other.

For $^{52}$Cr, which has permanent magnetic dipole moment $\mu = 6.0\,\mu_B$, the dipolar length $a_{dd} \equiv (\frac{\mu_0\mu^2}{4\pi})\frac{m}{3\hbar^2} = 16\,a_B$, where $\mu_B = \frac{e\hbar}{2m_e} \approx 9.274\times10^{-24}J/T$ ($T = 10^4G$) is the Bohr magneton and $a_B = \frac{4\pi\epsilon_0\hbar^2}{m_e e^2} \approx 5.292\times10^{-11}m$ ($m = 10^6\mu$m) is the Bohr radius.

Consider the ratio $\varepsilon_{dd} \equiv \frac{a_{dd}}{a} = \frac{C_{dd}}{3g} = 0.16$, then $a = 16\,a_B/0.16 = 100\,a_B = 5.292$ nm. The scattering length $a(B)$ can be controlled by a magnetic field $B$, in the vicinity of Feshbach resonance, which for $^{52}$Cr is [2]:

$$a(B) = a_{bg}\left(1 - \frac{\Delta B}{B - B_0}\right),$$

where $B_0 \approx 589.1$ G, $\Delta B = (1.4 \pm 0.1)$ G and $a_{bg} \approx 100\,a_B$.
Consider the approximation

$$\Psi(\vec{r}) = \sum_{i=1}^{3} \phi_i(\vec{r}) a_i,$$

where $\phi_i(\vec{r}) = w_0(\vec{r} - \vec{r_i})$ is the localized Wannier function in the center of well $i$ for a single particle. We are assuming the energies involved are not strong enough such that the atom can be kept in the lowest vibrational state (first band). The localized Wannier function is the ground state of $H_0$ with harmonic approximation.
Using the above approximation the hamiltonian reduces to

$$\begin{aligned} H = \; & \tfrac{U_0}{2}\textstyle\sum_{i=1}^{3} N_i(N_i-1) + \sum_{i=1}^{3}\epsilon_i N_i + U_{12}N_1N_2 + U_{23}N_2N_3 + U_{13}N_1N_3 \\ & -(J-\epsilon_{12})(a_1^\dagger a_2 + a_2^\dagger a_1) - (J-\epsilon_{23})(a_2^\dagger a_3 + a_3^\dagger a_2), \end{aligned}$$

where

$$\begin{aligned} J &= -\int d^3\vec{r}\,\phi_1^*(\vec{r}) H_0 \phi_2(\vec{r}), \\ U_0 &= U_{sr} + U_{dip}, \\ U_{sr} &= g\int d^3\vec{r}|\phi_1(\vec{r})|^4, \qquad U_{dip} = \int d^3\vec{r}d^3\vec{r'}|\phi_1(\vec{r})|^2|\phi_1(\vec{r'})|^2 V_{dd}(\vec{r}-\vec{r'}), \\ U_{ij} &= \int d^3\vec{r}d^3\vec{r'}|\phi_i(\vec{r})|^2|\phi_j(\vec{r'})|^2 V_{dd}(\vec{r}-\vec{r'}), \\ \epsilon_{ij} &= \int d^3\vec{r}\,\phi_i^*(\vec{r}) V_{break}(\vec{r})\phi_j(\vec{r}), \qquad j = i+1, \qquad i = 1,2 \\ \epsilon_i &= \int d^3\vec{r}\, V_{break}(\vec{r})|\phi_i(\vec{r})|^2, \qquad i = 1,2,3. \end{aligned}$$

By symmetry, $U_{12} = U_{23}$, the hamiltonian becomes

$$\begin{aligned} H = \; & \tfrac{U_0}{2}\textstyle\sum_{i=1}^{3} N_i(N_i-1) + \sum_{i=1}^{3}\epsilon_i N_i + U_{12}N_2(N_1+N_3) + U_{13}N_1N_3 \\ & -J_{12}(a_1^\dagger a_2 + a_2^\dagger a_1) - J_{23}(a_2^\dagger a_3 + a_3^\dagger a_2). \end{aligned} \tag{C.1}$$

Using the conservation of $N$, we find

$$\sum_{i=1}^{3} N_i(N_i-1) = N(N-1) - 2(N_1N_2 + N_2N_3 + N_1N_3).$$

Then, the effective hamiltonian is

$$\begin{aligned} H = \; & (U_{12}-U_0)N_2(N_1+N_3) + (U_{13}-U_0)\,N_1N_3 + \textstyle\sum_{i=1}^{3}\epsilon_i N_i \\ & -J_{12}(a_1^\dagger a_2 + a_2^\dagger a_1) - J_{23}(a_2^\dagger a_3 + a_3^\dagger a_2), \end{aligned}$$

where we define $J_{ij} \equiv J - \epsilon_{ij}$, $j = i+1$ and $i = 1, 2$.

In Figure C.2 below, are shown schematic representations of some units.

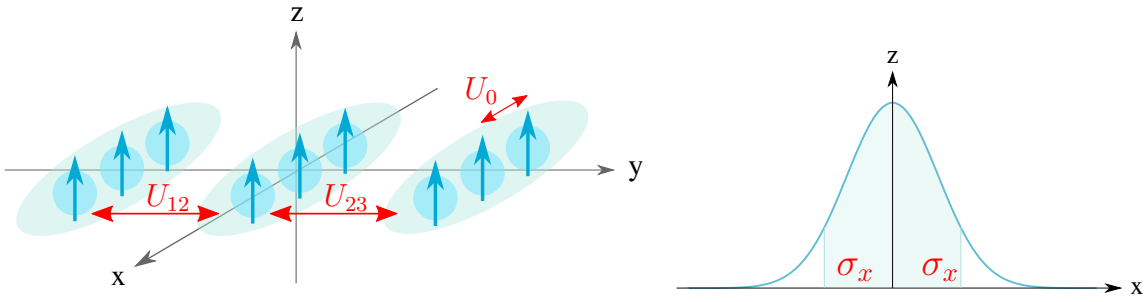


Figure C.2: Left panel: Schematic representation of the ultracold atoms distribution with indication of the resulting forces. The cigar-shapes (green), represent the dipolar Bose-Einstein condensates, whose Gaussian distribution occurs predominantly in the x-axis, schematized in the right panel.

# Experimental setup

Consider the experimental setup with three well potential generated by three Gaussian beam separated by a distance $l = 3\,\mu$m $(1.8\,\mu$m$)$(one beam for each potential). Each laser beam has potential given by

$$V_{\hat{x}}^{(i)} = -\frac{V_0}{1+\left(\frac{x}{x_R}\right)^2}\exp\left(-\frac{2}{w_0^2}\frac{(y-y_i)^2+z^2}{1+\left(\frac{x}{x_R}\right)^2}\right), \qquad x_R = \frac{\pi w_0^2}{\lambda} = \frac{1}{2}kw_0^2,$$

where $y_1 = -l$, $y_2 = 0$ and $y_3 = l$. The parameter $x_R$ is the Rayleigh length: the point along the propagation direction, from the waist, where the cross sectional area increased by a factor 2; $\lambda$ is the wavelength of the light and $w_0$ is the beam waist (see Fig. C.3 below). Note: the Gaussian beam propagating along the x-axis with wave number $k = 2\pi/\lambda$.

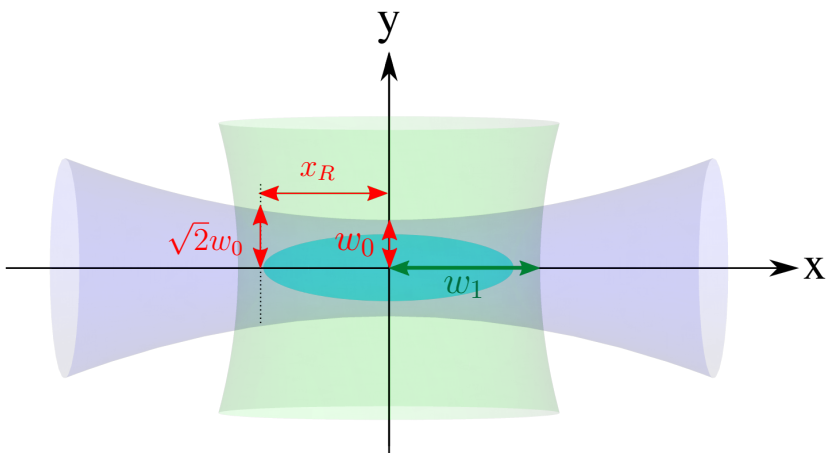


Figure C.3: Schematic cutout of beams trap with some reference. The blue beam represents one of the Gaussian beams, with waist $w_0 = 1\mu$m. The green region represents the transverse beam along the y-axis, with waist $w_0 = 6\mu$m, which provides $xz$-confinement. $x_R$ is the Rayleigh length. The cyan ellipse outlines the region where the condensate forms. It is centered in the focus of the lasers, at $x = y = 0$. The schematic is not scaled.

The breaking of integrability is generated by another transverse laser beam with the potential given by

$$V_{\hat{y}} = -\frac{V_1}{1+\left(\frac{y+\Delta y}{y_R}\right)^2}\exp\left(-\frac{2}{w_1^2}\frac{x^2+z^2}{1+\left(\frac{y+\Delta y}{y_R}\right)^2}\right), \qquad y_R = \frac{\pi w_1^2}{\lambda},$$

where $\Delta y = 0$ for integrable case and $\Delta y \neq 0$ for non integrable configuration. The complete potential can be given by a simplified expression

$$V(z,y,z) = V_{trap}(x,y,z) + V_{break}(y),$$

and

$$\begin{aligned} V_{trap}(x,y,z) &= -V_1 + \frac{1}{2}m\omega_r^2 z^2 + \frac{1}{2}m\omega_x^2 x^2 - V_0\sum_{i=1}^{3}\exp\left(-\frac{2}{w_0^2}(y-y_i)^2\right), \\ V_{break}(y) &= m\omega^2\Delta y\left(y+\frac{\Delta y}{2}\right), \end{aligned}$$

where the frequencies are given by

$$\omega_r = \sqrt{\frac{4V_0}{mw_0^2}}, \qquad \omega_x = \sqrt{\frac{2}{m}\left(\frac{V_0}{x_R^2}+\frac{2V_1}{w_1^2}\right)}, \qquad \omega = \sqrt{\frac{2V_1}{my_R^2}}.$$

For derivation of $V(x,y,z)$, we considered the approximations

$$\frac{2V_0}{w_0^2}+\frac{V_1}{y_R^2}\approx\frac{2V_0}{w_0^2},\qquad \frac{2V_0}{w_0^2}+\frac{2V_1}{w_1^2}\approx\frac{2V_0}{w_0^2},$$

which is valid for the waist $w_1$ sufficiently larger than $w_0$ (See Fig. C.3).

For the harmonic approximation of well $k$ we find,

$$V_{trap}^{(k)}(x,y,z) \;=\; -V_0-V_1+\frac{1}{2}m\omega_r^2\left[(y-y_k)^2+z^2\right]+\frac{1}{2}m\omega_x^2x^2.$$

Thus, the ground state of

$$H_0^{(2)}=-\frac{\hbar^2}{2m}\nabla^2+V_{trap}^{(2)},$$

is given by

$$\phi_2(x,y,z)=A\exp\left(-\eta_r(y^2+z^2)-\eta_x x^2\right),$$

where

$$A=\left(\frac{2\eta_r}{\pi}\right)^{1/2}\left(\frac{2\eta_x}{\pi}\right)^{1/4},\qquad \eta_r=\frac{m\omega_r}{2\hbar},\qquad \eta_x=\frac{m\omega_x}{2\hbar},$$

and the energy is given by

$$E=-V_0-V_1+\frac{1}{2}(2\hbar\omega_r+\hbar\omega_x).$$

The ground state of wells 1 and 3 are given by

$$\phi_1(x,y,z)=\phi_2(x,y+l,z),\qquad \phi_3(x,y,z)=\phi_2(x,y-l,z).$$

## Parameters $\epsilon$'s

The parameters $\epsilon_{12}$ and $\epsilon_{13}$ are given by

$$\begin{aligned}\epsilon_{12} &= \int d^3\vec{r}\,\phi_2^*(x,y+l,z)\,V_{break}(y)\,\phi_2(x,y,z)=-\frac{1}{2}m\omega^2\Delta y(l-\Delta y)\varepsilon,\\ \epsilon_{23} &= \int d^3\vec{r}\,\phi_2^*(x,y,z)\,V_{break}(y)\,\phi_2(x,y-l,z)=\frac{1}{2}m\omega^2\Delta y(l+\Delta y)\varepsilon,\end{aligned}$$

where

$$\varepsilon = \exp\left(-\frac{l^2}{2}\eta_r\right).$$

For parameters $\epsilon_1$, $\epsilon_2$ and $\epsilon_3$, we find

$$\begin{aligned}
\epsilon_1 &= \int d^3\vec{r}\,|\phi_2(x, y+l, z)|^2 V_{break}(y) = \frac{1}{2}m\omega^2\Delta y(\Delta y - 2l),\\
\epsilon_2 &= \int d^3\vec{r}\,|\phi_2(x, y, z)|^2 V_{break}(y) = \frac{1}{2}m\omega^2\Delta y^2,\\
\epsilon_3 &= \int d^3\vec{r}\,|\phi_2(x, y-l, z)|^2 V_{break}(y) = \frac{1}{2}m\omega^2\Delta y(\Delta y + 2l).
\end{aligned}$$

# Discussion about the integrability breaking term

Using the conservation $N_2 = N - N_1 - N_3$ and previous results, we find

$$\sum_{i=1}^{3}\epsilon_i N_i = (\epsilon_1 - \epsilon_2)N_1 + (\epsilon_3 - \epsilon_2)N_3 + \epsilon_2 N = m\omega^2\Delta y\, l(N_3 - N_1) + \epsilon_2 N.$$

Thus, the term of breaking of integrability has the form

$$H_{break} = \delta(N_3 - N_1),$$

where $\delta = m\omega^2\Delta y\, l$..

# Parameter $U_{sr}$

For the parameter $U_{sr}$, we find

$$U_{sr} = g\int d^3\vec{r}|\phi_2(\vec{r})|^4 = \frac{g}{\pi^{3/2}}\eta_r\sqrt{\eta_x}.$$

# Parameter $U_{ij}$ with polarization along the $Z$-axis

Consider $n(\vec{r}, d) = |\phi_2(x, y+d, z)|^2$ and we define

$$U(d) = \int d^3\vec{r}\,d^3\vec{r'}n(\vec{r}, d)n(\vec{r'}, -d)V_{dd}(\vec{r} - \vec{r'}).$$

Thus, with the above definition, we have

$$U_{dip} = U(0), \qquad U_{12} = U(l/2), \qquad U_{13} = U(l).$$

Using the Fourier transform of $n(\vec{r},d)$ and $V_{dd}(\vec{r})$, and cylindrical coordinates, we obtain

$$U(d)=\frac{C_{dd}}{(2\pi)^3}\int_0^{2\pi}d\theta\int_{-\infty}^{+\infty}dz\int_0^{+\infty}rdr\left[\frac{r^2\sin^2\theta}{r^2+z^2}-\frac{1}{3}\right]\exp\left[-\frac{r^2}{4\eta_r}-\frac{z^2}{4\eta_x}\right]\cos(2dr\cos\theta).$$

Now, integrating with respect $z$ and $\theta$, we find

$$\begin{aligned}U_{dip}=U(0) &= \frac{C_{dd}}{8\pi}\int_0^{+\infty}r\,dr\,e^{-\frac{r^2}{4\eta_r}}\left[e^{-\frac{r^2}{4\eta_x}}r\,\mathrm{erfc}\left(\frac{r}{2\sqrt{\eta_x}}\right)-\frac{4}{3}\sqrt{\frac{\eta_x}{\pi}}\right]\\ &= \frac{C_{dd}}{6\pi^{3/2}}\eta_r\sqrt{\eta_x}f(\kappa),\end{aligned}$$

where

$$f(\kappa)=\frac{1+2\kappa^2}{1-\kappa^2}-\frac{3\kappa^2}{(1-\kappa^2)^{3/2}}\,\mathrm{arctanh}(\sqrt{1-\kappa^2}),\qquad \kappa=\sqrt{\frac{\eta_x}{\eta_r}}.$$

Therefore,

$$U_0=U_{sr}+U_{dip}=\frac{\eta_r\sqrt{\eta_x}}{\pi^{3/2}}\left(g+\frac{C_{dd}}{6}f(\kappa)\right).$$

# Parameter $J$

Consider

$$\begin{aligned}J &= -\int d^3\vec{r}\,\phi_2(x,y+l,z)H_0\phi_2(x,y,z),\\ &= -\int d^3\vec{r}\,\phi_2(x,y+l,z)\left[H_0^{(2)}+V_{trap}(x,y,z)-V_{trap}^{(2)}(x,y,z)\right]\phi_2(x,y,z)\\ &= -\int d^3\vec{r}\,\phi_2(x,y+l,z)\left[E+V_{trap}(x,y,z)-V_{trap}^{(2)}(x,y,z)\right]\phi_2(x,y,z)\end{aligned}$$

where

$$E=-V_0-V_1+\frac{1}{2}(2\hbar\omega_r+\hbar\omega_x),$$

We find

$$J\varepsilon^{-1}=-\frac{1}{2}(2\hbar\omega_r+\hbar\omega_x)+V_1+V_0\sqrt{\frac{w_0\eta_r}{1+w_0\eta_r}}\varepsilon_1\left(\varepsilon_1^8+2\right)+\frac{l^2m\omega_r^2}{8}+\frac{m\omega_r^2}{8\eta_r},$$

where

$$\begin{aligned} \varepsilon &= \exp\left(-\frac{l^2\eta_r}{2}\right), \\ \varepsilon_1 &= \exp\left(-\frac{l^2\eta_r}{2+2w_0\eta_r}\right). \end{aligned}$$

we can also calculate

$$J_{13} = -\int d^3\vec{r}\,\phi_2(x, y+l, z) H_0 \phi_2(x, y-l, z),$$

which gives

$$J_{13}\varepsilon^{-4} = -\frac{1}{2}(2\hbar\omega_r + \hbar\omega_x) + V_1 + V_0\sqrt{\frac{w_0\eta_r}{1+w_0\eta_r}}(2\varepsilon_1^4 + 1) + \frac{l^2 m\omega_r^2}{2} + \frac{m\omega_r^2}{8\eta_r},$$

# Experimental parameters

The tables show experimental parameters and resulting values for two different dipolar atoms, Chromium and Dysprosium.

## Parameter values for $^{52}$Cr and $^{164}$Dy

| | Parameters | $^{52}$**Cr** | $^{164}$**Dy** |
|---|---|---|---|
| s-wave scattering length | $a/a_B$ | 0.2 | 1 |
| dipolar scattering length | $a_{dd}/a_B$ | 16 | 131 |
| wells distance | $l$ | $3\,\mu$m | $3\,\mu$m |
| 3 parallel and transverse beams | $\lambda$ | $1.064\,\mu$m | $1.064\,\mu$m |
| 3 parallel beams waist | $w_0$ | $1.5\,\mu$m | $1.5\,\mu$m |
| transverse beam waist | $w_1$ | $6\,\mu$m | $6\,\mu$m |
| trap frequency (y-z radius) | $\omega_r/(2\pi)$ | 38.8895 Hz | 12.6428 Hz |
| trap frequency (x axis) | $\omega_x/(2\pi)$ | 11.5358 Hz | 3.7502 Hz |
| transverse beam freq. (y axis) | $\omega/(2\pi)$ | 0.5821 Hz | 0.1892 Hz |

## Parameter results for $^{52}$Cr and $^{164}$Dy:

| | Results | $^{52}$Cr | $^{164}$Dy |
|---|---|---|---|
| tunneling coupling wells 1-2 and 2-3 | $J_{12}/h \simeq J_{23}/h$ | -12.514 Hz | -3.942 Hz |
| tunneling coupling wells 1-3 | $J_{13}/h$ | 1.105 Hz | 0.397 Hz |
| one-site interaction | $U_0/h$ | 0.0015 Hz | 0.0038 Hz |
| inter-well interaction | $U_{12}/h = U_{23}/h$ | 0.0022 Hz | 0.0060 Hz |
| inter-well interaction - integr. condition | $U_{13}/h = U_0/h$ | 0.0015 Hz | 0.0038 Hz |
| transverse beam displacement - break integr. | $\Delta y$ | $3\,\mu$m | $3\,\mu$m |
| breaking parameter | $\delta/h$ | 0.0157 Hz | 0.0052 Hz |

where $a_B$ is the Bohr radius and $h$ is the Planck constant. The values were calculated for $l = 3\,\mu$m, $\Delta y = 3\,\mu$m, $\lambda = 1.064\,\mu$m, $w_0 = 1.5\,\mu$m, $w_1 = 6\,\mu$m and $V_1 = V_0$.

# Appendix D

# Start of the resonant regime

The resonant regime occurs when the energy levels of the system are equidistantly distributed within a band $l = N - l$ (See Fig. 3.4 in Chapter 3). It is common to associate this regime to the Josephson regime (See Chapter 2, pg. 2), where $JN^{-1} \ll U \ll JN$. However, the threshold value of $UN/J$ that guarantees well-defined bands depends on the initial state, non-linearly, and there is no analytical function that directly models this transition, except for the effective Hamiltonian condition. Furthermore, the higher the $UN/J$, the slower the tunneling between the wells becomes, which can make the experimental implementation unfeasible. Thus, finding the ideal parameters, for the different initial states, became a great challenge.

Here, we present a method that can guide the choice of these parameters for the three-well model, but the idea can be extended to the four-well model. It is based on the fact that only a perfect resonant regime can be described equally by the general Hamiltonian and the relative effective Hamiltonian, simultaneously, as seen in Chapter 3. In this case, we can assume that $H = H_{eff}$, which depends on the initial configuration, so

$$\begin{aligned} H &\simeq H_{eff} \\ E &\simeq E_{eff} \\ \frac{U(N-2l)^2}{N^2} &\simeq \frac{N-l}{8U}\left(\frac{l+1}{N-2l-1} - \frac{l}{N-2l+1}\right) \\ U(l,N) &\simeq \frac{N}{2}\sqrt{\frac{N-l}{2(N-2l)^2}\left(\frac{l+1}{N-2l-1} - \frac{l}{N-2l+1}\right)}, \quad l < N/2 \end{aligned} \tag{D.1}$$

where $H$ is normalized by $N^2$. We note that since the energy $E(l) = E(N-l)$, where $l$ is the initial number of bosons in well 2 (subspace B) in the resonant regime, we have also that $U(l) = U(N-l)$. In Fig. D.1 is shown the curve of $U(l)$ as a function of $l$ (Eq. (D.1)), for N=60. Note that for $l = N - l$, $N$ even, the function has no solution. In this case the initial energy is zero and the band does not form.

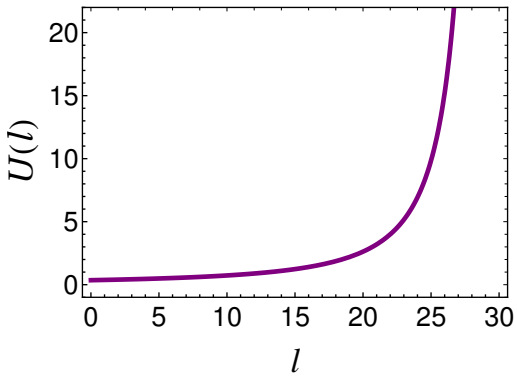


Figure D.1: $U(l)$ as function of $l$, for N=60. By symmetry, we have that $U(l) = U(N-l)$ (See Fig. D.2), and an indeterminacy arises for $l = (N-l)$.

In Figure D.2 are shown examples of dynamics for some parameters $U$ obtained through the Eq. (D.1), showing that this method could be a good way to investigate

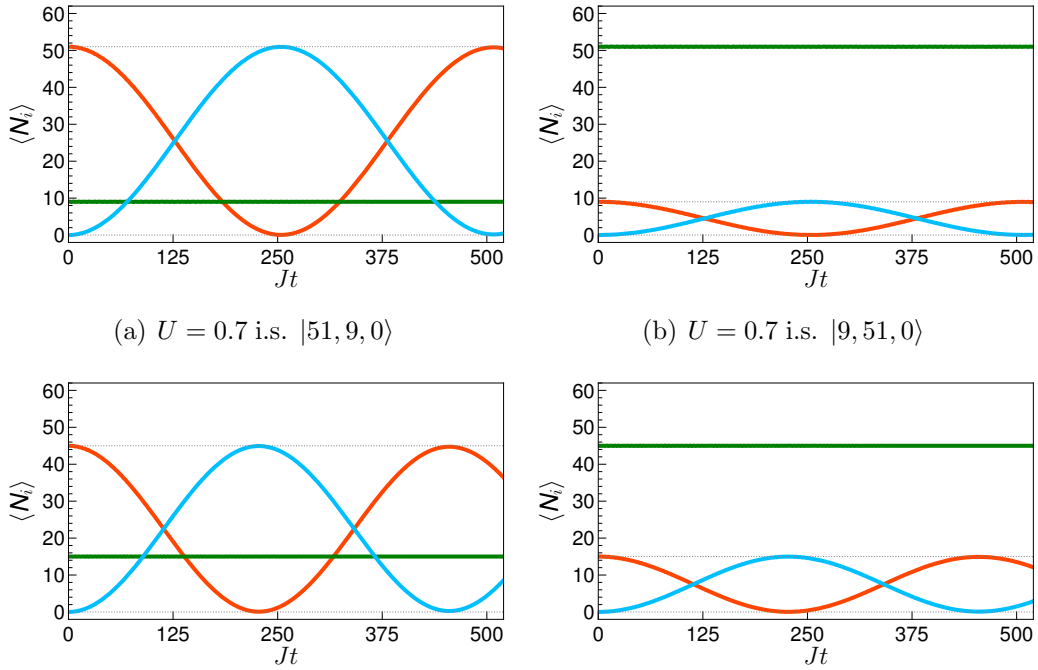


(a) $U = 0.7$ i.s. $|51, 9, 0\rangle$ (b) $U = 0.7$ i.s. $|9, 51, 0\rangle$

(c) $U = 1.23$ i.s. $|45, 15, 0\rangle$ (d) $U = 1.23$ i.s. $|15, 45, 0\rangle$

Figure D.2: Time evolution of the expectation value of $\langle N_1 \rangle$ (red line), $\langle N_2 \rangle$ (green line) and $\langle N_3 \rangle$ (blue line) for different initial states. The parameter $U$ used to evolve each initial state, was obtained through Eq. (D.1), for N=60. In all cases, the number of particles N=60 was considered.

the parameters that guide the beginning of the resonant regime, for different initial states.

# Bibliography


[1] C. E. Shannon. A mathematical theory of communication. *The Bell System Technical Journal*, 27(3):379–423, 1948.

[2] J. P. Dowling and G. J. Milburn. Quantum technology: the second quantum revolution. *Philos. Trans. Royal Soc. A*, 361(1809):1655–1674, 2003.

[3] M. A. Nielsen and I. L. Chuang. Quantum computation and quantum information. *Phys. Today*, 54(2):60, 2001.

[4] M. H. Anderson, J. R. Ensher, M. R. Matthews, C. E. Wieman, and E. A. Cornell. Observation of Bose-Einstein condensation in a dilute atomic vapor. *Science*, 269(5221):198–201, 1995.

[5] The Nobel Prize in Physics 2001. https://www.nobelprize.org/prizes/physics/2001/summary.

[6] L. Amico, M. Boshier, G Birkl, A. Minguzzi, C. Miniatura, L-C Kwek, D. Aghamalyan, V. Ahufinger, D Anderson, N. Andrei, et al. Roadmap on Atomtronics: State of the art and perspective. *AVS Quantum Sci.*, 3(3):039201, 2021.

[7] M. P. A. Fisher, P. B. Weichman, G. Grinstein, and D. S. Fisher. Boson localization and the superfluid-insulator transition. *Phys. Rev. B*, 40:546–570, Jul 1989.

[8] I. Bloch. Ultracold quantum gases in optical lattices. *Nat. Phys.*, 1(1):23–30, 2005.

[9] G. J. Milburn, J. Corney, Ewan M. Wright, and D.F. Walls. Quantum dynamics of an atomic Bose-Einstein condensate in a double-well potential. *Phys. Rev. A*, 55(6):4318, 1997.

[10] A. J. Leggett. Bose-Einstein condensation in the alkali gases: Some fundamental concepts. *Rev. Mod. Phys.*, 73:307–356, 2001.

[11] M. Albiez, R. Gati, J. Fölling, S. Hunsmann, M. Cristiani, and M. K. Oberthaler. Direct observation of tunneling and nonlinear self-trapping in a single bosonic Josephson junction. *Phys. Rev. Lett.*, 95:010402, 2005.

[12] S. Levy, E. Lahoud, I. Shomroni, and J. Steinhauer. The ac and dc Josephson effects in a Bose–Einstein condensate. *Nature*, 449(7162):579–583, 2007.

[13] T. Kinoshita, T. Wenger, and D. S. Weiss. A quantum newton's cradle. *Nature*, 440(7086):900–903, 2006.

[14] J.-S. Caux and J. Mossel. Remarks on the notion of quantum integrability. *J. Stat. Mech. Theory Exp.*, 2011(02):P02023, 2011.

[15] J. Larson. Integrability versus quantum thermalization. *J. Phys. B: At. Mol. Opt. Phys.*, 46(22):224016, 2013.

[16] T.C. Choy and F. D. M. Haldane. Failure of Bethe–Ansatz solutions of generalisations of the Hubbard chain to arbitrary permutation symmetry. *Phys. Lett. A*, 90(1):83–84, 1982.

[17] A. R. Kolovsky and A. Buchleitner. Quantum chaos in the Bose-Hubbard model. *Europhysics Lett. (EPL)*, 68(5):632–638, 2004.

[18] M. Hiller, T. Kottos, and T. Geisel. Complexity in parametric Bose-Hubbard Hamiltonians and structural analysis of eigenstates. *Phys. Rev. A*, 73:061604, Jun 2006.

[19] N. Oelkers and J. Links. Ground-state properties of the attractive one-dimensional Bose-Hubbard model. *Phys. Rev. B*, 75:115119, 2007.

[20] M. Hiller, T. Kottos, and T. Geisel. Wave-packet dynamics in energy space of a chaotic trimeric Bose-Hubbard system. *Phys. Rev. A*, 79:023621, Feb 2009.

[21] C. Kollath, G. Roux, G. Biroli, and A. M. Läuchli. Statistical properties of the spectrum of the extended Bose-Hubbard model. *J. Stat. Mech. Theory Exp.*, 2010(08):P08011, 2010.

[22] R. Bürkle, A. Vardi, D. Cohen, and J. R. Anglin. Probabilistic Hysteresis in Integrable and Chaotic Isolated Hamiltonian Systems. *Phys. Rev. Lett.*, 123:114101, Sep 2019.

[23] G. Nakerst and M. Haque. Eigenstate thermalization scaling in approaching the classical limit. *Phys. Rev. E*, 103:042109, 2021.

[24] L. H. Ymai, A. P. Tonel, A. Foerster, and J. Links. Quantum integrable multi-well tunneling models. *J. Phys. A Math. Theor.*, 50(26):264001, 2017.

[25] G. Santos, A. Foerster, and I. Roditi. A bosonic multi-state two-well model. *J. Phys. A: Math. Theor.*, 46(26):265206, 2013.

[26] T Lahaye, C Menotti, L Santos, M Lewenstein, and T Pfau. The physics of dipolar bosonic quantum gases. *Reports on Progress in Physics*, 72(12):126401, 2009.

[27] D. Petter, G. Natale, R. M. W. van Bijnen, A. Patscheider, M. J. Mark, L. Chomaz, and F. Ferlaino. Probing the roton excitation spectrum of a stable dipolar bose gas. *Phys. Rev. Lett.*, 122:183401, 2019.

[28] Gilberto Santos, Changrim Ahn, Angela Foerster, and Itzhak Roditi. Bethe states for the two-site Bose–Hubbard model: binomial approach. *Phys. Lett. B*, 746:186–189, 2015.

[29] L. Cao, I. Brouzos, S. Zöllner, and P. Schmelcher. Interaction-driven interband tunneling of bosons in the triple well. *New J. Phys.*, 13(3):033032, mar 2011.

[30] L. Cao, I. Brouzos, B. Chatterjee, and P. Schmelcher. The impact of spatial correlation on the tunneling dynamics of few-boson mixtures in a combined triple well and harmonic trap. *New J. of Phys.*, 14(9):093011, sep 2012.

[31] A. Benseny, J̇Gillet, and T. Busch. Spatial adiabatic passage via interaction-induced band separation. *Phys. Rev. A*, 93:033629, Mar 2016.

[32] J. A. Stickney, D. Z. Anderson, and A. A. Zozulya. Transistorlike behavior of a Bose-Einstein condensate in a triple-well potential. *Phys. Rev. A*, 75:013608, Jan 2007.

[33] M. K. Olsen and A. S. Bradley. Quantum ultracold atomtronics. *Phys. Rev. A*, 91:043635, 2015.

[34] Z. Zhang, V. Dunjko, and M. Olshanii. Atom transistor from the point of view of nonequilibrium dynamics. *New Journal of Physics*, 17(12):125008, 2015.

[35] O. V. Marchukov, A. G. Volosniev, M. Valiente, D. Petrosyan, and N. T. Zinner. Quantum spin transistor with a heisenberg spin chain. *Nature communications*, 7(1):1–6, 2016.

[36] R. Dumke, L. Amico, M. G. Boshier, K. Dieckmann, W. Li, T. C. Killian, et al. Roadmap on quantum optical systems. *J. Opt.*, 18(9):093001, aug 2016.

[37] T. Lahaye, T. Pfau, and L. Santos. Mesoscopic ensembles of polar bosons in triple-well potentials. *Phys. Rev. Lett.*, 104:170404, 2010.

[38] M. A. Baranov. Theoretical progress in many-body physics with ultracold dipolar gases. *Phys. Rep.*, 464(3):71–111, 2008.

[39] P. Jung, R. W. Helmes, and A. Rosch. Transport in almost integrable models: Perturbed Heisenberg chains. *Phys. Rev. Lett.*, 96:067202, 2006.

[40] B. Wilson, A. Foerster, C.C.N. Kuhn, I. Roditi, and D. Rubeni. A geometric wave function for a few interacting bosons in a harmonic trap. *Phys. Lett. A*, 378(16):1065–1070, 2014.

[41] I. Brouzos and A. Foerster. Trace of broken integrability in stationary correlation properties. *Phys. Rev. A*, 89:053623, 2014.

[42] L. Dell'Anna, G. Mazzarella, V. Penna, and L. Salasnich. Entanglement entropy and macroscopic quantum states with dipolar bosons in a triple-well potential. *Phys. Rev. A*, 87:053620, May 2013.

[43] K. W. Wilsmann, L. H. Ymai, A. P. Tonel, J. Links, and A. Foerster. Control of tunneling in an atomtronic switching device. *Comm. Phys.*, 1, 2018.

[44] A. P. Tonel, L. H. Ymai, K. Wittmann W., A. Foerster, and J. Links. Entangled states of dipolar bosons generated in a triple-well potential. *SciPost Phys. Core*, 2:3, 2020.

[45] L. Hwang, P. Kok, and J. P. Dowling. A quantum rosetta stone for interferometry. *J. Mod. Opt.*, 49(14-15):2325–2338, 2002.

[46] I. Afek, O. Ambar, and Y. Silberberg. High-NOON states by mixing quantum and classical light. *Science*, 328(5980):879–881, 2010.

[47] J. J . Bollinger, Wayne M. Itano, D. J. Wineland, and D. J. Heinzen. Optimal frequency measurements with maximally correlated states. *Phys. Rev. A*, 54:R4649–R4652, Dec 1996.

[48] A. N. Boto, P. Kok, D. S. Abrams, S. L. Braunstein, C. P. Williams, and J. P. Dowling. Quantum interferometric optical lithography: Exploiting entanglement to beat the diffraction limit. *Phys. Rev. Lett.*, 85:2733–2736, Sep 2000.

[49] C. F. Wildfeuer, A. P. Lund, and J. P. Dowling. Strong violations of bell-type inequalities for path-entangled number states. *Phys. Rev. A*, 76:052101, 2007.

[50] J. Pan, Z-B Chen, C-Y Lu, H. Weinfurter, A. Zeilinger, and M. Żukowski. Multiphoton entanglement and interferometry. *Rev. Mod. Phys.*, 84:777–838, 2012.

[51] J. Haas, M. Schwartz, Ul. Rengstl, M. Jetter, P. Michler, and B. Mizaikoff. Chem/bio sensing with non-classical light and integrated photonics. *Analyst*, 143(3):593–605, 2018.

[52] L. D'Alessio, Y. Kafri, A. Polkovnikov, and M. Rigol. From quantum chaos and eigenstate thermalization to statistical mechanics and thermodynamics. *Advances in Physics*, 65(3):239–362, 2016.

[53] M. V. Berry and M. Tabor. Level clustering in the regular spectrum. *Proc. R. Soc. Lond. A*, 356:375 – 394, 1977.

[54] E. P. Wigner. On the statistical distribution of the widths and spacings of nuclear resonance levels. In *Mathematical Proceedings of the Cambridge Philosophical Society*, volume 47, pages 790–798. Cambridge University Press, 1951.

[55] F. J. Dyson. Statistical theory of the energy levels of complex systems. ii. *J. Math. Phys.*, 3(1):157–165, 1962.

[56] D. Poilblanc, T. Ziman, J. Bellissard, F. Mila, and G. Montambaux. Poisson vs. GOE statistics in integrable and non-integrable quantum Hamiltonians. *EPL (Europhysics Letters)*, 22(7):537–542, 1993.

[57] M. A. Garcia-March, S. van Frank, M. Bonneau, J. Schmiedmayer, M. Lewenstein, and Lea F. Santos. Relaxation, chaos, and thermalization in a three-mode model of a Bose–Einstein condensate. *New J. Phys.*, 20(11):113039, 2018.

[58] D. Peter, K. Pawłowski, T. Pfau, and K. Rzażewski. Mean-field description of dipolar bosons in triple-well potentials. *J. Phys. B: At. Mol. Opt. Phys.*, 45(22):225302, 2012.

[59] A. P. Tonel, J. Links, and A. Foerster. Quantum dynamics of a model for two Josephson-coupled Bose–Einstein condensates. *J. Phys. A Math. Theor.*, 38(6):1235, 2005.

[60] L.-M. Duan, E. Demler, and M. D. Lukin. Controlling spin exchange interactions of ultracold atoms in optical lattices. *Phys. Rev. Lett.*, 91:090402, Aug 2003.

[61] A. B. Kuklov and B. V. Svistunov. Counterflow superfluidity of two-species ultracold atoms in a commensurate optical lattice. *Phys. Rev. Lett.*, 90:100401, 2003.

[62] S. Fölling, S. Trotzky, P. Cheinet, M. Feld, R. Saers, A. Widera, T. Müller, and I. Bloch. Direct observation of second-order atom tunnelling. *Nature*, 448(7157):1029–1032, 2007.

[63] H.-C. Chuang, E. A. Salim, V. Vuletic, D. Z. Anderson, and V. M. Bright. Multilayer atom chips for atom tunneling experiments near the chip surface. *Sensors and Actuators A: Phys.*, 165(1):101–106, 2011.

[64] D. Rubeni, J. Links, P. S. Isaac, and A. Foerster. Two-site Bose-Hubbard model with nonlinear tunneling: Classical and quantum analysis. *Phys. Rev. A*, 95:043607, 2017.

[65] T. Koch, T. Lahaye, J. Metz, B. Fröhlich, A. Griesmaier, and T. Pfau. Stabilization of a purely dipolar quantum gas against collapse. *Nature physics*, 4(3):218–222, 2008.

[66] I. Ferrier-Barbut, H. Kadau, M. Schmitt, M. Wenzel, and T. Pfau. Observation of quantum droplets in a strongly dipolar bose gas. *Phys. Rev. Lett.*, 116:215301, May 2016.

[67] G. Mazzarella, S. M. Giampaolo, and F. Illuminati. Extended Bose-Hubbard model of interacting bosonic atoms in optical lattices: From superfluidity to density waves. *Phys. Rev. A*, 73:013625, 2006.

[68] D. R. Dounas-Frazer, A. M. Hermundstad, and L. D. Carr. Ultracold bosons in a tilted multilevel double-well potential. *Phys. Rev. Lett.*, 99:200402, Nov 2007.

[69] J. Dobrzyniecki, X. Li, A. E. B. Nielsen, and T. Sowiński. Effective three-body interactions for bosons in a double-well confinement. *Phys. Rev. A*, 97:013609, Jan 2018.

[70] I. Bloch, J. Dalibard, and W. Zwerger. Many-body physics with ultracold gases. *Rev. Mod. Phys.*, 80(3):885–964, 2008.

[71] M. Fadel, T. Zibold, B. Décamps, and P. Treutlein. Spatial entanglement patterns and Einstein-Podolsky-Rosen steering in Bose-Einstein condensates. *Science*, 360(6387):409–413, 2018.

[72] P. Kunkel, M. Prüfer, H. Strobel, D. Linnemann, A. Frölian, T. Gasenzer, M. Gärttner, and M. K. Oberthaler. Spatially distributed multipartite entanglement enables EPR steering of atomic clouds. *Science*, 360(6387):413–416, 2018.

[73] K. Lange, J. Peise, B. Lücke, I. Kruse, G. Vitagliano, I. Apellaniz, M. Kleinmann, G. Tóth, and C. Klempt. Entanglement between two spatially separated atomic modes. *Science*, 360(6387):416–418, 2018.

[74] A. Omran et al. Generation and manipulation of Schrödinger cat states in Rydberg atom arrays. *Science*, 365(6453):570–574, 2019.

[75] T. J. Volkoff and C. M. Herdman. Generating accessible entanglement in bosons via pair-correlated tunneling. *Phys. Rev. A*, 100:022331, 2019.

[76] A. Polls I. Moreira and B. Juliá-Díaz. Entanglement structure of the two-component Bose-Hubbard model as a quantum simulator of a Heisenberg chain. *Sci. Rep.*, 9:9424, 2019.

[77] C. H. Bennett, H. J. Bernstein, S. Popescu, and B. Schumacher. Concentrating partial entanglement by local operations. *Phys. Rev. A*, 53:2046–2052, Apr 1996.

[78] B. C. Sanders. Quantum dynamics of the nonlinear rotator and the effects of continual spin measurement. *Phys. Rev. A*, 40:2417–2427, 1989.

[79] K. Bongs, W. P. Schleich, A. Roura, et al. Taking atom interferometric quantum sensors from the laboratory to real-world applications. *Nature Rev. Phys.*, 1(12):731–739, 2019.

[80] L. Pezzè, A. Smerzi, M. K. Oberthaler, R. Schmied, and P. Treutlein. Quantum metrology with nonclassical states of atomic ensembles. *Rev. Mod. Phys.*, 90:035005, 2018.

[81] C. Gross and I. Bloch. Quantum simulations with ultracold atoms in optical lattices. *Science*, 357(6355):995–1001, 2017.

[82] R. A. Pepino, J. Cooper, D. Z. Anderson, and M. J. Holland. Atomtronic circuits of diodes and transistors. *Phys. Rev. Lett.*, 103:140405, 2009.

[83] L. Amico, G. Birkl, Ma. Boshier, and L.-C. Kwek. Focus on atomtronics-enabled quantum technologies. *New Journal of Physics*, 19(2):020201, feb 2017.

[84] Andreas Nunnenkamp, Ana Maria Rey, and Keith Burnett. Generation of macroscopic superposition states in ring superlattices. *Phys. Rev. A*, 77:023622, 2008.

[85] K. Stiebler, Gertjerenken B., Teichmann K., and Weiss C. Spatial two-particle NOON-states in periodically shaken three-well potentials. *J. Phys. B: At. Mol. Opt. Phys.*, 44(5):055301, 2011.

[86] S. Ragole and J. M. Taylor. Interacting atomic interferometry for rotation sensing approaching the heisenberg limit. *Phys. Rev. Lett.*, 117:203002, 2016.

[87] T. Haug, R. Dumke, L.-C. Kwek, and L. Amico. Topological pumping in Aharonov–Bohm rings. *Commun. Phys.*, 2(1):1–9, 2019.

[88] S. Pandey et al. Hypersonic Bose–Einstein condensates in accelerator rings. *Nature*, 570(7760):205–209, 2019.

[89] T. Haug, J. Tan, M. Theng, R.r Dumke, L.-C. Kwek, and L. Amico. Readout of the atomtronic quantum interference device. *Phys. Rev. A*, 97:013633, Jan 2018.

[90] J. Polo, R. Dubessy, P. Pedri, H. Perrin, and A. Minguzzi. Oscillations and decay of superfluid currents in a one-dimensional bose gas on a ring. *Phys. Rev. Lett.*, 123:195301, 2019.

[91] E. Compagno, G. Quesnel, A. Minguzzi, L. Amico, and D. Feinberg. Multimode N00N states in driven atomtronic circuits. *Phys. Rev. Research*, 2:043118, Oct 2020.

[92] J. Daboul, X. Wang, and Barry C. Sanders. Quantum gates on hybrid qudits. *J. Phys. A Math. Theor.*, 36(10):2525–2536, 2003.

[93] A. Muthukrishnan and C. R. Stroud. Multivalued logic gates for quantum computation. *Phys. Rev. A*, 62:052309, 2000.

[94] Gavin K. Brennen, Dianne P. O'Leary, and Stephen S. Bullock. Criteria for exact qudit universality. *Phys. Rev. A*, 71:052318, May 2005.

[95] G. J. Pryde and A. G. White. Creation of maximally entangled photon-number states using optical fiber multiports. *Phys. Rev. A*, 68:052315, 2003.

[96] M. W. Mitchell, J. S. Lundeen, and A. M. Steinberg. Super-resolving phase measurements with a multiphoton entangled state. *Nature*, 429(6988):161–164, 2004.

[97] K. J. Resch, K. L. Pregnell, R. Prevedel, A. Gilchrist, G. J. Pryde, J. L. O'Brien, and A. G. White. Time-reversal and super-resolving phase measurements. *Phys. Rev. Lett.*, 98:223601, 2007.

[98] A. P. Tonel, L. H. Ymai, A. Foerster, and J. Links. Integrable model of bosons in a four-well ring with anisotropic tunneling. *J. Phys. A Math. Theor.*, 48(49):494001, 2015.

[99] D. S. Grün, K. W. Wittmann, L. H. Ymai, J. Links, and A. Foerster. Protocol designs for NOON states. *Commun. Phys.*, 5(1):36, 2022.

[100] R. Yamamoto, J. Kobayashi, K. Kato, T. Kuno, Y. Sakura, and Y. Takahashi. Site-resolved imaging of single atoms with a faraday quantum gas microscope. *Phys. Rev. A*, 96(3):033610, 2017.

[101] D. Okuno, Y. Amano, K. Enomoto, N. Takei, and Y. Takahashi. Schemes for nondestructive quantum gas microscopy of single atoms in an optical lattice. *New J. Phys.*, 22(1):013041, 2020.

[102] B. Yang et al. Quantum criticality and the tomonaga-luttinger liquid in one-dimensional bose gases. *Phys. Rev. Lett.*, 119(16):165701, 2017.

[103] B. Yang et al. Cooling and entangling ultracold atoms in optical lattices. *Science*, 369(6503):550–553, 2020.

[104] Y. H. Fung, A. V. Carpentier, P. Sompet, and M. Andersen. Two-atom collisions and the loading of atoms in microtraps. *Entropy*, 16(1):582–606, 2014.

[105] T. R. Bromley, I. A. Silva, G. Adesso, et al. There is more to quantum interferometry than entanglement. *Phys. Rev. A*, 95:052313, May 2017.

[106] W. H. Zurek, S. Habib, and J. P. Paz. Coherent states via decoherence. *Phys. Rev. Lett.*, 70:1187–1190, 1993.

[107] F. Buscemi, P. Bordone, and A. Bertoni. Linear entropy as an entanglement measure in two-fermion systems. *Phys. Rev. A*, 75:032301, Mar 2007.

[108] K. A. Matveev and A. I. Larkin. Parity effect in ground state energies of ultrasmall superconducting grains. *Phys. Rev. Lett.*, 78:3749–3752, 1997.

[109] G. Zurn, A. N. Wenz, S. Murmann, A. Bergschneider, T. Lompe, and S. Jochim. Pairing in few-fermion systems with attractive interactions. *Phys. Rev. Lett.*, 111:175302, 2013.

[110] S. Matsuo, S. Nakaharai, K. Komatsu, K. Tsukagoshi, T. Moriyama, T. Ono, and K. Kobayashi. Parity effect of bipolar quantum hall edge transport around graphene antidots. *Sci. Rep.*, 5(1):1–8, 2015.

[111] C. Schilling and R. Schilling. Number-parity effect for confined fermions in one dimension. *Phys. Rev. A*, 93:021601, 2016.

[112] E. T. Mannila, V. F. Maisi, H. Q. Nguyen, C. M. Marcus, and J. P. Pekola. Detecting parity effect in a superconducting device in the presence of parity switches. *Phys. Rev. B*, 100:020502, 2019.

[113] D. Agboola, P. S. Isaac, and J. Links. Energy-level crossings and number-parity effects in a bosonic tunneling model. *J. Phys. B: At. Mol. Opt. Phys.*, 51(14):145301, jun 2018.

[114] H.-N. Dai, B. Yang, A. Reingruber, H. Sun, X.-F. Xu, Y.-A. Chen, Z.-S. Yuan, and J.-W. Pan. Four-body ring-exchange interactions and anyonic statistics within a minimal toric-code hamiltonian. *Nat. Phys.*, 13(12):1195–1200, 2017.

[115] M. J. Gibbons, S. Y. Kim, K. M. Fortier, P. Ahmadi, and M. S. Chapman. Achieving very long lifetimes in optical lattices with pulsed cooling. *Phys. Rev. A*, 78:043418, Oct 2008.

[116] R. Islam, R. Ma, P. M. Preiss, M. Eric Tai, A. Lukin, M. Rispoli, and M. Greiner. Measuring entanglement entropy in a quantum many-body system. *Nature*, 528(7580):77–83, 2015.

[117] Y. Tang, W. Kao, K-Y Li, S. Seo, Krishnanand Mallayya, M. Rigol, S. Gopalakrishnan, and B. L. Lev. Thermalization near integrability in a dipolar quantum newton's cradle. *Phys. Rev. X*, 8:021030, 2018.

[118] C. Gross, T. Zibold, E. Nicklas, J. Esteve, and M. K. Oberthaler. Nonlinear atom interferometer surpasses classical precision limit. *Nature*, 464(7292):1165–1169, 2010.

[119] R. J. Lewis-Swan and K. V. Kheruntsyan. The ac and dc Josephson effects in a Bose–Einstein condensate. *Nature Commun.*, 5(3752), 2014.

[120] R. Lopes, A. Imanaliev, A. Aspect, M. Cheneau, D. Boiron, and C. I Westbrook. Atomic hong–ou–mandel experiment. *Nature*, 520(7545):66–68, 2015.

[121] J. I. Cirac, M. Lewenstein, K. Mølmer, and P. Zoller. Quantum superposition states of Bose-Einstein condensates. *Phys. Rev. A*, 57(2):1208, 1998.

[122] A. A. Bychek, D. N. Maksimov, and A. R. Kolovsky. NOON state of bose atoms in the double-well potential via an excited-state quantum phase transition. *Phys. Rev. A*, 97(6):063624, 2018.

[123] G. Vanhaele and P. Schlagheck. NOON states with ultracold bosonic atoms via resonance-and chaos-assisted tunneling. *Phys. Rev. A*, 103(1):013315, 2021.

[124] K. Góral, L. Santos, and M. Lewenstein. Quantum phases of dipolar bosons in optical lattices. *Phys. Rev. Lett.*, 88(17):170406, 2002.

[125] Y. Liao et al. Spin-imbalance in a one-dimensional fermi gas. *Nature*, 467(7315):567–569, 2010.

[126] G. Pagano et al. A one-dimensional liquid of fermions with tunable spin. *Nat. Phys.*, 10(3):198–201, 2014.

[127] M. T. Batchelor and A. Foerster. Yang–Baxter integrable models in experiments: from condensed matter to ultracold atoms. *J. Phys. A: Math. Theor.*, 49(17):173001, 2016.

[128] O. Breunig et al. Quantum criticality in the spin-1/2 heisenberg chain system copper pyrazine dinitrate. *Science Adv.*, 3(12):eaao3773, 2017.

[129] Z. Wang et al. Experimental observation of Bethe strings. *Nature*, 554(7691):219–223, 2018.

[130] S. Pilatowsky-Cameo et al. Positive quantum lyapunov exponents in experimental systems with a regular classical limit. *Phys. Rev. E*, 101(1):010202, 2020.

[131] N. Y. Yao, S. D. Bennett, C. R. Laumann, B. L. Lev, and Alexey V Gorshkov. Bilayer fractional quantum hall states with dipoles. *Phys. Rev. A*, 92(3):033609, 2015.

[132] S. Baier, M. J. Mark, D..... Petter, K. Aikawa, L. Chomaz, Zi Cai, M. Baranov, P. Zoller, and F. Ferlaino. Extended Bose-Hubbard models with ultracold magnetic atoms. *Science*, 352(6282):201–205, 2016.

[133] D. S. Grün, L. H. Ymai, A. P. Tonel, A. Foerster, and J. Links. Integrable atomtronic interferometry. *Phys. Rev. Lett.*, 129(2):020401, 2022.

[134] B. Yang et al. Observation of gauge invariance in a 71-site bose–hubbard quantum simulator. *Nature*, 587(7834):392–396, 2020.

[135] T. Fukuhara, S. Hild, J. Zeiher, P. Schauß, I. Bloch, Ma. Endres, and C. Gross. Spatially resolved detection of a spin-entanglement wave in a Bose-Hubbard chain. *Phys. Rev. Lett.*, 115(3):035302, 2015.

[136] F. Schäfer, T. Fukuhara, S. Sugawa, Y. Takasu, and Y. Takahashi. Tools for quantum simulation with ultracold atoms in optical lattices. *Nat. Rev. Phys.*, 2(8):411–425, 2020.

[137] S. Müller, J. Billy, E.A.L. Henn, H. Kadau, A. Griesmaier, M. Jona-Lasinio, L. Santos, and T. Pfau. Stability of a dipolar Bose-Einstein condensate in a one-dimensional lattice. *Phys. Rev. A*, 84(5):053601, 2011.

[138] V. Zelevinsky, B. A. Brown, N. Frazier, and M. Horoi. The nuclear shell model as a testing ground for many-body quantum chaos. *Phys. Rep.*, 276(2):85–176, 1996.

[139] F. Borgonovi, F. M. Izrailev, L. F. Santos, and V. G. Zelevinsky. Quantum chaos and thermalization in isolated systems of interacting particles. *Phys. Rep.*, 626:1, 2016.

[140] L. D' Alessio, Y. Kafri, A. Polkovnikov, and M. Rigol. From quantum chaos and eigenstate thermalization to statistical mechanics and thermodynamics. *Adv. Phys.*, 65(3):239–362, 2016.

[141] J. Maldacena, S. H. Shenker, and D. Stanford. A bound on chaos. *J. High Energy Phys.*, 2016(8):106, 2016.

[142] Forthcoming publication.

[143] K. Wittmann W., E. R. Castro, A. Foerster, and Lea F. Santos. Interacting bosons in a triple well: Preface of many-body quantum chaos. *Phys. Rev. E*, 105:034204, 2022.

[144] J. Links, A. Foerster, A. Tonel, and G. Santos. The two-site Bose-Hubbard model. *Ann. Henri Poincaré*, 7:1591, 2006.

[145] A. P. Tonel, J. Links, and A. Foerster. Behaviour of the energy gap in a model of Josephson coupled Bose–Einstein condensates. *J. Phys. A*, 38(31):6879–6891, 2005.

[146] H. Fritz. *Quantum Signatures of Chaos*. Springer-Verlag, Berlin, 1991.

[147] T. Guhr, A. Mueller-Gröeling, and H. A. Weidenmüller. Random Matrix Theories in Quantum Physics: Common Concepts. *Phys. Rep.*, 299:189, 1998.

[148] A. Pandey and R. Ramaswamy. Level spacings for harmonic-oscillator systems. *Phys. Rev. A*, 43:4237–4243, 1991.

[149] B. V. Chirikov and D. L. Shepelyansky. Shnirelman Peak in Level Spacing Statistics. *Phys. Rev. Lett.*, 74:518–521, 1995.

[150] L. F. Santos, F. Borgonovi, and F. M. Izrailev. Onset of chaos and relaxation in isolated systems of interacting spins: Energy shell approach. *Phys. Rev. E*, 85:036209, 2012.

[151] L. Pausch, E. G. Carnio, A. Buchleitner, and A. Rodríguez. Chaos in the Bose–Hubbard model and random two-body Hamiltonians. *New J. Phys.*, 23(12):123036, 2021.

[152] J. B. French and S.S.M. Wong. Validity of random matrix theories for many-particle systems. *Phys. Lett. B*, 33(7):449, 1970.

[153] T. A. Brody, J. Flores, J. B. French, P. A. Mello, A. Pandey, and S. S. M. Wong. Random-matrix physics: spectrum and strength fluctuations. *Rev. Mod. Phys.*, 53:385, 1981.

[154] M. A. Bastarrachea-Magnani, S. Lerma-Hernández, and J. G. Hirsch. Comparative quantum and semiclassical analysis of atom-field systems. I. Density of states and excited-state quantum phase transitions. *Phys. Rev. A*, 89:032101, 2014.

[155] M. Schiulaz, M. Távora, and Lea F. Santos. From few- to many-body quantum systems. *Quantum Sci. Technol.*, 3(4):044006, 2018.

[156] T. Fogarty, M. Á. García-March, Lea F. Santos, and N. L. Harshman. Probing the edge between integrability and quantum chaos in interacting few-atom systems. *Quantum*, 5:486, 2021.

[157] M. L. Mehta. *Random Matrices*. Elsevier Academic Press, Amsterdam, 2004.

[158] P. R. Zangara, A. D. Dente, E. J. Torres-Herrera, Ho. M. Pastawski, A. Iucci, and Lea F. Santos. Time fluctuations in isolated quantum systems of interacting particles. *Phys. Rev. E*, 88:032913, 2013.

[159] F. M. Izrailev. Simple models of quantum chaos: Spectrum and eigenfunctions. *Phys. Rep.*, 196(5):299 – 392, 1990.

[160] Lea F. Santos and M. Rigol. Onset of quantum chaos in one-dimensional bosonic and fermionic systems and its relation to thermalization. *Phys. Rev. E*, 81:036206, 2010.

[161] M. Rigol and L. F. Santos. Quantum chaos and thermalization in gapped systems. *Phys. Rev. A*, 82:011604(R), 2010.

[162] Lea F. Santos, F. Pérez-Bernal, and E. J. Torres-Herrera. Speck of chaos. *Phys. Rev. Research*, 2:043034, 2020.

[163] L. Leviandier, M. Lombardi, R. Jost, and J. P. Pique. Fourier Transform: A Tool to Measure Statistical Level Properties in Very Complex Spectra. *Phys. Rev. Lett.*, 56:2449–2452, 1986.

[164] T. Guhr and H.A. Weidenmüller. Correlations in anticrossing spectra and scattering theory. Analytical aspects. *Chem. Phys.*, 146:21 – 38, 1990.

[165] J. Wilkie and P. Brumer. Time-dependent manifestations of quantum chaos. *Phys. Rev. Lett.*, 67:1185–1188, 1991.

[166] Y. Alhassid and R. D. Levine. Spectral autocorrelation function in the statistical theory of energy levels. *Phys. Rev. A*, 46:4650–4653, 1992.

[167] T. Gorin and T. H. Seligman. Signatures of the correlation hole in total and partial cross sections. *Phys. Rev. E*, 65:026214, 2002.

[168] E. J. Torres-Herrera and Lea F. Santos. Dynamical manifestations of quantum chaos: correlation hole and bulge. *Philos. Trans. Royal Soc. A*, 375(2108):20160434, 2017.

[169] J. de la Cruz, S. Lerma-Hernández, and J. G. Hirsch. Quantum chaos in a system with high degree of symmetries. *Phys. Rev. E*, 102:032208, 2020.

[170] R. E. Prange. The spectral form factor is not self-averaging. *Phys. Rev. Lett.*, 78:2280, 1997.

[171] M. Schiulaz, E. J. Torres-Herrera, F.o Pérez-Bernal, and Lea F. Santos. Self-averaging in many-body quantum systems out of equilibrium: Chaotic systems. *Phys. Rev. B*, 101:174312, 2020.

[172] M. Winer and B. Swingle. Hydrodynamic theory of the connected spectral form factor. *Phys. Rev. X*, 12:021009, 2022.

[173] S. Lerma-Hernández, D. Villaseñor, M. A. Bastarrachea-Magnani, E. J. Torres-Herrera, L. F. Santos, and J. G. Hirsch. Dynamical signatures of quantum chaos and relaxation time scales in a spin-boson system. *Phys. Rev. E*, 100:012218, 2019.

[174] E. J. Torres-Herrera, A. M. García-García, and Lea F. Santos. Generic dynamical features of quenched interacting quantum systems: Survival probability, Density imbalance, and out-of-time-ordered correlator. *Phys. Rev. B*, 97:060303, 2018.

[175] M. Schiulaz, E. J. Torres-Herrera, and Lea F. Santos. Thouless and relaxation time scales in many-body quantum systems. *Phys. Rev. B*, 99:174313, 2019.

[176] L. A. Khalfin. Contribution to the decay theory of a quasi-stationary state. *Sov. Phys. JETP*, 6:1053, 1958.

[177] M. Távora, E. J. Torres-Herrera, and Lea F. Santos. Inevitable power-law behavior of isolated many-body quantum systems and how it anticipates thermalization. *Phys. Rev. A*, 94:041603, Oct 2016.

[178] Y. Yang, S. Iblisdir, J. I. Cirac, and M. C. Bañuls. Probing thermalization through spectral analysis with matrix product operators. *Phys. Rev. Lett.*, 124:100602, 2020.

[179] E. J. Torres-Herrera, J. Karp, M. Távora, and L. F. Santos. Realistic Many-Body Quantum Systems vs. Full Random Matrices: Static and Dynamical Properties. *Entropy*, 18:359, 2016.

[180] John W. Tukey. Exploratory data analysis., 1977. *Massachusetts: Addison-Wesley*, 1976.

[181] A. Solórzano, Lea F. Santos, and E. J. Torres-Herrera. Multifractality and self-averaging at the many-body localization transition. *Phys. Rev. Res.*, 3:L032030, 2021.

[182] F. Wegner. Inverse participation ratio in $2 + \varepsilon$ dimensions. *Z. Phys. B*, 36:209, 1980.

[183] F. Evers and A. D. Mirlin. Anderson transitions. *Rev. Mod. Phys.*, 80:1355–1417, 2008.

[184] Lea F. Santos and M. Rigol. Localization and the effects of symmetries in the thermalization properties of one-dimensional quantum systems. *Phys. Rev. E*, 82:031130, 2010.

[185] W. Beugeling, R. Moessner, and M. Haque. Off-diagonal matrix elements of local operators in many-body quantum systems. *Phys. Rev. E*, 91:012144, 2015.

[186] I. M. Khaymovich, M. Haque, and P. A. McClarty. Eigenstate thermalization, random matrix mheory, and behemoths. *Phys. Rev. Lett.*, 122:070601, 2019.

[187] P. Łydżba, Y. Zhang, M. Rigol, and L. Vidmar. Single-particle eigenstate thermalization in quantum-chaotic quadratic Hamiltonians. *Phys. Rev. B*, 104:214203, 2021.

[188] R. A. Kidd, M. K. Olsen, and J. F. Corney. Quantum chaos in a Bose-Hubbard dimer with modulated tunneling. *Phys. Rev. A*, 100:013625, 2019.

[189] R. A. Kidd, A. Safavi-Naini, and J. F. Corney. Thermalization in a Bose-Hubbard dimer with modulated tunneling. *Phys. Rev. A*, 102:023330, 2020.

[190] R.-B. Jin, R. Shimizu, M. Sasaki, et al. Simple method of generating and distributing frequency-entangled qudits. *Quantum Sci. Technol.*, 1(1):015004, 2016.

[191] M. Kues et al. On-chip generation of high-dimensional entangled quantum states and their coherent control. *Nature*, 546(7660):622–626, 2017.

[192] P. Imany, A. M. Weiner, et al. High-dimensional optical quantum logic in large operational spaces. *Npj Quantum Inf.*, 5(1):1–10, 2019.

[193] A. Z. Khoury, A. M. Souza, L. E. Oxman, I. Roditi, R. S. Sarthour, and I. S. Oliveira. Intrinsic bounds of a two-qudit random evolution. *Phys. Rev. A*, 97:042343, 2018.

[194] J. W. Z. Lau, K. S. Gan, R. Dumke, L. Amico, L.-C. Kwek, and T. Haug. Atomtronic multi-terminal Aharonov-Bohm interferometer. *arXiv preprint arXiv:2205.01636*, 2022.

[195] U. G. E. Perera, F. Ample, H. Kersell, Y. Zhang, G. Vives, J. Echeverria, M. Grisolia, G. Rapenne, C. Joachim, and S-W. Hla. Controlled clockwise and anticlockwise rotational switching of a molecular motor. *Nat. Nanotechnol*, 8(1):46–51, 2013.

[196] Y. Zhang, J. P. Calupitan, T. Rojas, R. Tumbleson, G. Erbland, C. Kammerer, T. M. Ajayi, S. Wang, L. A. Curtiss, A. T. Ngo, et al. A chiral molecular propeller designed for unidirectional rotations on a surface. *Nat. Commun*, 10(1):1–9, 2019.

[197] P. W. Claeys, S. De Baerdemacker, O. E. Araby, and J.-S. Caux. Spin polarization through floquet resonances in a driven central spin model. *Phys. Rev. Lett.*, 121:080401, 2018.

[198] J. Liouville. Note sur l'intégration des équations différentielles de la dynamique, présentée au bureau des longitudes le 29 juin 1853. *Journal de Mathématiques pures et appliquées*, pages 137–138, 1855.

[199] V. I. Arnol'd. *Mathematical methods of classical mechanics*, volume 60. Springer Science & Business Media, 2013.

[200] P. Calabrese, Fabian H. L. Essler, and G. Mussardo. Introduction to 'quantum integrability in out of equilibrium systems'. *J. Stat. Mech.*, 2016(6):064001, 2016.

[201] A. Einstein. Sobre o teorema quântico de sommerfeld e de epstein. *Rev. Bras. Ens. de Fis.[online]*, 27(1):103–107, 2005.

[202] J. Liouville. Note sur la théorie de la variation des constantes arbitraires. *Journal de mathématiques pures et appliquées*, pages 342–349, 1838.

[203] Hans Bethe. Zur theorie der metalle. *Zeitschrift für Physik*, 71(3):205–226, 1931.

[204] E. H. Lieb and W. Liniger. Exact analysis of an interacting bose gas. i. the general solution and the ground state. *Phys. Rev.*, 130:1605–1616, 1963.

[205] E. H. Lieb. Exact analysis of an interacting bose gas. ii. the excitation spectrum. *Phys. Rev.*, 130:1616–1624, 1963.

[206] E. K. Sklyanin, L. A. Takhtadzhyan, and L. D. Faddeev. Quantum inverse problem method. i. *Th. and Math. Phys.*, 40:688–706, 1979.

[207] L. D. Faddeev. History and perspectives of quantum groups. *Milan J. Math.*, 74(1):279–294, 2006.

[208] Luca Mezincescu and Rafael I. Nepomechie. Analytical Bethe Ansatz for quantum-algebra-invariant spin chains. *Nuclear Phys. B*, 372(3):597–621, 1992.

[209] A. Foerster and E. Ragoucy. Exactly solvable models in atomic and molecular physics. *Nucl. Phys. B*, 777(3):373–403, 2007.

[210] Y. Wang, W.-L. Yang, J. Cao, and K. Shi. *Off-diagonal Bethe ansatz for exactly solvable models*. Springer Berlin Heidelberg., 2015.

[211] R. J. Baxter. *Exactly Solved Models in Statistical Mechanics*. Academic Press, Australian, 1982.

[212] L. D. Faddeev. Algebraic aspects of the bethe ansatz. *International J. Modern Phys. A*, 10(13):1845–1878, 1995.

[213] H. M. Babujian, A. Foerster, and M. Karowski. Exact form factors of the SU (N) Gross–Neveu model and 1/n expansion. *Nucl. Phys. B*, 825(3):396–425, 2010.

[214] A. Foerster and M. Karowski. Algebraic properties of the Bethe ansatz for an spl (2, 1)-supersymmetric t-j model. *Nucl. Phys. B*, 396(2-3):611–638, 1993.

[215] V. E. Korepin and F. H.. Essler. *Exactly solvable models of strongly correlated electrons*. World Scientific, London, 1994.

[216] J. Links and A. Foerster. Solution of a two-leg spin ladder system. *Phys. Rev. B*, 62:65–68, 2000.

[217] G. Santos, A. Tonel, A. Foerster, and J. Links. Classical and quantum dynamics of a model for atomic-molecular Bose-Einstein condensates. *Phys. Rev. A*, 73:023609, 2006.

[218] M. Duncan, A. Foerster, J. Links, E. Mattei, N. Oelkers, and A. P. Tonel. Emergent quantum phases in a heteronuclear molecular Bose–Einstein condensate model. *Nucl. Phys. B*, 767(3):227–249, 2007.

[219] G. Santos, A. Foerster, J. Links, E. Mattei, and S. R. Dahmen. Quantum phase transitions in an interacting atom-molecule boson model. *Phys. Rev. A*, 81:063621, 2010.

[220] D. Rubeni, A. Foerster, E. Mattei, and I. Roditi. Quantum phase transitions in Bose–Einstein condensates from a Bethe ansatz perspective. *Nucl. Phys. B*, 856(3):698–715, 2012.

[221] N. Beisert, C. Ahn, L.F. Alday, Z. Bajnok, J.M. Drummond, L. Freyhult, N. Gromov, R.A. Janik, V. Kazakov, T. Klose, and G.P. Korchemsky. Review of Ads/CFT integrability: An overview. *Lett. Math. Phys.*, 99:3–32, 2012.